GROWTH, CHARACTERIZATION AND POST-PROCESSING OF INORGANIC AND HYBRID ORGANIC-INORGANIC THIN FILMS DEPOSITED USING ATOMIC AND MOLECULAR LAYER DEPOSITION TECHNIQUES

by

AZIZ ILMUTDINOVICH ABDULAGATOV

B.S. Honors, Dagestan State Technical University (Russian Federation), l998

A thesis submitted to the

Faculty of the Graduate School of the

University of Colorado in partial fulfillment

of the requirement for the degree of

Doctor of Philosophy

Department of Chemistry and Biochemistry

2012

This thesis entitled:
Growth, Characterization and Post-processing of Inorganic and Hybrid Organic-inorganic Thin Films Deposited using Atomic and Molecular Layer Deposition Techniques
written by Aziz Ilmutdinovich Abdulagatov
has been approved for the Department of Chemistry and Biochemistry

_____
Professor Steven M. George

_____
Professor Cortlandt G. Pierpont

Date_____

The final copy of this thesis has been examined by the signatories, and we find that both the content and the form meet acceptable presentation standards of scholarly work in the above mentioned discipline.

Abdulagatov, Aziz Ilmutdinovich (Ph.D., Chemistry)

Growth, Characterization and Post-processing of Inorganic and Hybrid Organic-inorganic Thin Films Deposited using Atomic and Molecular Layer Deposition Techniques

Thesis directed by Professor Steven M. George

Abstract

Atomic layer deposition (ALD) and molecular layer deposition (MLD) are advanced thin film coating techniques developed for deposition of inorganic and hybrid organic-inorganic films respectively.

Decreasing device dimensions and increasing aspect ratios in semiconductor processing has motivated developments in ALD. The beginning of this thesis will cover study of new ALD chemistry for high dielectric constant Y_2O_3. In addition, the feasibility of conducting low temperature ALD of TiN and TiAlN is explored using highly reactive hydrazine as a new nitrogen source. Developments of these ALD processes are important for the electronics industry.

As the search for new materials with more advanced properties continues, attention has shifted toward exploring the synthesis of hierarchically nanostructured thin films. Such complex architectures can provide novel functions important to the development of state of the art devices for the electronics industry, catalysis, energy conversion and memory storage as a few examples. Therefore, the main focus of this thesis is on the growth, characterization, and post-processing of ALD and MLD films for fabrication of novel composite (nanostructured) thin films.

Novel composite materials are created by annealing amorphous ALD oxide alloys in air and by heat treatment of hybrid organic-inorganic MLD films in inert atmosphere (pyrolysis).

The synthesis of porous TiO_2 or Al_2O_3 supported V_2O_5 for enhanced surface area catalysis was achieved by the annealing of inorganic TiV_xO_y and AlV_xO_y ALD films in air. The interplay between phase separation, surface energy difference, crystallization, and melting temperature of individual oxides were studied for their control of film morphology.

In other work, a class of novel metal oxide-graphitic carbon composite thin films was produced by pyrolysis of MLD hybrid organic-inorganic films. For example, annealing in argon of titania based hybrid films enabled fabrication of thin films of intimately mixed TiO_2 and nanographitized carbon. The graphitized carbon in the film was formed as a result of the removal of hydrogen by pyrolysis of the organic constituency of the MLD film. The presence of graphitic carbon allowed a 14 orders of magnitude increase in the electrical conductivity of the composite material compared fully oxidized rutile TiO_2.

To My Parents

ACKNOWLEDGEMENTS

First of all I would like to acknowledge my family for being patient with me. In particular, my father Ilmutdin and my mother Gulnaz, who made it possible that I could have a better life. I would like to acknowledge my dear wife Emily. This would not be possible without you. You are a great example to me of professionalism and wisdom. To my sister Alisa, nephew Khalil and my son Maximka who are my foundation. Great thanks to my in-laws Laurie Gibson and Lyle Powers. You have helped my family a lot through the years. I know I can always rely on you and it means a lot to me. I would like to acknowledge my role models - my dad Ilmutdin and uncle Zaid for their loyalty and devotion to science. You always were and always will be a great inspiration for me. I acknowledge my philosophy teacher in graduate school in Russia, Professor U.A. Radgabov who seeded in me affection for classical German philosophy that has had a tremendous influence on my world views.

Special thanks to my advisor Professor Steven George for believing in me and for providing me with the unique opportunity to explore and discover things which made me truly happy. I don't know what is ahead for me but I am sure I will miss my time in Steve's lab. I would like to thank my many current and former lab mates in particular Beau, Rik, Dragos, Andrew, Virginia, Rob, Jake, Jon, Ming, Jun, Layton, Daniel, Matthias, Byunghoon, Byoung H. Lee, Younghee, Zach, and Jackson for their professional assistance and friendship. I would like to thank our mechanical engineering department collaborators Professors YC Lee, Ronggui Yang

and their postdocs Li-Ann Liew, Wei Wang and graduate students Miao Tain, Yadong Zang. My collaborator from Colorado School of Mines, Dr. Prakash Periasamy, for his enthusiasm and interesting discussions. I would like to thank Professor Rishi Raj and his graduate student Kalvis Terauds for their assistance and opening for me an exciting area of nanomaterials and polymer derived ceramics.

I also would like to thank Professor A.A. Malygin from Saint-Petersburg State Institute of Technology (Russia) for introducing me to the world of Molecular Layering (one of the original names for ALD). For the past two years of my graduate research, I was moved by the work of ALD pioneers Professor V.B. Aleskovskii, corresponding member of the Russian Academy of Sciences, and Professor S.I. Kol'tsov. I found their unique, many-sided view on chemical assembly and great scientific intuition to be truly remarkable.

CONTENTS

CHAPTER

I. INTRODUCTION 1

1.1 Thin Film Technology 1

1.2 Atomic Layer Deposition: Principals and Attributes 4

1.2.1 Historical Aspects Development of ALD 7

1.3 Molecular Layer Deposition 9

1.4 Statement of Purpose 11

1.5 References 14

II. EXPERIMENTAL 17

2.1 Viscous Flow Reactor 17

2.2 Quartz Crystal Microbalance 18

2.3 X-ray Diffraction 20

2.4 X-ray Photoelectron Spectroscopy 22

2.5 Raman Spectroscopy 23

2.6 References 25

III. ATOMIC LAYER DEPOSITION OF Y_2O_3 USING TRIS(BUTYLCYCLOPENTADIENYL)YTTRIUM AND WATER 26

3.1 Introduction 26

3.2 Experimental 29

3.3 Results and Discussion 32

3.3.1 QCM Study and Deposition on Si 32

3.3.2 Proposed ALD Y_2O_3 Growth Mechanism 41
3.3.3 Film Characterization 44
3.3.4 Optical Properties 48
3.4 Conclusions 50
3.5 Acknowledgements 51
3.6 References 52

IV. ATOMIC LAYER DEPOSITION OF TiN USING $TiCl_4$ AND HYDRAZINE 56
4.1 Introduction 56
4.2 Experimental 59
4.3 Results and Discussion 62
4.3.1 QCM Study and Deposition on Si 62
4.3.2 X-ray Reflectivity and X-ray Diffraction Study 67
4.3.3 XPS and SEM Film Characterization 74
4.3.4 FTIR Study 79
4.3.5 Properties of ALD TiN_x and $TiAl_xN_y$ 81
4.3.5.1 Electrical Properties 85
4.3.5.2 Optical Properties 86
4.4 Conclusions 88
4.5 References 89

V. Al_2O_3 AND TiO_2 ATOMIC LAYER DEPOSITION ON COPPER FOR WATER CORROSION RESISTANCE 95
5.1 Introduction 95

5.2 Experimental 97

5.3 Results and Discussion 101

5.3.1 Nucleation and Growth of Al_2O_3 ALD on Copper 101

5.3.2 Characterization of Al_2O_3 ALD Films on Copper 105

5.3.3 TiO_2 ALD on Copper 108

5.3.4 Corrosion Protection of Cu using Al_2O_3 and TiO_2 ALD 110

5.3.5 Dissolution of Al_2O_3, ZnO and TiO_2/Al_2O_3 ALD Films 118

5.3.6 Wetting Properties of TiO_2 ALD Coated Copper 120

5.4 Conclusions 122

5.5 Acknowledgements 123

5.6 References 125

VI. MOLECULAR LAYER DEPOSITION OF HYBRID ALUMINA/SILOXANE THIN FILMS....129

6.1 Introduction 129

6.2 Experimental 131

6.3 Results and Discussion 134

6.3.1 MLD of Polydimethylsiloxane (PDMS) 134

6.3.2 Growth of Hybrid alumina/siloxane MLD using DMMCS 137

6.3.3 Growth of Hybrid alumina/siloxane MLD using DIPS....145

6.4 Conclusions 159

6.5 Acknowledgements 160

6.6 References 161

VII. ATOMIC LAYER DEPOSITION OF TiVxOy AND AlVxOy ALLOYS AND EFFECT OF ANNEALING ON FILM MORPHOLOGY 164

7.1 Introduction 164

7.2 Experimental 166

7.3 Results and Discussion 170

7.3.1 Nucleation and Growth of ALD V_2O_5 on Al_2O_3 and TiO_2 170

7.3.2 ALD of TiV_xO_y and AlV_xO_y 175

7.3.2.1 QCM Study 175

7.3.2.2 XRR and XPS Analysis 180

7.3.2.3 Optical Properties 182

7.3.3 Annealing Experiments 185

7.3.3.1 ALD $TiVO_3$ Oxide 185

7.3.3.2 ALD $AlVO_4$ Oxide 195

7.4 Conclusions 199

7.5 Acknowledgements 200

7.6 References 201

VIII. MOLECULAR LAYER DEPOSITION TITANICONE FILMS USING $TiCl_4$ AND ETHYLENE GLYCOL OR GLYCEROL: GROWTH AND PROPERTIES ..207

8.1 Introduction 207

8.2 Experimental 211

8.3 Results and Discussion 214

8.3.1 Titanicone MLD using $TiCl_4$ and Ethylene Glycol 214

8.3.1.1 Quartz Crystal Microbalance Studies 214

8.3.1.2 XRR and XPS Analysis 219

8.3.2 Titanicone MLD using $TiCl_4$ and Glycerol 224

8.3.2.1 Quartz Crystal Microbalance Studies 224

8.3.2.2 XRR and XPS Analysis 226

8.3.3 Titanicone Film Properties 228
8.3.3.1 Mechanical Properties 228
8.3.3.2 Effect of Thermal Annealing 229
8.3.3.3 Optical Properties 232
8.3.3.4 Effect of UV Exposure 235
8.4 Conclusions 237
8.5 Acknowledgements 238
8.6 References 240

IX. SYNTHESIS OF METAL OXIDE-CARBON COMPOSIT THIN FILMS BY PYROLYSIS OF MLD FILMS 244
9.1 Introduction 244
9.2 Experimental 246
9.3 Results and Discussion 249
9.3.1 Spectroscopic Characterization Pyrolyzed TiGL MLD Films 249
9.3.1.1 Raman Spectroscopy 249
9.3.1.2 X-ray Diffraction 252
9.3.1.3 Optical and SEM imaging 255
9.3.1.4 X-ray Photoelectron Spectroscopy 256
9.3.2 Electrical Properties of Pyrolyzed TiGL Films 259
9.3.3 Pyrolysis of Various Matalacone MLD Films 262
9.4 Conclusions 270
9.5 Acknowledgements 271
9.6 References 272

BIBLIOGRAPHY 279

TABLES

Table

6.1 Vibrational frequencies observed in the FTIR difference spectra in Fig. 6.9 after the DIPS, TMA and H_2O exposures and their assignments.....155

FIGURES

Figure

1.1 Two half-reactions of ALD Al_2O_3……..5

1.2 Two half-reactions of MLD Alucone……10

2.1 Schematic view of hot wall viscous flow reactor for thin film ALD and MLD growth.....17

2.2 Geometry of bulk diffraction from a stack of X-Y atomic planes……...20

2.3 Principle of X-ray photoelectron spectroscopy……22

3.1 QCM response during Y_2O_3 ALD linear growth regime using 8/10/0.2/150 deposition timing……..32

3.2 QCM mass gain and mass loss during individual precursor exposures when the 8/10/0.2/150 timing used……..33

3.3 QCM measured Y_2O_3 growth rate as function of $Y(CpBut)_3$ dose time deposited using the X/10/0.2/150 timing sequence……34

3.4 (a) QCM response during first Y_2O_3 ALD cycles on alumina surface deposited using 1/60/1/60 timing (b) QCM response after ~500 ALD cycles when 8/60/1/60 timing used. ……..35

3.5 QCM measured non self-limiting Y_2O_3 growth during $Y(CpBut)_3$ uptake when X/60/1/60 timing used. ……..37

3.6 Ellipsometer measured Y_2O_3 film thickness on Si<100> versus purge time for warring water doses and purge times deposited using the 2/10/Y/X timing.....38

3.7 Ellipsometer measured Y_2O_3 film deposited on Si<100> using the 8/10/0.2/150 timing conditions as a function of the number of deposition cycles…….....39

3.8 Y_2O_3 growth rate versus deposition temperature measured by ellipsometer for 50 A-B cycled deposited on silicon substrate using 8/10/0.2/150 timing.……..40

3.9 Proposed reaction pathways for Y_2O_3 ALD using $Y(CpBut)_3$ and water.……43

3.10 XRD spectrum of a 350 Å thick Y_2O_3 film deposited on Si<100> using 8/10/0.2/150 timing.....44

3.11 RBS spectrum of 500 Å Y_2O_3 film deposited on Si<100> with timing sequence 8/10/1/150.....46

3.12 XPS survey scan of the O (1s) region acqured from 335 Å thick Y_2O_3 film deposited using 8/10/0.2/150 timing at 230°C (solid line) and O (1s) region spectra of the same sample after Ar^+ sputtering (dashed line) 47

3.13 Ellipsometer measured refractive index of as deposited and ALD alumina capped Y_2O_3 films compared to previously reported refractive index data for Y_2O_3 exposited to air and those measured in vacuum.....49

4.1 (a) TiN_x linear growth monitored by the QCM during ALD deposition using 3/40/3/40 timing at 200°C and 225°C.....63

4.2 (a) Expanded view of QCM profile during ALD TiN_x deposition using 3/40/3/40 timing at 225°C.....64

4.3 TiN_x mass gain per cycle vs. different $TiCl_4$ exposure times during deposition at 200°C and 225°C using x/40/3/40 timing sequence. 65

4.4 TiN_x mass gain per cycle vs. N_2H_4 exposure times during deposition at 200°C and 225°C using 3/40/x/40 timing sequence.....66

4.5 XRR obtained growth rate and film density of ALD TiN_x films deposited on Si<100> using 300 cycles and 3/40/3/40 timing sequence at different temperatures.....68

4.6 XRR determined TiN_x film thicknesses vs. number of deposition cycles obtained by deposition at 275°C on Si<100> using 3/40/3/40 ALD timing sequence.....69

4.7 GIXRD difractogram obtained for 600 Å thick TiN_x ALD film grown using 3/40/3/40 timing at 275°C.....72

4.8 XPS depth profile for 300 Å thick TiN_x ALD film grown using 3/40/3/40 timing at 275°C.....75

4.9 XPS depth profile for 600 Å $TiAl_xN_y$ ALD film grown using 3/50/4.5/50/4/50/4.5/50 timing sequence at 275°C.....76

4.10 SEM images of 4:1 aspect ratio silicon patterned trench after 2000 cycles of ALD TiN_x deposited at 275°C where (a) is the image of the top of the trench and (b) of the bottom of the trench……78

4.11 FTIR difference spectra after exposure of $TiCl_4$ and N_2H_4 during the 3th TiN_x ALD cycle at 200°C and 275°C. Each spectrum is referenced to the spectrum previous to reactant exposure……80

4.12 Comparison of the FTIR difference spectra after the 2th cycle exposure of NH_3 at 350°C, 425°C and N_2H_4 exposure at 275°C during TiN_x ALD. Each spectrum is referenced to the spectrum of previous reactant exposure. ……84

4.13 Proposed reaction mechanism of N_2H_4 with $TiCl_x$ terminated surface at different TiN_x deposition temperatures……85

4.14 Optical constants (n and k) of the 600 Å TiN_x films deposited at 275°C compared to TiN reference data [62]……87

5.1 Mass gain versus time recorded during first five Al_2O_3 ALD cycles on copper plated QCM sensor at 177°C……102

5.2 (a) Mass gain versus cycle number for Al_2O_3 ALD on copper-plated QCM sensor at 177°C showing TMA mass gain, H_2O mass gain and total mass gain. (b) Ratio of the TMA mass gain and the H_2O mass gain versus cycle number for the mass gains shown in (a)……103

5.3 Atomic concentration versus sputtering cycle for Al_2O_3 ALD film with a thickness of 620 Å deposited on copper substrate at 177°C……106

5.4 Defect density versus electroplating time for Al_2O_3 ALD film with a thickness of 250 Å deposited on copper substrate at 177°C……107

5.5 AFM images of: (a) 300 cycles of TiO_2 ALD grown on copper substrate at 120°C; and (b) TiO_2 capping layer with a thickness of 180 Å on Al_2O_3 adhesion layer with a thickness of 40 Å grown on copper substrate at 120°C……109

5.6 Optical microscope images of copper substrates after 75 hours in water at 90°C with: (a) no coating; and (b) Al_2O_3 ALD coating with thickness of 200 Å grown at 120°C……111

5.7 Optical microscope images of copper substrates after 75 hours in water at 90°C with: (a) 300 cycles of TiO_2 ALD at 120°C; and (b) TiO_2 capping layer with a thickness of 180 Å on Al_2O_3 adhesion layer with a thickness of 40 Å grown at 120°C……113

5.8 Optical microscope images of copper substrates after 900 hours in water at 90°C with: (a) TiO_2 capping layer with a thickness of 37 Å; and (b) TiO_2 capping layer with a thickness of 37 Å. The TiO_2 capping layers were on Al_2O_3 adhesion layers with a thickness of 40 Å. TiO_2 and Al_2O_3 ALD were performed at 120°C……114

5.9 Optical microscope images of copper substrates after 900 hours in water at 90°C with: (a) TiO_2 capping layer with a thickness of 127 Å; and (b) TiO_2 capping layer with a thickness of 242 Å. The TiO_2 capping layers were on Al_2O_3 adhesion layers with a thickness of 40 Å. TiO_2 and Al_2O_3 ALD were performed at 120°C…115

5.10 Corroded area on copper substrate derived using ImageJ versus time in water at 25°C and 90°C for bare copper and copper coated with Al_2O_3 ALD, ZnO ALD, and both Al_2O_3 and TiO_2 ALD. The film thicknesses were 200 Å for the Al_2O_3 coating and 250 Å for the ZnO coating. For the TiO_2/Al_2O_3 coating, the Al_2O_3 adhesion layer thickness was 55 Å and the TiO_2 capping layer thickness was 200 Å. All ALD films were grown at 120°C……117

5.11 Effective film thickness on copper substrate versus time in 90°C water for Al_2O_3, ZnO and TiO_2/Al_2O_3 ALD coatings. For the TiO_2/Al_2O_3 coating, the Al_2O_3 adhesion layer thickness was 55 Å and the TiO_2 capping layer thickness was 200 Å. All ALD films were grown at 120°C……..119

5.12 Water contact angle measurements for: (a) bare woven copper mesh with 5 µm wire size; and (b) copper mesh with TiO_2 capping layer thickness of 100 Å on Al_2O_3 adhesion layer thickness of 55 Å. The TiO_2 and Al_2O_3 ALD films were grown at 120°C……121

6.1 QCM signal during PDMS CVD with 200s long doses of D3 (a); and 400s long doses of D5 (b) on an ALD Al_2O_3……..134

6.2 QCM signal during PDMS CVD using one 400s long D5 exposure and number of consecutive doses of D3 on ALD Al_2O_3 surface at 200°C reaction temperature……..135

6.3 Schematic representation of alumina/siloxane MLD using DMMCS four step deposition processes……137

6.4 QCM measured mass gain versus time for four step alumina/siloxane MLD using DMMCS. (a) Growth over 30 reaction cycles, (b) expanded view of growth during three reaction cycles……..138

6.5 In situ FTIR difference spectra after TMA, H_2O, and DMMCS exposures during hybrid MLD film growth at 180°C. a) TMA-H_2O after TMA exposure on a film previously reacted with H_2O, b) H_2O-TMA after H_2O exposure on a film previously reacted with TMA, c) DMMCS-H_2O after DMMCS exposure on a film previously reacted with H_2O, and d) H_2O-DMMCS after H_2O exposure on a film previously reacted with DMMCS……142

6.6 Schematic representation of precursor dosing arrangement during three step alumina/siloxane MLD using DIPS……144

6.7 QCM measured mass gain versus time for three step MLD using DIPS. (a) Growth over 50 reaction cycles, (b) expanded view of growth during three reaction cycles……145

6.8 FTIR spectra during the growth of hybrid MLD film using DIPS after 2, 6, 10, and 15 MLD cycles at 150°C……149

6.9 FTIR difference spectra after TMA, H_2O, and DIPS exposures during MLD film growth at 150°C. a) TMA-H_2O after TMA exposure on a film previously reacted with H_2O, b) DIPS-TMA after DIPS exposure on a film previously reacted with TMA, and d) H_2O-DIPS after H_2O exposure on a film previously reacted with DIPS……151

6.10 Integrated absorbance for a) Al-C deformations versus number of TMA microdoses, b) Si-C deformations versus number of DIPS microdoses, and c) O-H stretching vibrations versus number of H_2O microdoses, acquired at 150°C reactor temperature……156

6.11 TEM image of hybrid MLD film deposited using DIPS three step process at 150°C on ~12 Å thick seed layer of ALD alumina……157

7.1 QCM measurements of mass gain versus time for V_2O_5 ALD growth on Al_2O_3 ALD surfaces using $VOCl_3$ and H_2O. (a) Nucleation over 5 cycles using a timing sequence of (3, 25, 3, 25) at 115°C. (b) Change in growth rate per cycle over 55 cycles at 90, 115, 135, and 200°C deposition temperatures……170

7.2 QCM measurements of mass gain versus time for V_2O_5 ALD growth on TiO_2 ALD surfaces using $VOCl_3$ and H_2O at 115°C. (a) Nucleation over 5 reaction cycles using a timing sequence of (3, 25, 3, 25). (b) Change in growth rate over 55 cycles……173

7.3 QCM measurements of mass gain versus time for AlV_xO_y ALD using TMA, $VOCl_3$, and H_2O during steady state growth at 115°C. (a) Expanded view of growth during two reaction cycles of (1:1) AlV_xO_y ALD using timing sequence of (1, 30, 3,

30) for TMA/H_2O and (2, 30, 3, 30) for $VOCl_3/H_2O$ cycles. (b) Expanded view of growth during one reaction cycles of (1:8) AlV_xO_y ALD using the same cycle timing……..……175

7.4 QCM measurements of mass gain versus time for TiV_xO_y ALD using $TiCl_4$, $VOCl_3$, and H_2O during steady state growth at 115°C. (a) Expanded view of growth during two reaction cycles of (1:1) TiV_xO_y ALD using timing sequence of (3, 30, 4, 30) and (3, 30, 4, 30) for $TiCl_4/H_2O$ and $VOCl_3/H_2O$ cycles. (b) Expanded view of growth during one reaction cycle of (1:8) TiV_xO_y ALD using the same cycle timing……..……..……177

7.5 QCM measurements of mass gain versus time for (1:1) and (1:8) of AlV_xO_y, TiV_xO_y ALD during steady state deposition using timing sequence of (1, 30, 3, 30) for TMA/H_2O, and (3, 30, 4, 30) for $TiCl_4/H_2O$ and $VOCl_3/H_2O$ cycles at 115°C……..……..179

7.6 Optical constants of $AlVO_4Cl_{0.2}$, $TiVO_6$, Al_2O_3, and TiO_2 ALD films. The $AlVO_4Cl_{0.2}$ and $TiVO_6$ alloys were deposited with (1:8) arrangement and timing of (1, 30, 3, 30) for TMA/H_2O, and (3, 30, 4, 30) for $TiCl_4/H_2O$ and $VOCl_3/H_2O$ cycles at 115°C. (a) Refractive index versus wavelength and (b) Imaginary part of complex dielectric constant versus photon energy……..……...182

7.7 SEM images of the surface of 360 Å thick $TiVO_6$ ALD films annealed in air for 2 hours at (a) 450°C, (b) 500°C, (c) 550°C..……..……185

7.8 HRTEM images and electron diffraction patterns of the nanocrystals grown on the surface of the 360 Å thick $TiVO_6$ ALD film annealed in air for 2 hours at 450°C……..……..……...188

7.9 HRTEM images and electron diffraction patterns of (a) nanowires grown at on the surface of the 360 Å thick $TiVO_6$ ALD film after annealing in air for 2 hours at 500°C. (b) nanoparticles grown at on the surface of the 360 Å thick $TiVO_6$ ALD film after annealing in air for 2 hours at 550°C……..……..191

7.10 Raman spectra of bare Si<100> wafer and 360 Å thick $TiVO_6$ ALD film annealed in air for 2 hours at 450, 500, and 550°C……..……193

7.11 SEM images of the surface of 770Å thick $AlVO_4Cl_{0.2}$ ALD films annealed in air for 2 hours at (a) 500°C, (b) 550°C, (c) 630°C……..……195

7.12 Raman spectra of bare Si<100> wafer and 770Å thick $AlVO_4Cl_{0.2}$ ALD film annealed in air for 2 hours at 500, 550, and 630°C……..……197

8.1 Schematic of titanicone MLD using $TiCl_4$ and ethylene glycol (EG)……208

8.2 Schematic of titanicone MLD using $TiCl_4$ and glycerol (GL)……209

8.3 QCM measurements of mass gain versus time for titanicone growth on Al_2O_3 ALD surfaces using $TiCl_4$ and EG at 115°C. (a) Growth over 80 reaction cycles using a timing sequence of (5, 35, 8.5, 35). (b) Expanded view of growth during four reaction cycles……214

8.4 QCM measurements of mass gain versus reactant dose time for titanicone growth in the steady state regime at 90°C, 100°C and 115°C. (a) Mass gain versus $TiCl_4$ dose time using a timing sequence of (X, 35, 2.5, 35). (b) Mass gain versus EG dose time using a timing sequence of (5, 35, X, 35)……216

8.5 QCM measurements of mass gain versus purge time after $TiCl_4$ dose at 90°C, 100°C, 115°C and 135°C with a timing sequence of (5, X, 8.5, 35)……218

8.6 XRR measurements of film thickness versus cycle number for titanicone growth on Si<100> wafers using $TiCl_4$ and EG at 115°C with a timing sequence of (5, 35, 8.5, 35)……219

8.7 XRR measurements of growth rate and density versus temperature for titanicone growth on Si<100> wafers using $TiCl_4$ and EG with a timing sequence of (5, 35, 8.5, 35). The film thicknesses and density were measured after 50 reaction cycles……220

8.8 Alternative schematic of titanicone MLD using $TiCl_4$ and ethylene glycol. This schematic shows chlorine incorporated in the titanicone film and a larger fraction of "double reactions" than the schematic in Figure 1……222

8.9 QCM measurements of mass gain versus time for titanicone growth on TiO_2 ALD surfaces using $TiCl_4$ and GL at 130°C. (a) Growth over 90 reaction cycles using a timing sequence of (1, 30, 1, 30). (b) Expanded view of growth during four reaction cycles……224

8.10 XRR measurements of growth rate and density versus temperature for titanicone growth on Si<100> wafers using $TiCl_4$ and GL with a timing sequence of (1, 30, 1, 30). The film thicknesses and density were measured after 50 reaction cycles……225

8.11 Nanoindentation measurements of load versus displacement for titanicone films with a thickness of ~500 nm. The titanicone films were grown using EG and

GL at 115°C and 150°C with timing sequences of (4.5, 60, 4.5, 60) and (1, 30, 1, 30), respectively……..……..227

8.12 XRR measurements of film thickness versus annealing temperature in air for titanicone films grown using EG and GL at 115°C and 150°C, with timing sequences of (5, 35, 8.5, 35) and (1, 30, 1, 30), respectively.……..……..229

8.13 XRR measurements of electron density versus annealing temperature in air for titanicone films grown using EG and GL at 115°C and 150°C, with timing sequences of (5, 35, 8.5, 35) and (1, 30, 1, 30), respectively. The electron density of the TiO_2 ALD films grown using $TiCl_4$ and H_2O at 115°C is shown for comparison..……230

8.14 Optical constants of titanicone MLD and TiO_2 ALD films. The titanicone films were grown using EG and GL at 115°C and 150°C with timing sequences of (5, 35, 8.5, 35) and (1, 30, 1, 30), respectively. The TiO_2 ALD film was grown at 115°C. (a) Refractive index versus wavelength and (b) Imaginary part of complex dielectric constant versus photon energy……..……..…232

8.15 XRR measurements of film thickness versus UV exposure for titanicone films grown at 115°C using $TiCl_4$ and EG with a timing sequence of (5, 35, 8.5, 35) and alucone films grown at 115°C using TMA and EG with a timing sequence of (1, 35, 4.5, 35) ……..……..234

9.1 Schematic of TiGL MLD using $TiCl_4$ and glycerol (GL) ……..……243

9.2 Raman spectra of as deposited 500 nm TiGL film and pyrolyzed from 600 to 900°C…….....248

9.3 GIXRD diffractograms of TiGL films pyrolzed from 600 to 900°C……..251

9.4 Optical image of a surface of TiGL film pyrolyzed at 800°C (a); SEM of the surface of the 800°C pyrolyzed TiGL film (b)……..……...253

9.5 XPS depth profile of TiGL films pyrolyzed at 800°C (a); and 900°C (b).……255

9.6 Dependence of electrical sheet resistance of TiGL films on heart treatment temperature……..……..258

9.7 Various organic alcohol molecules used during metalcone MLD…..……..260

9.8 Schematic of TiEG MLD using $TiCl_4$ and ethylene glycol (EG)……...261

9.9 Surface morphology from SEM for TiGL (a), and TiEG films (b), both

pyrolyzed at 900°C……..……..262

9.10 Raman spectra for TiGL and TiEG films and pyrolyzed at 900°C……..263

9.11 Raman spectra of different alucone MLD films pyrolyzed at 900°C……...264

9.12 SEM image of a surface of the AlEG film pyrolyzed at 900°C……..……..266

9.13 Raman spectra of ZnGL, ZnHQ, ZrEG, HfEG, and MnEG MLD films pyrolyzed at 900°C……..……..267

CHAPTER I

INTRODUCTION

1.1 Thin Film Technology

Thin films are deposited onto bulk materials (substrates) to obtain properties unachievable or not readily available in the substrate alone. Therefore, one can ask question, "What properties are needed for the application at hand?" These properties can be generally categorized as optical, electrical, magnetic, chemical, mechanical, thermal and others. Typical applications within these categories could be reflective/antireflective coating, insulation, data storage, protection against oxidation or corrosion, hardness, and barrier layers as a few examples. Sometimes a coating has multiple properties. For example, titanium nitride (TiN) films on cutting tools offer hardness, low friction at the same time it can be used for decorative applications due to its rich, gold color [1] .

Additional functionality can be also gained by depositing multiple layers of different types of materials. Optical filters can contain tens to as much as hundreds of layers alternating between high and low indices of refraction [2]. When alternating layers are made using nanometer thick semiconducting materials such as GaAs and (AlGa)As, the result is material that has superior electrical properties compare to any other bulk material and related to the constructed periodicity rather than by atomic periodicity [3]. Therefore, thin film technology opens a possibility of engineering materials with defined properties and unknown in bulk form.

This chapter will examine different types of vapor phase thin film deposition techniques. The difference between thin-film and thick-film technology is that the latter involves deposition of particles and it does not offer the control or the material quality of thin-film technology.

Vapor phase thin-film deposition techniques have a number of important advantages over liquid-phase techniques: applicability to a wide variety of substrates, possibility of deposition in narrow trenches, micro cracks, and access to the surface during deposition for analysis.

The source of the film-forming material may be a solid, liquid, vapor, or gas phases. Solid materials need to be vaporized to transport them to the substrate, and that can be done by simple heating or by an electron beam, laser ablation, or positive ions (sputtering). These methods are categorized as physical vapor deposition (PVD). PVD allows film deposition only in line-of-sight of the material substrate which is a considerable limitation. This becomes critical when conformal deposition on particles and complex nano features is needed. PVD can only achieve aspect ratios of less than 5:1 [4].

In Chemical Vapor Deposition (CVD), the source materials for deposition are supplied as a gas, vapor from liquid or vaporized solids. CVD utilizes molecular precursors that have a much higher vapor pressure therefore higher growth rates are achieved. CVD deposition occurs as a result of gas phase chemical reaction or decomposition of precursor with subsequent condensation of their products onto the depositing heated surface. In CVD, the local growth rate is determined by steady-

state precursor arrival flux and/or surface kinetics. In both PVD and CVD, film contamination and source-material or precursor supply rate are the major issues. For example, for CVD, contamination issues can arise from incomplete precursor reaction and premature precursor condensation.

In contrast to the above presented thin film deposition methods, atomic layer deposition (ALD) uses self-limiting chemical reactions between gaseous precursors and a solid surface to deposit materials in a layer-by-layer fashion [5]. This process results in a unique combination of attributes, including sub-nm precision, the capability to engineer surfaces and interfaces, and unparalleled conformality over high-aspect ratio and nanoporous structures [6]. ALD thin films can be deposited conformally with aspect ratio as high as 5000:1 [7].

ALD is considered as a variant of CVD, however, the techniques have a number of distinct differences. ALD utilizes self-limiting chemical reactions to achieve atomic-level control over film thickness and composition without the need for line-of-site access to the precursor source [5]. In CVD, the substrate surface temperature is often hotter than the temperature used in ALD, causing precursor dissociation at or near the growth surface, for continuous growth. In ALD, the thickness is controlled by the number of reaction cycles as opposed to flux and time, therefore allowing the capability to synthesize films with atomic level controlled thickness. This feature also provides the capability of fabricating thin film alloy films with precise composition. All these specific aspects of ALD make it a unique material science tool.

Research in ALD has grown substantially starting in the late 1990s and early 2000s, most notably for high dielectric constant insulators. For example, the manufacturing of high speed electronic logic circuits is possible with ALD due to the ability to control feature thickness at the nanometer and subnanometer scale [8].

1.2 Atomic Layer Deposition: Principles and Attributes

The synthesis capabilities of ALD have been widely studied. The ALD method allows the synthesis of single and multicomponent monolayer nanostructures on solid surfaces with different chemical compositions and allows atom-by-atom chemical assembly of surface nano-, micro- and macrostructures by repeated sequences of chemical reactions.

The key idea of atomic layer deposition is the *sequential growth of monolayers of structural units, having a given chemical composition, on the surface of a solid through chemical reactions between the surface functional groups and the gas-phase reagents under thermodynamically favorable conditions (i.e. $\Delta G < 0$)* [9]. *The reaction step is self-terminating as it proceeds until all surface functional groups are reacted* [10].

For example, ALD Al_2O_3 thin films are deposited by sequential surface reactions of trimethylaluminum (TMA) and H_2O in vacuum (~1 Torr) [11]. The ALD process consists of several reaction steps which comprise one basic deposition unit or ALD cycle. The two reaction steps, termed "half-reactions", involved in the ALD Al_2O_3 cycle are illustrated in Fig. 1.1.

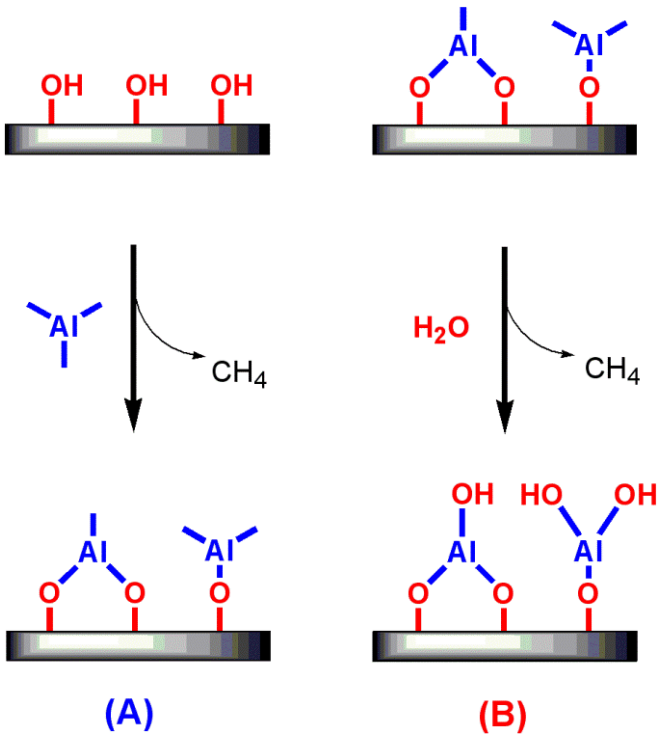

Figure 1.1 Two half-reactions of ALD Al_2O_3.

In the cycle, TMA and H_2O are pulsed into the reactor one at a time, separated by a period of purging of the gas. In these sequential reaction steps, the product of the first surface reaction becomes a reactant for the second surface reaction. The reaction is carried out to complete reaction of all active hydroxyl groups available under the experimental conditions. If the second surface reaction returns the surface back to the initial state, then atomic layer-controlled growth of a desired amount of material can be achieved using alternating ABAB… cycles. The purging step ensures that the surface reaction byproducts and un-reacted precursors are cleared away before another reactant is introduced. This is one of the major differences between ALD and chemical vapor deposition (CVD) where chemicals are introduced into the reaction zone at the same time. The schematic for

surface chemistry of ALD Al_2O_3 presented in Fig. 1.1 shows only the limiting case and the actual mechanism is more complex.

Investigation of properties of the products obtained by atomic layer deposition has revealed a number of fundamental aspects that distinguish this technique from traditional methods of synthesis of materials. These are the some effects that have been observed: 1) abrupt changes in the properties of the substrate after the application of 1 to 4 ALD cycles, 2) physical shielding of a substrate after deposition of 4 to 6 monolayers by ALD and formation of a surface with completely new functionalities and properties, 3) the effect of a multicomponent ALD alloy system [12].

For example, abrupt increase in mechanical strength of a nanoparticle was observed after several ALD cycles. This effect has been used to mechanically reinforce nanoparticles used as an electrode in lithium ion batteries or fillers for composite materials [13, 14]. Effect of shielding or re-functionalization of a surface can be used to improve adhesion of nanoparticles in polymer composite [14]. One other application is shielding copper from water corrosion using robust ALD coating in microelectromechanical heat exchangers (MEMS) [15]. The effect of a multicomponent system has been well demonstrated on ALD titanium, chromium, phosphorus multilayers of vanadium oxide for catalysis application. By changing electronic and chemical bond environment around vanadium oxide by varying multilayer stack high selectivity in industrially important catalytic processes can be

achieved [16]. This precise engineering chemical property of a surface is possible only by ALD where composition can be controlled on atomic level.

1.2.1 Historical Aspects Development of ALD

The origin of ALD has been historically attributed to Suntola and co-workers in Finland where it was developed under the name "atomic layer epitaxy". However, the less commonly acknowledged origin of ALD dates back to the work by the group of Professor Aleskovskii in the Soviet Union during the 1960s [11].

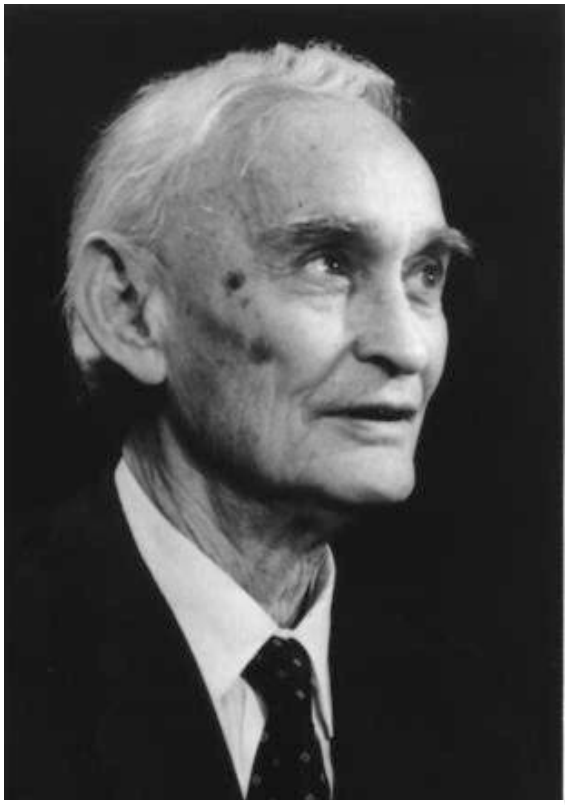

Corresponding member of the Russian Academy of Sciences Professor V.B. Aleskovskii

(1912 - 2006)

On June 3th of 2012, the Russian scientific community celebrated the 100th birthday of Professor Valentin Broisovich Aleskovskii, distinguished Chemist, Corresponding Member of Russian Academy of Sciences, founder of the first Department of Solid State Chemistry in the Soviet Union, Chancellor of Saint-Petersburg Technological Institute (1965-1975), Chancellor of Saint-Petersburg State University (1975-1986) and World War II veteran.

In his doctoral dissertation in 1952, Aleskovskii wrote about his "matrix" hypothesis where he discusses a chemical assembly. This statement constitutes the first known writing on the ALD method.

Aleskovskii came back to that original idea after similar process of solid-phase peptide synthesis was demonstrated by Prof. R.B Merrifield in 1963 for which he was awarded Nobel Prize in chemistry in 1984 [17]. Aleskovskii's hypothesis was developed by his students to the method of gas phase chemical assembly of solids which was termed "molecular layering". The principles of molecular layering proposed by V. B. Aleskovskii were first described by his student Professor S.I. Koltsov in the early 1960s [17]. After the main principles of molecular layering were established, its research expanded to former communist bloc countries such as DDR (eastern Germany) and Bulgaria [18]. Outside of the communist bloc, this technique was developed 20 years later and is now known as atomic layer deposition (ALD). At present, ALD is one of the most important methods for synthesis of nanomaterials for electronics and other areas of solid-phase materials science.

Aleskovskii is the author of more than 450 publications, including 12 books and textbooks, and more than 150 patents. Aleskovskii was a talented teacher who trained a number of specialists in the physical chemistry of solids, among them more than 25 doctoral and 100 master's graduates. For his scientific and pedagogical activities, Aleskovskii was decorated with numerous honorary titles and government awards both inside of Russia and abroad.

The Western scientific community was not aware of this work until very recently [10]. It is important to be aware of this research since a substantial amount of knowledge in ALD was accumulated by Aleskovskii's scientific school over the years.

1.3 Molecular Layer Deposition

Molecular layer deposition (MLD) is a recently developed technique that builds upon the basic ALD method. While ALD had been developed to deposit exclusively inorganic thin films, MLD is based on self-limiting surface reactions where one or both reactants are organic molecules. This allows the additional capabilities to grow purely organic or hybrid organic-inorganic thin films [2].

MLD of hybrid organic-inorganic films offers many new possibilities for the growth of functional thin films [8]. Organic-inorganic hybrid and nano hybrid materials comprise of both organic and inorganic components intimately mixed, wherein at least one of the component domains has dimensions ranging from a few angstroms to several nanometers [19, 20]. The properties of these hybrid materials are governed by the individual contributions of both the organic and inorganic components as well as the inner interfacial contributions. The main objective behind the development of these coatings is to achieve the synergistic combination of both the components to obtain new properties. Some useful properties of these materials include scratch, impact, and abrasion resistance, excellent heat, UV-radiation stability, solvent resistance, flexibility and toughness [20, 21].

One of the first hybrid organic-inorganic films was an aluminum alkoxide polymer film grown using trimethylaluminum (TMA) and ethylene glycol (EG) [22]. This hybrid organic-inorganic is just one of a large family of aluminum alkoxides known as “alucones” [23]. Schematic showing the surface chemistry of alucone growth using TMA and EG presented in Figure 1.2 [22].

There are similarities between the growth of alucone MLD using TMA and EG and Al_2O_3 ALD using TMA and H_2O which is shown in Fig. 1.2.

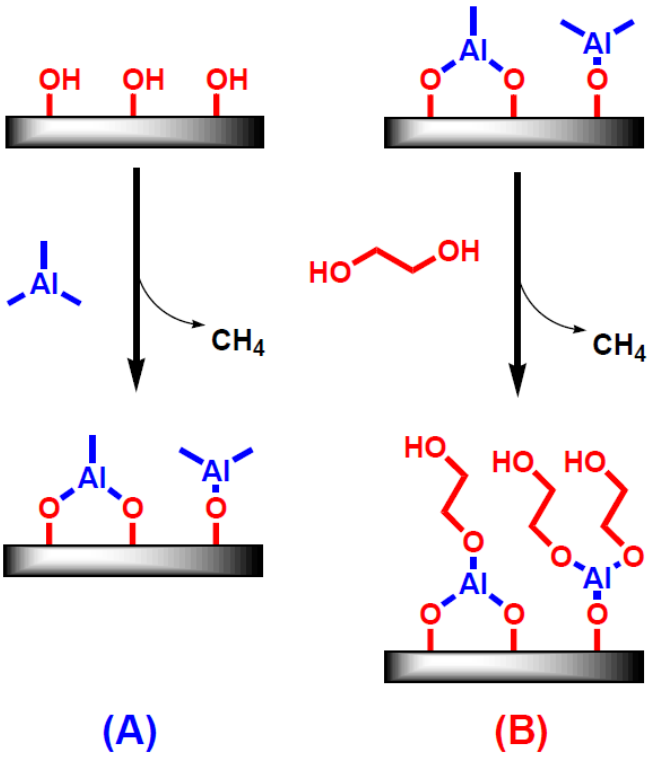

Figure 1.2 Two half-reactions of MLD Alucone [22].

As shown in the figure, the full ethylene glycol molecules are incorporated into the growing film during MLD whereas in ALD films, growth is achieved by one atomic layer at the time.

One of the specific effects observed during the deposition of MLD films is diffusion of precursors into the bulk of the growing film. This was clearly demonstrated using in situ quartz crystal microbalance (QCM) for three-step ABC MLD using trimethylaluminum, ethanolamine, and maleic anhydride [24]. In these experiments some trimethylaluminum was shown to react with surface species while the remaining unreacted molecules would diffuse into the low density hybrid

film. These effects may result in non-self-limiting surface reactions [24]. Therefore during the MLD deposition process, it is important to provide enough time for reactants to diffuse out from the film before introducing a second reactant to avoid condensation. Failing to do this can lead to CVD type growth that can result in poor control of film thickness and uniformity.

Many other hybrid organic-inorganic films can be fabricated using organometallic and organic precursors [25]. Alucones are part of the large family of hybrid organic-inorganic thin films defined by reacting organometallics and organic alcohols known collectively as "metalcones" [8, 26]. Metalcones have a number of potentially important applications in nanotechnology. For example, alucones have been shown to be successful sacrificial layers in the formation of air gaps in nanoelectromechanical systems [27]. They have also been considered for use as gas diffusion barriers for use in flexible electronics and solar cells [28]. Another possibility is using the hybrid organic-inorganic films as a template for creating porous metal oxide films by annealing MLD films in air [8]. These porous materials are useful for gas separation at high pressures [29], in catalysis and gas sensing [8].

Given these capabilities, ALD and MLD could play a central role in achieving several key technological advances from the next generation of electronics to renewable energy applications [6].

1.4 Statement of Purpose

Atomic and molecular layer depositions are two advanced techniques for deposition of various inorganic, hybrid organic-inorganic and purely organic thin

films with the ability of atomic/molecular level composition control. Despite being very versatile, these deposition methods have their limitations. The nature of some of these limitations lies in basic thermodynamic boundaries. This thesis seeks to explore the way to overcome these limitations and extend the spectrum of synthesizable thin films by high temperature post-processing (heat treatment in air or inert atmosphere) of inorganic ALD and hybrid organic - inorganic MLD films. This concept is powerful but yet largely unexplored by the ALD/MLD research community.

Although this thesis covers several different topics such as surface chemistry of ALD Y_2O_3, TiN, MLD of alumina/siloxane, and corrosion protection of copper by ALD, the main results in this thesis are the identification and analysis of the key processes governing phase development in thin films upon heat treatment of ALD and MLD films. During the research process, several dominant phenomena such as self-organization, phase separation and solid-state reaction were identified. Although these processes are well known in solid state physics of bulk materials these are not well studied for thin films. Interestingly, these processes can transform not only the composition of the original films but also can alter their morphology. Therefore, films with advanced composition and nano architecture can be potentially synthesized.

This research is intended to contribute to the overall knowledge of complex physical-chemical processes occurring in thin films upon heat treatment to

effectively manipulate these processes in order to synthesize novel functional thin films with pre-defined composition, morphology, and properties.

1.5 References

1. Ishihara, K., et al., Characterization of Cvd-Tin Films Prepared with Metalorganic Source. Japanese Journal of Applied Physics Part 1-Regular Papers Short Notes & Review Papers, 1990. **29**(10): p. 2103-2105.

2. Lange, S., et al., Pulse magnetron sputtering in a reactive gas mixture of variable composition to manufacture multilayer and gradient optical coatings. Thin Solid Films, 2006. **502**(1-2): p. 29-33.

3. Klem, J.F., et al., Characterization of Thin Algaas/Ingaas/Gaas Quantum-Well Structures Bonded Directly to Sio2/Si and Glass Substrates. Journal of Applied Physics, 1989. **66**(1): p. 459-462.

4. Rossnagel, S.M., Sherman, A. and Turner, F., Plasma-enhanced atomic layer deposition of Ta and Ti for interconnect diffusion barriers. Journal of Vacuum Science & Technology B, 2000. **18**(4): p. 2016-2020.

5. George, S.M., Atomic Layer Deposition: An Overview. Chemical Reviews, 2010. **110**(1): p. 111-131.

6. Elam, J.W., Dasgupta, N.P., and Prinz, F.B., ALD for clean energy conversion, utilization, and storage. Mrs Bulletin, 2011. **36**(11): p. 899-906.

7. Elam, J.W., et al., Conformal coating on ultrahigh-aspect-ratio nanopores of anodic alumina by atomic layer deposition. Chemistry of Materials, 2003. **15**(18): p. 3507-3517.

8. Parsons, G.N., George, S.M. and Knez, M., Progress and future directions for atomic layer deposition and ALD-based chemistry. Mrs Bulletin, 2011. **36**(11): p. 865-871.

9. Malygin, A.A., The Molecular Layering Method as a Basis of Chemical Nanotechnology Natural Microporous Materials in Environmental Technology NATO ASI Series, 1999. **362**: p. 487-495.

10. Parsons, G.N., George, S.M., Knez, M.,, Progress and future directions for atomic layer deposition and ALD-based chemistry. MRS Bull. , 2011. **36**: p. 865.

11. Puurunen, R.L., Surface chemistry of atomic layer deposition: A case study for the trimethylaluminum/water process. Journal of Applied Physics, 2005. **97**(12).

12. Malygin, A.A., Molecular layering technology and some of its applications. Russian Journal of Applied Chemistry, 1996. **69**(10): p. 1419-1426.

13. Riley, L.A., et al., Improved Mechanical Integrity of ALD-Coated Composite Electrodes for Li-Ion Batteries. Electrochemical and Solid State Letters, 2011. **14**(3): p. A29-A31.

14. Malygin, A.A., Trifonov, S.A., and Tsvetkova, M.N., Perspectives of application of the molecular layer deposition technique for controlling operational properties of materials for shipbuilding. Russian Journal of General Chemistry, 2010. **80**(10): p. 2181-2191.

15. Abdulagatov, A.I., et al., Al2O3 and TiO2 Atomic Layer Deposition on Copper for Water Corrosion Resistance. Acs Applied Materials & Interfaces, 2011. **3**(12): p. 4593-4601.

16. Malygin, A.A., Synthesis of multicomponent oxide low-dimensional systems on the surface of porous silicon dioxide using the molecular layering method. Russian Journal of General Chemistry, 2002. **72**(4): p. 575-589.

17. Aleskovskii, V.B., Chemistry and Technology of Solids. Journal of Applied Chemistry of the Ussr, 1974. **47**(10): p. 2207-2217.

18. Malygin, A.A., The molecular layering nanotechnology: Basis and application. Journal of Industrial and Engineering Chemistry, 2006. **12**(1): p. 1-11.

19. Sanchez, C., et al., Applications of hybrid organic-inorganic nanocomposites. Journal of Materials Chemistry, 2005. **15**(35-36): p. 3559-3592.

20. Mammeri, F., et al., Mechanical properties of hybrid organic-inorganic materials. Journal of Materials Chemistry, 2005. **15**(35-36): p. 3787-3811.

21. Sanchez, C., et al., Optical properties of functional hybrid organic-inorganic nanocomposites. Advanced Materials, 2003. **15**(23): p. 1969-1994.

22. Dameron, A.A., et al., Molecular layer deposition of alucone polymer films using trimethylaluminum and ethylene glycol. Chemistry of Materials, 2008. **20**(10): p. 3315-3326.

23. Lee, Y., et al., Molecular Layer Deposition of Aluminum Alkoxide Polymer Films Using Trimethylaluminum and Glycidol. Langmuir, 2011. **27**(24): p. 15155-15164.

24. Seghete, D., et al., Importance of Trimethylaluminum Diffusion in Three-Step ABC Molecular Layer Deposition Using Trimethylaluminum, Ethanolamine, and Maleic Anhydride. Langmuir, 2010. **26**(24): p. 19045-19051.

25. George, S.M., Yoon, B. and Dameron, A.A., Surface Chemistry for Molecular Layer Deposition of Organic and Hybrid Organic-Inorganic Polymers. Accounts of Chemical Research, 2009. **42**(4): p. 498-508.

26. George, S.M., et al., Metalcones: Hybrid Organic-Inorganic Films Fabricated Using Atomic and Molecular Layer Deposition Techniques. Journal of Nanoscience and Nanotechnology, 2011. **11**(9): p. 7948-7955.

27. Seghete, D., et al., Sacrificial layers for air gaps in NEMS using alucone molecular layer deposition. Sensors and Actuators a-Physical, 2009. **155**(1): p. 8-15.

28. Miller, D.C., et al., The mechanical robustness of atomic-layer- and molecular-layer-deposited coatings on polymer substrates. Journal of Applied Physics, 2009. **105**(9).

29. Yu, M.A., et al., H-2 Separation Using Defect-Free, Inorganic Composite Membranes. Journal of the American Chemical Society, 2011. **133**(6): p. 1748-1750.

CHAPTER II

EXPERIMENTAL

2.1 Viscous Flow Reactor

ALD and MLD systems investigated in a hot wall viscous flow reactor, schematically presented in Figure 2.1.

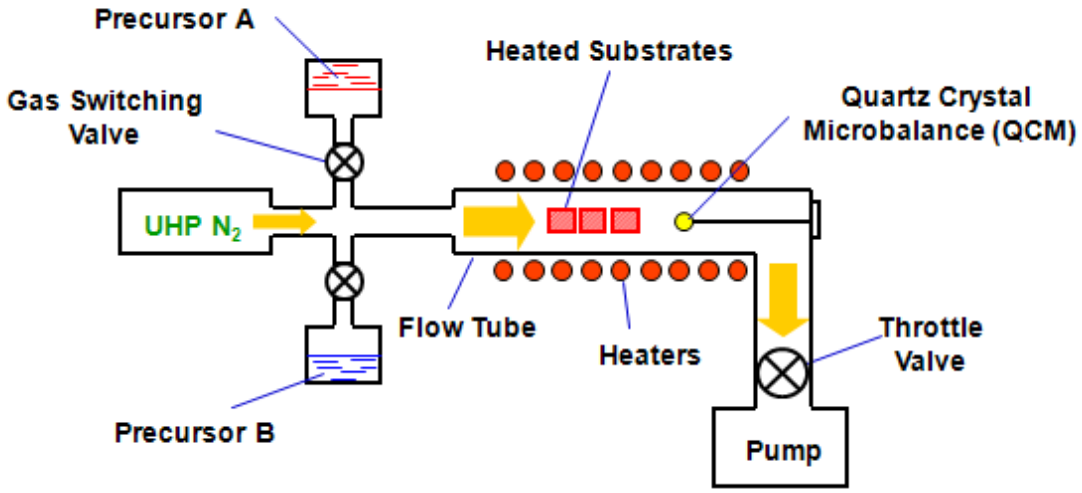

Figure 2.1 Schematic view of hot wall viscous flow reactor for thin film ALD and MLD growth.

The reactor was built using only stainless steel components. The main part of the reactor is the heated reactor flow tube which has a 1.375 in. inside diameter and is 18 inches long. The reactor flow tube is resistively heated using two external heaters set to the desired deposition temperature. The first heater is located close to the reactant inject zone and is used as a preheat zone for reactant gases. This heater was usually 5°C higher temperature than the second heater. The second heater was used to heat the main part of the reactor, where depositing substrates

and in situ monitoring equipment is located. Both heaters were controlled with a Eurotherm temperature controller. Samples loaded inside of the flow tube are were heated by radiation and convection from the hot walls. This heating arrangement allows the simultaneous deposition on multiple samples with different geometries. Most of the time ALD and MLD films were deposited on pre-cut silicon wafer substrates.

Ultrahigh purity nitrogen flowed continuously from the reactant line, through the flow tube, and into the exhaust mechanical pump. The mechanical pump is an Alcatel-Adixen 2010 with a pumping speed of 3.2 l/s. The flow tube pressure is monitored by a capacitance manometer. Typically, the reactor is operated at a pressure of ~1 Torr.

This reactor uses a gas pulse valve that allows introduction of gaseous and high vapor pressure liquid precursors into the reactor. Reactants were entrained into the nitrogen flow and delivered to the reaction zone where samples were deposited. Mostly ALD and MLD films were deposited on pre-cut silicon wafer substrates that were later used for ex situ analysis.

A personal computer equipped with analog and digital input/output boards was used to control valve pulse sequence and monitoring the reactor's pressure. This reactor was equipped with quartz crystal microbalance (QCM) located downstream of the sample substrates. QCM is a powerful in situ technique for measuring relative mass changes in real time during ALD.

2.2 Quartz Crystal Microbalance

The vibrating quartz crystal mass-deposition monitor, or quartz crystal microbalance, is one of the most powerful and widely used diagnostic instruments in thin film technology [1].

Every new MLD or ALD system researched in this thesis has started with QCM measurements. QCM enabled us to study surface chemistries and identify optimal growth condition such as: temperature and precursor saturation exposures (Torr·s). In addition, it allowed us to quickly evaluate ALD/MLD reactor performance by using well studied in literature chemistries, one of which is ALD Al_2O_3 which uses trimethylaluminum (TMA) and water [2]. If the reactor had a leak in the atmosphere, the overall growth rate of Al_2O_3 would be dramatically increased and its QCM profile would be non-consistent with TMA and water chemistry.

QCM uses piezoelectric crystalline quartz wafers that generate an oscillating voltage across itself when vibrating at its resonant frequency, and this voltage can be amplified and fed back to drive the crystal at this frequency [1]. Quartz wafers used in this work were polished and had resonant frequency of ~6 MHz. Polished crystals have minimal surface roughness so this results in more accurate measurements [2]. Electrical coupling is done with thin film gold electrodes deposited on opposite faces of a thin 1 cm in diameter quartz wafer that has the proper crystallographic orientation. The QCM sensors were supplied by Colorado Crystal Corporation (Longmont, CO). In order to monitor growth, one side of the QCM crystal was exposed to the precursor flux. The mass loading changes the crystal's resonant frequency. The frequency of the QCM is monitored using a

Maxtek TM400 thin film deposition monitor. The deposition monitor converts the QCM frequency to a mass per unit area. The QCM instrumentation has a mass resolution of 0.3 ng/cm^2 (which accounts for sub monolayer resolution) when the temperature is stable to within 0.1°C [2]. Measurements of relative mass gain is always much more accurate than making an absolute measurement since the exact area of deposition on a crustal is not known.

The techniques described below are used for film analysis after deposition.

2.3 X-ray Diffraction

Through many decades X-ray diffraction (XRD) has proved to be the most useful diffraction for bulk structure analysis [3]. The geometry of diffraction will be introduced for the case of X-ray diffraction from the 2D lattice.

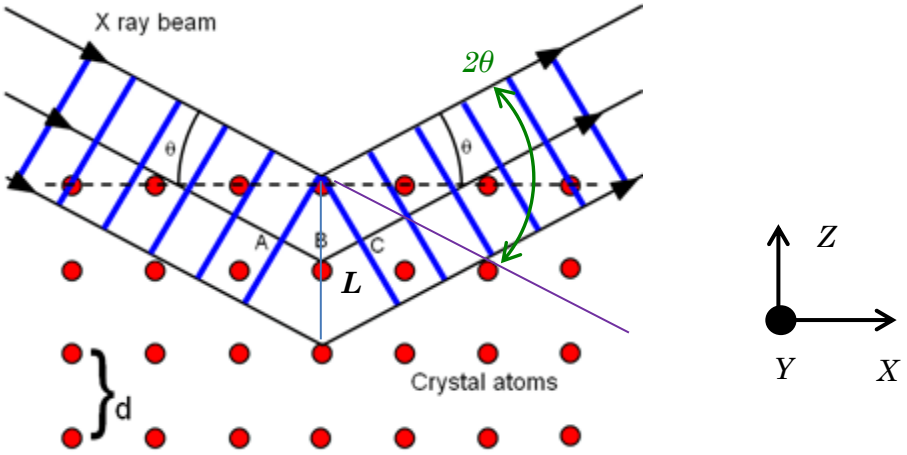

Figure 2.2 Geometry of bulk diffraction from a stack of X-Y atomic planes [4].

In Fig. 2.2, the incident beam penetrates the lattice and scatters from each of the atoms in 2D array. When incident and scattering angles, θ, are equal as measured from some plane of atoms in the lattice (the X-Y plane), the path lengths of rays scattered off of any of the atoms in that plane will be the same. This results in

constructive interference of those rays. The path-length difference between beams reflected from successive planes in the Z direction is the distance 2L shown in Fi. 2.2. For constructive interference, 2L must be an integral multiple $2L= 2d \sin\theta$, where d is the plane spacing. This is known as Bragg condition. In polycrystalline films obtained in the course of this work, degree of preferential orientation is measured using monochromatic X-rays and "2θ". In this case, the thin film surface is oriented in the X-Y plane of Fig.2.2 and θ is measured from that plane. The θ is scanned by rotating the sample about the Y axis. At the same time, the X-ray detector is rotated through 2θ to keep it at the specular angle with respect to the film surface. At values of 2θ, the atomic periodicity d perpendicular to the surface satisfies the Bragg condition. The d value identifies the atomic plane, and the peak intensity is a qualitative measure of the degree of texturing; that is, intensity increases with the fraction of crystallites in the film, at which the atomic plane is parallel to the surface. The width of the peak, Δ(2θ) (in radians), at half of its maximum intensity, is a measure of the size of crystal grains that can be estimated from Scherrer formula $a= 0.9\lambda/\Delta(2\theta)\cos\theta$, where λ is the X-ray wavelength [1].

The grazing-incidence mode of XRD (GIXRD) has often been used in works described in this thesis. The GIXRD was used to examine crystal structure within a few nm of the surface. This is a good method to use when the thin films deposited on crystalline substrate, enabling us to distinguish the film from the substrate diffraction features. The film surface is in the X-Z plane in Fig. 2.2., and the

incident and reflected beams are almost parallel to it, so that the d of planes perpendicular to the film surface is being measured [5, 6].

2.3 X-ray Photoelectron Spectroscopy

An energetic probe beam of electrons or photons can eject an electron out of an inner shell of a near-surface atoms into vacuum, as shown in Fig. 2.3.

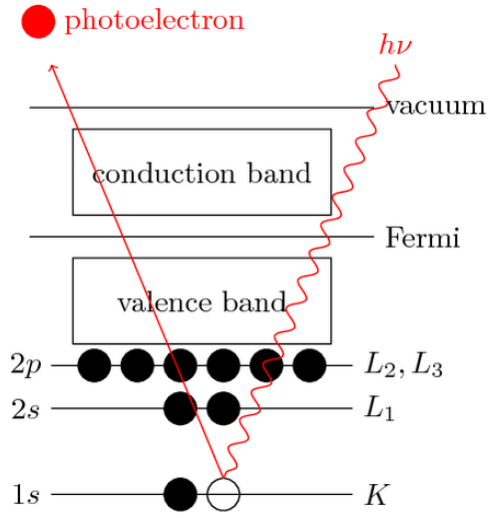

Figure 2.3 Principle of X-ray photoelectron spectroscopy [7].

The escaping electron or photoelectron is known as a secondary electron or photoelectron. In X-ray photoelectron spectroscopy (XPS), the chemical elements are identified by peaks in the energy spectrum of the escaping electrons, as the positions of these peaks are determined by the energy levels of the electron shells in the probed atom. The escape energy provides insight into the chemical bonding when the atomic inner shell shifts a few eV with a different bonding configuration.

XPS data for various thin film samples reported in this thesis were obtained in situ for the samples previously exposed to air, in the process transferring from

the ALD/MLD reactor to XPS chamber. Therefore, all the examined samples had trace amounts of residual carbon in survey XPS spectra. When we needed a quantitative analysis of the atomic fraction of each element in the bulk of the film(s), depth profiling was performed. Depth profiling of composition achieved scanning by sputtering away the film during analysis, using Ar^+ ion beam scanned over an area larger than the electron collection area which ensured a spatially uniform sputtering rate.

2.4 Raman Spectroscopy

Both bond frequency and lattice-vibration (phonon) frequencies can be measured by Raman spectroscopy. Light passing through transparent materials is weakly scattered from individual atoms by dipole interaction. Most of the light undergoes Rayleigh scattering, which radiates at the incident frequency, but some undergoes Raman scattering, which is shifted down (Stokes shift) or up (anti-Stokes) in frequency by the transfer of a quantum of energy into or out of a vibrational mode of the molecule or a phonon of the lattice to which the scattering atom is bonded. Raman measurements on annealed and pyrolyzed samples studied in this work were performed using high-intensity Ar^+ laser beam (green) with 532 nm wavelength, where spectrum of the scattered light was collected in the perpendicular direction. Perfect bonding order exhibits sharp Raman-scattering peaks, where amorphous and polycrystalline materials have broad peaks because of the variation in bonding among the scattering atoms [1].

In conclusion, Raman spectroscopy has been useful for tracking change in in such carbon phases as hydrogenated carbon or nanocrystalline graphite during pyrolysis of hybrid organic-inorganic films.

2.5 References

1. Smith, D.L., Thin-film deposition: principles and practice. McGraw-Hill Inc., 1995.

2. Elam, J.W., M.D. Groner, and S.M. George, Viscous flow reactor with quartz crystal microbalance for thin film growth by atomic layer deposition. Review of Scientific Instruments, 2002. **73**(8): p. 2981-2987.

3. Oura, K., Lifshits, V. G., Saranin, A. A., Zotov, A. V., Katayama, M., Surface science. Springer-Verlag Berlin 2003: p. 66.

4. http://tap.iop.org/atoms/xray/530/page_47297.html.

5. Segmuller, A., Characterization of Epitaxial Thin-Films by X-ray-Diffraction. Journal of Vacuum Science & Technology a-Vacuum Surfaces and Films, 1991. **9**(4): p. 2477-2482.

6. Clemens, B.M. and J.A. Bain, Stress Determination in Textured Thin-Films Using X-ray-Diffraction. Mrs Bulletin, 1992. **17**(7): p. 46-51.

7. http://www.texample.net/tikz/examples/principle-of-X-ray-photoelectron-spectroscopy-xps/.

CHAPTER III

ATOMIC LAYER DEPOSITION OF Y_2O_3 USING TRIS(BUTYLCYCLOPENTADIENYL)YTTRIUM AND WATER

3.1 Introduction

Because of its unique combination of dielectric, optical and thermal properties, yttrium oxide has been a subject of research in the field of material science for many years. Yttria has a high dielectric constant of 10 [1], broad optical transmission range of 0.25-8 μm [2], and high melting point of 2439°C [1]. Due to its low lattice-mismatch and high chemical comparability with silicon, Y_2O_3 has been considered as a potential gate dielectric for microelectronic devices [3-5]. Several important applications for Y_2O_3 films and its alloys include: waveguide materials in optics devices [6,7]; buffer layer for ferroelectrics and superconductors [8,9], and high melting point protective coatings [10,11].

In the past decade, a number of gas and liquid phase deposition techniques have been employed to deposit Y_2O_3 films. Typical vapor phase deposition processes involve different modifications of physical vapor deposition (PVD) [12-16] and chemical vapor deposition (CVD) [17-20] techniques. While these techniques deposit fairly good quality yttria films, low thickness control and high deposition temperatures can be significant disadvantages for these methods. In recent years yttrium oxide has been deposited by the atomic layer deposition (ALD) method [21-28]. In contrast to conventional CVD deposition, ALD thin films are deposited by alternating exposures of reactants into the reaction zone separated by a purging or evacuation period. During the purging period, excess reactant and reaction

byproducts are purged from the reaction vessel. The key difference between ALD and other techniques is the self-limiting nature of the process and the capability to coat extremely complex shapes and high aspect ratio nanostructures with a high quality, conformal layer [29].

In previous ALD publications, Y_2O_3 deposition was achieved by using the following class of metal precursors: ß-diketonate - tris(2,2,6,6-tetramethyl-3,5-heptanedione)yttrium ($Y(thd)_3$) [21-24], $Y(thd)_3$(bipyridyl) [22], $Y(thd)_3$(1,10-phenanthroline) [22]; cyclopentadienyl -tris(cyclopentadienyl)yttrium (YCp_3) [25], tris(methylcyclopentadienyl)yttrium ($Y(CpMe)_3$) [25], tris(ethylcyclopentadienyl)yttrium ($Y(CpEt)_3$) [26]; acetamidinate - tris(N,N'-diisopropylacetamidinate)yttrium ($Y(^iPr_2amd)_3$) [27]. In these experiments, oxygen, ozone, oxygen radicals, and water, were used as oxygen sources. The poor reactivity of ß-diketonates used in combination with oxygen [21], ozone [21-23] and oxygen radicals [24] to deposit yttria films typically resulted in relatively high carbon impurities (>1%) with poor electrical and optical properties consequently limiting its potential applications. However, significant progress has been made in ALD deposition of Y_2O_3 films when cyclopentadienyl [25,26] and acetamidinate [27] yttrium precursors in combination with water have been introduced. In both cases, a low level of carbon impurities of yttria films (0.5% or less) has been reported. The cyclopentadienyl (Cp) type precursors exhibited a high ALD growth rate of up to 1.7 Å/cycle compared with 0.8 Å/cycle when acetamidinate precursors were used. In general, cyclopentadienyl precursors have attracted considerable attention in the

ALD community. The ligands are easily cleaved with water leaving behind a low amount of carbon impurities. Also, ALD films grown with cyclopentadienyl precursors have shown high growth rates [28]. Reactivity with water is desirable since the use of more aggressive oxygen sources such as ozone can be avoided. Nevertheless, the negative effect of Y_2O_3 water absorption on self-limiting ALD and film dielectric performance has been observed [27].

In this work, our efforts concentrated on study of ALD of Y_2O_3 using tris(butylcyclopentadienyl)yttrium ($Y(CpBut)_3$) and water as an oxygen source. $Y(CpBut)_3$ is an attractive commercially available precursor since it is liquid at room temperature. This should lead to a higher precursor volatility than for other cyclopentadienyl precursors which has been an issue for vapor phase deposition [29]. According to the DFT calculations, the presence of bulky butyl groups attached to the Cp ligand is expected to make $Y(CpBut)_3$ more reactive than any other Cp based yttrium precursor [29].

The in situ quartz crystal microbalance (QCM) employed in this work allowed us to not only optimize deposition processes, but also to gain insight into the growth mechanism for yttria ALD. In particular, QCM enabled us to detect a gradual increase in water absorption during Y_2O_3 deposition and to probe the effects of water dose length and post-dose purge time on film growth rate. Based on results from previous experimental and theoretical publications [29,30], we were able to analyze our QCM data and propose a mechanism for $Y(CpBut)_3$ and water reaction on a surface.

Although Y_2O_3 has desirable optical properties, it has received less attention than other oxides because of its strong water absorption [31]. The cubic polycrystalline structure of ALD yttria [25-27] is particularly relevant for optical applications since polycrystalline materials with non-cubic crystal structures tend to have the greatest scattering [2]. Thus, in this work we made an emphasis on characterization of the optical properties of ALD Y_2O_3 including studies of the effect of in situ alumina capping on the optical performance.

3.2 Experimental

Y_2O_3 ALD was carried out in a viscous-flow, hot-wall type ALD reactor described in detail in early work [32]. The yttrium oxide was deposited using tris(butylcyclopentadienyl)yttrium ($Y(CpBut)_3$), with 99.9% purity, obtained from Strem Chem. Inc. (Newburyport, MA, U.S.A.) and chromatography-grade water. The metal precursor was handled in a glove box because of its air and moisture sensitivity. Ultra high purity (99.999%) nitrogen was used as the purge and carrier gas in the reactor where a base pressure was maintained at 0.9 Torr. QCM measurements were performed using AT- cut, 6 MHz resonant frequency, quartz sensor crystals with a polished, gold sputtered surface (Colorado Crystal Corporation, Loveland, CO, U.S.A.). The QCM was equipped with a backside purge in order to prevent deposition on the backside of the QCM crystal. Error bars in the QCM uptake figures represent a standard deviation of 20 ALD cycle data points.

For ex situ analysis, precut Si<100> silicon wafers with 2.5cm x 2.5cm dimensions were used as substrates for Y_2O_3 ALD films with deposition

temperatures ranging from 200°C to 320°C. The substrates were cleaned using isopropanol followed by spin-drying and outgassing in the reactor for 30 minutes before deposition. All silicon substrates used for Y_2O_3 characterization had ~25 Å layer of native oxide. The error bars for each data point in the graphs for deposition on silicon substrate represents a variation in yttria thickness over three samples deposited in same run. The yttria ALD deposition timing, given in seconds (s), was: $t_1/t_2/t_3/t_4$ where t_1 is the $Y(CpBut)_3$ exposure time, t_2 is the purge following the $Y(CpBut)_3$ exposure, t_3 is the H_2O exposure, and t_4 is the purge after the H_2O exposure. During the deposition, the yttrium precursor and water were kept at 170°C and 25°C, respectively. $Y(CpBut)_3$ is found to be thermally stable even when kept at 170°C extended period of time. In the course of the yttria deposition, nitrogen was passed through a stainless steel bubbler containing the heated precursor during dosing and diverted to bypass the bubbler during purge time. The Al_2O_3 ALD was performed using alternative exposures of 95% pure trimethyl aluminum (TMA, Sigma-Aldrich) and chromatography-grade water.

An ellipsometer (J. A. Woollam Co. (M-44STD), U.S.A.) was used to determine thickness and refractive index of deposited ALD yttria films. Thickness was measured at three different wavelengths 418.5, 594.6 and 763.2 nm and refractive index was measured by scanning from 418.5 nm to 754.7 nm at an incident angle of 75°. Y_2O_3 refractive index of yttria films was calculated using the measured thickness of yttria and sub layers (Al_2O_3 and SiO_2) determined by X-ray reflectivity (XRR) and fixing these values in the ellipsometer's n and k fitting model.

XRR and X-ray diffraction (XRD) data were collected using a high resolution X-ray diffractometer (Bede Scientific D1) with Cu X-ray tube working at λ=1.54 Å and filament current of 40 mA. The obtained data were fit using REFS fitting software from Bede Scientific Inc. The XRR was used to determine the density, roughness and thickness of the Y_2O_3 films. For the XRD analysis, the samples were held at ω=1° and the detector scanned from 25° to 60° (2θ). XRD measurements were performed to determine the crystalline structure and grain size of the Y_2O_3 films.

Rutherford backscattering spectrometry (RBS) was carried out on a National Electrostatics Corporation spectrometer with a He^+ beam of energy 2.0 MeV and Ortec Ultra ion detectors with energy resolution of 18 keV (dE/E). RBS was employed for a precise determination of the Y to O ratio of the deposited Y_2O_3 film.

X-ray photoelectron spectroscopy (XPS) was used to examine the carbon impurities and binding state of the oxygen atoms in the yttrium oxide film. XPS scans were performed using a Physical Electronics PHI 5400 spectrometer with a monochromatic Al Kα X-ray source with energy of 1486.6 eV. XPS survey scans were performed with electron pass energy of 187 eV and resolution of 0.8 eV. The photoelectrons were collected using a hemispherical analyzer. Depth profile measurements were done using in situ 1.5 keV Ar^+ sputter gun and individual peaks were scanned with a resolution of 0.125 eV and electron pass energy of 58.7 eV.

Atomic force microscope (AFM) measurements were performed using an Autoprobe CP instrument from Thermomicroscopes atop an air table (Integrated Dynamics Engineering, Randolph, MA, U.S.A.). AFM images were acquired in noncontact mode. All scans were 5 × 5 μm performed at a scan rate of 0.8 Hz using rectangular cantilevers "A" tip from MikroMasch Company, San Jose, CA, U.S.A.

3.3 Results and Discussion

3.3.1 QCM Study and Deposition on Si

Using QCM, Y_2O_3 ALD was investigated at reactor temperatures of 225 and 230°C. Figure 3.1 shows the QCM response during growth of yttrium oxide by alternating exposures of $Y(CpBut)_3$ and water at 230°C using 8/10/0.2/150 deposition timing.

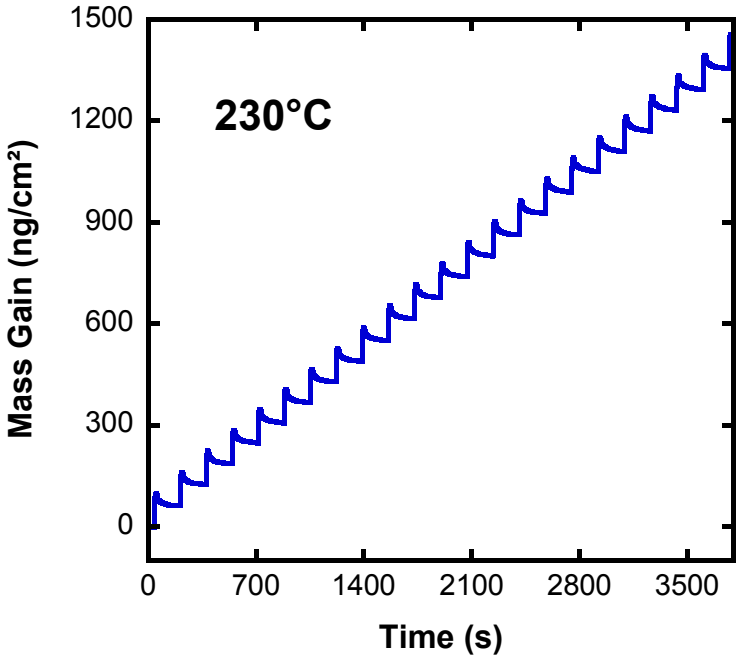

Figure 3.1 QCM response during Y_2O_3 ALD linear growth regime using 8/10/0.2/150 deposition timing.

The total mass gain per cycle from the slope of the mass/time graph in Fig. 3.1 is 62 ng/cm^2. As can be seen in this figure, Y_2O_3 ALD displays reproducible, linear, mass increase with time.

The QCM mass changes during reaction cycle at 230°C are presented in detail in Figure 3.2.

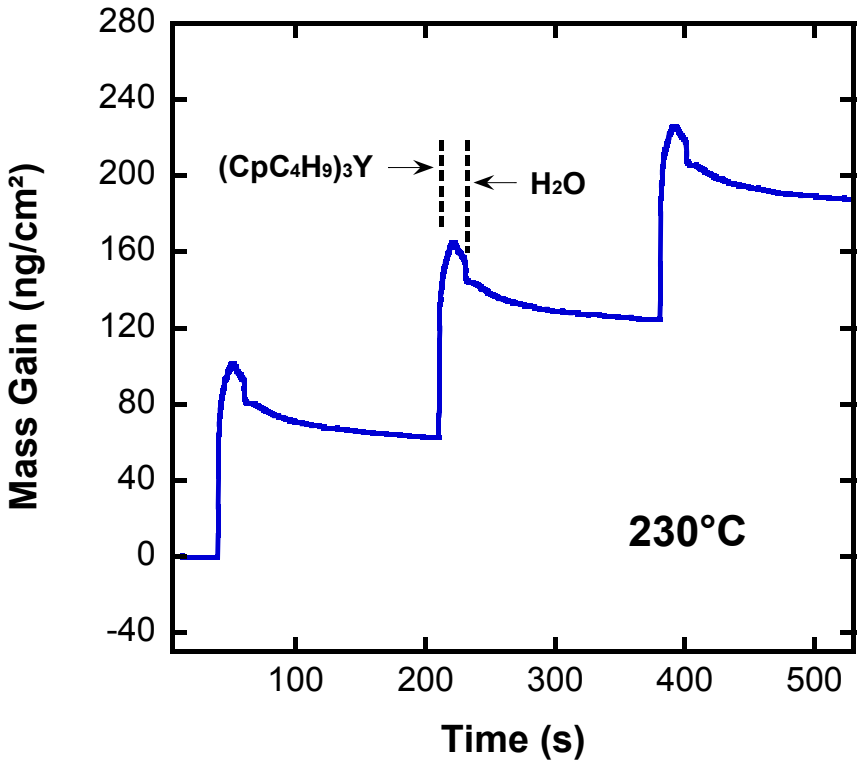

Figure 3.2 QCM mass gain and mass loss during individual precursor exposures with 8/10/0.2/150 timing.

In this figure, $Y(CpBut)_3$ exposure resulted in a mass gain of 102 ng/cm^2 with a small mass loss during the inert purge. An additional mass loss of 31 ng/cm^2 after water dosing results in an overall mass increase of 62 ng/cm^2 per cycle.

Results of QCM measured metal precursor uptake obtained at 230°C are shown in Figure 3.3.

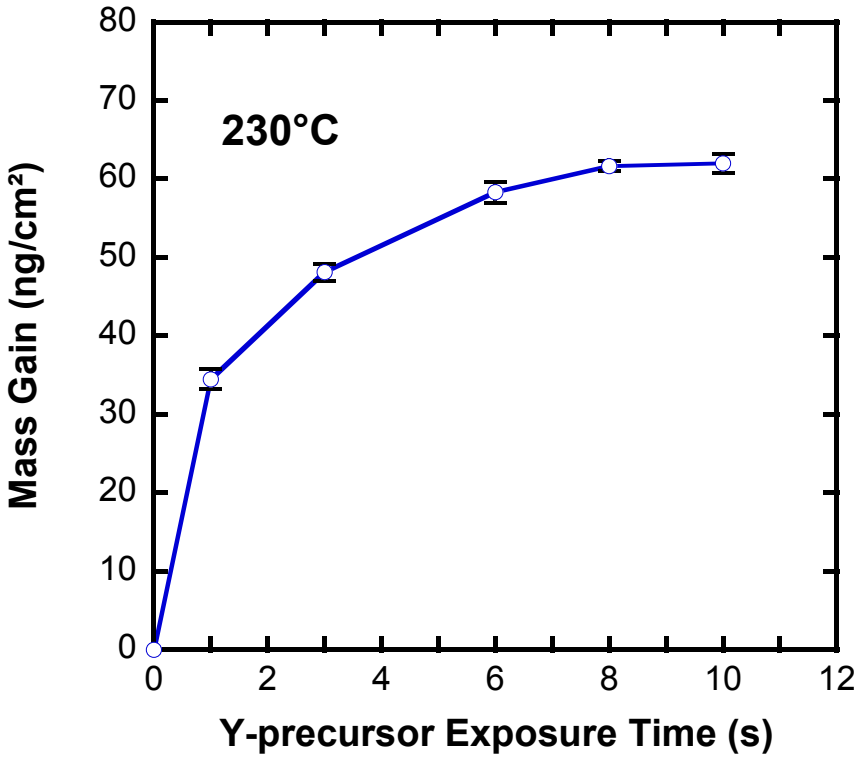

Figure 3.3 QCM measured Y_2O_3 growth rate as a function of $Y(CpBut)_3$ dose time deposited using a X/10/0.2/150 timing sequence.

Prior to precursor uptake, the QCM was initially coated with ~50 Å of ALD Al_2O_3 in order to obtain a uniform hydroxylated surface. The timing sequence used during uptake was X/10/0.2/150 where X is the variable $Y(CpBut)_3$ dose time. The $Y(CpBut)_3$ dose time was varied to determine the exposure time required for the reaction to reach saturation. From Fig. 3.3, it can be concluded that $Y(CpBut)_3$ saturation is reached after about 8 s precursor dose. The partial pressure of $Y(CpBut)_3$ was below the reactor's nitrogen base pressure, therefore, exposure volume could not be determined. Water exposures of 0.2s with partial pressures of

~3 mTorr yielded a total water exposure of 6×10^2 L (1 L = 1×10^{-6} Torr·s). For ex situ Y_2O_3 film characterization, a 8/10/0.2/150 deposition timing was utilized to ensure that the $Y(CpBut)_3$ and water doses were in the saturation regime.

Figure 3.4 shows the QCM response during Y_2O_3 growth at 225 C at different times during $Y(CpBut)_3$ uptake when X/60/1/60 timing was used. The QCM profile during the first few ALD cycles (1/60/1/60) on a freshly deposited alumina surface (blue line) and the QCM data after 500 ALD cycles when 8/60/1/60 dose timing was used (red line) are shown for comparison in Figure 3.4. In this set of data, a water exposure of 1.0 s with partial pressures of 50 mTorr was used, yielding a total water exposure of 5×10^4 L (1 L = 1×10^{-6} Torr s). It should be pointed out that this water volume is two orders of magnitude higher than that used for deposition in Fig. 3.1-3.3 when 0.2s water dose was employed. A mass loss during the 60s purge time after the $Y(CpBut)_3$ dose was consistently observed by QCM for 225 and 230°C deposition temperatures. In Fig. 3.2 this mass loss is obscured by the short (10s) purges after the $Y(CpBut)_3$ dose.

QCM data in Fig. 3.4 indicates an unusual behavior during water exposures in Y_2O_3 ALD. For the first ten to twenty cycles, water appears to successfully remove ligands from yttrium precursor as shown trace (a).

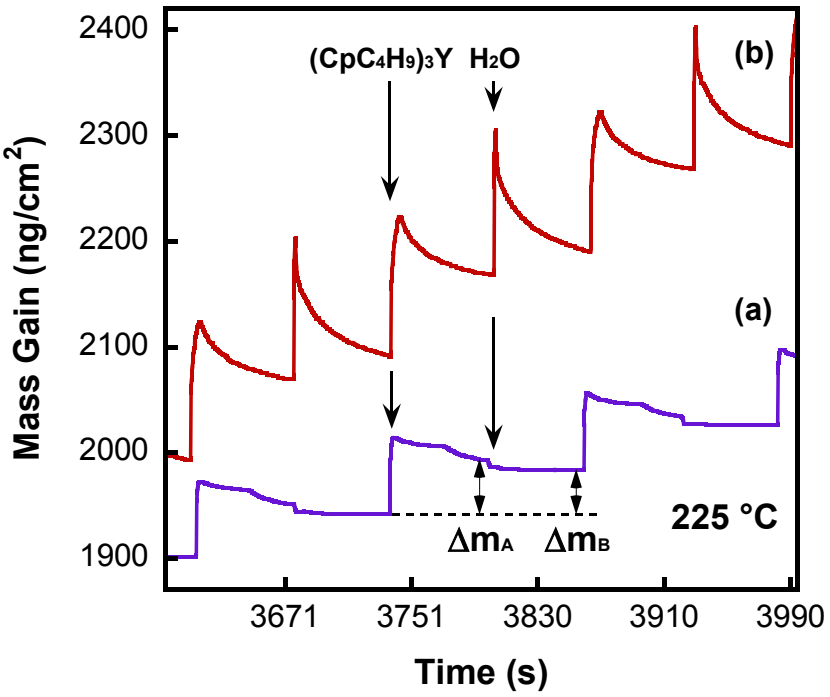

Figure 3.4 (a) QCM response during first Y_2O_3 ALD cycles on alumina surface deposited using 1/60/1/60 timing. (b) QCM response after ~500 ALD cycles when 8/60/1/60 timing was used.

At later times however (trace b), a significantly different process emerges that can be explained by water absorption into the yttria film which becomes more prominent as film thickness increases. In this case, the water absorption into the film causes every $Y(CpBut)_3$ dose to be exposed to the water diffusing out of the bulk, causing an undesired CVD type effect and non-self-limiting ALD behavior is therefore observed during $Y(CpBut)_3$ uptake (Fig. 3.5). Other studies of Y_2O_3 ALD support the idea that during the film deposition the film can absorb water and that extended water purge time is needed [27]. Reported spectroscopic studies of the yttria surface confirm that water molecules strongly interact with Y_2O_3 surface to

form hydroxides [33]. This specific water absorption behavior was attributed to the relatively high basicity of bulk yttria due to the large ionic radius of the metal ion [33, 34].

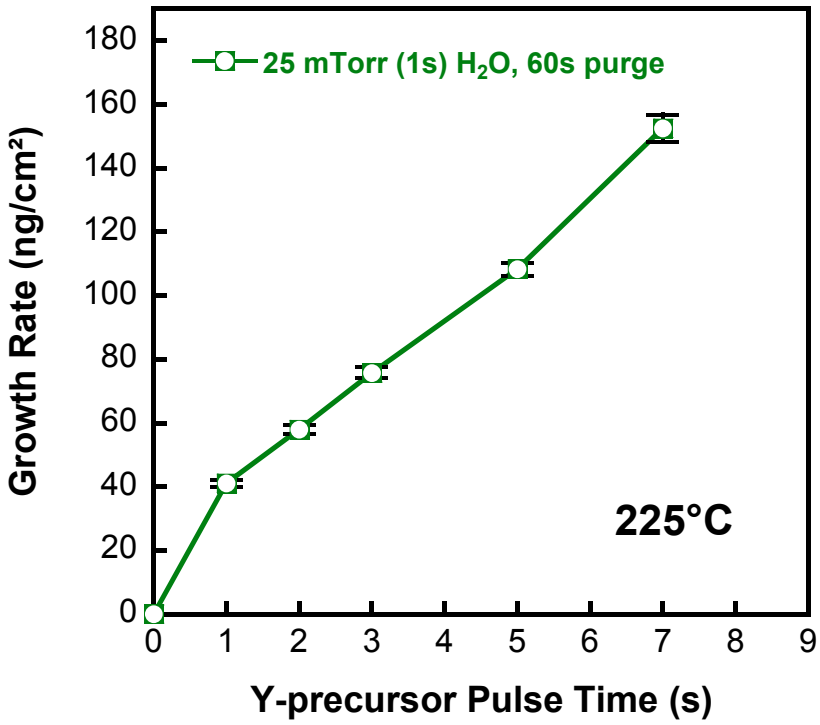

Figure 3.5 QCM measured non-self-limiting Y_2O_3 growth during $Y(CpBut)_3$ uptake demonstrated by the non-saturating behavior observed for X/60/1/60 timing.

In order to avoid complications due to water absorption as described above we examined the effect of reducing the water dose and extending the water purge time on the growth rate of Y_2O_3 (Fig. 3.6). In this experiment 50 ALD cycles of Y_2O_3 films were deposited on silicon substrates at 230°C using 2s of $Y(CpBut)_3$ exposures while varying the water dose from 3 mTorr to 25 mTorr and purge time from 45s to 150s. As demonstrated in Fig. 3.6 small water doses of 0.2s (6×10^2 L) and purge times greater than 100s are necessary to minimize the water absorption effect on

ALD yttria growth. From this figure it can be seen that deposited yttria films show a more uniform thicknesses from sample to sample.

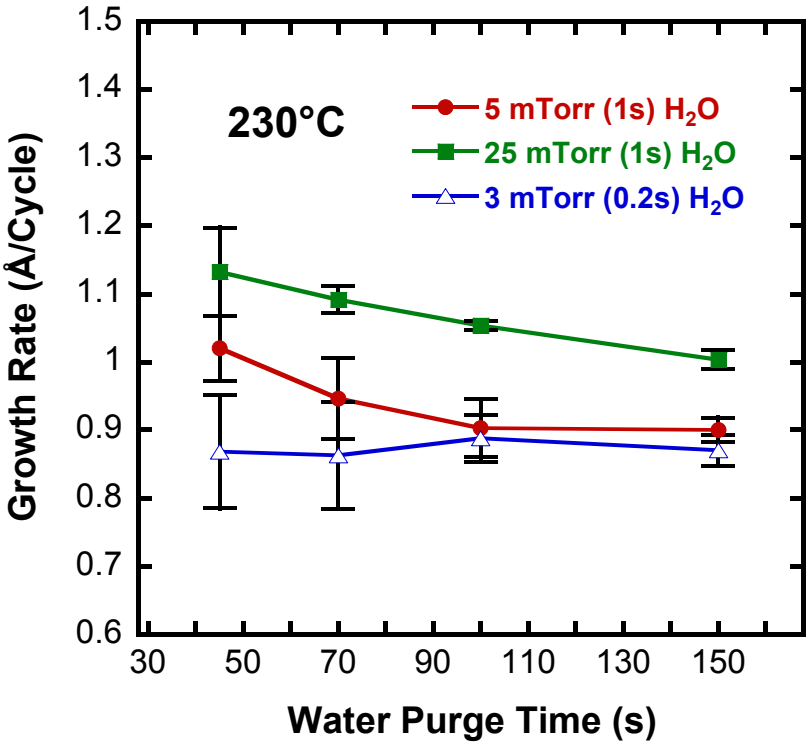

Figure 3.6 Ellipsometer measured Y_2O_3 film thickness on Si<100> versus purge time for varying water dose and purge times deposited using 2/10/Y/X timing.

Therefore, future Y_2O_3 ALD in this work was performed using 8/10/0.2/150 deposition timing to ensure yttrium precursor saturation and full water desorption.

The thickness of Y_2O_3 films deposited on Si<100> as a function of the number of deposition cycles is presented in Figure 3.7. A rise in growth rate from 1.4 to 1.7 Å/cycle was observed with increasing numbers of cycles until around 300 cycles after which the growth rate stayed relatively constant. In these experiments, a thickness variation between samples deposited in the same run was observed to be ~9% for 400 cycle deposition.

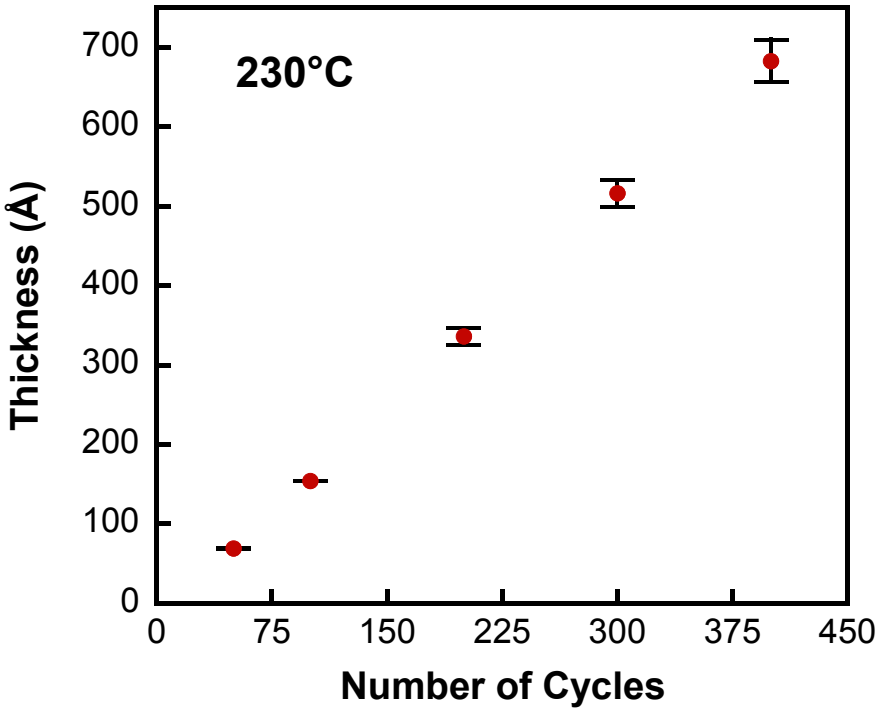

Figure 3.7 Ellipsometry measured Y_2O_3 film deposited on Si<100> using 8/10/0.2/150 timing conditions as a function of the number of deposition cycles.

A gradual increase in ALD growth rates has been observed previously for crystalline materials and is attributed to a change in the morphology of the crystal size evolving with increasing film thickness [35-37]. An increase in the water absorption rate with increasing yttria film thickness could also contribute to the observed change in growth rate.

Yttrium oxide growth rate versus deposition temperatures was investigated from 200 to 320°C (Fig. 3.8). In this experiment yttria films were deposited on Si<100> using 50 ALD cycles for each temperature. At 255°C yttria growth rate reaches a maximum of 1.5 Å/cycle.

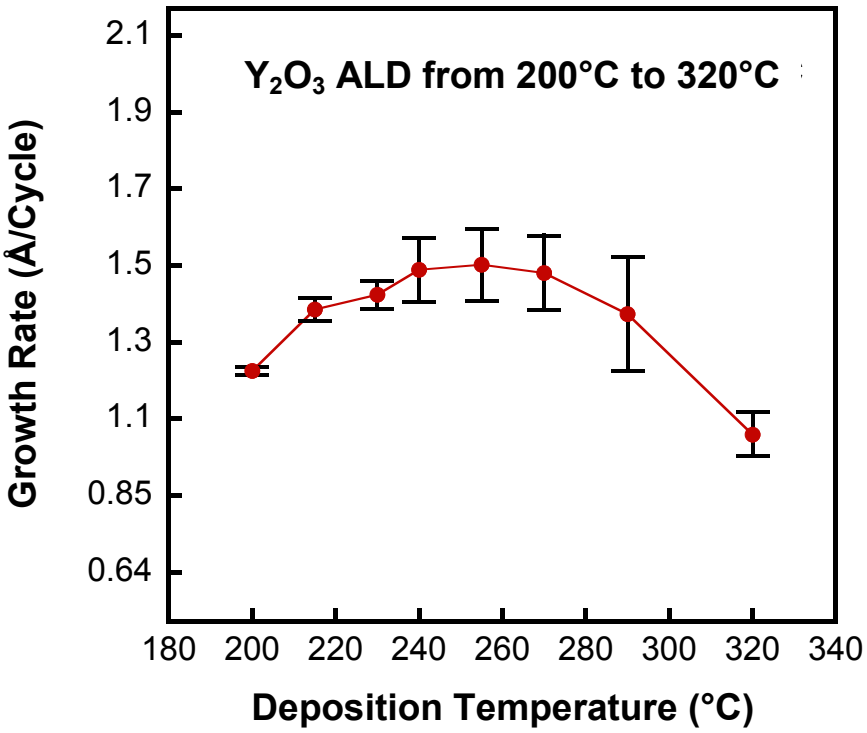

Figure 3.8 Y_2O_3 growth rate versus deposition temperature measured by ellipsometry for 50 A-B cycles deposited on silicon substrate using 8/10/0.2/150 timing.

This growth rate is slightly higher than that reported for yttria ALD using $Y(CpEt)_3$ [26], $Y(CpMe)_3$, and $Y(Cp)_3$ [25]. The decline in deposition rate at temperatures higher than 270°C is attributed to decomposition of the $Y(CpBut)_3$. The thickness gradient from sample to sample for the Y_2O_3 films increases with increasing deposition temperature reaching a maximum of 23% at 290°C which could be a result of precursor decomposition. At 320°C the precursor is most likely decomposing in gas phase before reaching the substrate which results in very small film growth rates. The ALD window from 230 to 290°C observed in this work falls in

the same temperature range reported for most ALD metal oxides deposited using Cp type precursors and water.

3.3.2 Proposed ALD Y_2O_3 Growth Mechanism

In this section QCM data presented in Fig. 3.4 (trace a) is utilized to investigate the surface chemistry of ALD Y_2O_3. This data was obtained using 1/60/1/60 deposition timing at 225°C in the early stages of deposition where water absorption is not an issue. Long 60s purges after $Y(CpBut)_3$ dosing enable the QCM to monitor the surface reaction after precursor dose. The yttra deposition half-reactions can be presented as:

Reaction A $\quad]\text{-}(OH)_x + Y(CpBut)_3 \rightarrow]\text{-}(O)_x\text{-}Y(CpBut)_{3-x} + x\ (HCpBut)$

Reaction B $\quad]\text{-}(O)_x\text{-}Y(CpBut)_{3-x} + 3/2\ H_2O \rightarrow]\text{-}(O)_{1.5}\text{-}Y(OH)_x + 3\text{-}x\ (HCpBut)$

Where ( ]) represents the depositing surface and x is the fraction of the ligands left after each precursor exposure. The byproduct of A-B reactions is HCpBut designated arbitrarily. The mass gain during $Y(CpBut)_3$ molecule adsorption and mass loss following water dose, predicted from A-B reaction scheme are both observed by QCM shown in Fig. 3.4 (trace a). In this figure, a 1s dose of $Y(CpBut)_3$ resulted in peak mass increase of 70.7 ng/cm^2 which is leveled off at 50.8 ng/cm^2 (Δm_A) after purge time with an additional mass loss of 6.7 ng/cm^2 after 1s water exposure with a total mass gain after full cycle of 44 ng/cm^2 (Δm_B). It is worth mentioning that the QCM captured the two stage mass loss during the purge time after $Y(CpBut)_3$ exposure as shown in Fig. 3.4 (trace a). Using the ratio $\Delta m_B/\Delta m_A$ =

0.87 and calculated from the A-B reaction atomic masses $\Delta m_A(YO_{1.5})$ = 133 and $\Delta m_B(Y(CpBut)_3$ - x·HCpBut)= 452-122x, the value of x can be calculated to x = 2.6. This indicates that the fraction of -CpBut ligands remaining after the first half-reaction is equal to 13.3%. This calculation procedure is similar to one previously published [35]. The comparable result was also obtained in [38] during QCM measurements of Y_2O_3 ALD deposition using $Y(CH_3Cp)_3$ and water chemistry. In [38], 17% of CH_3Cp ligands have been reported to remain on the surface after $Y(CH_3Cp)_3$ dose. The difference in the number of ligands remaining in this work compared to results in [38] is likely originating from the difference in size of butyl and methyl groups attached to the Cp ligands as well as differences in the duration of precursor purge times. Nevertheless, both observations indicate that most ligands are lost during the purge time after metal precursor dose. DFT calculations of the first half-reaction of the Y_2O_3 ALD for the $Y(Cp)_3$/water system show energetic favorability through relief of steric congestion around the yttrium center leaving one Cp ligand per yttrium atom [30]. Therefore, QCM mass loss measured during metal precursor purge time could be interpreted as a desorption of Cp ligands that recombine with neighboring H atom (from –OH group on the surface). The yttrium atom ultimately branches with neighboring oxygen atom as shown in pathway I of Fig. 3.9. However, one can easily estimate that for reaction (A) to take place in this pathway, 33.3% of (-CpBut) ligands need to remain on the surface. Therefore, based on the experimental results in this work, the first half reaction of

Y_2O_3 ALD must result in multiple yttria atoms bound to one Cp ligand as shown in pathway II of Fig. 3.9.

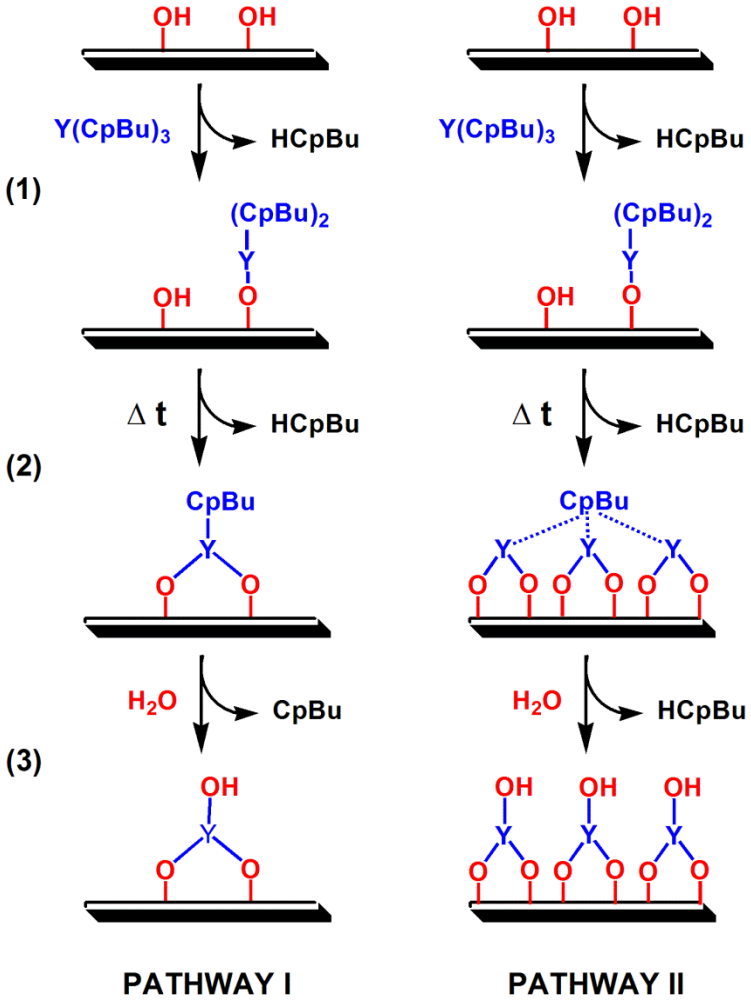

Figure 3.9 Proposed reaction pathways for Y_2O_3 ALD using $Y(CpBut)_3$ and water.

This reaction scenario is most likely facilitated by strong steric effects of bulky (-CpBut) ligands and its strong Brønsted basicity in comparison with its Lewis basicity [29]. Last, the reaction proceeds with maximum ligand elimination resulting in high yttrium atom coverage which consequently results in a high Y_2O_3 growth rate. In other words, the amount of mass added per cycle in weight of yttrium atoms is larger than would be expected if total surface coverage was

achieved with Y-(CpBut) ligands. For this reason, multiple yttrium atoms are proposed to be bound to a single organic ligand. An analogous reaction mechanism was proposed for La_2O_3 ALD using $La(Cp)_3$ and water chemistry based on DFT estimates of a size of Cp ligand [39].

It is possible that in the second half reaction, unreacted hydroxyl groups from prior A-B cycles become centers for hydrogen bonding and water absorption during the ALD process by proceeding in more complex manner than what is depicted in pathway II.

3.3.3 Film Characterization

The crystalline orientation of a 350 Å thick yttria film deposited at 230°C on Si<100> determined from a XRD θ-2θ diagram is presented in Figure 3.10. The Y_2O_3 exhibited peaks and their relative intensities closely match cubic polycrystalline Y_2O_3 (PDF number 88-5592, JCPDS-ICDD 2002) as shown by Miller indices in Fig. 3.10. In this figure, Y_2O_3 orientation of (222) is the most intense peak and (400) the second most intense. All previously reported XRD patterns for ALD Y_2O_3 films [21,22,25-27] also exhibit cubic polycrystalline structure where (222) and (400) planes show the highest intensity (meaning that the highest intensity depends on ALD growth conditions). From the most intense (222) reflection peak in Fig. 3.9 the average grain size for 350 Å thick yttria film is estimated to be ~8.5 nm. This value was obtained by applying the Scherrer equation [40]. $Y(OH)_3$ crystalline phases have not been detected by XRD which could potentially be formed due to water absorption issues.

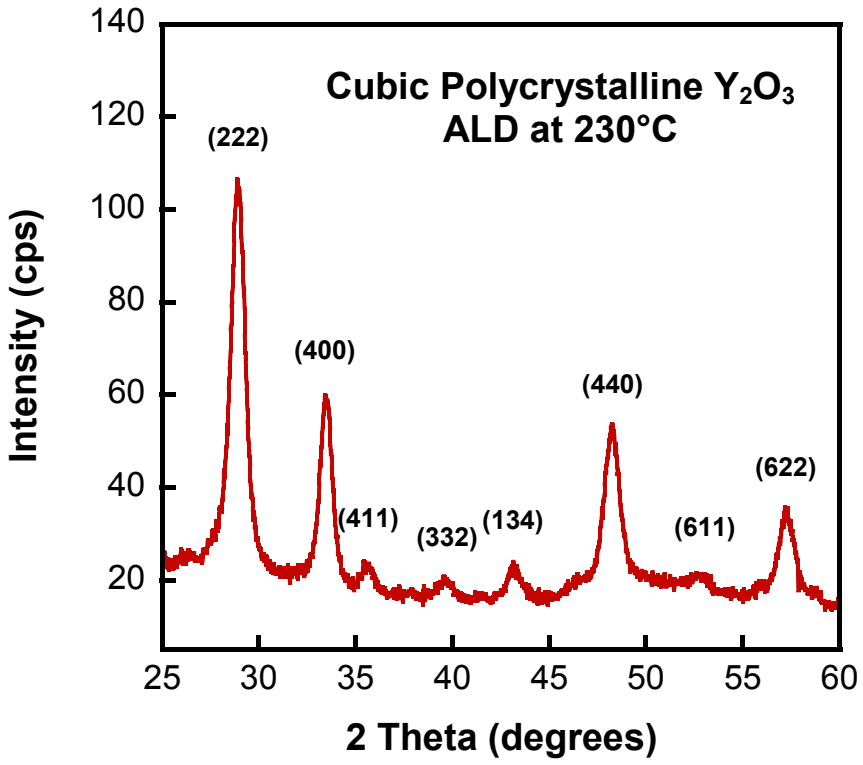

Figure 3.10 XRD spectrum of a 350 Å thick Y_2O_3 film deposited on Si<100> using 8/10/0.2/150 timing.

XRR density measurements were performed on a series of Y_2O_3 films deposited at 230°C using 8/10/0.2/150 timing. Density values varied from 93 to 98% of the reference yttria density of 5.03 g/cm^3 [1]. Using an average density of 95% a growth rate of 1.3 Å/cycle can be calculated with the 62 ng/cm^2/cycle growth observed in Fig. 3.3. This value is in slight disagreement with 1.4-1.7 Å/cycle growth rate observed for yttria deposited on Si<100> (Fig. 3.7). This is due to differences in film thickness along precursor flow and changes in films crystallinity. The XRR was also used to verify thickness values obtained from ellipsometry and indicated good agreement between two techniques.

The surface morphology of the deposited films was analyzed by AFM. A series of 2-D root-mean-squared (RMS) measurements performed on a 350 Å thick Y_2O_3 film revealed a roughness of ~4 Å for 5x5μm AFM scans. This value closely matched RMS values observed for ALD yttria films obtained for $Y(CpEt)_3$ /water [26] deposited under similar conditions. However, this roughness value is in slight disagreement with roughness values of ~7.5 Å obtained from XRR in which RMS values were obtained by averaging over the whole sample. This inconsistency could be a result of a thickness gradient that could be observed visually for thick yttria films. It should be noted that the roughness of ALD yttria can differ depending on films thickness and deposition temperature [25].

Rutherford backscattering spectrometry (RBS) was used to determine stoichiometry and composition of a 500 Å thick Y_2O_3 film deposited on Si <100> at 230°C (Figure 3.11). As discussed previously, incomplete water desorption during ALD of Y_2O_3 can potentially be a problem due to the formation of $Y(OH)_3$ or YOOH in the film.

XPS can be a useful tool to determine the level of the hydroxylation of the yttria film based on shifts in biding energy of constituting atoms. Figure 3.12 presents three XPS scans of the O(1s) region for a 335 Å ALD Y_2O_3 film deposited at 230°C. The survey scan (solid line) shows splitting of the O(1s) signal indicating two binding states of oxygen. The O(1s) peak position at 529.15eV is consistent with Y-O binding energy in Y_2O_3 [41]. Appearence of a second peak located at 531.5eV is attributed to the presence of residual carbon on the surface (Y-O-C) and to YO-OH

terminal bonds as a result of exposure to the atmosphere and is consistent with that observed in literature for Y_2O_3 [27,42-45].

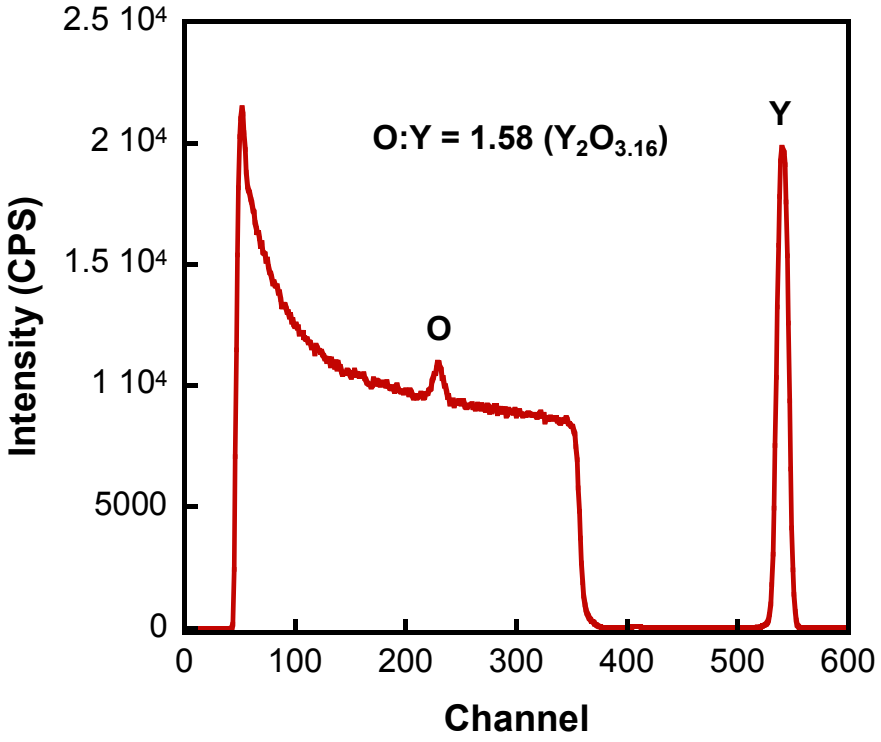

Figure 3.11 RBS spectrum of 500 Å Y_2O_3 film deposited on Si<100> with timing sequence 8/10/1/150.

The first sputtered scan (dotted line) shows a large O(1s) peak at 528.37 eV with a small shoulder at around 531.25 eV due to the presence of $Y(OH)_3$ [46]. XPS scans after additional sputtering show a shifted oxygen peak to lower energy ~527.5 eV (dashed line) without peak spliting. The results obtained in Fig. 3.11 indicate that the Y_2O_3 film probably absorbed water from the air forming a yttrium hydroxide top layer while leaving the bulk film intact. The O(1s) peak shift toward 527.5 eV (dashed line) is attributed to an artifact due to preferential argon ion sputtering of oxygen.

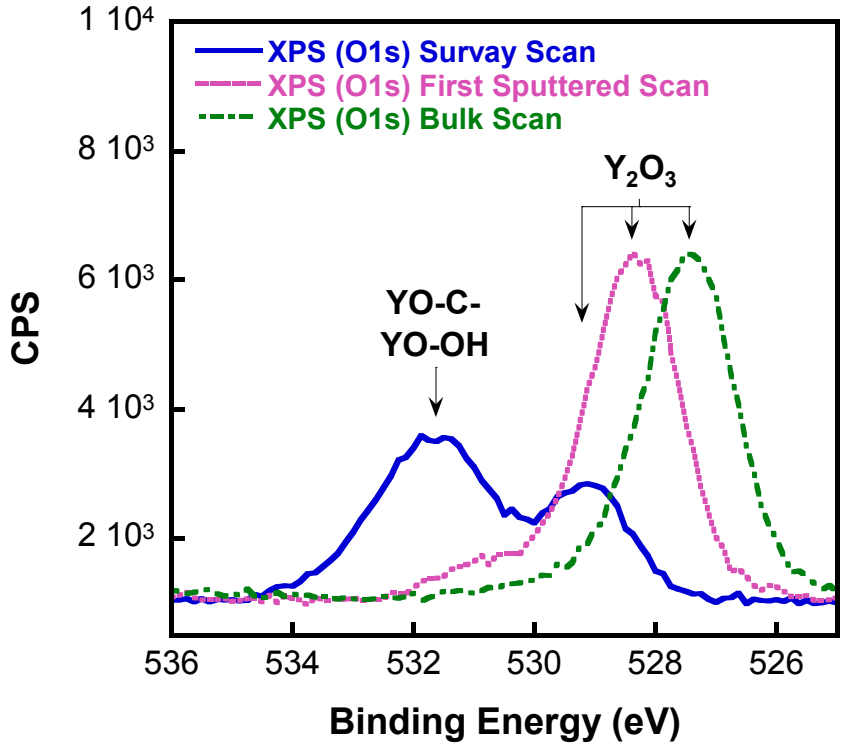

Figure 3.12 XPS survey scan of the O (1s) region acquired from a 335 Å thick Y_2O_3 film deposited using 8/10/0.2/150 timing at 230°C (solid line) and O (1s) region spectra of the same sample after Ar^+ sputtering (dashed line).

XPS did not detect carbon impurities in sputtered samples deposited at 230°C in agreement with the RBS data. A reduction of the number hydroxyl groups on the surface of Y_2O_3 can be achieved by high temperature annealing with complete elimination by in situ capping [31,47,27].

3.3.4 Optical Properties

The obtained refractive indexes (n) of an as-deposited ALD Y_2O_3 film and of an in situ ALD alumina capped Y_2O_3 film as function of wavelength are presented in Figure 3.13. The thickness of the uncapped Y_2O_3 film was 343.2 Å. The capped film included a 28.2 Å Al_2O_3 cap on a 306.4 Å yttria film as determined from XRR.

The refractive index of the uncapped ALD Y_2O_3 showed a value of ~1.87 with no visible change over the measured wavelength spectrum. As shown in Fig. 3.12, the index values obtained in this work are comparable to the values from reference data [48-51].

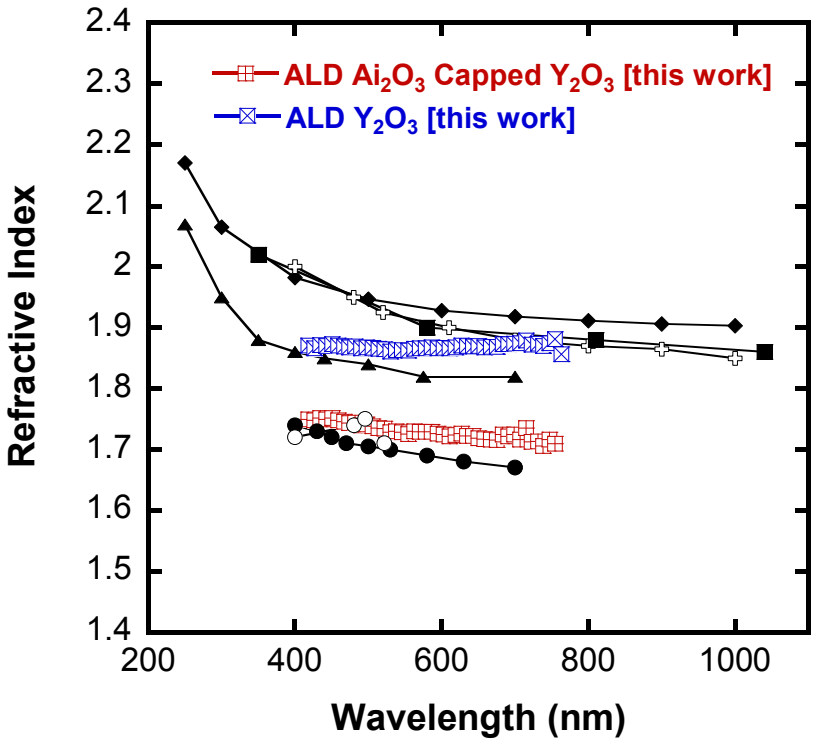

Figure 3.13 Ellipsometry measured refractive index of as-deposited and ALD alumina capped Y_2O_3 films compared to previously reported refractive index data for Y_2O_3 exposited to air and those measured in vacuum (circles).

Index values can be dependent on the method of film preparation and the measurement technique [52,53]. The extinction coefficient (k) values for the uncapped Y_2O_3 film estimated from the ellipsometer's fitting program were always zero, indicating that the deposited film is highly transparent.

Alumina capped Y_2O_3 showed a refractive index from 1.75 to 1.70 for a wavelength varying from 418.5 to 754.7 nm. From Fig. 3.12, these index values are on average ~6% lower than for uncapped-air exposed ALD yttria film. The extinction coefficient values in this case were about 0.05 indicating some light absorption by the film. The index data for the capped film agree remarkably well with the previously reported refractive index data for Y_2O_3 measured in vacuum [51,54]. This data suggests that the presence of absorbed water and formation of layers of yttrium hydroxide and yttrium carbonates are the main reason for the increase in refractive index for uncapped Y_2O_3. It has also been observed that yttria's water absorption capabilities could originate from defects in crystal structure [51]. Some of the losses in high refractive index materials, such as polycrystalline Y_2O_3, are attributed to surface reflection and light scatter [2,52], therefore, refractive index reduction can be partially attributed to changes in reflectance due to the presence of an amorphous alumina cap. The in situ capping is believed to also improve transmission in the infrared region of the optical spectra where major losses are observed for Y_2O_3 films [52,53].

3.4 Conclusions

Crystalline Y_2O_3 films with maximum growth rates of 1.7 Å/Cycle were successfully deposited using Tris(butylcyclopentadienyl)yttrium(III) and water. The yttrium precursor showed low volatility but at the same time was thermally stable and exhibited high reactivity towards water. QCM data indicated that some water absorption is observed after many ALD cycles possibly through hydroxide

formation. We demonstrated that water dose time and purge time tuning is needed to achieve self-limiting behavior. This suggests that yttria may be a good candidate for waterless ALD chemistry. QCM data also showed that the surface reaction proceeds with a high level of -CpBut ligand elimination. Calculations show that only 13.3% of the -CpBut ligands remain on the surface after metal precursor exposure.

A wide variety of applied characterization techniques confirmed the excellent quality of yttria films deposited at 230°C. XPS scans indicate that water absorbed on the surface of the yttria film does not penetrate far into the bulk film and only forms a thin yttrium hydroxide layer near the top.

Comparison of the refractive index data with those obtained in vacuum suggests that ALD Al_2O_3 capping is a viable way to avoid water absorption on the surface. This is suggested through the similarity of the capped yttrium film's refractive index with vacuum deposited yttria. This result can potentially extend applicability of ALD Y_2O_3 in the future.

3.5 Acknowledgements

Personnel support was provided by Synkera Technologies, Inc. (Longmont, CO, U.S.A) as part of DOD N045-008-0122 grant. I would like to personally thank my colleagues Dr. B. Burton, Dr. R. Wind, and Dr. J. McCormick for their support during work on this project.

3.6 References

1. Hand Book of Chemistry and Physics, 89th Edition 2008-2009.

2. Harris, D.C., Durable 3-5 mu m transmitting infrared window materials. Infrared Physics & Technology, 1998. **39**(4): p. 185-201.

3. Swamy, V., N.A. Dubrovinskaya, and L.S. Dubrovinsky, High-temperature powder X-ray diffraction of yttria to melting point. Journal of Materials Research, 1999. **14**(2): p. 456-459.

4. Huignard, A., et al., Growth by laser ablation of Y2O3 and Tm : Y2O3 thin films for optical applications. Journal of Materials Chemistry, 2000. **10**(2): p. 549-554.

5. Gaboriaud, R.J., et al., Yttrium sesquioxide, Y2O3, thin films deposited on Si by ion beam sputtering: microstructure and dielectric properties. Thin Solid Films, 2001. **400**(1-2): p. 106-110.

6. Kahn, A., et al., Low threshold monocrystalline Nd:(Gd, Lu)2O3 channel waveguide laser. Optics Express, 2009. **17**(6): p. 4412-4418.

7. Kahn, A., et al., Amplification in epitaxially grown Er:(Gd, LU)2O3 waveguides for active integrated optical devices. Journal of the Optical Society of America B-Optical Physics, 2008. **25**(11): p. 1850-1853.

8. Miu, D., et al., alpha-Axis growth of ferroelectric SrBi2Ta2O9 thin films on silicon. Materials Letters, 2005. **59**(10): p. 1243-1247.

9. Suzuki, K., Tanaka, K., Fu, D. S.,, Electroceramics In Japan VII (Key Engineering Materials). 2004. **269**: p. 49-52.

10. Lu, F.X., et al., Magnetron sputtered oxidation resistant and antireflection protective coatings for freestanding diamond film IR windows. Diamond and Related Materials, 2009. **18**(2-3): p. 244-248.

11. Dukel'skii, K.V. and S.K. Evstrop'ev, Forming protective nanosize Y2O3 coatings on crystal phosphors. Journal of Optical Technology, 2008. **75**(11): p. 737-740.

12. Shi, G.D., et al., Influence of Metal-Layer Thickness on Annealing behaviors of a NiCoCrAl/YSZ Multiscalar Microlaminate produced by EB-PVD. Journal of Alloys and Compounds, 2009. **476**(1-2): p. 830-835.

13. Wang, Y.Q., et al., High temperature cyclic oxidation behavior of Y2O3-ZrO2 thermal barrier coatings irradiated by high-intensity pulsed ion beam. Journal of Central South University of Technology, 2009. **16**(1): p. 13-17.

14. Xu, Z.H., et al., Double-ceramic-layer thermal barrier coatings of La2Zr2O7/YSZ deposited by electron beam-physical vapor deposition. Journal of Alloys and Compounds, 2009. **473**(1-2): p. 509-515.

15. Montero, X., et al., Spinel and Perovskite Protection Layers Between Crofer22APU and La0.8Sr0.2FeO3 Cathode Materials for SOFC Interconnects. Journal of the Electrochemical Society, 2009. **156**(1): p. B188-B196.

16. Tanaka, M., et al., Delamination toughness of electron beam physical vapor deposition (EB-PVD)Y2O3-ZrO2 thermal barrier coatings by the pushout method: Effect of thermal cycling temperature. Journal of Materials Research, 2008. **23**(9): p. 2382-2392.

17. Dubourdieu, C., et al., Addition of yttrium into HfO2 films: Microstructure and electrical properties. Journal of Vacuum Science & Technology A, 2009. **27**(3): p. 503-514.

18. Shimada, S., et al., Thermal plasma CVD of PSZ and double layered TiN/PSZ coatings by injection of alkoxides solutions with H2O. Surface & Coatings Technology, 2008. **202**(19): p. 4644-4652.

19. Alarcon-Flores, G., et al., Optical and structural characteristics of Y2O3 thin films synthesized from yttrium acetylacetonate. Journal of Materials Science, 2008. **43**(10): p. 3582-3588.

20. Pan, T.M. and K.M. Liao, Structural properties and sensing characteristics of Y2O3 sensing membrane for pH-ISFET. Sensors and Actuators B-Chemical, 2007. **127**(2): p. 480-485.

21. Mölsä, H., Niinistö, L., Utriainen, M., , Growth of yttrium oxide thin films from ß-diketonate precursor. Advanced Materials for Optics and Electronics, 1994. **4**(6): p. 389–400.

22. Putkonen, M., et al., Low-temperature ALE deposition of Y2O3 thin films from beta-diketonate precursors. Chemical Vapor Deposition, 2001. **7**(1): p. 44-50.

23. Gusev, E.P., et al., Ultrathin high-K metal oxides on silicon: processing, characterization and integration issues. Microelectronic Engineering, 2001. **59**(1-4): p. 341-349.

24. Van, T.T. and J.P. Chang, Radical-enhanced atomic layer deposition of Y2O3 via a beta-diketonate precursor and O radicals. Surface Science, 2005. **596**(1-3): p. 1-11.

25. Niinisto, J., M. Putkonen, and L. Niinisto, Processing of Y2O3 thin films by atomic layer deposition from cyclopentadienyl-type compounds and water as precursors. Chemistry of Materials, 2004. **16**(15): p. 2953-2958.

26. Majumder, P., et al., Atomic layer deposition of Y2O3 films on silicon using tris(ethylcyclopentadienyl) yttrium precursor and water vapor. Journal of the Electrochemical Society, 2008. **155**(8): p. G152-G158.

27. de Rouffignac, P., J.S. Park, and R.G. Gordon, Atomic layer deposition of Y2O3 thin films from yttrium tris(N,N'-diisopropylacetamidinate) and water. Chemistry of Materials, 2005. **17**(19): p. 4808-4814.

28. Puurunen, R.L., Surface chemistry of atomic layer deposition: A case study for the trimethylaluminum/water process. Journal of Applied Physics, 2005. **97**(12).

29. Elliott, S.D., Improving ALD growth rate via ligand basicity: Quantum chemical calculations on lanthanum precursors. Surface & Coatings Technology, 2007. **201**(22-23): p. 9076-9081.

30. Ren, J., et al., Surface reaction mechanism of Y2O3 atomic layer deposition on the hydroxylated Si<100>-2 x 1: A density functional theory study. Applied Surface Science, 2009. **255**(16): p. 7136-7141.

31. Niu, D., R.W. Ashcraft, and G.N. Parsons, Water absorption and interface reactivity of yttrium oxide gate dielectrics on silicon. Applied Physics Letters, 2002. **80**(19): p. 3575-3577.

32. Elam, J.W., M.D. Groner, and S.M. George, Viscous flow reactor with quartz crystal microbalance for thin film growth by atomic layer deposition. Review of Scientific Instruments, 2002. **73**(8): p. 2981-2987.

33. Kuroda, Y., et al., Specific adsorption behavior of water on a Y2O3 surface. Langmuir, 2000. **16**(17): p. 6937-6947.

34. Smith, D.W., An Acidity Scale for Binary Oxides. Journal of Chemical Education, 1987. **64**(6): p. 480-482.

35. Elam, J.W., et al., Atomic layer deposition of In2O3 using cyclopentadienyl indium: A new synthetic route to transparent conducting oxide films. Chemistry of Materials, 2006. **18**(15): p. 3571-3578.

36. Elam, J.W., Z.A. Sechrist, and S.M. George, ZnO/Al2O3 nanolaminates fabricated by atomic layer deposition: growth and surface roughness measurements. Thin Solid Films, 2002. **414**(1): p. 43-55.

37. Ritala, M., et al., Growth of Titanium-Dioxide Thin-Films by Atomic Layer Epitaxy. Thin Solid Films, 1993. **225**(1-2): p. 288-295.

38. Elam, J.W., ALD workshop at 8th International Conference on Atomic Layer Deposition - ALD 2008.

39. Elliott, S.D., 8th International Conference on Atomic Layer Deposition - ALD 2008.

40. Scherrer, P., Goett. Nachr., 1918. **2**: p. 98.

41. Crist, B.V., Handbook of Monochromatic XPS Spectra, 2000.

42. Chambers, J.J., et al., Effects of surface pretreatments on interface structure during formation of ultra-thin yttrium silicate dielectric films on silicon. Applied Surface Science, 2001. **181**(1-2): p. 78-93.

43. Ulrich, M.D., et al., Bonding and structure of ultrathin yttrium oxide films for Si field effect transistor gate dielectric applications. Journal of Vacuum Science & Technology B, 2003. **21**(4): p. 1792-1797.

44. Durand, C., et al., Structural and electrical characterizations of yttrium oxide films after postannealing treatments. Journal of the Electrochemical Society, 2005. **152**(12): p. F217-F225.

45. Durand, C., et al., Microstructure and electrical characterizations of yttrium oxide and yttrium silicate thin films deposited by pulsed liquid-injection plasma-enhanced metal-organic chemical vapor deposition. Journal of Applied Physics, 2004. **96**(3): p. 1719-1729.

46. Barr T.L. Electron Spectroscopy for Chemical Analysis Examination of Rare Earth and Near Rare Earth Species, Quantitative Surface Analysis of

Materials. ASTM STP 643; McIntyre N.S. Ed.; American Society for Testing and Materials: Philadelphia, 178; pp 83-104.

47. Niu, D., et al., Chemical, physical, and electrical characterizations of oxygen plasma assisted chemical vapor deposited yttrium oxide on silicon. Journal of the Electrochemical Society, 2003. **150**(5): p. F102-F109.

48. Nigara, Y., Measurement of the Optical Constants of Yttrium Oxide. Jpn. J. Appl. Phys., 1968. **7**: p. 404-408.

49. Heitmann, W., Reactively Evaporated Films of Scandia and Yttria. Applied Optics, 1973. **12**(2): p. 394-397.

50. Masetti, E., Piegari, A.M., Tirabassi, A.,, Optical characterization of low-absorbing thin films in the visible and infrared spectrum (SPIE Proceedings Paper). Optical Thin Films and Applications, 1990. **1270**: p. 125-437.

51. Atanassov, G., R. Thielsch, and D. Popov, Optical-Properties of TiO2, Y2O3 and Ceo2 Thin-Films Deposited by Electron-Beam Evaporation. Thin Solid Films, 1993. **223**(2): p. 288-292.

52. Edited By Palik, E.D., Handbook of Optical Constants of Solids, Academic Press, 1998.

53. Bezuidenhout, D.F. and R. Pretorius, The Optical-Properties of Evaporated Y2O3 Films. Thin Solid Films, 1986. **139**(2): p. 121-132.

54. Arnon, O. and J. Chou, Wide Band Measurement of the Refractive-Index of Optical Thin-Films during Their Deposition. Thin Solid Films, 1982. **89**(3): p. 268-268.

CHAPTER IV

ATOMIC LAYER DEPOSITION OF TiN USING $TiCl_4$ AND HYDRAZINE

4.1 Introduction

Atomic layer deposition (ALD) has attracted considerable attention in the past two decades due to its unique capability for producing highly conformal, defect-free thin films on high aspect ratio structures [1, 2]. ALD is a thin film growth method based on sequential, self-limiting surface reactions [3]. Because the surface reactions are self-limiting, ALD can deposit extremely conformal thin films with atomic layer control [3]. In addition, ALD is demonstrated to be able to deposit high purity materials at relatively low temperatures [4].

Advances in ALD have been for the most part driven by the interests of the semiconductor industry [1, 2, 5]. The International Technology Roadmap for Semiconductors (ITRS) has included ALD for high dielectric constant gate oxides in the MOSFET structure and for copper diffusion barriers in back-end interconnects [1, 6]. The necessity for ultrathin barrier films for copper interconnects has led to intensive studies on conductive ALD metal nitrides such as TaN, TiN and WN [7].

TiN became one of the most studied among ALD metal nitrides and has been deposited by a variety of precursors and methods [7, 8]. The first reported TiN ALD processes involved use of metal halides (MH) $TiCl_4$ [9-16] or TiI_4 [17], and NH_3 as nitrogen source and reducing agent. Using $TiCl_4/NH_3$ chemistry, cubic ALD TiN can be grown with rates of 0.2 to 0.3 Å/Cycle at temperatures ranging from 350°C to 500°C [16, 18]. TiN films deposited at 400°C contain 6 atomic % Cl and ~0.5 at. % Cl

when deposited at 500°C, with oxygen impurities varying from ~32 at. % for 340 Å thick TiN films down to ~9 at. % for 1400 Å films [18]. Little or no difference has been observed in terms of growth rate, deposition temperature and amount of impurities when TiI_4 was used instead of $TiCl_4$ [17].

It has been realized that high deposition temperatures and the presence of halide contaminants are significant drawbacks of $TiCl_4$(TiI)/NH_3 ALD systems, limiting their applicability in industry [7]. Initial steps to reduce the TiN deposition temperature and minimize its impurities from $TiCl_4$ led to the use of zinc [18, 19], trimethylaluminum (TMA) [20], and H_2/N_2 plasma [21] to promote more energetic reduction of the Ti^{4+} ion to Ti^{3+}. Alternatively, the use of different metal precursors such as metal organic (MO) alkyl amides like tetrakis(diethylamido)titanium (TEMAT) [22], tetrakis(dimethylamido)titanium (TDMAT) [23, 24] in combination with NH_3 enabled the lowering of the TiN deposition temperature to 200°C and below. However, use of MO precursors results in the growth of low density TiN films with high levels of impurities and unacceptable adhesion to copper [8]. Relatively good quality TiN_x has been demonstrated using plasma assisted MO-ALD processes at low deposition temperatures [25, 26].

In the search for a more reactive nitrogen source, 1,1-dimethylhydrazine (DMHy) was tried in combination with $TiCl_4$ [27]. Using this chemistry, ALD TiN_x can be grown with a rate of 0.2 Å/cycle at 250°C. Overall this chemistry enabled the reduction of the deposition temperature, however, deposited TiN_x films suffer from

a high level of impurities such that films obtained at 300°C contain ~16 at. % of chlorine and ~6 at. % of carbon [27].

ALD TiAlN has been considered as a possible substitute for TiN due to its high oxidation resistance and good electrical conductivity performance [7]. Besides applications in electronics, titanium aluminum nitride films have important applications including hard coating [28]. More recently it has been considered for solar energy conversion applications [29]. In the past, thermal $TiAl_xN_y$ ALD films were deposited using $TiCl_4/NH_3$/TMA [20], $TiCl_4$/dimethylaluminum hydride ethylpiperdine (DMAH-EPP) [30], or TDMAT/NH_3/DMAH-EPP [31].

Since deposition of a good quality thermal ALD TiN film at temperatures below 300°C remains a challenge, in this work we examined an alternative chemistry where ALD TiN_x was grown using $TiCl_4$ and hydrazine (N_2H_4). This new chemistry relies on favorable thermochemistry; use of hydrazine as a reducing agent compared to other nitrogen sources. This favorability was clearly demonstrated in the comparison with ammonia, which is most commonly used as a nitrogen precursor [32].

$$TiCl_4 + 8/6NH_3(g) \rightarrow TiN + 4HCl(g) + 1/6N_2(g) \qquad \Delta G_{250°C} = -2 \text{ kcal/mole}$$

$$TiCl_4 + N_2H_4(g) \rightarrow TiN + 4HCl(g) + 1/2N_2(g) \qquad \Delta G_{250°C} = -50 \text{ kcal/mole}$$

From these Gibbs free energy calculations it is apparent that at 250°C TiN deposition using hydrazine is much more thermodynamically favorable than deposition using ammonia. This difference arises from the fact that NH_3, serves as a less effective reagent. This is manifested in $\cdot NH_2$ radical formation enthalpies,

which are 461 kJ/mole for NH_3 and 297 kJ/mole for N_2H_4 respectively [27]. In addition, the absence of alkyl substituents in the hydrazine molecule will insure an absence of the carbon contamination observed earlier for the $TiCl_4$/DMHy ALD system [27]. Previously, hydrazine had been successfully utilized for the deposition of metal nitrides using MOCVD for AlN [33], GaN [34], ALD for Si_3N_4 [35], TaN [36] and nitridation process to obtain transition metal nitrides [37]. In addition, we demonstrated feasibility of using $TiCl_4$/TMA/N_2H_4 chemistry for deposition of ALD $TiAl_xN_y$ at 275°C where trimethylaluminum (TMA) was used as the aluminum source.

In order to gain a better understanding of the surface processes during ALD TiN_x growth, we used in situ monitoring techniques such as quartz crystal microbalance (QCM) and Fourier transform infrared spectroscopy (FTIR). TiN_x and $TiAl_xN_y$ films were characterized using XPS, XRR, and GIXRD to determine the presence of impurities, film growth rate, density, and crystallinity. Electrical and optical properties of deposited films were evaluated using four point probe and spectroscopic ellipsometry techniques, respectively.

4.2 Experimental

ALD of TiN_x was investigated using $TiCl_4$ and N_2H_4 in a hot walled viscous-flow type ALD reactor described in detail elsewhere [38]. Titanium tetrachloride with a purity of 99.8% was obtained from Strem Chemical, Inc. (Newburyport, MA, U.S.A.). The hydrazine used had a 98% (99.5% lot) purity level obtained from Sigma-Aldrich, Inc. (Milwaukee, WI, U.S.A.). Both chemicals were transferred to

glass containers in a glove bag in an inert gas environment. $TiCl_4$ and N_2H_4 had both been degassed using 2-3 cycles of freeze-pump-thaw process before use. Extra precaution needs to be taken when handling hydrazine owing to its explosive nature [39]. During TiN_x ALD the precursors were kept at room temperature. Hydrazine has a vapor pressure of 14 mm Hg at 25°C [39]. The trimethylaluminium (TMA) with 97% purity used for ALD $TiAl_xN_y$ deposition was supplied by Sigma-Aldrich, Inc.. Ultra high purity (UHP 99.999%) grade nitrogen served as a carrier gas. The ALD reactor base pressure was maintained at 0.9 Torr at all times.

Pre-cut 1x1 inch size silicon wafers (Si<100>) were used as a substrate for ex situ X-ray analysis of deposited TiN_x and $TiAl_xN_y$ films. A Sematech Inc. (Austin, TX, U.S.A.) patterned silicon wafer was used to determine the TiN_x film conformality in 4/1 aspect ratio trenches as analyzed by scanning electron microscopy (SEM). All substrates were cleaned with acetone and isopropanol and allowed to degas and equilibrate in the ALD reaction chamber for 30 minutes before film deposition. Silicon wafers used in this work for the ALD films characterization had a ~25 Å native oxide layer. The error bars for each data point in the graphs involving deposition on silicon substrate represent a variation in TiN_x thickness for three samples deposited in same run over a distance of 20 cm.

Quartz crystal microbalance measurements were performed using gold plated, polished quartz crystals with resonant frequencies of 6 MHz obtained from Colorado Crystal Corp. (Loveland, CO, U.S.A). Detailed information about the QCM instrumentation used in these experiments can be obtained from previous

publication [38]. Prior to each precursor uptake, the QCM was coated with ~60 Å of ALD alumina (Al_2O_3) deposited using TMA and water chemistry. Error bars in QCM uptake figures represent the standard deviation of 20 ALD cycles.

The ALD reactant pulse and purge timing (in seconds) throughout this chapter are designated as $t_1/t_2/t_3/t_4$ where t_1 is the $TiCl_4$ exposure time, t_3 is the N_2H_4 dose time, and t_2, t_4 are purge times after the first and second reactant doses respectively. Timing for ALD $TiAl_xN_y$ deposition is similar to that for TiN but with an additional TMA dose, purge, and subsequent dose with hydrazine again after TMA.

The XRR and GIXRD scans were performed using a Bede D1 high resolution X-ray diffractometer from Bede Scientific Inc. (Englewood, CO, U.S.A.). This X-ray diffractometer is equipped with a Cu X-ray tube working at λ=1.54 Å. Data were collected using a filament current of 40 mA and a voltage of 40 kV. Raw data were fit using REFS fitting software from Bede Scientific Inc.. From XRR data fitting, film thicknesses, densities, and surface roughness were determined. For the grazing incidence XRD analysis, the samples were held at ω=1° and the detector (2θ) scanned from 20 to 80°.

XPS survey and depth profile data were acquired using a Perkin-Elmer 5600 (Waltham, MA, U.S.A.) photoelectron spectrometer system with monochromatic Al Kα X-rays (12 mA, 12 kV), with Ar^+ sputtering ability. SEM images were obtained with a beam voltage and current of 5.0 keV and 10 μA, respectively.

Transmission FTIR spectroscopy studies of TiN_x deposition were performed at 200°C and 275°C. High surface area spherical ZrO_2 particles were used in the FTIR measurements to obtain a high signal to noise ratio. The ZrO_2 particles with an average diameter of 30 nm were supplied by Sigma-Aldrich, Inc.. The deposition substrate was prepared by pressing zirconium particles into a photoetched tungsten grid and placing it in an IR beam shining through a reaction chamber. The walls of the FTIR chamber were maintained at ~120°C at all times and the tungsten grid with zirconium particles was resistively heated to a suitable reaction temperature. The FTIR scans were taken with a Nicolet Magna 560 FTIR spectrometer equipped with a nitrogen-cooled MCT-B infrared detector. This IR experimental setup is described in earlier publication [40].

Refractive indexes of deposited TiN_x and $TiAl_xN_y$ films were determined using an ellipsometer from J. A. Woollam Co. (M-44STD) **(**Lincoln, NE, U.S.A.) by scanning from 418.5 nm to 754.7 nm at an incident angle of 75°. In order to obtain accurate refractive index data, the thicknesses of deposited ALD TiN_x and $TiAl_xN_y$ films and underlying native SiO_2 layer were determined by XRR. Obtained thickness data were input as fixed parameters in the ellipsometer's fitting model from which parameters n and k were determined.

The resistivity of the deposited TiN_x films was measured using a standard four-point probe setup.

4.3 Results and Discussion

4.3.1 QCM Study and Deposition on Si

QCM investigations of ALD TiN_x deposition using $TiCl_4$ and N_2H_4 were performed at 200°C and 225°C reactor temperatures. Figure 4.1 shows QCM responses during TiN_x deposition while using the 3/40/3/40 timing sequence at both temperatures.

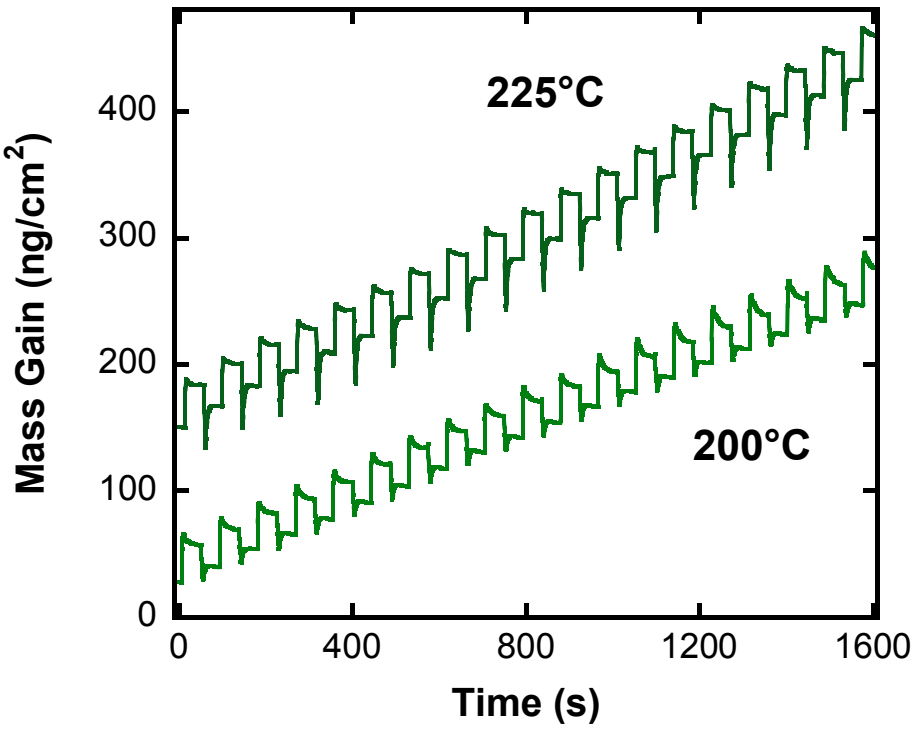

Figure 4.1 (a) TiN_x linear growth monitored by the QCM during ALD deposition using 3/40/3/40 timing at 200°C and 225°C.

The TiN_x growth rates obtained from slope fitting are 12.6 ng/cm^2 and 16 ng/cm^2 for 200°C and at 225°C respectively. This indicates that the reaction gains efficiency with the increase in temperature. Fig. 4.1 shows that the $TiCl_4/N_2H_4$ ALD system displays reproducible, linear growth. The QCM also showed that during the nucleation period on freshly deposited ALD Al_2O_3, TiN_x growth would typically start with a high mass gain of ~30 ng/cm^2 during the first cycle and gradually drop to an

equilibrium value in the course of the next 10-12 cycles. This behavior is consistent with a "substrate-enhanced" nucleation mechanism [41].

Figure 4.2 displays an expanded view of the QCM response during individual $TiCl_4$ and N_2H_4 pulses at 225°C. In this figure, 3s of $TiCl_4$ exposure resulted in a mass gain of 36 ng/cm^2 (Δm_B), followed by a sharp transient mass decrease during a 3s dose of N_2H_4, followed by a mass increase, with a resulting net mass gain of 16 ng/cm^2 per cycle (Δm_A).

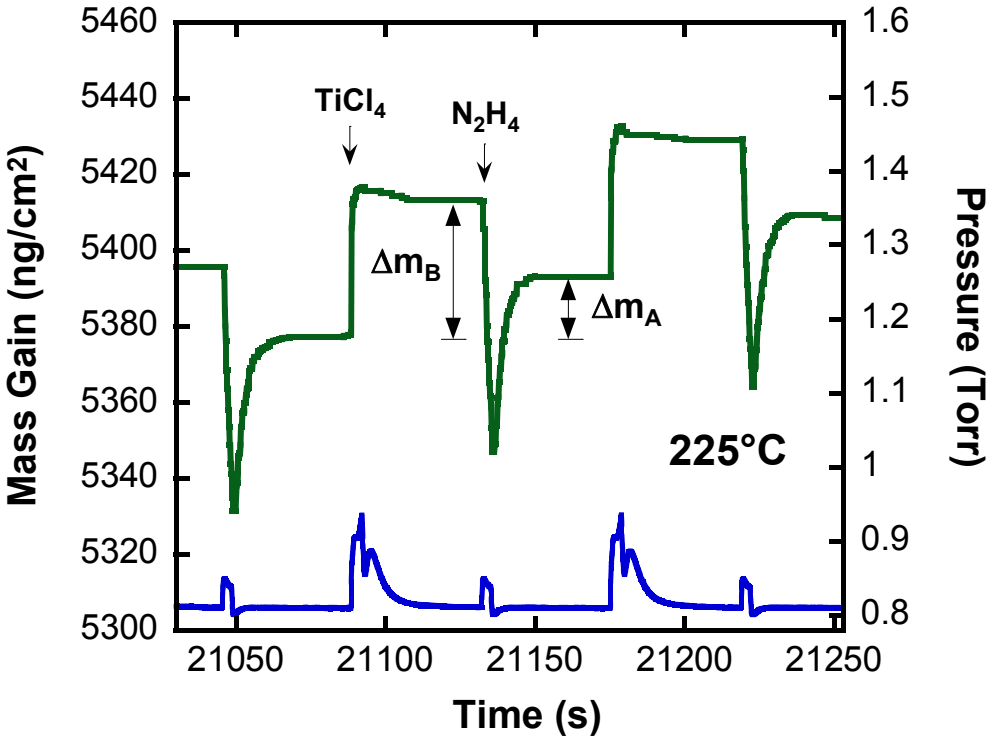

Figure 4.2 (a) Expanded view of QCM profile during ALD TiN_x deposition using 3/40/3/40 timing at 225°C.

We attribute the apparent mass drop during the N_2H_4 exposures to transient heating of the QCM crystal, produced by the relatively high heat capacity of hydrazine, and possibly the exothermicity of the reaction on the surface. These

temperature induced transients have been observed before during ALD processes involving ozone [42] and high heat capacity gases [43]. It is worth noticing from Fig. 4.1 that the transient feature during the N_2H_4 dose becomes more pronounced when the reaction temperature is increased which is viewed as an indication that the reaction is more efficient at higher temperatures.

The QCM precursor uptakes for 200°C and 225°C deposition temperatures are presented in Figures 4.3 and 4.4.

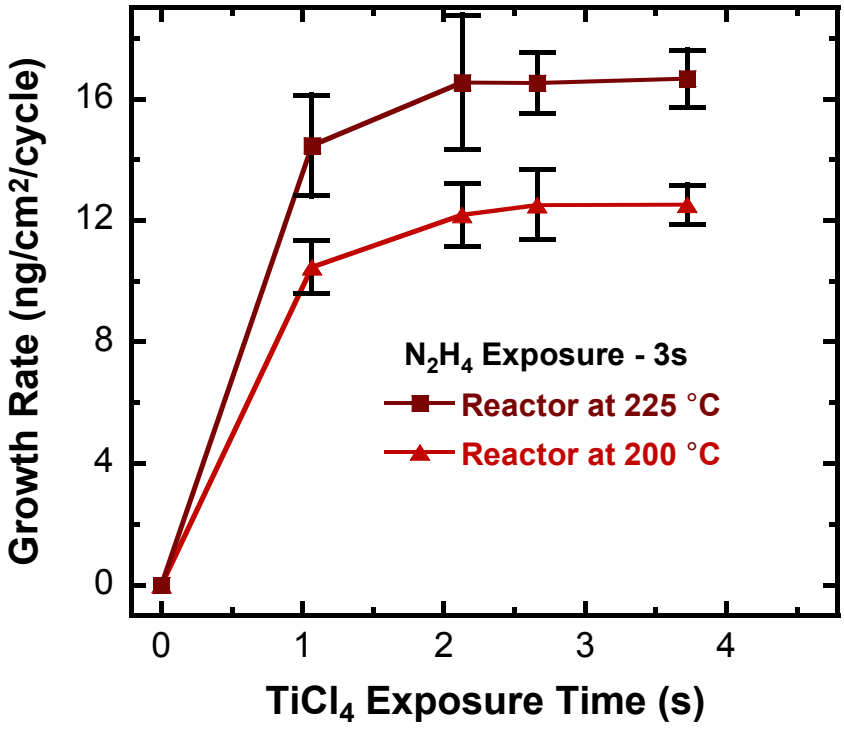

Figure 4.3 TiN_x mass gains per cycle vs. different $TiCl_4$ exposure times during deposition at 200°C and 225°C using x/40/3/40 timing sequence.

The timing sequence used for the $TiCl_4$ uptake was x/40/3/40, where the N_2H_4 dose was fixed at 3 s. Likewise, N_2H_4 uptake results were obtained using 3/40/x/40 timing where the $TiCl_4$ dose was fixed at 3 s, shown in Fig. 4.4.

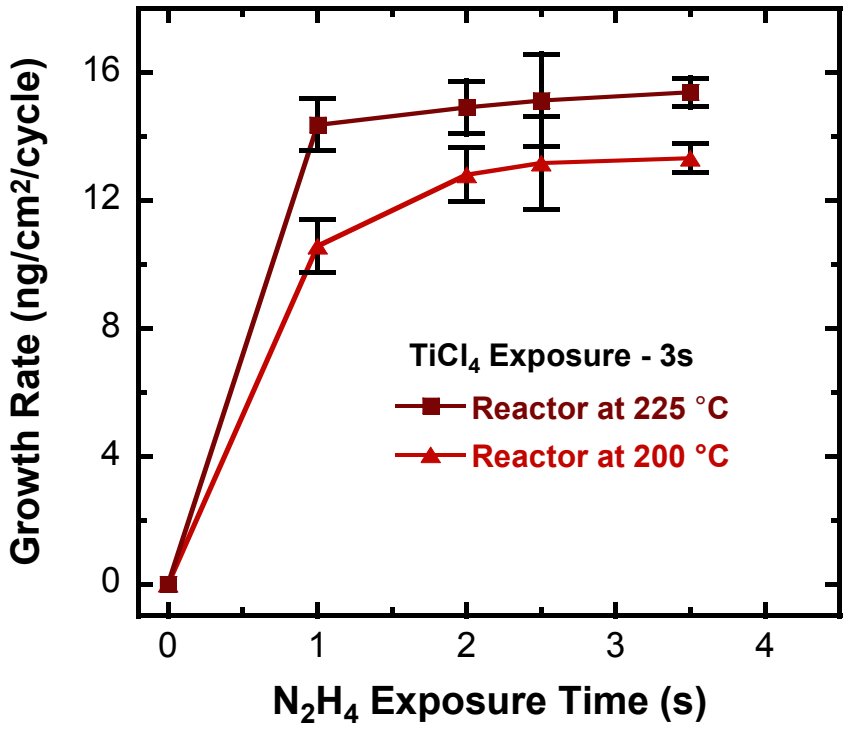

Figure 4.4 TiN_x mass gain per cycle vs. N_2H_4 exposure times during deposition at 200°C and 225°C using 3/40/x/40 timing sequence.

In these experiments, the precursor exposure time was varied to determine the dose time required for the ALD half reactions to reach saturation. Results presented in Figures 4.3 and 4.4 indicate that at both deposition temperatures, the mass gain reaches a plateau at ~3s doses of $TiCl_4$ and N_2H_4, and small or no mass increase occurs for longer exposures. This behavior suggests that the $TiCl_4/N_2H_4$ reaction is self-limiting. Large error bars in data presented in Fig. 4.3 and 4.4 are attributed to uncertainties owing to temperature fluctuations on the surface of the QCM crystal. The maximum TiN_x growth rates obtained from the uptake graphs are 12.6 ng/cm^2 per cycle and 16.5 ng/cm^2 per cycle at 200°C and 225°C reaction temperatures, respectively.

At 200°C and 225°C, a $TiCl_4$ exposure of 3s resulted in partial pressures of 125 mTorr, yielding a total $TiCl_4$ exposure of 37.5×10^4 L (1 L = 1×10^{-6} Torr s). For the 3s of N_2H_4 exposure, the partial pressure of N_2H_4 was 40 mTorr, yielding a total N_2H_4 exposure of 12×10^4 L.

The ALD timing of 3/40/3/40 was utilized in all further experiments to make certain that the $TiCl_4$ and N_2H_4 doses had reached saturation. The 40 s purge times were used to insure sufficient time for full removal of reactant and reaction byproducts during deposition.

4.3.2 X-ray Reflectivity and X-ray Diffraction Study

ALD TiN_x was deposited on Si<100> at temperatures varying from 150°C to 350°C. Figure 4.5 presents the XRR determined change in ALD TiN_x film growth rate and density versus deposition temperature. These TiN_x films were deposited using 300 ALD cycles on silicon wafers with ~30 Å seed layer of ALD Al_2O_3.

At 150°C the TiN_x growth rate is 0.46 Å/cycle and this drops down to 0.3 Å/cycle at 200°C, after which the growth rate increases nearly linearly until 275°C. At 275°C the growth rate reaching value of ~0.38 Å/cycle. Further increases in deposition temperature are believed to result in N_2H_4 decomposition, as evidenced by an abrupt decrease in the film growth rate at 300°C and 350°C and an increase in the film thickness gradients, shown with a large error bar at 300°C. At 350°C hydrazine most likely decomposes in the gas phase before reaching the deposition substrate, which results in a smaller gradient in film thickness.

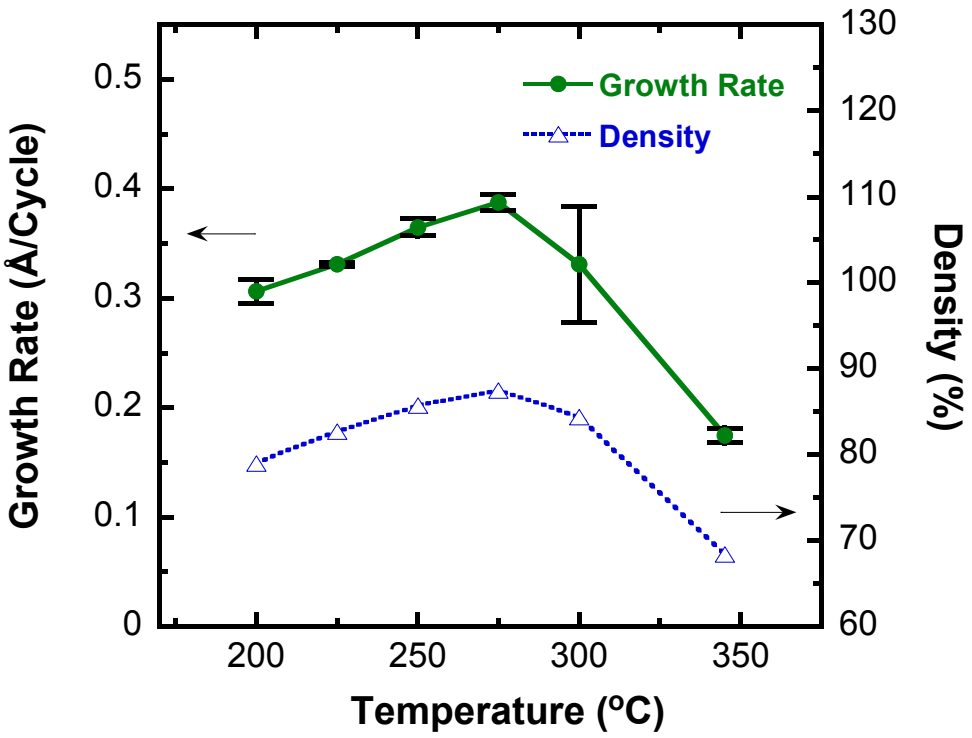

Figure 4.5 XRR obtained growth rate and film density of ALD TiN_x films deposited on Si<100> using 300 cycles and 3/40/3/40 timing sequence at different temperatures.

Figure 4.5 also shows that high film density is favored at high deposition temperatures reaching its peak value of 4.6 g/cm^3 at 275°C. The decrease in TiN_x film density at 300°C and 350°C is considered additional evidence of N_2H_4 decomposition. Similar to density, XRR measurements showed an increase in the root mean square (RMS) roughness of TiN_x films with increasing deposition temperature. The film roughness changed from an RMS value of 5 Å at 200°C to 7.2 Å at 275°C for ~100 Å thick TiN_x films. The high growth rate and density of TiN_x deposited at 275°C suggest that it is the best temperature to grow ALD TiN_x using $TiCl_4/N_2H_4$ chemistry.

XRR was also used to confirm linear growth of ALD TiN_x with increasing number of ALD cycles at 275°C. Figure 4.6 shows thicknesses of TiN_x films versus number of ALD cycles deposited using a timing sequence of 3/40/3/40. The TiN_x growth rate of 0.36 Å/cycle was obtained from the slope of the fitted line in Fig. 4.6.

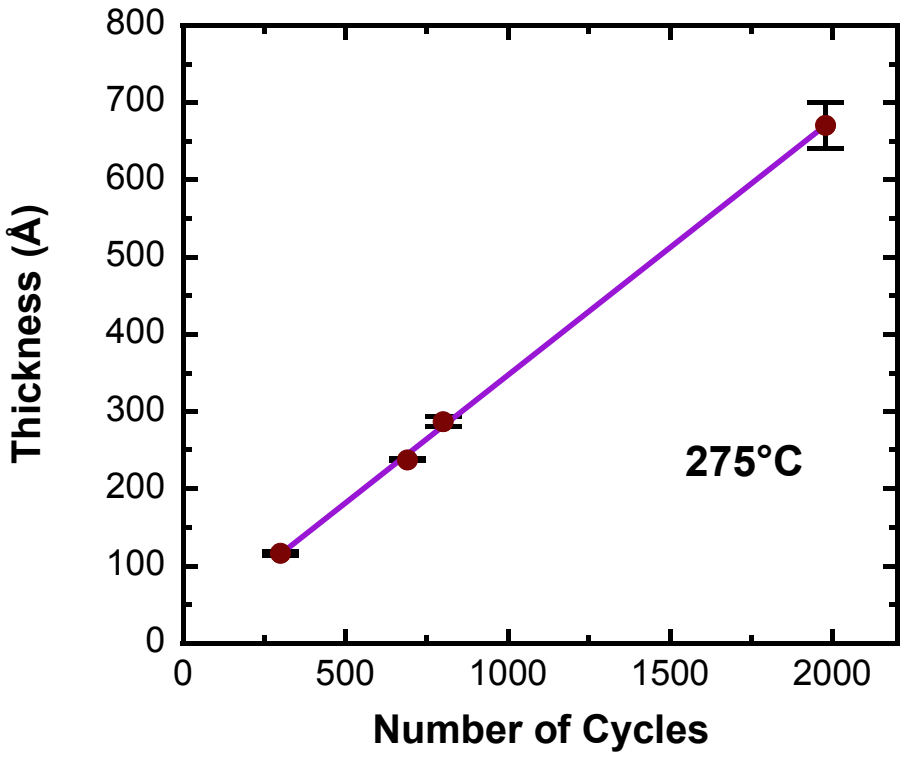

Figure 4.6 XRR determined TiN_x film thicknesses vs. number of deposition cycles obtained by deposition at 275°C on Si<100> using 3/40/3/40 ALD timing sequence. Slight variation in TiN_x film thickness along the flow direction of the reactor was detected at high numbers of deposition cycles. A maximum of ~9% difference in thickness between the front and back samples was observed for 2000 cycles run along a distance of 20 cm. Similar behavior has been previously observed during ALD deposition of materials with crystalline structure [42]. Surface roughness variation was observed for TiN_x films of different thicknesses. Therefore, 120 Å

thick TiN_x film deposited at 275°C showed RMS roughness of 7.2 Å, but 670 Å thick films deposited at the same temperature exhibit RMS roughness of 12 Å.

In the past, TiN_x films deposited using $TiCl_4/NH_3$ chemistry have measured growth rates of 0.4 Å/cycle at 350°C using the atomic layer CVD (AL-CVD) deposition technique [44]. Substitution of ammonia for tert-butylamine [45], allylamine [45] and dimethylhydrazine [27] with $TiCl_4$ results in growth rates of 0.03 Å/cycle (400°C), 0.15 Å/cycle (400°C) and 0.11 Å/cycle (200°C) respectively. However, metal organic MO-ALD systems using TDMAT, TDEAT and TEMAT with NH_3 deposited at 200°C were reported to have TiN_x growth rates ranging from 1.0-5.0 Å/cycle [22, 46]. In comparison to these systems, $TiCl_4/N_2H_4$ ALD shows an improvement in growth rate at lower deposition temperatures, although it has a lower growth rate compared to MO-ALD and MH and MO plasma assisted processes. Many systems with high grow rates have significant disadvantages in terms of TiN film purity.

Using a $TiCl_4/N_2H_4/TMA/N_2H_4$ precursor dose sequence, ALD $TiAl_xN_y$ films were deposited at 275°C using 3/50/4.5/50/4/50/4.5/50 deposition timing. This precursor dosing order was found to be the best combination to obtain the lowest impurity ALD $TiAl_xN_y$ films, from an earlier report by Juppo et al. [20] for the $TiCl_4/TMA/NH_3$ system. In this work, $TiAl_xN_y$ films were deposited using a TMA exposure of 4s producing partial pressures of 100 mTorr, yielding a total of 1×10^5 L exposure. The hydrazine doses of 4.5s used in the deposition resulted in partial pressures of 50 mTorr, which is equivalent to 0.5×10^5 L exposure. For these

precursors, the dosing time was chosen arbitrarily and no uptakes were performed to determine optimal saturation conditions.

X-ray reflectivity showed a $TiAl_xN_y$ growth rate of ~1.8 Å per cycle and a film density of ~3.4 g/cm^3. This growth rate is much higher than the 0.36 Å/Cycle for ALD TiN_x grown at the same temperature. XRR data also revealed a $TiAl_xN_y$ film thickness gradient of ~20% between the back and front samples along the precursor flow after 600 ALD cycles. This can be attributed to under-saturation of the precursors, and possibly formation of byproducts with long residence times which needed longer purge times for removal. Deposited $TiAl_xN_y$ films showed RMS roughness values on the order of 6.5 Å for ~700 Å thick films. This roughness value is low compared to roughness of TiN_x films obtained at comparable conditions.

Earlier reports on ALD $TiAl_xN_y$ deposited using $TiCl_4$/TMA/NH_3 chemistry with the same precursor pulsing sequence showed a maximum growth rate of 0.3 Å/cycle at 400°C [20]. ALD $TiAl_xN_y$ films deposited using $TiCl_4$/DMAH-EPP/NH_3 chemistry showed a growth rate of 1.67 Å/cycle when deposited at 350°C [30]. Therefore, $TiAl_xN_y$ ALD films deposited in this work using hydrazine show high growth rates at relatively low deposition temperatures.

The crystallinity of TiN_x and $TiAl_xN_y$ films deposited at 275°C on Si<100> was determined from grazing incidence X-ray diffraction (GIXRD) experiments. A 600 Å thick TiN_x film exhibited a peak pattern matching polycrystalline cubic TiN (PDF number 87-0633, JCPDS-ICDD 2002) as shown by Miller indices on Figure 4.7.

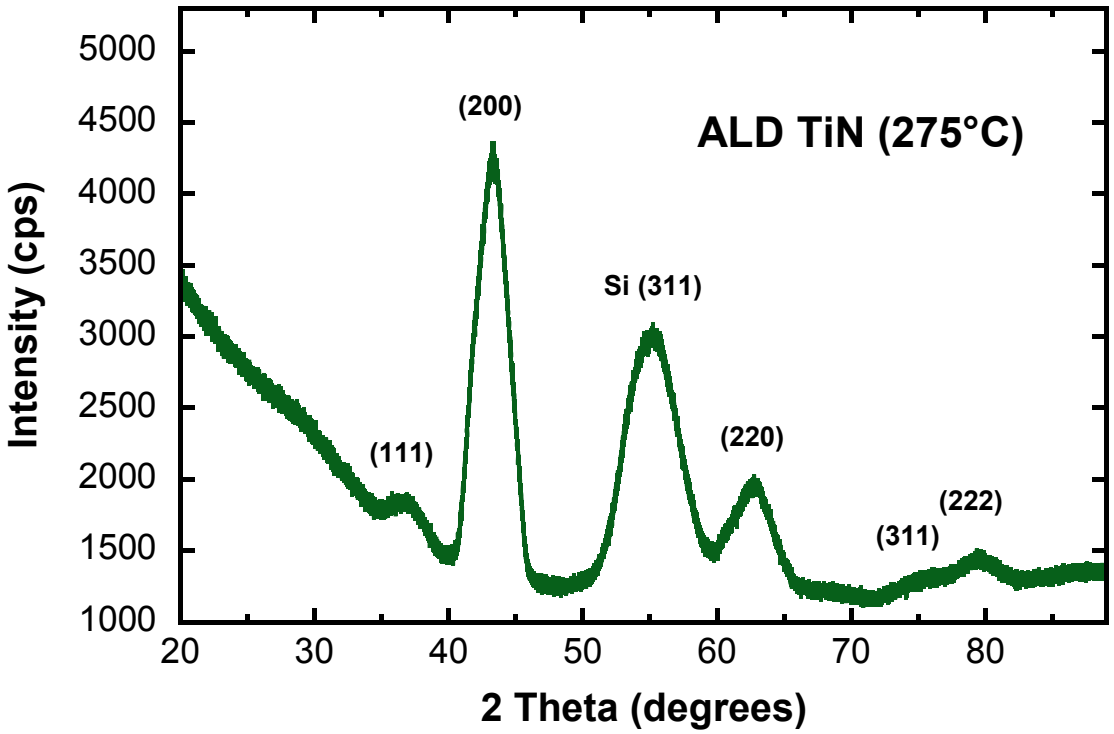

Figure 4.7 GIXRD diffractogram obtained for 600 Å thick TiN_x ALD film grown using 3/40/3/40 timing at 275°C.

A similar pattern was observed for the 300 Å thick TiN_x films. However, the TiN_x peaks in this figure are shifted toward higher diffraction angles with respect to their nominal positions. Similar observations were made for previous ALD deposited TiN_x films and this was attributed to incorporation of oxygen in the film, causing peak shifts [17, 18]. In Figure 4.7, (200) is the most intense orientation and (220) is the second most intense diffraction plane.

Previous TiN_x ALD systems typically resulted in cubic polycrystalline or amorphous TiN_x depending on deposition temperature and the level of impurities. The XRD of TiN_x films deposited using $TiCl_4/NH_3$ or TiI_4/NH_3 chemistries exhibits the (200) plane as the most preferred orientation when deposited below 400°C, and

(111) is the most intense peak at temperatures above 400°C [17, 18, 44]. The crystallinity data of the TiN_x film in Fig. 4.7 supports that at lower deposition temperatures, TiN_x films are more likely oriented in the (200) plane rather than the more energetically favorable (111) [18]. It is also noticeable that TiN_x films deposited using $TiCl_4$ and NH_3 at 400°C do not exhibit crystallinity for 300 Å thick films likely due to their rapid oxidation in air. In contrast, 300 Å films deposited in this work showed crystalline structure, which suggests higher density in the films grown using hydrazine. The TiN_x films grown using 1,1-dimethylhydrazine and $TiCl_4$ at 300°C exhibited only weakly crystalline films with the only detected reflection being at (200), possibly due to the presence of 6 at. % of carbon impurities [27].

A GIXRD scan of a 700 Å thick $TiAl_xN_y$ film showed a similar diffraction pattern to TiN_x, where peaks were slightly shifted toward higher diffraction angles. This effect was assigned to smaller aluminum atoms substituting for titanium in the TiN lattice [20]. Analogous to TiN_x, the $TiAl_xN_y$ showed the (200) plane was most intense and (220) was the second most intense. Diffraction peak intensities of $TiAl_xN_y$ films were lower than those of TiN_x films, implying that $TiAl_xN_y$ is less crystalline.

In other work, $TiAl_xN_y$ ALD films deposited at 400°C using $TiCl_4$/TMA/NH_3 chemistry showed weak crystallinity, with (111) and (200) planes as the most intense peaks [20]. ALD $TiAl_xN_y$ films deposited at 200°C using TDMAT and

DMAH–EPP as the aluminum sources have been reported to be amorphous [31, 47]. However, this film had high carbon impurity on the level of 25 at. %.

As a general result, TiN_x as well as $TiAl_xN_y$ films deposited using hydrazine exhibit crystallinity at lower deposition temperatures than typically observed for thermally deposited MH-ALD titanium nitride films.

4.3.3 XPS and SEM Film Characterization

Figure 4.8 presents an XPS depth profile of a 300 Å thick TiN_x film deposited at 275°C. This figure shows that the film contains ~14 at. % oxygen in the bulk of the film, with chlorine content below the detection limit of the XPS (~1%) and N:Ti ratios of ~9/10. Also interesting is that oxygen is evenly distributed through the bulk of the film, and this is thought to be caused by preferential oxidation of TiN through grain boundaries, as indicated by a number of oxidation studies [48].

An XPS survey scan of a 140 Å thick TiN_x film deposited at 150°C showed the presence of ~9 at. % chlorine and ~38 at. % oxygen impurities. TiN_x films deposited at 200 °C had a chlorine concentration below the detection limit and an oxygen level of ~28 at. %. Oxygen incorporation appears to depend on film density; an inverse relationship between the concentration of oxygen in the film and its density is observed. Since most of the oxidation of TiN_x films is believed to take place after samples are exposed to air, one should expect much less oxidation for thicker TiN_x films or in situ capped films.

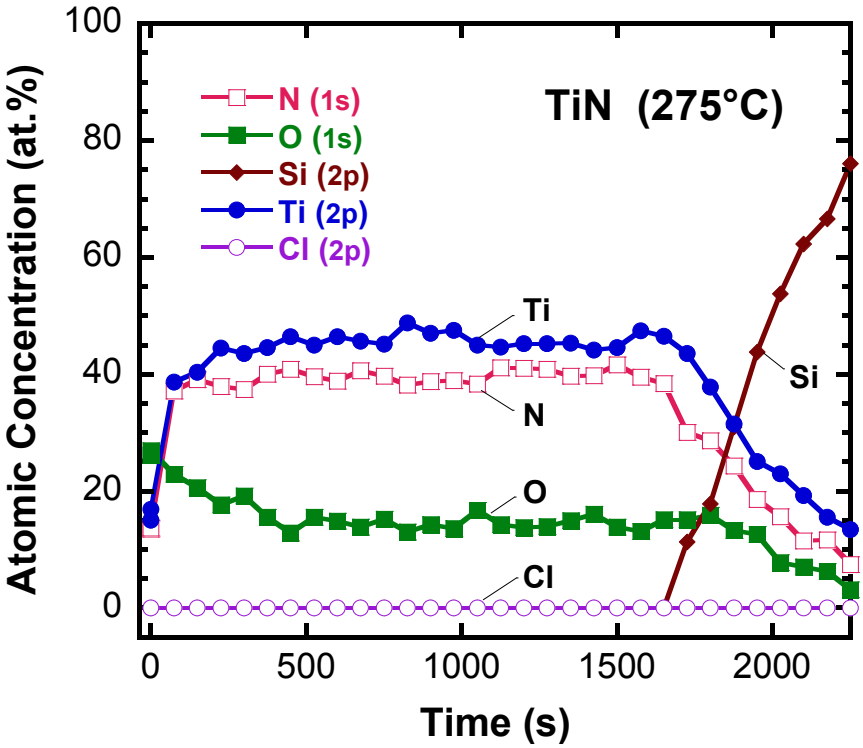

Figure 4.8 XPS depth profile for 300 Å thick TiN_x ALD film grown using 3/40/3/40 timing at 275°C.

The ALD TiN_x films deposited using $TiCl_4$ and NH_3 chemistry are reported to have oxygen content of 32 at. % for 340 Å thick films deposited at 500°C, determined from RBS [18]. However, this number can be reduced down to 9 at. % for thicker films [18]. Much poorer film quality was observed for MO-ALD TiN systems. For example, ALD TiN_x films deposited using TDMAT and NH_3 chemistry at 180°C and 200°C have been shown to have 40-45 at. % of oxygen and 6-10 at. % of carbon impurities [24, 49]. Absence of carbon and chlorine impurities are one of the advantages of the $TiCl_4/N_2H_4$ system compared to $TiCl_4$/DMHy ALD where the levels of impurities were at ~16 at. % of chlorine and ~6 at. % of carbon for the films obtained at 300°C [27].

Figure 4.9 shows a depth profile of the 600 Å thick TiAlNx film deposited at 275°C on pre-deposited TiN_x.

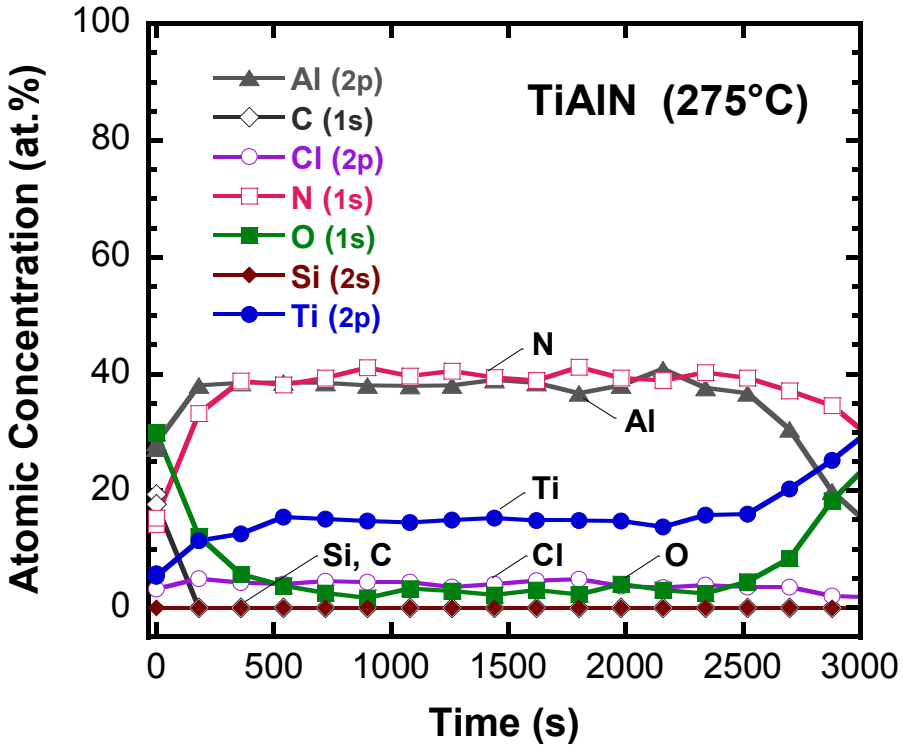

Figure 4.9 XPS depth profile for 600 Å $TiAl_xN_y$ ALD film grown using 3/50/4.5/50/4/50/4.5/50 timing sequence at 275°C.

This figure shows the presence of ~3 at. % oxygen and ~4 at. % chlorine and that the level of carbon impurities was below the detection limit. The absence of carbon impurities suggests that the reaction between TMA and N_2H_4 proceeds to completion. The presence of chlorine impurities possibly results from the trapping of reaction byproducts which suggest the necessity for further TiAlNx ALD optimization. Fig. 4.9 also shows that the $TiAl_xN_y$ film has a high atomic concentration of aluminum (~40 at. %) compared to ~15 at. % of titanium. Juppo et. al. [20] demonstrated earlier that aluminum concentration in the film can be

manipulated by using different pulsing arrangements. Low concentration of oxygen in the deposited $TiAl_xN_y$ films implies that it is less susceptible to oxidation than TiN_x films, consistent with finding in previous publications [20].

For comparison, ALD $TiAl_xN_y$ deposition using $TiCl_4$/TMA/NH_3 chemistry at 400°C resulted in a film with ~6 at. % of chlorine, ~0.6 at. % oxygen, ~6 at. % carbon and ~13 at. % of aluminum. The slightly higher concentration of oxygen in $TiAl_xN_y$ films observed in this work can be partially attributed to water contamination for the hydrazine. Nevertheless, the use of hydrazine enables elimination of carbon impurities and reduction of deposition temperature.

The ability to conformally coat on a trench is one of the important demonstrations of feasibility for an ALD system. Figure 4.10 displays the cross-sectional SEM images of a 4:1 ratio patterned silicon wafer after 2000 ALD cycles of TiN_x at 275°C. Due to the aspect ratio of the trenches, extended purge times with deposition timing of 3/60/3/60 were adapted for the TiN_x deposition. This film was capped with 50 Å of ALD Al_2O_3 to obtain good image contrast. The SEM images revealed that the trenches are conformally coated with a ~700 Å ALD TiN_x thickness film. The SEM micrograph of the bottom of the trench (Fig. 4.10b) shows that the TiN_x ALD coating reproduced sharp corners and uniformly coated the top of the trench (Fig. 4.10a). Excellent conformality of deposited ALD TiN_x is partially attributable to the high heat capacity of hydrazine and effectiveness of hydrazine as a reagent.

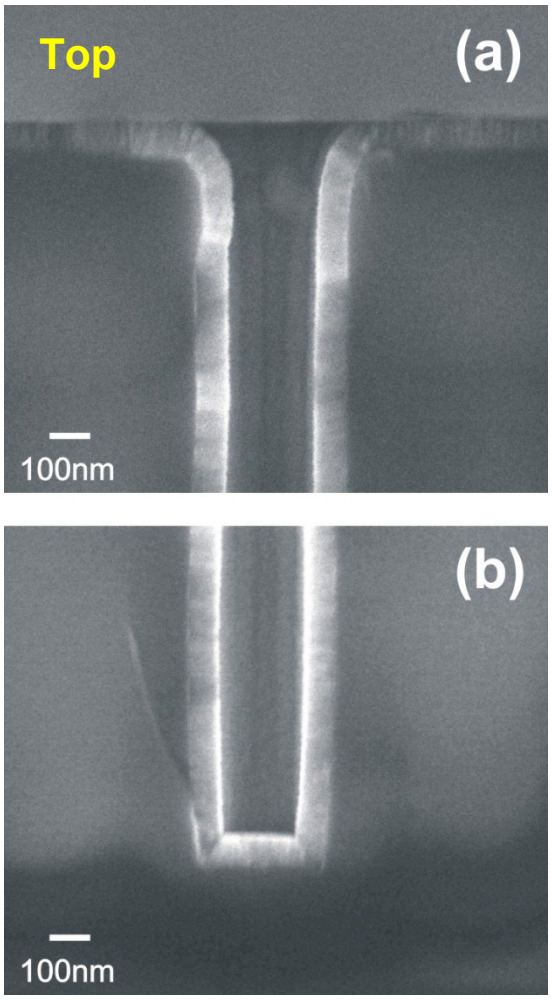

Figure 4.10 SEM images of 4:1 aspect ratio silicon patterned trench after 2000 cycles of ALD TiN_x deposited at 275°C where (a) is the image of the top of the trench and (b) of the bottom of the trench.

The relatively high heat capacity of hydrazine $Cp_{225°C}$ = 70.56 J/(mol K) [50] compared to ammonia $Cp_{225°C}$ = 42.21 J/(mol K) [51] is believed to be one the important contributing factors providing enough thermal energy to drive surface reaction to completion and supply enough kinetic energy to the byproducts to produce highly conformal films at relatively low deposition temperatures. This is

potentially advantageous since short purge times can be utilized during the ALD TiN deposition process to compensate for lower growth rate.

4.3.4 FTIR Studies

FTIR was employed to examine surface species after $TiCl_4$ and N_2H_4 exposures during the process of TiN_x ALD. Figure 4.11 shows the FTIR difference spectra obtained for 200°C and 275°C reaction temperatures by subtracting the spectra from the previous reactions. These spectra were obtained after $TiCl_4$ and N_2H_4 exposures during each half reaction for the third ALD cycle on alumina coated ZrO_2 particles. In the presented FTIR difference spectra, negative absorbance features indicate a loss of surface species and positive absorbance features indicate a gain of surface species.

A loss of surface species was observed after $TiCl_4$ exposure at both 200°C and 275°C reaction temperatures. However, characteristic Ti-Cl modes around 500 cm^{-1} wavenumbers [52] could not be detected since the absorption bands are located at a lower frequency than the detection limit. The reaction during $TiCl_4$ exposure is assumed to result in the formation of monodentate and bidentate Ti-Cl_x species, as has been observed previously during infrared studies of the ALD $TiCl_4/NH_3$ system [52]. During the second half cycle, N_2H_4 exposure at 200°C resulted in the appearance of bands at 3320, 3268, 1609, 1515 and 1309 cm^{-1}, which are attributed to $–NH_2$ antisymmetric, symmetric, scissoring, and wagging modes respectively [53]. Small peaks at 1233 and 1147 cm^{-1} wavelengths are in close proximity to

earlier reported N-N stretching and $-NH_2$ rocking vibrations of molecular hydrazine [54].

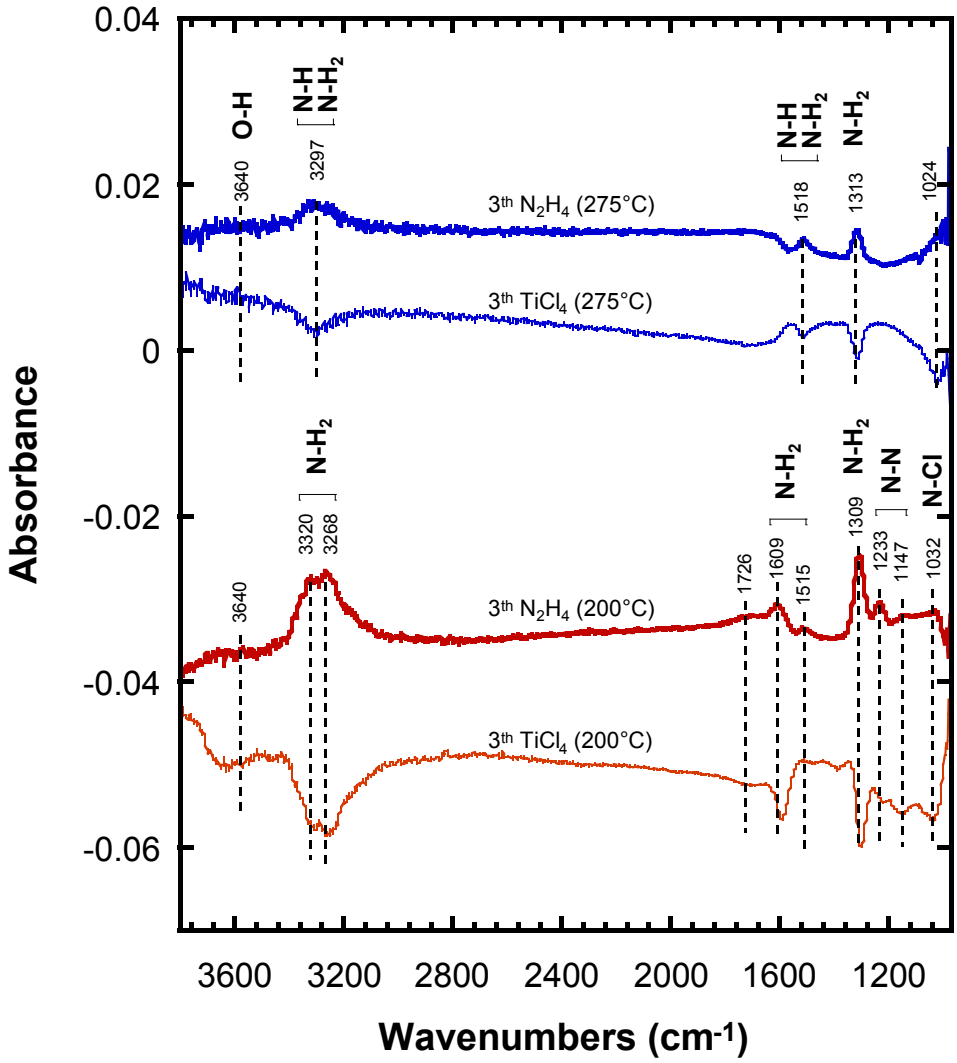

Figure 4.11 FTIR difference spectra after exposure of $TiCl_4$ and N_2H_4 during the 3th TiN_x ALD cycle at 200°C and 275°C. Each spectrum is referenced to the spectrum previous to reactant exposure.

This can be attributed to the presence of either coordinated unreacted hydrazine molecules or hydrazinium salts. However, evidence of characteristic vibrational signatures of hydrazine chlorides such as hydrazinium(1+)chloride

(N_2H_5Cl) or hydrazinium(2+)dichloride ($N_2H_6Cl_2$), or NH_4Cl salt have not been found at either reaction temperature [52, 55, 56]. A weak peak at 1032 cm^{-1} can be tentatively assigned to the N-Cl bend based on previous assignments for IR spectra of NH_2Cl [57].

A different reaction pathway is observed during the $TiCl_4$ and N_2H_4 reaction at 275°C. The observed vibrational frequencies at 3297, 1518 and 1313 cm^{-1} are attributed to the stretching, scissoring, and wagging modes of a primary amine ($-NH_2$). These assignments are based on previously observed infrared signatures of hydrazine on TiO_2 at temperatures varying from 25°C to 350°C [54, 58]. Since the difference between–NH_2 and =NH (secondary amine) is indistinguishable due to the overlap of the N–H stretching and N–H deformation regions both primary and secondary amines could be present on the surface. In this instance, presence of the scissoring mode at 1518 cm^{-1} is the only distinction between primary and secondary amines.

The absorption band at 3640 cm^{-1} observed at 200°C and to some extent appearing at 275°C, is indicative of the presence of –OH species on the surface. This can be attributed to presence of hydrazine hydrate impurities in the hydrazine precursor. Small peaks at 1726 and 1024 cm^{-1} shown at 200°C and 275°C respectively have not been identified. A broad background peak centered around 1300 cm^{-1} was also not assigned.

4.3.4 Proposed ALD TiN_x Growth Mechanism

At 150°C TiN_x deposition is believed to proceed through formation of hydrazinium salts. The high melting temperature of these salts, 90°C and 198°C for N_2H_5Cl and $N_2H_6Cl_2$ respectively, [59] suggests that they could be present on the surface. The presence of ~9 at. % chlorine was confirmed by XPS. In addition, XRR measurements showed unusually high growth rate of 0.46 Å/Cycle at 150°C, and a thickness gradient between the front and back reactor samples; these are consistent with a condensation type reaction.

The FTIR spectrum at 200°C suggests the presence of primary amine $-NH_2$ groups on the surface after hydrazine exposure. No clear distinction can be made between $-NH_2$ bound to the Ti atom and $–NH_2$ of molecular hydrazine. Nevertheless, the observed linear growth at 200°C indicates the presence of bound species on the surface and therefore demonstrates the feasibility of the reaction between $TiCl_4$ and N_2H_4. From the XRR results, deposition at this temperature produces films with low density, probably due to steric effects from adsorbed molecular hydrazine and large $-NH_2$ groups. No evidence for hydrazine or ammonia salts has been found by FTIR.

The ALD of TiN_x at 275°C exhibits maximum film growth rate and density. More perfect IR spectrum flipping can be observed at this temperature compared to 200°C, as shown in Fig. 4.5. The IR spectrum after hydrazine exposure indicates the presence of surface bound primary amine, a conclusion drawn from the absence N-N stretch peaks of molecular hydrazine. Some secondary amine =NH species are believed to have formed on the surface, though if so, they are masked by the

presence of the primary amine peaks. The overall hydrazine dissociative absorption on the surface is believed to proceed according to $N_2H_4 \rightarrow 2NH_{2ad} \rightarrow 2NH_{ad} + 2H$, where the ratio between the number of primary and secondary amine species on the surface is temperature dependent.

This behavior is easily demonstrated when FTIR spectra obtained during ALD TiN_x using $TiCl_4/NH_3$ and $TiCl_4/N_2H_4$ chemistries are directly compared. Figure 4.12 represents spectra during the second half reaction after NH_3 dosing at 350°C, 425°C and N_2H_4 at 275°C temperatures. A similarity in observed surface species during ammonia exposure at 350°C and hydrazine at 275°C is apparent. At the 425°C reaction temperature, the $TiCl_4/NH_3$ spectrum lacks a peak at 1313 cm^{-1} (-NH_2 wagging) suggesting that only =NH type species are on the surface with 3297 and 1518 cm^{-1} vibrations. The bands of a secondary amine at 3436 and 1558 cm^{-1} wavenumbers were earlier observed by Snyder et al. [52] at 400°C on silica particles by TiN_x ALD infrared investigations for the $TiCl_4/NH_3$ system. A gradual decrease in intensity of the –NH_2 scissoring mode, when starting at 127°C, with complete removal by 400°C was previously observed by Dillon et. al [60].

In addition, the shift in the TiN_x growth mechanism is believed to be manifested in the change of TiN film crystallinity, from (200) plane diffraction as the most preferred orientation at temperatures below 400°C, to (111) at higher temperatures where predominantly =NH species are present. During $TiCl_4/N_2H_4$ ALD at temperatures above 275°C, hydrazine decomposes in the gas phase, which is noticeable from the fall of the growth rate and the film density.

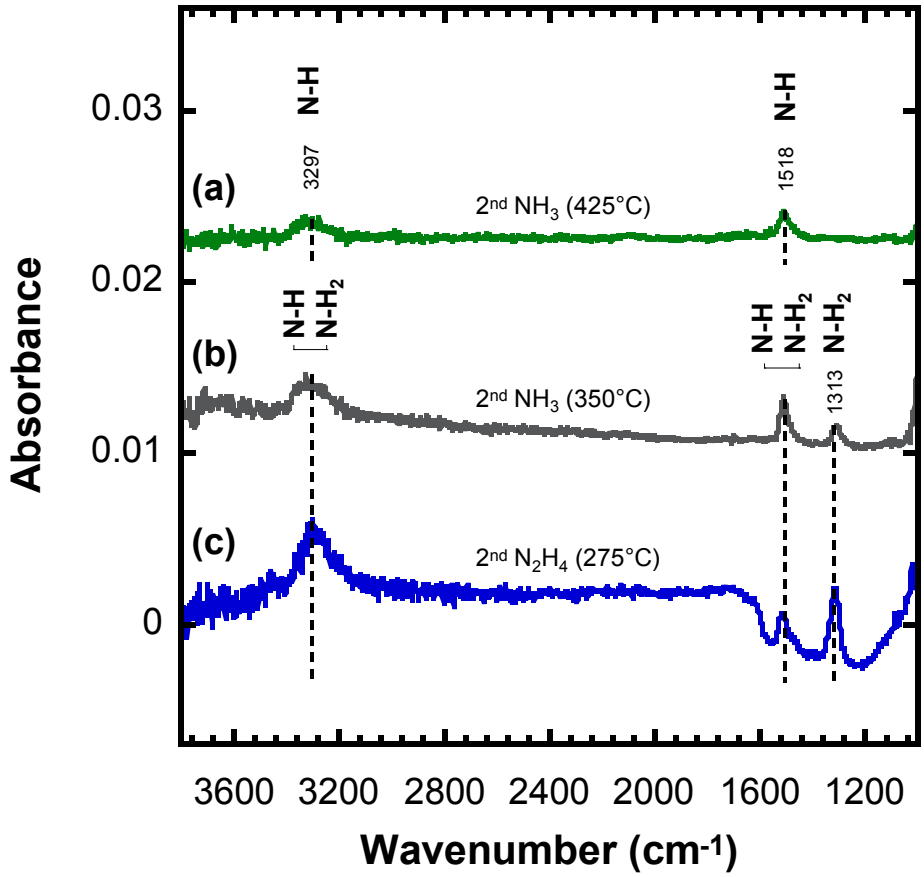

Figure 4.12 Comparison of the FTIR difference spectra after the 2th cycle exposure of NH_3 at 350°C, 425°C and N_2H_4 exposure at 275°C during TiN_x ALD. Each spectrum is referenced to the spectrum of the previous reactant exposure.

This is also consistent with the reported decomposition temperature for liquid hydrazine, which is ~300°C [61]. Gas phase hydrazine decomposition is well studied in the literature and can be presented in the simplified equation $3N_2H_4 \rightarrow 4(1 - x)NH_3 + (1 + 2x)N_2 + H_2$, where more hydrogen appears at increased temperatures [59].

The proposed reaction mechanism for the second half reaction during the TiN_x ALD process at various deposition temperatures is summarized in Fig. 4.13.

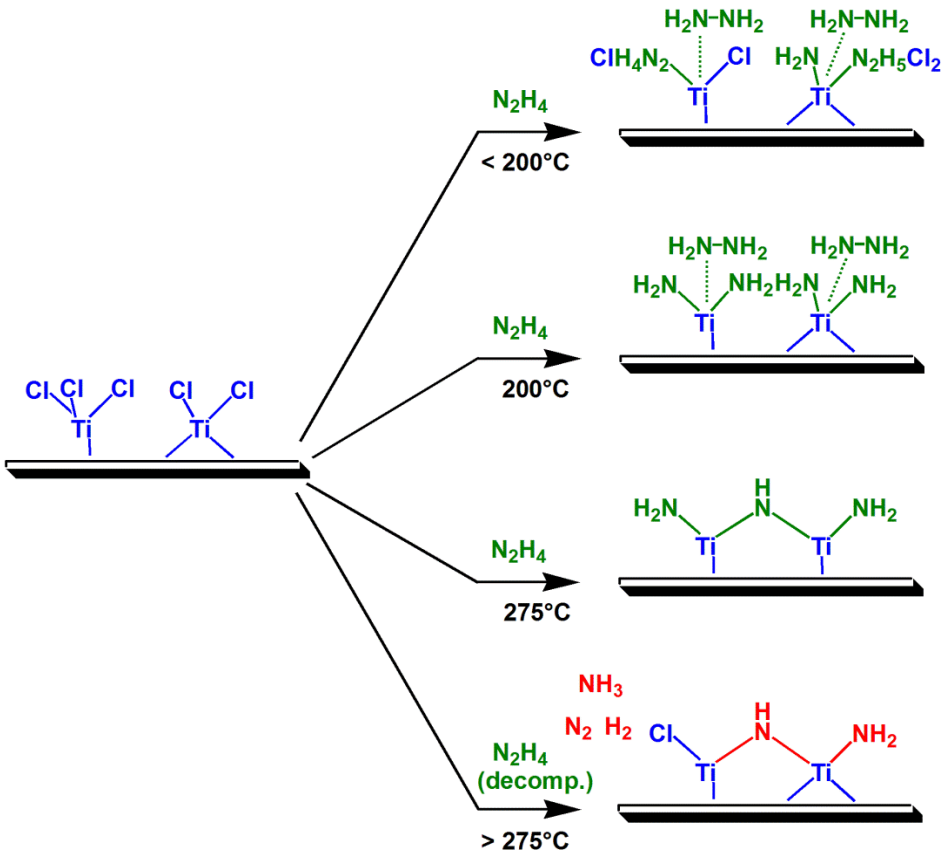

Figure 4.13 Proposed reaction mechanism of N_2H_4 with $TiCl_x$ terminated surface at different TiN_x deposition temperatures.

4.3.5 Properties of ALD TiN_x and $TiAl_xN_y$ films

4.3.5.1 Electrical Properties

The electrical properties of TiN_x films are good indicators of their quality. Resistivity of TiN_x films deposited at 275°C on silicon wafers was measured using the four-point probe method. A TiN_x film with a thickness of 300 Å exhibited a resistivity of 350 μΩ·cm. Previous thermally deposited ALD TiN_x films using $TiCl_4/NH_3$ (350°C), $TiCl_4$/DMHy (300°C) chemistries have been shown to exhibit resistivities of 340 and 1000 μΩ·cm respectively [27, 44]. MO-ALD deposited TiN_x

films typically exhibit high resistivity due to the presence of large amounts of carbon and oxygen impurities. The films deposited by plasma assisted MH-ALD show lower film resistivity but still require relatively high deposition temperatures [21].

The film resistivity observed in this work is relatively low considering the presence of ~15% oxygen in the film. As was demonstrated in an earlier publication by Ritala et al., resistivity of the TiN_x films is highly dependent on the level of oxidation, and consequently is a function of film thickness [18]. Therefore, one can expect improvement in electrical performance for thicker TiN_x films using $TiCl_4/N_2H_4$ chemistry.

4.3.5.2 Optical Properties

The color of the TiN_x films deposited at 275°C varied from golden for 300 Å thick films to dark red for 680 Å films. This color pattern is similar to that observed for thermal ALD using $TiCl_4/NH_3$ chemistry [16, 18], however, this system exhibits gold and dark violet colors only when the thickness of TiN_x films reaches 1600 Å and 2300 Å respectively at 500°C [16]. This difference can be attributed to the higher density of TiN_x films deposited in this work, which allows them to exhibit similar optical properties at lower film thicknesses.

The optical constants (n and k) of ALD TiN_x and $TiAl_xN_y$ deposited at 275°C were measured using a spectroscopic ellipsometer. Refractive indexes of 300 Å thick ALD TiN_x deposited in this work and TiN reference data are presented in Figure 4.14 [62].

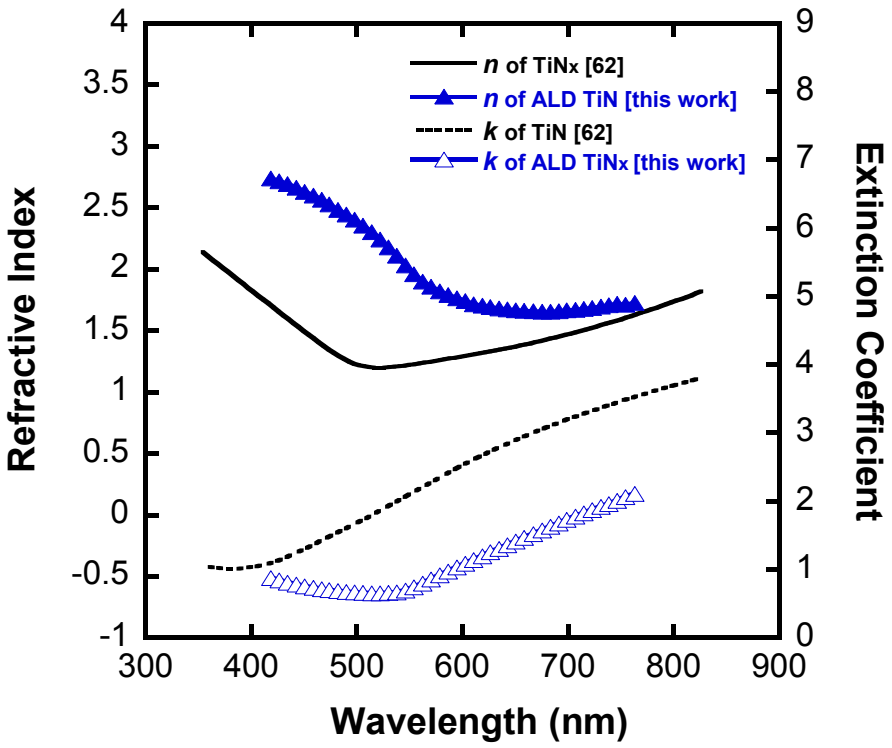

Figure 4.14 Optical constants (n and k) of the 600 Å TiN_x films deposited at 275°C compare to TiN reference data [62].

Optical constants from TiN reference data were measured by electron energy loss spectroscopy (EELS) [62]. The hydrazine ALD deposited TiN_x exhibits similar optical properties to the reference TiN specimen. Relatively high values for the refractive indexes and low values for the extinction coefficients of ALD TiN_x are attributable to the presence of TiO_2 in the film, which adds optical transparency to the film.

Similar to ALD TiN_x, 300 Å $TiAl_xN_y$ films deposited in this work were golden color; however, 700 Å films exhibited a deep blue color. Refractive indexes of ALD $TiAl_xN_y$ in this work showed the material to have similar optical behavior as $TiAl_xN_y$ obtained by DC/RF magnetron spattered technique [29].

4.4 Conclusions

In this work we demonstrated that $TiCl_4/N_2H_4$ chemistry enables deposition of highly uniform, chlorine free ALD TiN_x films in a temperature window ranging from 200°C to 275°C. The experiments performed reveal that, depending on the temperature of molecular adsorption, condensation and dissociative adsorption can be observed. TiN_x ALD deposition at 275°C is found to be the most favorable in terms of highest film density and growth rate. The TiN_x films can be deposited at temperatures below 275°C at the expense of film density. The QCM observed temperature transient during the deposition process at 200 and 225°C indicates thermal favorability of the $TiCl_4/N_2H_4$ system. This was manifested in the deposition of highly conformal TiN_x film shown by SEM. Oxygen was found to be a major impurity in deposited TiN_x films. Most TiN_x oxidation is believed to occur after exposure to air, though the presence of hydrazine hydride impurities in hydrazine precursor may have contributed to oxidation during the deposition process. It has been shown that electrical and optical performance of ALD TiN_x films are governed by the amount of film oxidation. The ALD $TiAl_xN_y$ deposited using $TiCl_4/N_2H_4$/TMA chemistry is shown to be less susceptible to oxidation than TiN_x films, and exhibited higher growth rates, which make them more attractive substitutes to TiN. Notably, hydrazine is found to be a good reagent to remove methyl groups from TMA, resulting in carbon free $TiAl_xN_y$ films as demonstrated in this work.

4.5 References

1. George, S.M., Atomic Layer Deposition: An Overview. Chemical Reviews, 2010. **110**: p. 111-131.

2. Puurunen, R.L., Surface chemistry of atomic layer deposition: A case study for the trimethylaluminum/water process. Journal of Applied Physics, 2005. **97**(12).

3. George, S.M., A.W. Ott, and J.W. Klaus, Surface chemistry for atomic layer growth. Journal of Physical Chemistry, 1996. **100**(31): p. 13121-13131.

4. Groner, M.D., et al., Low-temperature Al2O3 atomic layer deposition. Chemistry of Materials, 2004. **16**(4): p. 639-645.

5. Niinisto, L., et al., Advanced electronic and optoelectronic materials by Atomic Layer Deposition: An overview with special emphasis on recent progress in processing of high-k dielectrics and other oxide materials. Physica Status Solidi a-Applied Research, 2004. **201**(7): p. 1443-1452.

6. Technology Roadmap for Semiconductors. http://www.itrs.net/.International, 2007.

7. Kim, H., Atomic layer deposition of metal and nitride thin films: Current research efforts and applications for semiconductor device processing. Journal of Vacuum Science & Technology B, 2003. **21**(6): p. 2231-2261.

8. Zaera, F., The surface chemistry of thin film atomic layer deposition (ALD) processes for electronic device manufacturing. Journal of Materials Chemistry, 2008. **18**(30): p. 3521-3526.

9. Ahn, C.H., et al., Characteristics of TiN thin films grown by ALD using TiCl(4)and NH3. Metals and Materials International, 2001. **7**(6): p. 621-625.

10. Satta, A., et al., Growth mechanism and continuity of atomic layer deposited TiN films on thermal SiO2. Journal of Applied Physics, 2002. **92**(12): p. 7641-7646.

11. Juppo, M., A. Rahtu, and M. Ritala, In situ mass spectrometry study on surface reactions in atomic layer deposition of TiN and Ti(Al)N thin films. Chemistry of Materials, 2002. **14**(1): p. 281-287.

12. Kim, J., et al., Physical properties of highly Conformal TiN thin films grown by atomic layer deposition. Japanese Journal of Applied Physics Part 1-Regular Papers Short Notes & Review Papers, 2003. **42**(3): p. 1375-1379.

13. Kim, J., et al., Properties including step coverage of TiN thin films prepared by atomic layer deposition. Applied Surface Science, 2003. **210**(3-4): p. 231-239.

14. Tiznado, H. and F. Zaera, Surface chemistry in the atomic layer deposition of TiN films from TiCl4 and ammonia. Journal of Physical Chemistry B, 2006. **110**(27): p. 13491-13498.

15. Elers, K.E., et al., TiCl4 as a precursor in the TiN deposition by ALD and PEALD. Journal of the Electrochemical Society, 2005. **152**(8): p. G589-G593.

16. Hiltunen, L., et al., Nitrides of Titanium, Niobium, Tantalum and Molybdenum Grown as Thin-Films by the Atomic Layer Epitaxy Method. Thin Solid Films, 1988. **166**(1-2): p. 149-154.

17. Ritala, M., et al., Atomic layer epitaxy growth of TiN thin films from TiI4 and NH3. Journal of the Electrochemical Society, 1998. **145**(8): p. 2914-2920.

18. Ritala, M., et al., Atomic Layer Epitaxy Growth of Tin Thin-Films. Journal of the Electrochemical Society, 1995. **142**(8): p. 2731-2737.

19. Ritala, M., et al., Effects of intermediate zinc pulses on properties of TiN and NbN films deposited by atomic layer epitaxy. Applied Surface Science, 1997. **120**(3-4): p. 199-212.

20. Juppo, M., et al., Trimethylaluminum as a reducing agent in the atomic layer deposition of Ti(Al)N thin films. Chemical Vapor Deposition, 2001. **7**(5): p. 211-217.

21. Heil, S.B.S., et al., Low-temperature deposition of TiN by plasma-assisted atomic layer deposition. Journal of the Electrochemical Society, 2006. **153**(11): p. G956-G965.

22. Min, J.S., et al., Atomic layer deposition of TiN films by alternate supply of tetrakis(ethylmethylamino)-titanium and ammonia. Japanese Journal of Applied Physics Part 1-Regular Papers Short Notes & Review Papers, 1998. **37**(9A): p. 4999-5004.

23. Kim, H.K., et al., Metalorganic atomic layer deposition of TiN thin films using TDMAT and NH3. Journal of the Korean Physical Society, 2002. **41**(5): p. 739-744.

24. Elam, J.W., et al., Surface chemistry and film growth during TiN atomic layer deposition using TDMAT and NH3. Thin Solid Films, 2003. **436**(2): p. 145-156.

25. Kim, J.Y., et al., Remote plasma enhanced atomic layer deposition of TiN thin films using metalorganic precursor. Journal of Vacuum Science & Technology A, 2004. **22**(1): p. 8-12.

26. Kim, J.Y., et al., Remote plasma-enhanced atomic-layer deposition of TiN by using TDMAT with a NH3 plasma. Journal of the Korean Physical Society, 2004. **45**(6): p. 1639-1643.

27. Juppo, M., M. Ritala, and M. Leskela, Use of 1,1-dimethylhydrazine in the atomic layer deposition of transition metal nitride thin films. Journal of the Electrochemical Society, 2000. **147**(9): p. 3377-3381.

28. Bejarano, G., J. Caicedo, and J.M. Saldana, Mechanical and tribological properties enhancement of heat treated AISI 4340 steel by using a TiN/TiAlN multilayer coating system. Revista Facultad De Ingenieria-Universidad De Antioquia, 2008(44): p. 36-42.

29. Barshilia, H.C., et al., Optical properties and thermal stability of TiAlN/AlON tandem absorber prepared by re active DC/RF magnetron sputtering. Solar Energy Materials and Solar Cells, 2008. **92**(11): p. 1425-1433.

30. Koo, J., et al., Study on the characteristics of TiAlN thin film deposited by atomic layer deposition method. Journal of Vacuum Science & Technology a-Vacuum Surfaces and Films, 2001. **19**(6): p. 2831-2834.

31. Kim, J.Y., et al., Compositional variations of TiAlN films deposited by metalorganic atomic layer deposition method. Japanese Journal of Applied Physics Part 1-Regular Papers Short Notes & Review Papers, 2002. **41**(2A): p. 562-565.

32. HSC Chemistry, E., Outokumpu Research Oy: Pori, Finland, 2002.

33. Fujieda, S., M. Mizuta, and Y. Matsumoto, Low-temperature metalorganic chemical vapour deposition of AIN for surface passivation of GaAs. Advanced Materials for Optics and Electronics, 1996. **6**(3): p. 127-134.

34. Fujieda, S., M. Mizuta, and Y. Matsumoto, Growth-Characterization of Low-Temperature Mocvd Gan - Comparison between N2h4 and Nh3. Japanese Journal of Applied Physics Part 1-Regular Papers Short Notes & Review Papers, 1987. **26**(12): p. 2067-2071.

35. Morishita, S., S. Sugahara, and M. Matsumura, Atomic-layer chemical-vapor-deposition of silicon-nitride. Applied Surface Science, 1997. **112**: p. 198-204.

36. Burton, B.B., A.R. Lavoie, and S.M. George, Tantalum nitride atomic layer deposition using (tert-butylimido) tris(diethylamido) tantalum and hydrazine. Journal of the Electrochemical Society, 2008. **155**(7): p. D508-D516.

37. Vogt, K.W., L.A. Naugher, and P.A. Kohl, Low-Temperature Nitridation of Transition-Metals with Hydrazine. Thin Solid Films, 1995. **256**(1-2): p. 106-115.

38. Elam, J.W., M.D. Groner, and S.M. George, Viscous flow reactor with quartz crystal microbalance for thin film growth by atomic layer deposition. Review of Scientific Instruments, 2002. **73**(8): p. 2981-2987.

39. Schmidt, E.W., Hydrazine and its Derivatives: Preparation, Properties, Applications; . 2nd ed., 2001.

40. Goldstein, D.N., J.A. McCormick, and S.M. George, Al2O3 Atomic Layer Deposition with Trimethylaluminum and Ozone Studied by in Situ Transmission FTIR Spectroscopy and Quadrupole Mass Spectrometry. Journal of Physical Chemistry C, 2008. **112**(49): p. 19530-19539.

41. Puurunen, R.L. and W. Vandervorst, Island growth as a growth mode in atomic layer deposition: A phenomenological model. Journal of Applied Physics, 2004. **96**(12): p. 7686-7695.

42. Elam, J.W., et al., Atomic layer deposition of In2O3 using cyclopentadienyl indium: A new synthetic route to transparent conducting oxide films. Chemistry of Materials, 2006. **18**(15): p. 3571-3578.

43. Rocklein, M.N. and S.M. George, Temperature-induced apparent mass changes observed during quartz crystal microbalance measurements of atomic layer deposition. Analytical Chemistry, 2003. **75**(19): p. 4975-4982.

44. Jeon, H., et al., Study on the characteristics of TiN thin film deposited by the atomic layer chemical vapor deposition method. Journal of Vacuum Science & Technology a-Vacuum Surfaces and Films, 2000. **18**(4): p. 1595-1598.

45. Juppo, M., et al., Atomic layer deposition of titanium nitride thin films using tert-butylamine and allylamine as reductive nitrogen sources. Electrochemical and Solid State Letters, 2002. **5**(1): p. C4-C6.

46. Kim, J.Y., et al., Comparison of TiN films deposited using tetrakisdimethylaminotitanium and tetrakisdiethylaminotitanium by the atomic layer deposition method. Japanese Journal of Applied Physics Part 1-Regular Papers Short Notes & Review Papers, 2003. **42**(7A): p. 4245-4248.

47. Kim, J.Y., et al., Comparison of TiN and TiAlN as a diffusion barrier deposited by atomic layer deposition. Journal of the Korean Physical Society, 2002. **40**(1): p. 176-179.

48. Logothetidis, S., et al., Room temperature oxidation behavior of TiN thin films. Thin Solid Films, 1999. **338**(1-2): p. 304-313.

49. Musschoot, J., et al., Atomic layer deposition of titanium nitride from TDMAT precursor. Microelectronic Engineering, 2009. **86**(1): p. 72-77.

50. Scott, D.W., et al., Hydrazine - Heat Capacity, Heats of Fusion and Vaporization, Vapor Pressure, Entropy and Thermodynamic Functions. Journal of the American Chemical Society, 1949. **71**(7): p. 2293-2297.

51. Tillner-Roth, R., Harms-Watzenberg, F., Baehr, H.D., Eine neue Fundamentalgleichung für Ammoniak. DKV-Tagungsbericht 1993(20): p. 167-181.

52. Snyder, M.Q., et al., An infrared study of the surface chemistry of titanium nitride atomic layer deposition on silica from TiCl4 and NH3. Thin Solid Films, 2006. **514**(1-2): p. 97-102.

53. Giguere, P.A. and I.D. Liu, On the Infrared Spectrum of Hydrazine. Journal of Chemical Physics, 1952. **20**(1): p. 136-140.

54. Amores, J.M.G., et al., An FT-IR study of ammonia adsorption and oxidation over anatase-supported metal oxides. Applied Catalysis B-Environmental, 1997. **13**(1): p. 45-58.

55. Devillepin, J. and A. Novak, Infrared and Raman-Spectra of Crystals of Hydrazinium Chloride and Bromide at Low-Temperature .1. Intramolecular Vibrations. Molecular Crystals and Liquid Crystals, 1974. **27**(3-4): p. 391-415.

56. Snyder, R.G. and J.C. Decius, The Infrared Spectra of N2h6cl2 and N2h6f2. Spectrochimica Acta, 1959. **13**(4): p. 280-290.

57. Moore, G.E. and R.M. Badger, The Infrared Spectra and Structure of the Chloramines and Nitrogen Trichloride. Journal of the American Chemical Society, 1952. **74**(23): p. 6076-6080.

58. Chuang, C.C., J.S. Shiu, and J.L. Lin, Interaction of hydrazine and ammonia with TiO2. Physical Chemistry Chemical Physics, 2000. **2**(11): p. 2629-2633.

59. Troyan, J.E., Properties, Production, and Uses of Hydrazine. Industrial and Engineering Chemistry, 1953. **45**(12): p. 2608-2612.

60. Dillon, A.C., et al., Ammonia Decomposition on Silicon Surfaces Studied Using Transmission Fourier-Transform Infrared-Spectroscopy. Journal of Vacuum Science & Technology a-Vacuum Surfaces and Films, 1991. **9**(4): p. 2222-2230.

61. Heubusch, H.P., Pugmire T. K, The Compatibility of Stainless Steels with Nitrogen Tetroxide and Hydrazine AIAA Paper 90-2063, 1990. **A90-43356**: p. 36.

62. Palik, E.D., Handbook of Optical Constants of Solids. 1998: p. 303-311.

CHAPTER V

Al_2O_3 AND TiO_2 ATOMIC LAYER DEPOSITION ON COPPER FOR WATER CORROSION RESISTANCE

5.1 Introduction

Copper is an important structural material with a high thermal conductivity. Copper is used extensively in plumbing water and for water heat exchangers. Although copper has a reasonable water corrosion resistance, finite corrosion rates of ~1 mg/dm^2/day occur in pure water with 1 ml/l oxygen concentration [1]. The corrosion occurs by means of an electrochemical mechanism in which areas remote from one another on an atomic scale serve as anodes and cathodes [2, 3]. Copper corrosion is dependent on solutes in water [4-6], the pH of water [5, 7] and the water temperature [4, 8].

Many gas phase and wet chemical techniques have been employed to protect copper from corrosion. Previous attempts have utilized coatings deposited by chemical vapor deposition (CVD) [9, 10]. In addition, copper surfaces have been chemically protected using wet chemical treatments using self-assembled monolayers [11-13], organic azoles [14-16] and polymers [17-19]. Other approaches for copper corrosion protection have utilized plasma [20] and electrochemical [21] deposition techniques. All of these methods have their limitations and may not be robust enough to prevent copper corrosion in water at elevated temperatures.

In this paper, Al_2O_3 and TiO_2 atomic layer deposition (ALD) coatings on copper were explored as ultrathin protective coatings to prevent corrosion by water.

ALD is a gas phase coating technique based on sequential, self-limiting surface chemical reactions [22]. ALD can provide atomic level control of film thickness and deposit extremely conformal coatings on high aspect ratio structures [22, 23]. Al_2O_3 is a well-defined ALD system and is performed using trimethylaluminum (TMA) and H_2O [24-26]. Al_2O_3 ALD has been used previously as a corrosion resistant coating [27, 28]. TiO_2 ALD is also a well-established ALD system and is accomplished using $TiCl_4$ and H_2O [29]. TiO_2 ALD has been reported to protect stainless steel [27, 30] and CrN [31] from electrochemical corrosion.

Al_2O_3 ALD is known to form nearly pinhole-free films [32]. Al_2O_3 ALD has also been shown to be an excellent gas diffusion barrier on polymers [33-35]. Recent measurements of the water vapor transmission rate (WVTR) through Al_2O_3 films on polymer have demonstrated that Al_2O_3 ALD films with thicknesses of >10 nm have equivalent barrier properties to glass [33]. Al_2O_3 ALD films can also protect polymers from atomic oxygen and vacuum ultraviolet (VUV) attack [36, 37]. However, Al_2O_3 ALD films are susceptible to corrosion by water [38]. Consequently, the Al_2O_3 ALD barrier must be protected to prevent water corrosion. TiO_2 is known to display excellent water resistance [39, 40]. TiO_2 ALD can be used to protect the Al_2O_3 ALD layer from water corrosion.

The nucleation and growth of Al_2O_3 ALD on copper at 177°C was studied using in situ quartz crystal microbalance (QCM) measurements to confirm that Al_2O_3 ALD grows efficiently on copper surfaces. The pinhole density in the Al_2O_3 ALD coatings on copper was also measured using electroplating techniques. Optical

microscopy was employed to monitor copper corrosion in water at 25°C and 90°C using Al_2O_3 ALD, TiO_2 ALD and TiO_2/Al_2O_3 ALD coatings grown at 120°C. Ellipsometry studies also observed the film thickness of Al_2O_3, TiO_2, ZnO and TiO_2/Al_2O_3 coatings versus time in water at 90°C. Contact angle measurements characterized H_2O wetting on TiO_2-coated copper wire mesh substrates.

5.2 Experimental

Al_2O_3, TiO_2 and ZnO ALD were performed in a viscous-flow, hot-wall type ALD reactor described in detail elsewhere [41]. The Al_2O_3 ALD was deposited using 97% pure TMA (Sigma-Aldrich, U.S.A.) and chromatography-grade water at 120°C and 177°C. Nucleation on copper substrates was explored at the optimum growth temperature of 177°C for Al_2O_3 ALD [25]. Al_2O_3 ALD films were deposited at 120°C for the studies of copper corrosion. This lower temperature was employed because this study was motivated by the problem of copper corrosion in microelectromechanical systems (MEMS) devices that contain thermally sensistive polymers [42].

The TiO_2 ALD was deposited using 98% pure $TiCl_4$ (Strem Chemicals Inc., U.S.A.) and water at 120°C. Titanium tetrachloride is a stable precursor with good vapor pressure at room temperature and was considered as the best metal precursor for TiO_2 deposition. TiO_2 ALD using titanium (IV) isopropoxide and H_2O was not employed because this system requires temperatures from 250 to 325°C [43] that are not compatible with most polymers. Titanium(IV) dimethylamide (TDMAT) and

H_2O was not used for TiO_2 ALD because TDMAT has thermal decomposition problems and is known to yield very poor TiN ALD films at low temperatures [44].

The ZnO ALD was deposited using diethylzinc (Sigma-Aldrich, U.S.A.) and H_2O at 120°C. During Al_2O_3, TiO_2 and ZnO ALD, the metal precursors and H_2O were maintained at room temperature. Ultra high purity (99.999%) grade nitrogen (Airgas, CO, U.S.A.) was used as the purge and carrier gas in the ALD reactor. With pumping using a mechanical pump, the flowing N_2 gas defined a base pressure of 0.9 Torr. All the films in this paper were grown using ALD techniques unless stated otherwise.

QCM measurements were performed using AT- cut, 6 MHz resonant frequency, unpolished, copper-plated quartz crystal sensors (Inficon Inc.,U.S.A.). The QCM sensor was coated with 7 μm thick copper film. Copper was deposited by using electron beam evaporation. A layer of titanium with a thickness of 200 Å served as the adhesion layer between the quartz crystal and the copper film. The QCM crystal was mounted in a bakeable sensor housing and sealed using high temperature conductive epoxy and purged with nitrogen to prevent deposition on the backside of the crystal [41]. The copper-plated crystal turned a bright red color, indicating the presence of thick layer of copper oxide, after epoxy curing in the QCM housing in air at 200°C for two hours. Typically, copper heated to 200 °C in air has as a oxide layer consisting of a mixture of Cu(I) and Cu(II) [45].

Precut, copper-plated, silicon wafers with dimensions of 2.5 cm × 2.5 cm were used as the copper substrates for the copper corrosion studies. These wafers

were covered with a 15 µm polished copper film deposited using electron beam evaporation. The copper was evaporated onto a 250 Å thick tantalum adhesion layer (Montco Silicon Technologies Inc., U.S.A.). X-ray photoelectron spectroscopy (XPS) analysis of these copper substrates indicated the presence of a native oxide layer in the Cu(I) oxidation state. The thickness of the CuO_2 oxide layer was determined to be ~30 Å using spectroscopic ellipsometry. All of the substrates referred to in this work as copper were assumed to have a native copper oxide layer on the surface.

A spectroscopic ellipsometer (J.A. Woollam Co., U.S.A.) was used to determine the thickness and refractive index of the deposited TiO_2 and Al_2O_3 films. The thickness was measured using three different wavelengths (418.5, 594.6 and 763.2 nm) at an incident angle of 75°. Refractive indexes of deposited TiO_2 and Al_2O_3 were obtained using the Tauc-Lorentz and Cauchy models, respectively. A Gaertner Ellipsometer L117 (Skokie, Illinois, U.S.A.) was used to monitor changes in film thickness after immersion in water. The thickness was obtained at three different locations for each measurement.

Auger electron spectroscopy (AES) and X-ray photoelectron spectroscopy (XPS) were used to examine the composition of the Al_2O_3 ALD film on copper surfaces. AES measurements were conducted at the University of Minnesota College of Science and Engineering Characterization Facility on a Physical Electronics scanning Auger spectrometer (PHI Model 545). Depth profile data was obtained with 3 keV Ar^+ sputtering. XPS scans were performed at the University of

Colorado using a Physical Electronics (PHI Model 5600) spectrometer with a monochromatic Al Kα X-ray source with energy of 1486.6 eV. XPS survey scans were performed with an electron pass energy of 187 eV and a resolution of 0.8 eV.

Surface morphologies of the ALD films deposited on copper substrates were determined using atomic force microscopy (AFM). Measurements were performed using an Autoprobe CP instrument from Thermomicroscopes atop an air table (Integrated Dynamics Engineering, U.S.A.). AFM images were acquired in noncontact mode. All scans were 5 μm × 5 μm and performed at a scan rate of 0.8 Hz using "A" tip rectangular cantilevers (MikroMasch Company, U.S.A.).

Copper electroplating was utilized to visualize defects in the Al_2O_3 ALD films deposited on copper [46]. The electroplating solvent was composed of 1.0 M H_2SO_4 and 0.4 M $CuSO_4$ [46]. Because Al_2O_3 is a dielectric, copper only grew at defect sites in the Al_2O_3 film where the electrolytic solution established contact with the conductive substrate during electroplating. After the electroplating, the defects were revealed as copper bumps. These defects were analyzed and counted using optical (Nikon ECLIPSE LV150, Japan) and scanning electron microscopy (SEM) (Jeol Limited JSM-6480LV, Japan) techniques.

Corrosion protection properties of the ALD films were investigated by immersing coated substrates into chromatography grade water at room temperature and 90°C. Coated copper substrates were fully immersed in water that was heated to a precision of ± 2.5°C using a hotplate (Thermo Fisher Scientific Inc., U.S.A.). After sample removal and prior to any analysis, the samples were dried

with nitrogen gas. Thickness data and optical images of the copper substrates were measured every one to four days. An optical microscope (Nikon ECLIPSE LV150, Japan) was used to record the optical images.

The optical images were analyzed using ImageJ [47]. All of the images of the bare and coated copper substrates were obtained under the same conditions and recorded with 10 × magnification and 1280 × 1024 capture resolution. The images were recorded at the same region of the sample versus time to track the changes. The images were made binary by the ImageJ processing software. The greyscale darkness of the copper substrates before water immersion was used as the reference to define the threshold darkness. The copper corrosion area was defined as the relative fraction of pixels in the image that had a darkness above the threshold darkness.

The wettability of TiO_2-coated copper meshes with 50 μm wire diameters was examined using water contact angle measurements. The contact angle was measured using 1 μl water droplets. The images were processed using First Ten Angstroms imaging software (First Ten Angstroms, Inc., U.S.A.).

5.3 Results and Discussion

5.3.1 Nucleation and Growth of Al_2O_3 ALD on Copper

Al_2O_3 ALD on copper was investigated at 177°C on a QCM with a copper-plated quartz crystal. The dose times for TMA and H_2O were 1 s with 30 s purge times after each pulse. TMA and H_2O exposures were 12×10^4L (1 L=1×10^{-6}

Torr·s) and 4×10^4 L, respectively. Figure 5.1 shows the QCM response during the first 5 ALD cycles.

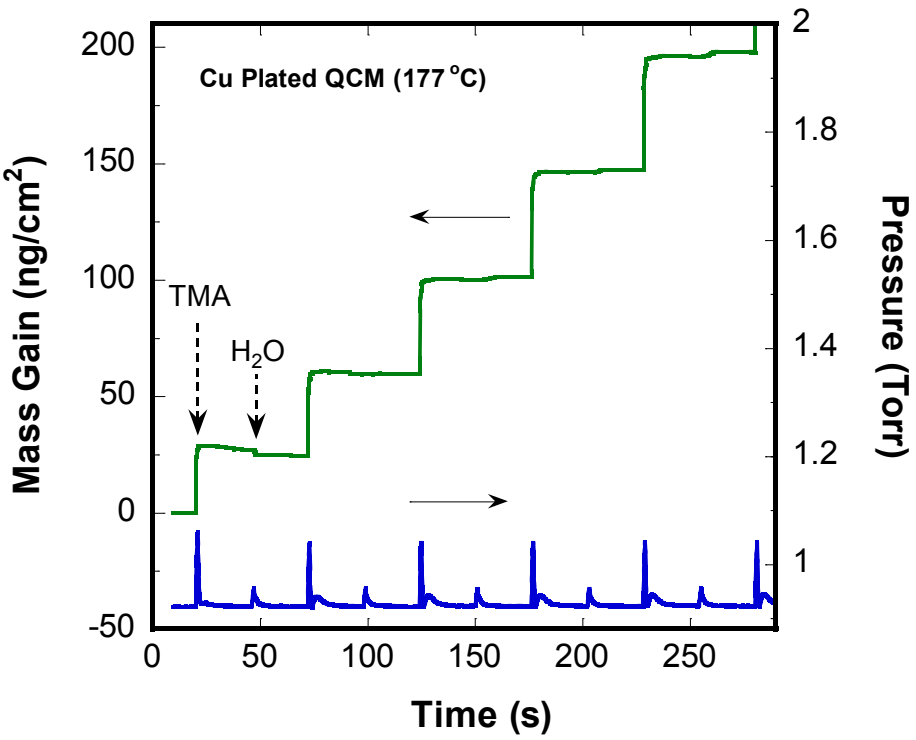

Figure 5.1 Mass gain versus time recorded during first five Al_2O_3 ALD cycles on copper-plated QCM sensor at 177°C.

Al_2O_3 nucleates readily on the copper substrate. In the first cycle, the TMA dose resulted in a mass gain of 27 ng/cm^2 and the water dose resulted in a mass loss of 2 ng/cm^2. The total mass gain per cycle (MGPC) was 25 ng/cm^2/cycle. Figure 1 shows that the total mass gain increases progressively through the first 5 cycles.

Figure 5.2a displays the mass gains for TMA (Δm_A), H_2O (Δm_B) and Al_2O_3 ($\Delta m_A + \Delta m_B$) for 205 ALD cycles.

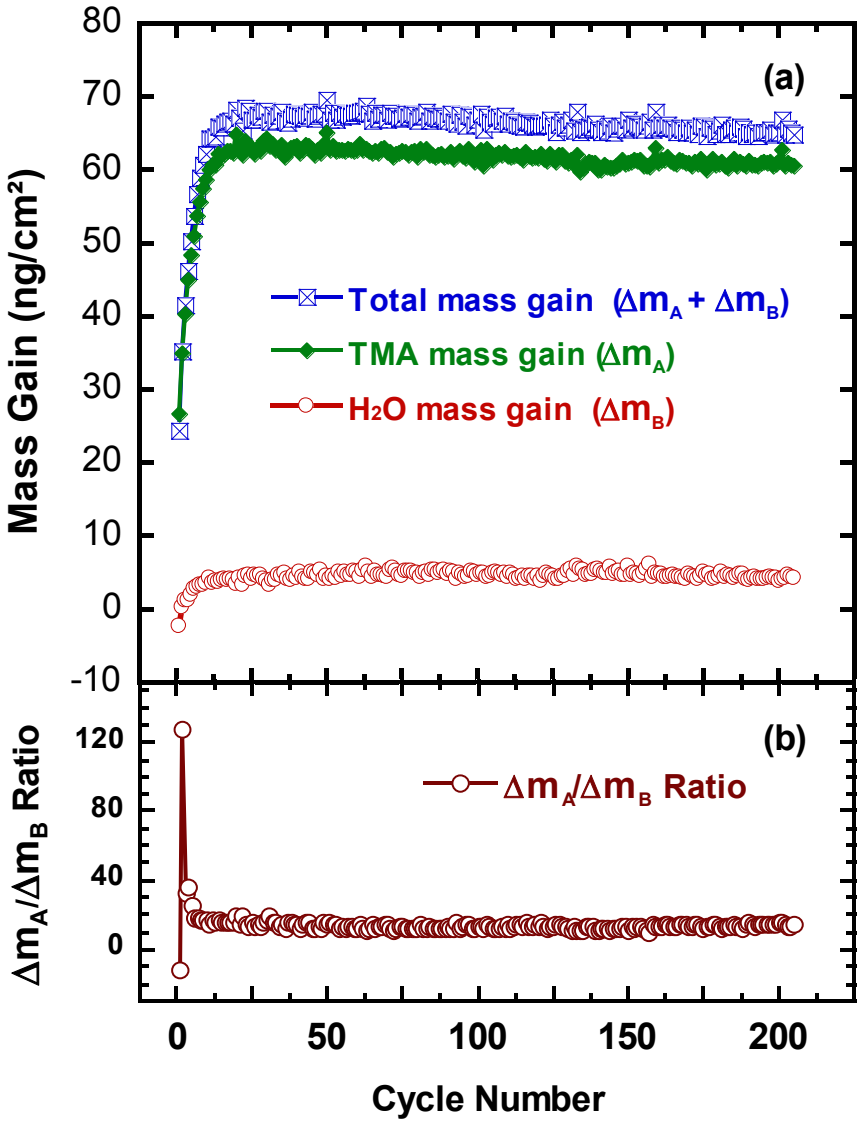

Figure 5.2 (a) Mass gain versus cycle number for Al_2O_3 ALD on copper-plated QCM sensor at 177°C showing TMA mass gain, H_2O mass gain and total mass gain. (b) Ratio of the TMA mass gain and the H_2O mass gain versus cycle number for the mass gains shown in (a).

Nucleation occurs over the first 15-20 ALD cycles. The total mass gain increases and reaches a maximum value of ~68 ng/cm²/cycle. Figure 5.2b shows the $\Delta m_A/\Delta m_B$ ratio for individual mass gains of TMA and water. The $\Delta m_A/\Delta m_B$ ratio starts at a

high value and quickly decreases and levels off at a steady state value of ~13 after 20 cycles. The negative value of the ratio on the first cycle is due to the initial mass loss during first water dose. The steady state ratio value of ~13 is slightly higher than the ratio of ~10 observed earlier during Al_2O_3 ALD on a polished, gold-plated, QCM crystal under the same reaction conditions [41].

The QCM profiles shown in Figure 5.1 are consistent with the chemistry for Al_2O_3 ALD growth using TMA and water [41, 48]. However, the Al_2O_3 growth rate of ~65 ng/cm^2/cycle observed after the nucleation period is about 2 times higher than the growth rate observed on polished QCM sensors. This higher mass gain per cycle is attributed to the difference in surface area between the polished and unpolished QCM sensors [41]. As the roughness of the QCM crystal surface decreases with the number of ALD cycles, the Al_2O_3 ALD MGPC should approach a MGPC of ~38 ng/cm^2/cycle that has been reported for polished QCM sensors at 177°C [41, 48]. Slightly smaller MGPCs ranging from 31 to 37 ng/cm^2/cycle are observed at 125°C depending on TMA and H_2O exposures [49].

The slow Al_2O_3 growth during the first several ALD cycles indicates that the surface of the copper oxide on the copper substrate may have few hydroxyl groups. Another possibility is that the copper oxide surface may be covered with carbonaceous species. There was no attempt to clean the copper oxide surface prior to the Al_2O_3 ALD. Nucleation periods of 10-20 cycles are similar to the nucleation periods observed for Al_2O_3 ALD on a variety of polymer substrates [50].

5.3.2 Characterization of Al_2O_3 ALD Films on Copper

The thickness of the Al_2O_3 films deposited on copper was measured using ellipsometry. Measurements of the film thickness versus number of cycles yielded an Al_2O_3 ALD growth rate of 1.2 Å/cycle at 177°C. This value is in good agreement with the growth rate observed for Al_2O_3 ALD on silicon substrates [25]. The color of the copper substrate coated with 620 Å of Al_2O_3 was deep red. The refractive index of 1.6 at 633 nm for the Al_2O_3 film deposited on copper matched previously reported values for Al_2O_3 ALD films [48].

Auger electron spectroscopy (AES) was used to examine the chemical composition of the Al_2O_3 ALD film. Figure 5.3 displays the AES depth profile of a 620 Å thick Al_2O_3 film deposited on a copper substrate at 177°C. There is a uniform distribution of aluminum and oxygen atoms throughout the entire film with no traces of copper in the bulk of the film. The deviation from stoichiometric Al_2O_3 with slightly lower oxygen than expected can be attributed to the preferential sputtering of light atoms during the AES depth profile. Impurities in the film were below the detection limit of the instrument.

Pinholes in the Al_2O_3 ALD film on copper were evaluated using an electroplating technique [46]. Al_2O_3 samples were prepared by deposition of Al_2O_3 films with a thickness of 250 Å on 4 inch copper wafers at 177°C using the same reaction conditions as employed for the QCM studies.

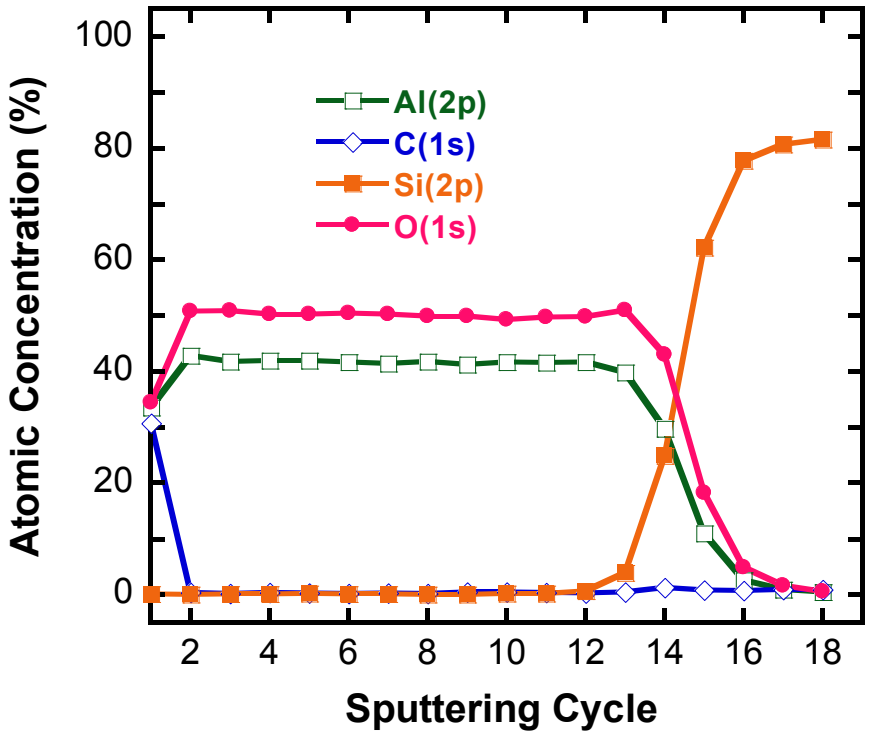

Figure 5.3 Atomic concentrations versus sputtering cycle for Al_2O_3 ALD film with a thickness of 620 Å deposited on copper substrate at 177°C.

UHP grade nitrogen was used to remove residual particles from the surface of the copper substrate. The copper substrate was then loaded into an ALD reactor that was larger than the ALD reactor that was used for the other ALD coatings. This larger ALD reactor was housed in a class 100 clean room environment. The substrate was placed in the ALD reactor for 30 minutes to allow for temperature equilibration prior to the start of the Al_2O_3 ALD.

The Al_2O_3-coated copper substrates were then subjected to electroplating prior to examination by SEM. Very few defects as revealed by copper bumps were observed after the electroplating process. Only ~4 defects per cm^2 were observed

after 20 min of electroplating time. Figure 5.4 shows that the number of defects increases with the increase in electroplating time.

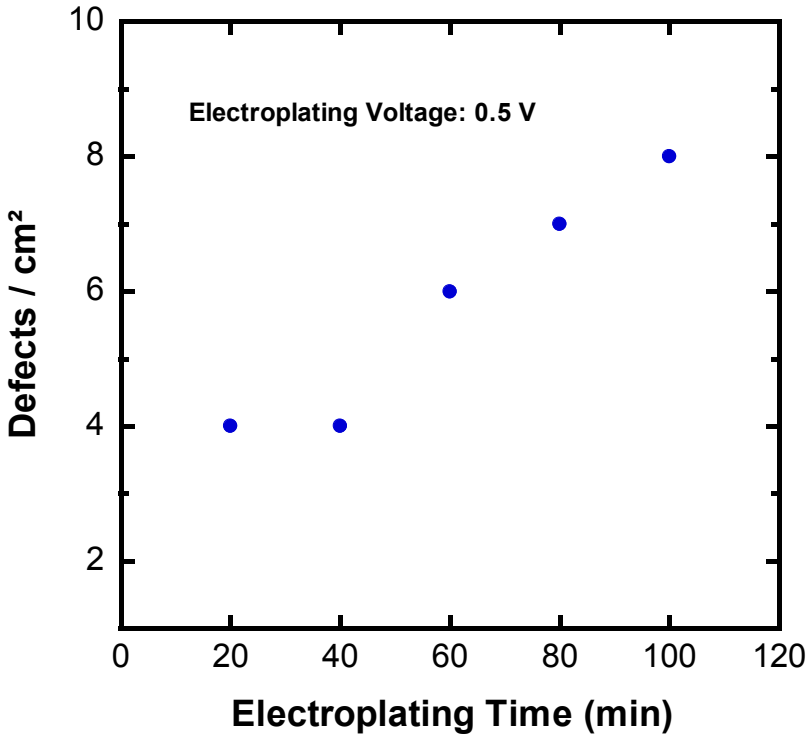

Figure 5.4 Defect densities versus electroplating time for Al_2O_3 ALD film with a thickness of 250 Å deposited on copper substrate at 177°C.

After 100 minutes of electroplating, the Al_2O_3 ALD film on copper had only 8 defects per cm^2. This defect density compares with the lowest density of 38 defects per cm^2 obtained earlier under the same electroplating conditions for Al_2O_3 ALD films with a thickness of 250 Å deposited on nickel substrates [46]. The nickel substrates were formed by the resistive evaporation of nickel on silicon wafers.

The defects in the Al_2O_3 films are most likely caused by residual particle contamination. Although the copper substrates were cleaned in a class 100 clean room environment prior to Al_2O_3 ALD, there still may be some particles that adhere

to the copper substrate or particles that are not easily removed from the initial copper substrate. The excellent WVTRs measured for Al_2O_3 ALD-coated polymers suggest that the Al_2O_3 films are comparable to glass and do not contain intrinsic defects [33, 34].

5.3.3 TiO_2 ALD on Copper

Although Al_2O_3 ALD is an excellent barrier film, the Al_2O_3 films are susceptible to water corrosion [38]. In contrast, TiO_2 is much more resilient to water corrosion [39, 40]. Consequently, TiO_2 ALD was grown on the copper substrates at 120°C and then examined using ex situ XPS analysis. The XPS measurements after 300 cycles of $TiCl_4$ and water showed the presence of adventitious carbon C (51.30 at. %) together with Cl (1.42 at. %), O (30.25 at. %), Ti (11.78 at. %) and Cu (5.24 at. %). Based on the previously reported TiO_2 ALD growth rate of 0.6 Å/cycle [51], the expected TiO_2 film thickness is ~180 Å. The presence of copper in the XPS spectrum indicates either that the TiO_2 film thickness is less than the photoelectron penetration depth of ~50 Å or that the TiO_2 ALD film did not nucleate well on the copper substrates.

AFM results for TiO_2 films on copper substrates also were consistent with nucleation difficulties for TiO_2 ALD. Figure 5.5a shows a 1 μm × 1 μm AFM scan of a copper substrate after TiO_2 ALD using 300 cycles of $TiCl_4$ and H_2O at 120°C.

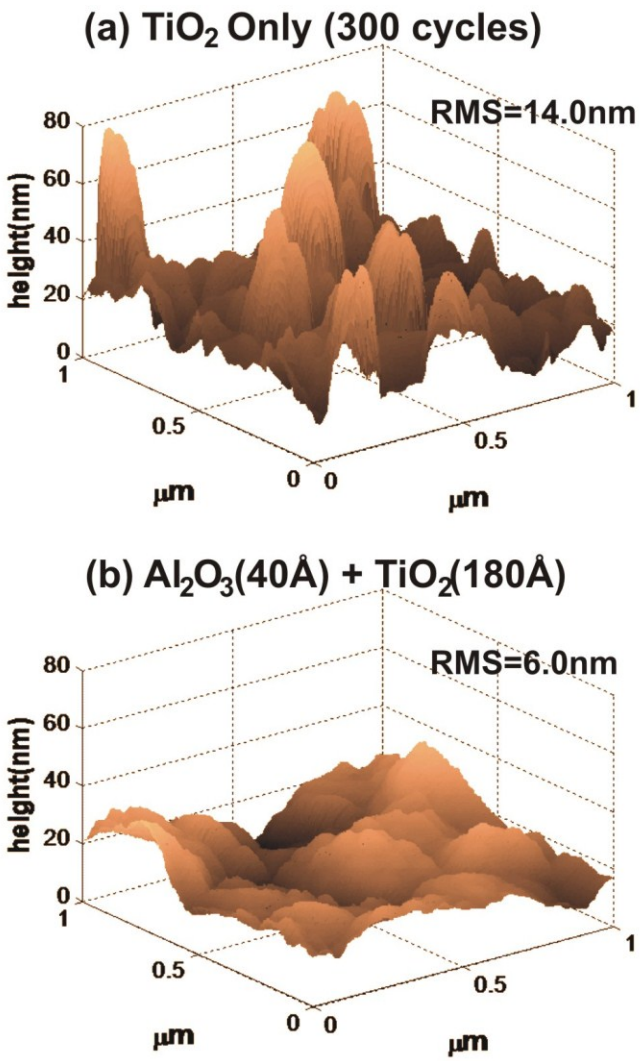

Figure 5.5 AFM images of: (a) 300 cycles of TiO_2 ALD grown on copper substrate at 120°C; and (b) TiO_2 capping layer with a thickness of 180 Å on Al_2O_3 adhesion layer with a thickness of 40 Å grown on copper substrate at 120°C.

The surface is very rough with a root-mean-square (RMS) roughness of 14.0 nm. In comparison, the initial copper substrate had a RMS roughness of 5.5 nm. The roughness of the TiO_2-coated substrate is consistent with the nucleation of scattered TiO_2 islands that grow and yield a rough surface.

In contrast to TiO_2 ALD, Al_2O_3 ALD can nucleate readily on the copper substrate. An adhesion layer of Al_2O_3 may facilitate the subsequent TiO_2 ALD. Figure 5b shows an AFM image of a copper surface after depositing a ~40 Å adhesion layer of Al_2O_3 ALD using 40 cycles of TMA and H_2O at 120°C followed by 300 cycles of $TiCl_4$ and H_2O to grow the TiO_2 coating at 120°C. This surface has an RMS roughness value of 6.0 nm that is nearly identical to the initial copper substrate.

The smoothness of the TiO_2 capping layer demonstrates that the Al_2O_3 adhesion layer can ensure proper nucleation and conformality of the TiO_2 ALD films. Ellipsometery measurements of TiO_2 ALD films grown on the Al_2O_3 adhesion layer on copper were consistent with the previously reported TiO_2 ALD growth rate of 0.6 Å/cycle [51]. In addition, XPS scans performed on the same samples revealed no traces of copper and a Cl/Ti atomic percentage ratio of 0.034. This chlorine concentration is comparable to a previously reported Cl/Ti atomic percentage ratio of 0.047 for TiO_2 ALD using the same conditions [52].

5.3.4 Corrosion Protection of Cu Using Al_2O_3 and TiO_2 ALD

Optical imaging was used to examine the water corrosion of copper substrates immersed in water at 90°C. Figure 5.6a shows the surface of an uncoated copper substrate after immersion in hot water at 90°C for 75 hours.

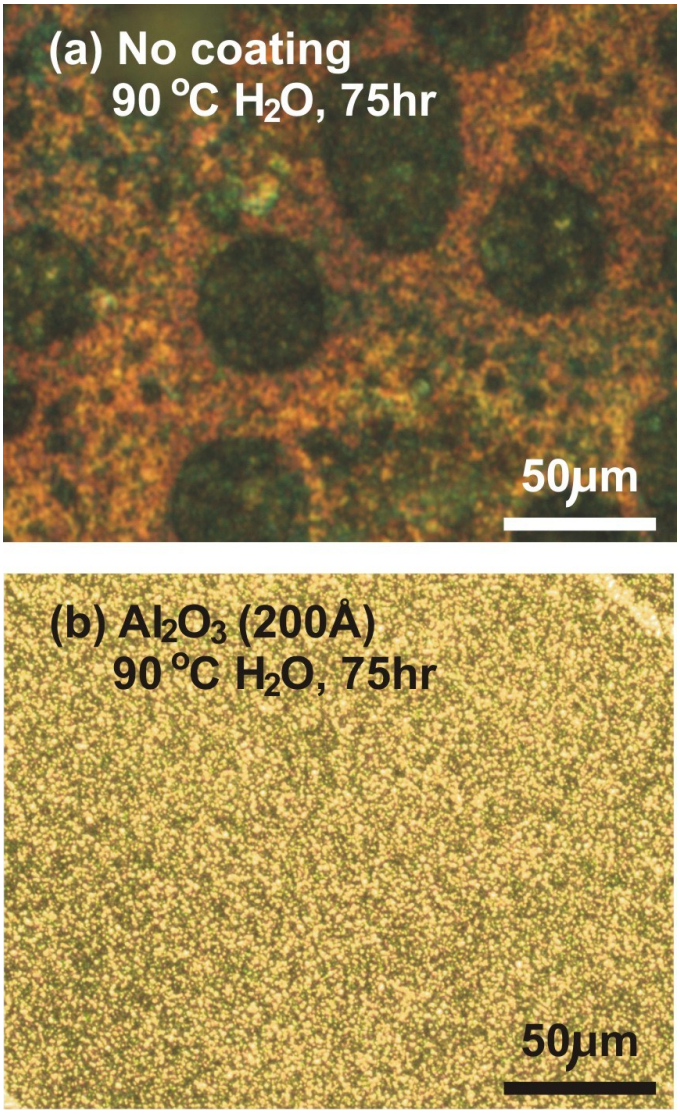

Figure 5.6 Optical microscope images of copper substrates after 75 hours in water at 90°C with: (a) no coating; and (b) Al_2O_3 ALD coating with thickness of 200 Å grown at 120°C.

This copper substrate has corroded significantly leading to discoloring and multiple structured features. In comparison, the original copper substrate was a uniform golden brown color with no structure.

Figure 5.6b displays the image of a copper substrate coated with 165 cycles of Al_2O_3 ALD at 120°C after immersion in water at 90°C for 75 hours. The 165 cycles are sufficient to deposit an Al_2O_3 thickness of ~200 Å on the copper substrate. The copper substrate has again corroded and developed many fine features. The Al_2O_3 film by itself is not capable of protecting the copper substrate from water corrosion.

Figure 5.7a shows the image of a copper substrate coated with 300 cycles of TiO_2 ALD at 120°C without an Al_2O_3 adhesion layer after immersion in water at 90°C for 75 hours. This copper substrate is also badly corroded as evidenced by the discoloration and multiple features. The corrosion is expected because the TiO_2 film does not nucleate efficiently on the copper substrate. Consequently, there are probably open copper areas on the substrate that begin to corrode very quickly in the hot water.

Water corrosion resistance was observed for TiO_2 capping layers on the Al_2O_3 adhesion layers on copper substrates. Figure 5.7b displays the image of a copper substrate that was first coated with an Al_2O_3 layer thickness of ~40 Å at 120 °C. Subsequently, TiO_2 was grown on the Al_2O_3 layer using 300 cycles of $TiCl_4$ and H_2O at 120°C to produce a TiO_2 layer thickness of ~180 Å. This sample was much more resistant to corrosion after immersion in water for 75 hours at 90°C. Only a few small discolored regions were observed in the image.

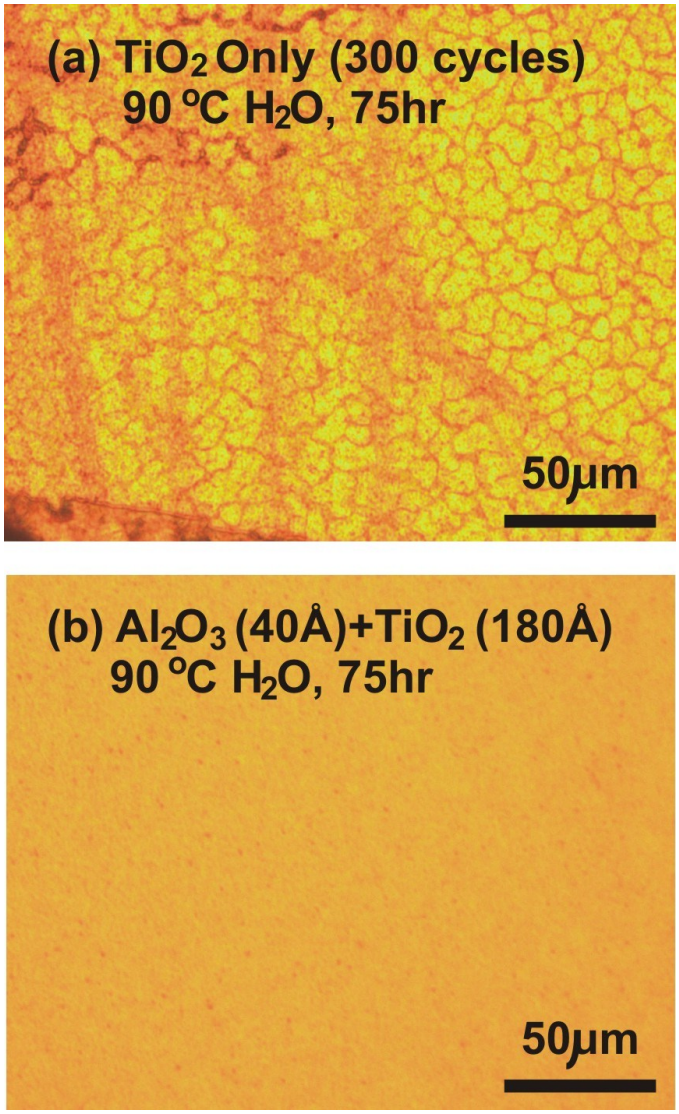

Figure 5.7 Optical microscope images of copper substrates after 75 hours in water at 90°C with: (a) 300 cycles of TiO_2 ALD at 120°C; and (b) TiO_2 capping layer with a thickness of 180 Å on Al_2O_3 adhesion layer with a thickness of 40 Å grown at 120°C.

After establishing that the TiO_2 layer was resistant to water corrosion, optical imaging was used to determine the extent of corrosion as a function of TiO_2 coating thickness on the Al_2O_3 layer on copper substrates. TiO_2 capping layer thicknesses were explored from 37 Å to 242 Å. The Al_2O_3 adhesion layers had a

thickness of ~40 Å. All of these samples were immersed in water at room temperature and 90°C for 900 hours.

Optical images of various samples that were immersed in hot water at 90°C for 900 hours are shown in Figures 5.8 and 5.9.

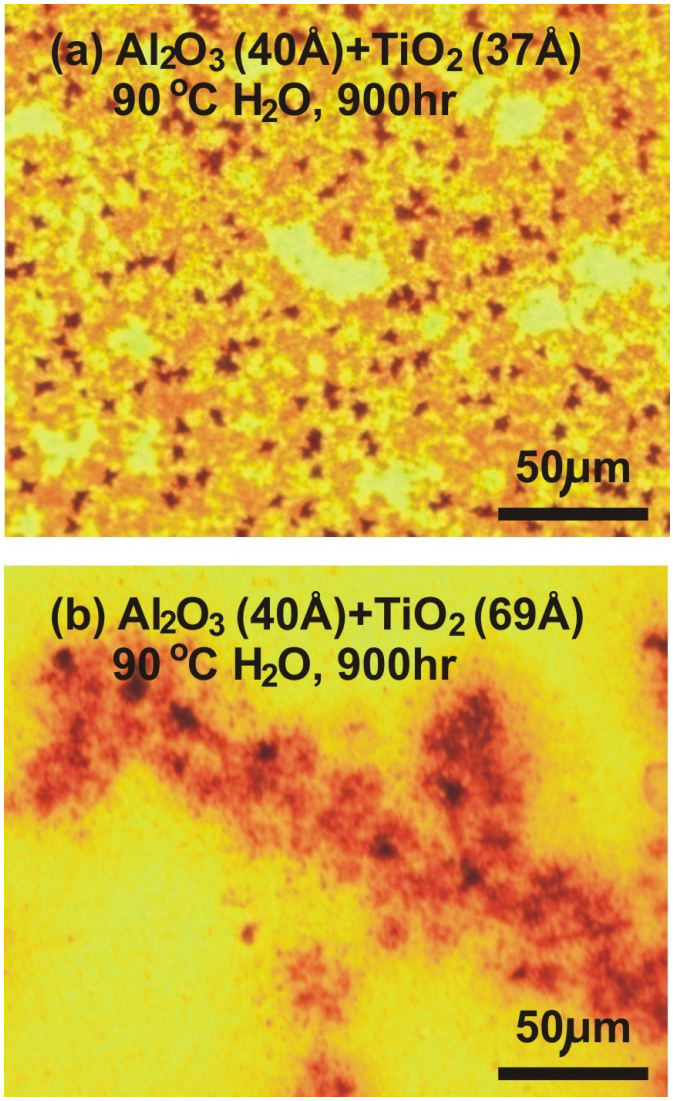

Figure 5.8 Optical microscope images of copper substrates after 900 hours in water at 90°C with: (a) TiO_2 capping layer with a thickness of 37 Å; and (b) TiO_2 capping

layer with a thickness of 37 Å. The TiO_2 capping layers were on Al_2O_3 adhesion layers with a thickness of 40 Å. TiO_2 and Al_2O_3 ALD were performed at 120°C.

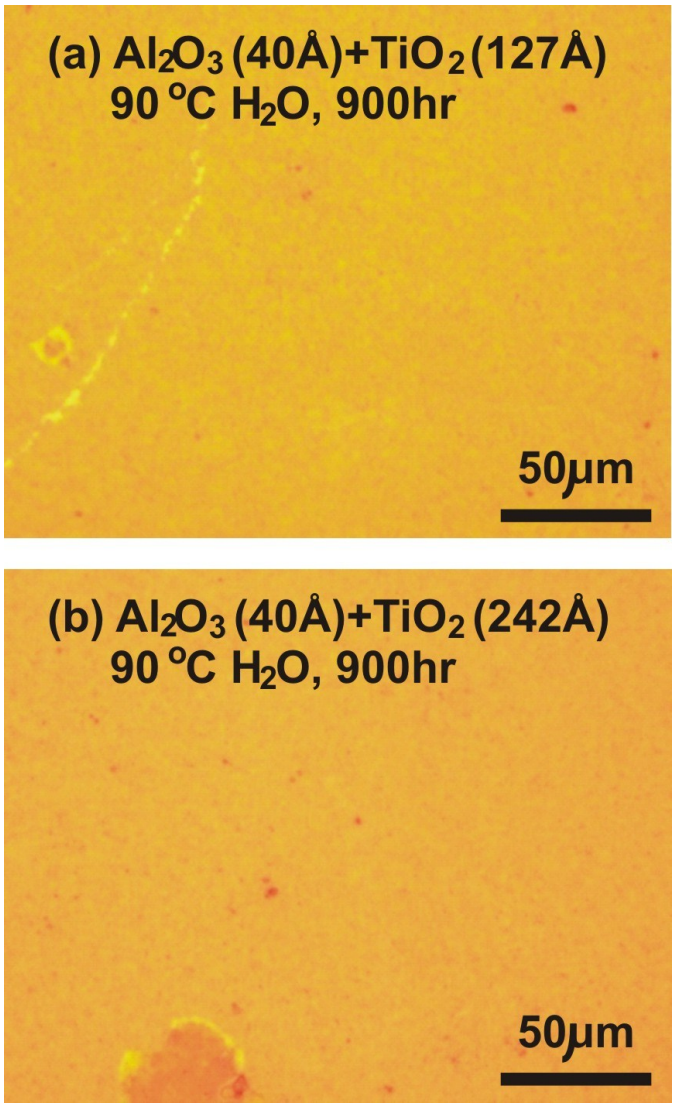

Figure 5.9 Optical microscope images of copper substrates after 900 hours in water at 90°C with: (a) TiO_2 capping layer with a thickness of 127 Å; and (b) TiO_2 capping layer with a thickness of 242 Å. The TiO_2 capping layers were on Al_2O_3 adhesion layers with a thickness of 40 Å. TiO_2 and Al_2O_3 ALD were performed at 120°C.

The results for the TiO_2 thicknesses of 37 Å and 69 Å in Figures 5.8a and 5.8b, respectively, reveal that thinner TiO_2 thicknesses are insufficient to protect the copper substrate from water corrosion. The copper substrates are discolored and covered with multiple features.

The results for the TiO_2 thicknesses of 127 Å and 242 Å in Figures 5.9a and 5.9b, respectively, show that the thicker TiO_2 thicknesses are sufficient to provide a significant degree of protection. Only a few corrosion regions exist. These corroded regions are mostly circular spots that are consistent with corrosion through pinhole defects. The samples in Figures 5.9a and 5.9b also retain their original golden brown color. These thicker TiO_2 coatings are nearly sufficient to prevent corrosion in water at 90°C for 900 hours.

The corroded area of the copper substrate was quantified using ImageJ processing software during tests lasting over 120 days. The corrosion was quantified by setting a threshold for the darkness of an individual pixel. The golden brown color of the initial copper substrate was set just below the darkness threshold. The dark, discolored corroded regions of the substrate were then all darker than the darkness threshold. After setting this darkness threshold, the corroded area of the copper substrates could be monitored versus time.

Figure 5.10 shows the results from this ImageJ processing for a variety of coated copper substrates including Al_2O_3, TiO_2, TiO_2/Al_2O_3 and ZnO. These samples were immersed in hot water at 90°C. Some comparative results are also shown for tests performed in water at room temperature.

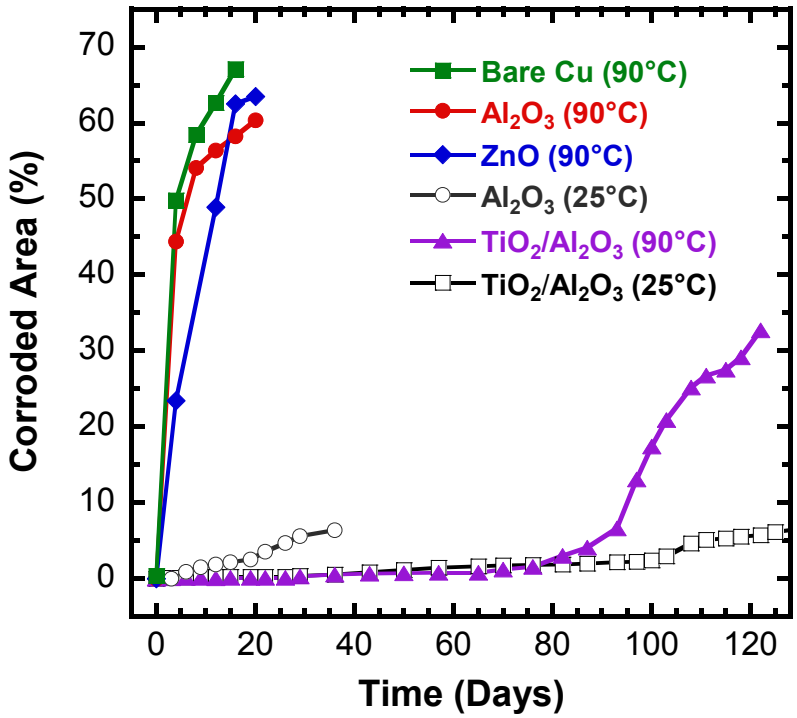

Figure 5.10 Corroded area on copper substrate derived using ImageJ versus time in water at 25°C and 90°C for bare copper and copper coated with Al_2O_3 ALD, ZnO ALD, and both Al_2O_3 and TiO_2 ALD. The film thicknesses were 200 Å for the Al_2O_3 coating and 250 Å for the ZnO coating. For the TiO_2/Al_2O_3 coating, the Al_2O_3 adhesion layer thickness was 55 Å and the TiO_2 capping layer thickness was 200 Å. All ALD films were grown at 120°C.

Figure 5.10 reveals that the copper substrates coated with an Al_2O_3 adhesion layer with a thickness of ~55 Å and a TiO_2 capping layer with a thickness of ~200 Å can survive for ~80 days prior to any observed corrosion in water at 90°C. This same coating can survive for >100 days in water at 25°C with a much slower corrosion rate after reaching the threshold for some observable corrosion. The Al_2O_3 adhesion layer with a thickness of 55 Å was grown using 50 cycles of TMA and

water. This slightly larger adhesion layer thickness should not affect the TiO_2 ALD nucleation or the corrosion rate.

In contrast, Figure 5.10 reveals that the copper substrates covered with only an Al_2O_3 film with a thickness of ~200 Å or a ZnO film with a thickness of ~250 Å corrode almost immediately in hot water at 90°C. For both of these coatings, the corroded areas are >50% after 5 days. These results are only marginally better than the uncoated copper substrate in hot water at 90°C. The copper substrate with an Al_2O_3 film with a thickness of ~200 Å in water at room temperature corrodes much more slowly. Corrosion is observed from nearly the beginning. However, the corrosion rate is much slower than the corrosion rate at 90°C.

The optical images also revealed that scratched regions of the uncoated or coated copper substrate led to more darkening and corrosion than unscratched regions of the substrate. The scratched regions displayed more corrosion both before and after coating. The scratches probably introduce more active surface sites that are more susceptible to chemical change.

5.3.5 Dissolution of Al_2O_3, ZnO and TiO_2/Al_2O_3 ALD Films

The best corrosion resistance in water at 90°C was obtained with copper substrates covered with an Al_2O_3 adhesion layer with a thickness of 55 Å and then coated with a TiO_2 capping layer with a thickness of ≥ 200 Å at 120°C. However, these coated copper substrates displayed corrosion after >80 days. This corrosion may be related to the dissolution of the TiO_2/Al_2O_3 films. To test this idea,

ellipsometry was used to measure the thickness of the TiO_2/Al_2O_3 film versus time during immersion in water at 90°C.

Figure 5.11 displays the "effective" film thickness measured by ellipsometry versus time for Al_2O_3, ZnO and TiO_2/Al_2O_3 films during immersion in water at 90°C.

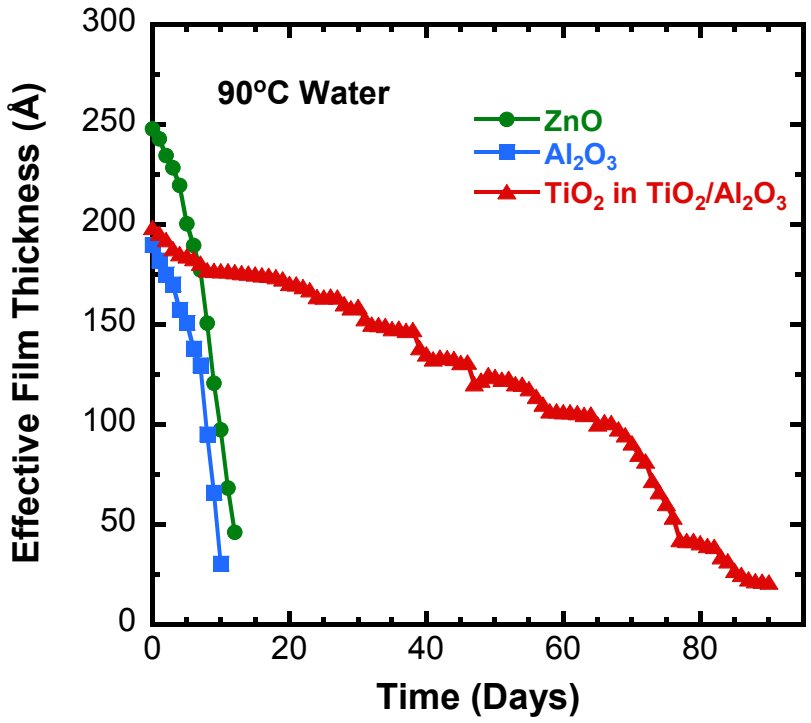

Figure 5.11 Effective film thickness on copper substrate versus time in 90°C water for Al_2O_3, ZnO and TiO_2/Al_2O_3 ALD coatings. For the TiO_2/Al_2O_3 coating, the Al_2O_3 adhesion layer thickness was 55 Å and the TiO_2 capping layer thickness was 200 Å. All ALD films were grown at 120°C.

The film thickness is "effective" because the corrosion does not produce perfectly homogeneous films. There are some corrosion pits as evidenced by the optical microscope images in Figures 5.8 and 5.9. In addition, the effective film thickness is shown for only the TiO_2 component of the TiO_2/Al_2O_3 film. The separation of the

TiO_2 and Al_2O_3 layers was accomplished by assuming an Al_2O_3 adhesion layer thickness of 55 Å under the TiO_2 capping layer in the fit of the ellipsometry data.

Figure 5.11 shows that the Al_2O_3 and ZnO films dissolve very quickly in less than 10-15 days. In contrast, the TiO_2 capping layer on the Al_2O_3 adhesion layer starts with a thickness of ~200 Å and progressively dissolves over ~90 days. The loss of the TiO_2 layer thickness is fairly linear and suggests that the TiO_2 layer is dissolving in water at 90°C with zero-order kinetics. Additional experiments with different thicknesses of the TiO_2 capping layer on the Al_2O_3 adhesion layer could confirm the zero-order dissolution kinetics.

There are correlations between the corroded area percentage results in Figure 5.10 and the effective film thicknesses in Figure 5.11. For the TiO_2/Al_2O_3 film, the corroded area starts to increase when the TiO_2 layer is removed by dissolution. This correlation indicates that the corrosion resistance is determined by the TiO_2 ALD film thickness. The TiO_2/Al_2O_3 coating can protect the copper substrate until the TiO_2 capping layer on the Al_2O_3 adhesion layer is dissolved after ~90 days in water at 90°C.

5.3.6 Wetting Properties of TiO_2 ALD Coated Copper

H_2O wetting on the TiO_2 capping layers on the Al_2O_3 adhesion layers on copper were investigated using the sessile drop method to determine the water contact angle. The TiO_2 capping layers on the Al_2O_3 adhesion layers were deposited at 120°C on copper meshes with 50 µm wire diameters. The size of the water

droplet for the contact angle measurements was limited to 1 µl to avoid gravitational effects. All TiO_2 samples were protected from ultraviolet (UV) light exposure prior to testing. This precaution was necessary since the wetting properties of TiO_2 are sensitive to UV light [53].

Figures 5.12a and 5.12b show the results after adding a water droplet to the copper wire meshes before and after the deposition of TiO_2 capping layers on the Al_2O_3 adhesion layers.

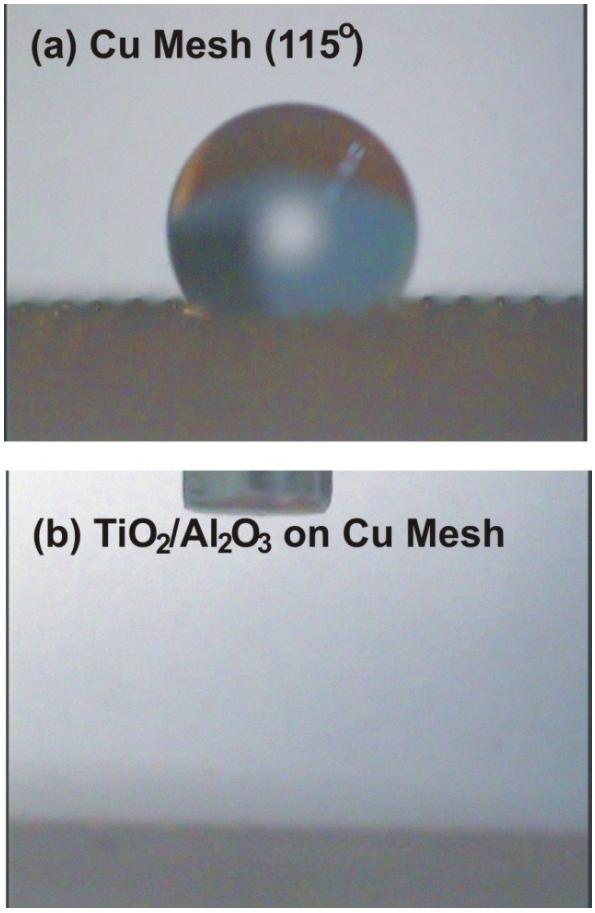

Figure 5.12 Water contact angle measurements for: (a) bare woven copper mesh with 5 µm wire size; and (b) copper mesh with TiO_2 capping layer thickness of 100 Å

on Al_2O_3 adhesion layer thickness of 55 Å. The TiO_2 and Al_2O_3 ALD films were grown at 120°C.

Figure 5.12a shows that a large contact angle of 115° is measured on the uncoated copper wire mesh. This large contact angle is typical for substrates where the water bridges the tops of the substrate features. The water droplet rests on flat solid tops and air gaps between them as described by the Cassie–Baxter model [54]. According to this model, the apparent contact angle is determined by contributions from both the solid tops and the air gaps.

Figure 5.12b shows the result after adding a water droplet to the surface of the TiO_2-coated copper wire mesh. The TiO_2-coated copper mesh rapidly and completely wicks the water droplet. This wettability is consistent with a low contact angle and presence of strong capillary forces. A slight difference in wetting speed was observed when water droplets were placed on dry versus wet copper meshes. Slower water spreading was observed on wet meshes. These TiO_2-coated copper wire meshes should be very useful for heat exchangers employing thermal transport based on water adsorption and desorption.

5.4 Conclusions

Al_2O_3 and TiO_2 ALD were used to fabricate ultrathin protective coatings on copper to prevent water corrosion. Al_2O_3 or TiO_2 ALD alone was not effective to prevent water corrosion of copper. Although the Al_2O_3 ALD films covered copper uniformly with a nearly pinhole-free film, the Al_2O_3 films easily dissolved in water at 90°C. The TiO_2 ALD films had nucleation difficulties and did not completely

cover the underlying copper substrate leading to facile copper corrosion. In contrast, a composite coating formed by an Al_2O_3 adhesion layer on copper and then a TiO_2 capping layer on the Al_2O_3 adhesion layer proved to be very resistant to water corrosion.

Optical microscopy images revealed that TiO_2 capping layers as thin as ~200 Å on Al_2O_3 adhesion layers with a thickness of ~55 Å could prevent copper corrosion from water exposures at 90°C for ~80 days. Ellipsometry measurements revealed that Al_2O_3 films with a thickness of ~200 Å dissolved in water at 90°C in ~10 days. In comparison, TiO_2 capping layers with thicknesses of ~200 Å on Al_2O_3 adhesion layers with thicknesses of ~55 Å protected the underlying copper substrate for ~90 days in water at 90°C. The TiO_2 ALD coatings were also hydrophilic and facilitated H_2O wetting of copper wire mesh substrates.

5.5 Acknowledgements

This project is supported by the Defense Advanced Research Projects Agency (DARPA) Thermal Ground Plane Program, Managed by Dr. Tom Kenny (N66001-08-C-2006). The views, opinions, and/or findings contained in this article/presentation are those of the author/presenter and should not be interpreted as representing the official views or policies, either expressed or implied, of the Defense Advanced Research Projects Agency or the Department of Defense. The AES analysis was performed at the University of Minnesota Characterization Facility that receives partial support from the National Science Foundation through the National Nanotechnology Infrastructure Network (NNIN) program.

5.6 References

1. Leidheiser Jr., H., The Corrosion of Copper, Tin, and Their Alloys. 1971, New York: John Wiley and Sons, Inc.

2. Feng, Y., et al., The corrosion behaviour of copper in neutral tap water .2. Determination of corrosion rates. Corrosion Science, 1996. **38**(3): p. 387-395.

3. Feng, Y., et al., The corrosion behaviour of copper in neutral tap water .1. Corrosion mechanisms. Corrosion Science, 1996. **38**(3): p. 369-385.

4. Jeon, B., et al., Atomistic insights into aqueous corrosion of copper. Journal of Chemical Physics, 2011. **134**(23).

5. Pehkonen, S.O., A. Palit, and X. Zhang, Effect of specific water quality parameters on copper corrosion. Corrosion, 2002. **58**(2): p. 156-165.

6. Sobue, K., et al., Effect of free carbon dioxide on corrosion behavior of copper in simulated water. Surface and Coatings Technology, 2003. **169**: p. 662-665.

7. Feng, Y., et al., Corrosion mechanisms and products of copper in aqueous solutions at various pH values. Corrosion, 1997. **53**(5): p. 389-398.

8. Boulay, N. and M. Edwards, Role of temperature, chlorine, and organic matter in copper corrosion by-product release in soft water. Water Research, 2001. **35**(3): p. 683-690.

9. Lau, K.H., A. Sanjurjo, and B.J. Wood, Aluminum and alumina coatings on copper by chemical vapor deposition in fluidized bed reactors. Surface and Coatings Technology, 1992. **54**(1-3): p. 234-240.

10. Sanjurjo, A., et al., Titanium-based coatings on copper by chemical vapor deposition in fluidized bed reactors. Surface and Coatings Technology, 1991. **49**(1-3): p. 110-115.

11. Itoh, M., H. Nishihara, and K. Aramaki, A Chemical Modification of Alkanethiol Self-Assembled Monolayers with Alkyltrichlorosilanes for the Protection of Copper Against Corrosion. Journal of The Electrochemical Society, 1994. **141**(8): p. 2018-2023.

12. Itoh, M., H. Nishihara, and K. Aramaki, Preparation and Evaluation of Two-Dimensional Polymer Films by Chemical Modification of an Alkanethiol Self-Assembled Monolayer for Protection of Copper Against Corrosion. Journal of The Electrochemical Society, 1995. **142**(11): p. 3696-3704.

13. Yamamoto, Y., H. Nishihara, and K. Aramaki, Self-Assembled Layers of Alkanethiols on Copper for Protection Against Corrosion. Journal of The Electrochemical Society, 1993. **140**(2): p. 436-443.

14. Brusic, V., et al., Copper Corrosion With and Without Inhibitors. Journal of The Electrochemical Society, 1991. **138**(8): p. 2253-2259.

15. Wu, Y.C., et al., Effect of KI on Improving Copper Corrosion Inhibition Efficiency of Benzotriazole in Sulfuric Acid Electrolytes. Journal of The Electrochemical Society, 1993. **140**(10): p. 2791-2800.

16. Youda, R., H. Nishihara, and K. Aramaki, A SERS study on inhibition mechanisms of benzotriazole and its derivatives for copper corrosion in sulphate solutions. Corrosion Science, 1988. **28**(1): p. 87-96.

17. Brusic, V., M. Angelopoulos, and T. Graham, Use of polyaniline and its derivatives in corrosion protection of copper and silver. Journal of The Electrochemical Society, 1997. **144**(2): p. 436-442.

18. Cicileo, G.P., et al., Comparative study of organic inhibitors of copper corrosion. Corrosion Science, 1999. **41**(7): p. 1359-1375.

19. Tallman, D.E., et al., Electroactive conducting polymers for corrosion control Part 1. General introduction and a review of non-ferrous metals. Journal of The Electrochemical Society, 2002. **6**(2): p. 73-84.

20. Lin, Y. and H. Yasuda, Effect of plasma polymer deposition methods on copper corrosion protection. Journal of Applied Polymer Science, 1996. **60**(4): p. 543-555.

21. Patil, S., S.R. Sainkar, and P.P. Patil, Poly(o-anisidine) coatings on copper: synthesis, characterization and evaluation of corrosion protection performance. Applied Surface Science, 2004. **225**(1-4): p. 204-216.

22. George, S.M., Atomic Layer Deposition: An Overview. Chemical Reviews, 2010. **110**: p. 111-131.

23. Elam, J.W., et al., Conformal coating on ultrahigh-aspect-ratio nanopores of anodic alumina by atomic layer deposition. Chemistry of Materials, 2003. **15**(18): p. 3507-3517.

24. Dillon, A.C., et al., Surface chemistry of Al2O3 deposition using Al(CH3)3 and H2O in a binary reaction sequence. Surface Science, 1995. **322**(1-3): p. 230-242.

25. Ott, A.W., et al., Al3O3 thin film growth on Si<100> using binary reaction sequence chemistry. Thin Solid Films, 1997. **292**(1-2): p. 135-144.

26. Puurunen, R.L., Surface chemistry of atomic layer deposition: A case study for the trimethylaluminum/water process. Journal of Applied Physics, 2005. **97**(12): p. 121301.

27. Marin, E., et al., Corrosion protection of AISI 316 stainless steel by ALD alumina/titania nanometric coatings. Journal of Coatings Technology and Research, 2011. **8**(5): p. 655-659.

28. Matero, R., et al., Atomic layer deposited thin films for corrosion protection. Journal de Physique IV, 1999. **9**(P8): p. 493-499.

29. Ritala, M., et al., Growth of Titanium-Dioxide Thin-Films by Atomic Layer Epitaxy. Thin Solid Films, 1993. **225**(1-2): p. 288-295.

30. Shan, C.X., X.H. Hou, and K.L. Choy, Corrosion resistance of TiO2 films grown on stainless steel by atomic layer deposition. Surface and Coatings Technology, 2008. **202**(11): p. 2399-2402.

31. Shan, C.X., et al., Improvement in corrosion resistance of CrN coated stainless steel by conformal TiO2 deposition. Surface and Coatings Technology, 2008. **202**(10): p. 2147-2151.

32. Groner, M.D., et al., Electrical characterization of thin Al2O3 films grown by atomic layer deposition on silicon and various metal substrates. Thin Solid Films, 2002. **413**(1-2): p. 186-197.

33. Carcia, P.F., et al., Gas diffusion ultrabarriers on polymer substrates using Al2O3 atomic layer deposition and SiN plasma-enhanced chemical vapor deposition. Journal of Applied Physics, 2009. **106**(2): p. 023533.

34. Carcia, P.F., et al., Ca test of Al2O3 gas diffusion barriers grown by atomic layer deposition on polymers. Applied Physics Letters, 2006. **89**(3): p. 031915.

35. Groner, M.D., et al., Gas diffusion barriers on polymers using Al2O3 atomic layer deposition. Applied Physics Letters, 2006. **88**(5): p. 051907.

36. Cooper, R., et al., Protection of polymer from atomic-oxygen erosion using Al2O3 atomic layer deposition coatings. Thin Solid Films, 2008. **516**(12): p. 4036-4039.

37. Minton, T.K., et al., Protecting Polymers in Space with Atomic Layer Deposition Coatings. ACS Applied Materials & Interfaces, 2010. **2**(9): p. 2515-2520.

38. Dameron, A.A., et al., Gas diffusion barriers on polymers using multilayers fabricated by Al2O3 and rapid SiO2 atomic layer deposition. The Journal of Physical Chemistry C, 2008. **112**(12): p. 4573-4580.

39. Sun, Q.F., et al., Improvement of water resistance and dimensional stability of wood through titanium dioxide coating. Holzforschung, 2010. **64**(6): p. 757-761.

40. Taruta, S., et al., Effect of titania addition on crystallization process and some properties of calcium mica-apatite glass-ceramics. Journal of Non-Crystalline Solids, 2003. **321**(1-2): p. 96-102.

41. Elam, J.W., M.D. Groner, and S.M. George, Viscous flow reactor with quartz crystal microbalance for thin film growth by atomic layer deposition. Review of Scientific Instruments, 2002. **73**(8): p. 2981-2987.

42. Liu, C., Recent developments in polymer MEMS. Advanced Materials, 2007. **19**(22): p. 3783-3790.

43. Ritala, M., et al., Titanium Isopropoxide as a Precursor in Atomic Layer Epitaxy of Titanium-Dioxide Thin-Films. Chemistry of Materials, 1993. **5**(8): p. 1174-1181.

44. Elam, J.W., et al., Surface chemistry and film growth during TiN atomic layer deposition using TDMAT and NH3. Thin Solid Films, 2003. **436**(2): p. 145-156.

45. Cocke, D.L., et al., The low-temperature thermal oxidation of copper,Cu3O2, and its influence on past and future studies. Vacuum, 2005. **79**(1-2): p. 71-83.

46. Zhang, Y.D., et al., Electroplating to visualize defects in Al2O3 thin films grown using atomic layer deposition. Thin Solid Films, 2009. **517**(11): p. 3269-3272.

47. ImageJ. http://rsbweb.nih.gov/ij/. 2010.

48. Groner, M.D., et al., Low-temperature Al2O3 atomic layer deposition. Chemistry of Materials, 2004. **16**(4): p. 639-645.

49. Wind, R.A. and S.M. George, QCM Studies of Al2O3 ALD using TMA & H2O at 125C. The Journal of Physical Chemistry A, 2010. **114**: p. 1281-1289.

50. Wilson, C.A., R.K. Grubbs, and S.M. George, Nucleation and growth during Al2O3 atomic layer deposition on polymers. Chemistry of Materials, 2005. **17**(23): p. 5625-5634.

51. Aarik, J., et al., Anomalous effect of temperature on atomic layer deposition of titanium dioxide. Journal of Crystal Growth, 2000. **220**(4): p. 531-537.

52. Triani, G., et al., Low temperature atomic layer deposition of titania thin films. Thin Solid Films, 2010. **518**(12): p. 3182-3189.

53. Ye, Q., et al., Hydrophilic properties of nano-TiO2 thin films deposited by RF magnetron sputtering. Vacuum, 2007. **81**(5): p. 627-631.

54. Roach, P., N.J. Shirtcliffe, and M.I. Newton, Progess in superhydrophobic surface development. Soft Matter, 2008. **4**(2): p. 224-240.

CHAPTER VI

MOLECULAR LAYER DEPOSITION OF HYBRID ALUMINA/SILOXANE THIN FILMS

6.1 Introduction

Polymer chemistry and technology has become one of the major areas of nanotechnology and material science [1]. Without losing sight of the widespread importance of organic polymers with carbon backbones, attention is being focused increasingly toward polymers that contain inorganic elements as well as organic components. Polydimethylsiloxane (PDMS) is one of the most studied and most important inorganic polymers with regard to commercial applications [1]. Unique structural features make the siloxane backbone one of the most flexible polymers [1]. Polydimethylsiloxane has a low Young's modulus of E ≈ 750 kPa, a shear elastic modulus of G ≈ 250 kPa, a glass transition temperature of Tg ≈ -125°C, and it is thermally stable up to 350°C [2, 3]. Polysiloxanes applications include contact lenses, soft-lithography, elastomers, electrical insulators, protective coatings, microfluidics, and body implants [1, 4].

Previously, PDMS-like polymers have been deposited in the gas phase by conventional means, including hot-filament, and plasma-enhanced chemical vapor deposition techniques using cyclic siloxanes: hexamethylcyclotrisiloxane (D3) and octamethylcyclotetrasiloxane (D4) [5-8].

In this work, initial efforts were concentrated on MLD of PDMS by means of sequential exposure of the homobifunctional precursor:

bis(dimethylamino)dimethylsilane (BDMS) or the heterobifunctional precursor: dimethylmethoxychlorosilane (DMMCS) with water at reaction temperatures between 60 and 230°C. The quartz crystal microbalance growth monitor showed that during MLD growth, surface reactions would either a) terminate after ~15 cycles with mass loss after dosing stopped or b) have a negligible growth rate. Chemical vapor deposition (CVD) of PDMS was also attempted using cyclic siloxanes such as decamethylcyclopentasiloxane (D5) and hexamethylcyclotrisiloxane (D3). In this case, extended doses of D3 or D5 would typically result in a large initial mass gain and a significant mass loss after dosing was stopped. This mass reduction was very similar to that observed for BDMS/H_2O and DMMCS/H_2O systems. These poor results using cyclic siloxanes led us to take a new approach, where [-Si$(CH_3)_2$-O-] and [-Si$(C_3H_7)_2$-O-] were incorporated into growing ALD Al_2O_3 films by using DMMCS and a new precursor diisopropoylisopropoxysilanol (DIPS) respectively. This stabilized the growth of the film, preventing the mass loss that was observed for the pure PDMS MLD. In both MLD systems, inorganic backbone formation was based on a condensation step to produce [-$(R)_2$Si-O-Al-] bonds. Use of the heterobifunctional precursors DMMCS and DIPS prevented double reactions, ensuring continuation of film growth. QCM was used to examine the linearity of the MLD film growth and self-limiting behavior of the system. FTIR allowed us to identify the species formed during the surface reactions and to confirm their self-limiting behavior. Thin film characterization techniques allowed examination of the properties and composition of deposited MLD

films. X-ray reflectivity (XRR) was used to determine film growth rate, density and roughness. X-ray photoelectron spectroscopy (XPS) was employed to determine the elemental composition and level of impurities in deposited films.

In the past, many siloxane-based hybrid organic-inorganic nanocomposites have been synthesized by sol-gel techniques involving metal alkoxides and substituted silicon alkoxides [9, 10]. These materials are known to have intermediate properties between ceramic and organic materials. Some of the important applications for such materials include biocompatible coatings, contact lens materials, and photorefractive optics [11].

6.2 Experimental

The MLD films were deposited in a hot-wall viscous-flow reactor described in detail in previous publications [12]. Dimethylmethoxychlorosilane (DMMCS) with an impurity level <10% of dimethyldichlorosilane was obtained from Gelest, Inc. (Morrisville, PA, U.S.A.). The DMMCS has a vapor pressure of 25 mm Hg at 25°C, as reported by the supplier. Chromatography grade water (Honeywell Inc., Muskegon, MI, U.S.A.) was used as the water precursor. The DMMCS and H_2O were degassed using three cycles of freeze-pump-thaw before use. The diisopropoylisopropoxysilanol (DIPS) is not commercially available and was synthesized by Air Products and Chemicals, Inc. (Allentown, PA, U.S.A.). The precursor purity was 89%, and had ~11% impurities in the form of diisopropyldiisopropoxysilanol. The DIPS is a solid at room temperature, and was heated to 80°C during the experiment to attain sufficient vapor pressure. The cyclic

siloxanes D5 and D3 were obtained from Sigma-Aldrich, Inc. (Milwaukee, WI, U.S.A.). During the CVD experiments, D5 was heated to 70°C and D3 was kept at room temperature. The trimethylaluminum (TMA) used in ALD Al_2O_3 was 97% pure and was supplied by Sigma-Aldrich, Inc. (Milwaukee, WI, U.S.A.). Ultra high purity (UHP, 99.999%) grade nitrogen was used as a carrier gas to maintain the reactor's base pressure of one Torr.

The reactant pulse and purge timing is designated as (t_1, t_2, t_3, t_4) where t_1 is the silane or silanol exposure time, t_2 is the purge time after the exposure, t_3 is the water dose time, and t_4 is the purge time after the water exposure.

In situ QCM measurements were performed using AT- cut, 6 MHz resonant frequency, polished, gold-plated, quartz crystal sensors (Colorado Crystal Corporation, CO, U.S.A.). The QCM crystal was mounted in a Maxtek BSH-150 bakeable sensor housing (Inficon, NY, U.S.A.) and sealed using high-temperature conductive epoxy (Epoxy Technology, H21D Kit, MA, U.S.A.). The QCM was purged with N_2 to prevent deposition on the backside of the crystal. [12].

Pre-cut 1x1 inch size silicon wafers (Si<100>) were used as a substrate for ex situ X-ray analysis (XRR, XPS) of deposited MLD films. The silicon substrates were cleaned with acetone and isopropanol and allowed to degas and equilibrate in the MLD reactor for 30 minutes before deposition. All silicon wafers were used as purchased with a ~25 Å native silicon oxide layer.

The X-ray reflectivity (XRR) scans were performed using a Bede D1 high resolution X-ray diffractometer from Bede Scientific Inc. (Englewood, *CO,* U.S.A.).

This X-ray diffractometer is equipped with a Cu X-ray tube and monochromator for CuKα radiation at λ=1.54 Å. The XRR analysis was performed with CuKα1 radiation at λ=1.540 Å after removing the CuKα2 radiation at λ=1.544 Å using a channel cut crystal. A filament current of 40 mA and a voltage of 40 kV were used for the measurements. An XRR scan was performed using a 10 arcsec step size and a 5 s acquisition time. For each sample, the data were fit using REFS fitting software from Bede Scientific to determine the film thickness, density, and roughness.

X-ray photoelectron spectroscopy (XPS) survey scans were performed using a Physical Electronics PHI Model 5600 spectrometer with a monochromatic AlKα X-ray source with energy of 1486.6 eV. The scans were performed with electron pass energy of 187 eV and a resolution of 0.8 eV. The photoelectrons were collected using a hemispherical analyzer. XPS measurements were employed to determine the elemental composition and level of impurities in deposited films.

The FTIR studies of alumina/siloxane MLD using DMMCS were performed at 180°C in a hot-wall viscous flow reactor equipped with an Nicolet Nexus 670 FTIR spectrometer [13]. The FTIR measurements for the MLD system using DIPS were performed at 150°C in a hot-wall viscous flow reactor equipped with a Nicolet Magna 560 FTIR spectrometer [14]. In both cases high surface area, spherical ZrO_2 nanoparticles were used as a substrate to achieve a high signal to noise ratio. The nanoparticles had an average diameter of 30 nm, and were supplied by Sigma-Aldrich, Inc. (Milwaukee, WI, U.S.A.). Nitrogen flow maintained the base pressure

of the systems at about one Torr. The ZrO_2 nanoparticles and QCM crystals were pre-coated with ALD Al_2O_3 prior to MLD deposition for good initial nucleation.

6.3 Results and Discussion

6.3.1 MLD of Polydimethylsiloxane (PDMS)

The MLD of PDMS was explored using either bifunctional: bis(dimethylamino)dimethylsilane (BDMS) or heterobifunctional: dimethylmethoxychlorosilane (DMMCS) and water. Figure 6.1 shows QCM data for 60 cycles of the BDMS/H_2O MLD deposited using a 1,30,1,30 timing sequence at 150°C on ALD Al_2O_3 surface. The mass gain spike observed in the QCM data during the BDMS dose is attributed to the temperature difference between the quartz crystal and the precursor [15]. Figure 1 also shows that after about 30 BDMS/water cycles, the film growth terminated and total mass gain leveled off at ~78 ng/cm^2. After 60 cycles the dosing was stopped and the film was left at the base pressure for equilibration. During that period about 34 ng/cm^2 of the initial total mass gain was lost during this purge time of approximately 1500 s. ~44 ng/cm^2 of grown film remained. The MLD BDMS/H_2O growth was investigated at reaction temperatures between 120 and 200°C, where slight or no change in growth behavior was observed. In this temperature range, the resulting mass gain after the final long purge would typically be between 50 and 150 ng/cm^2. A similar result was observed when MLD PDMS was attempted using DMMCS and H_2O chemistry.

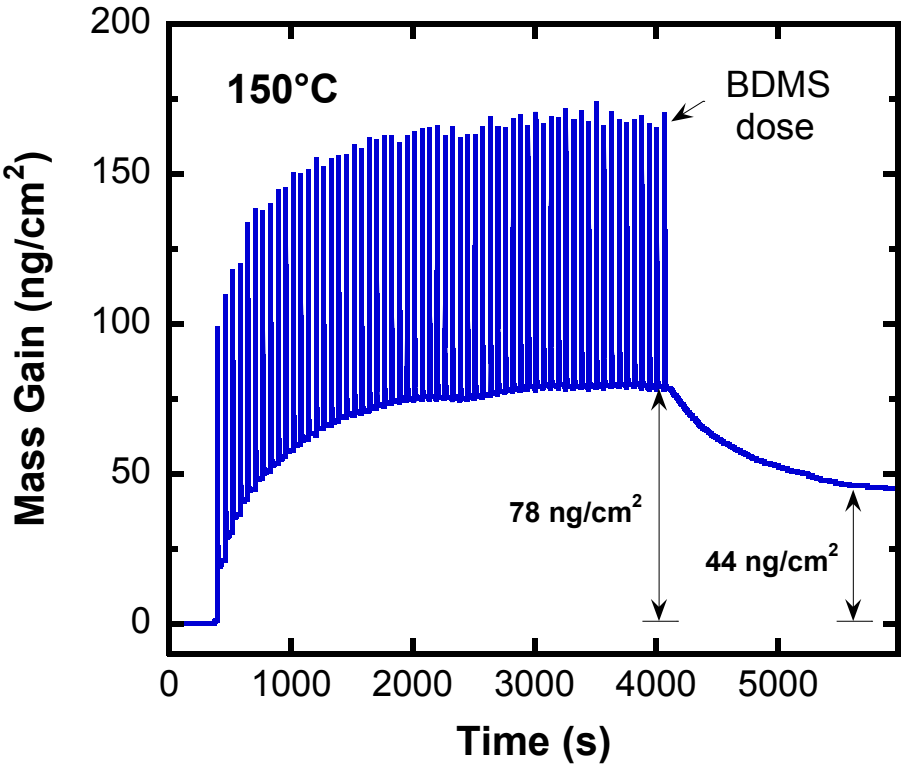

Figure 6.1 QCM signal during PDMS MLD using BDMS/H_2O chemistry at a 150°C reaction temperature.

CVD deposition of PDMS was attempted using cyclic siloxanes D5 and D3. In this experiment thin films were deposited by means of extended exposure of D5 or D3. Continuous growth of PDMS was expected by means of constant ring opening polymerization during exposure. Figure 6.2a shows the QCM mass change during 200 s long doses of D3 at 120, 150, and 200°C on pre-deposited ALD Al_2O_3. QCM mass gain during 400 s long doses of D5 at 120 and 200°C on ALD alumina surface are depicted on Fig. 6.2b. D3 is a more strained molecule than D5, therefore, higher growth rate was expected for D3 [16]. However, as shown in Fig. 6.2a, 200 s dose times of D3 resulted in a total mass gain of only ~50 ng/cm^2 at 120, 150, and 200°C and continuous growth was not observed. The D5 exposure initially resulted in a

high mass gain of about 300 ng/cm² at 200°C, however, 50% of this mass gain was lost after the exposure was stopped.

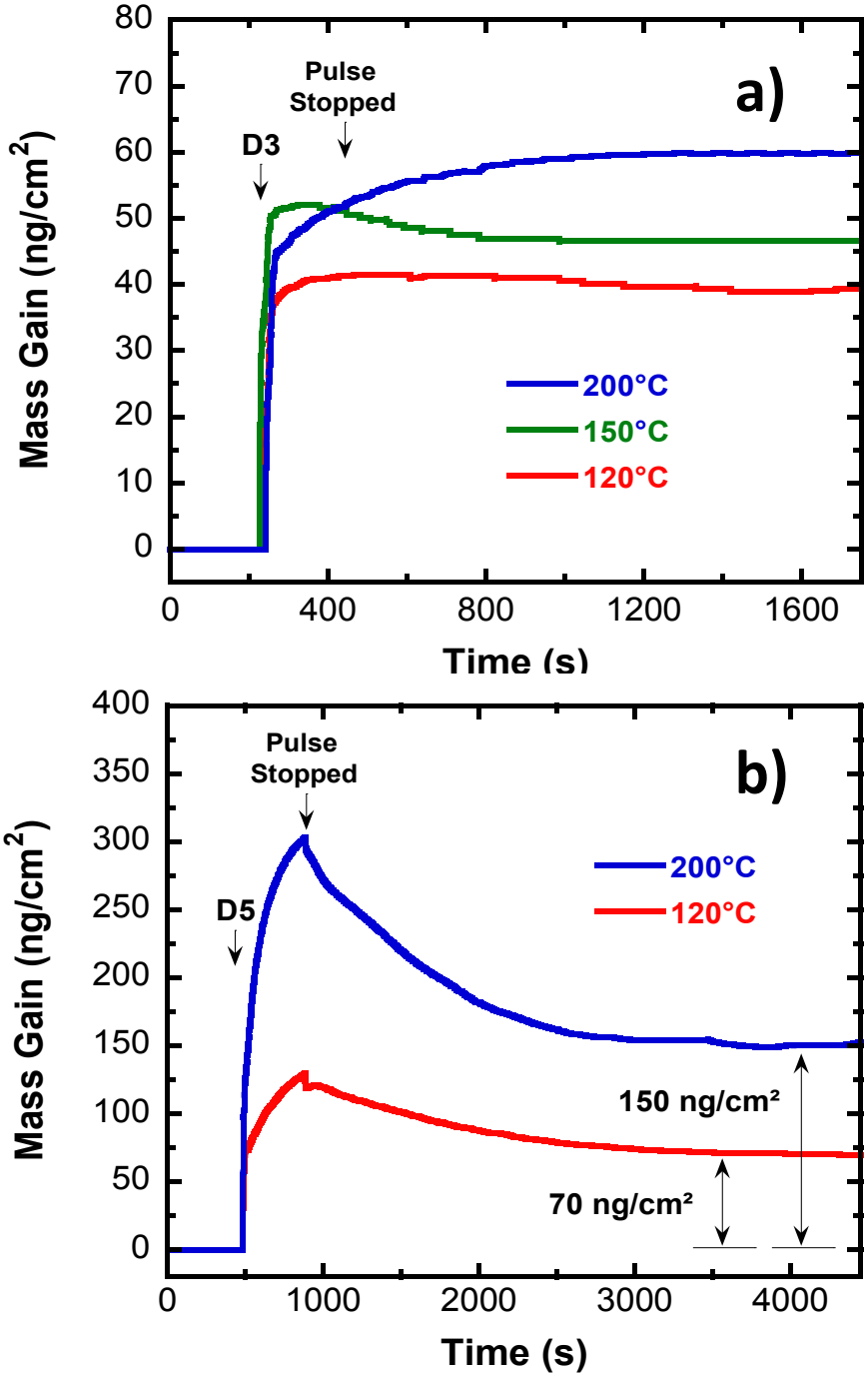

Figure 6.2 QCM signal during PDMS CVD with 200 s long dose times of D3 (a); and 400 s long dose times of D5 (b) deposited on ALD Al_2O_3.

Therefore, we conclude there is no significant difference in the growth behavior between D3 and D5 from 100 to 200°C. Both systems showed low total mass gains with D3 mass gains generally lower than D5. Similar with the MLD process, the resulting mass gain was between 50 and 150 ng/cm^2, for a similar temperature range, which corresponds to a film thickness on the order of several monolayers.

MLD and CVD films grown at 90°C showed no mass losses after the precursor dosing was stopped. Nevertheless, the growth rates at this temperature were negligible after an initial ~50 ng/cm^2 was deposited. For the CVD process, this agrees with previous reports where slow CVD of PDMS was achieved using D3 and water at 80°C on various oxide surfaces [8]. However, it has been previously reported that, at this temperature, unreacted cyclic molecules were detected by FTIR indicating a condensation type reaction [17, 18]. No film growth during MLD or CVD of PDMS was observed for a reaction temperate of 60°C.

The mass losses observed in Figures 6.1 and 6.2 are attributed to PDMS surface depolymerization via leaving groups in the form of cyclic oligomers [19]. Depolymerization via cyclisation is observed in solution-based PDMS synthesis as well as high temperature decomposition and is believed to be governed by ring-chain equilibrium thermodynamics [20].

6.3.2 Growth of Hybrid siloxane/alumina MLD using DMMCS

A hybrid alumina/siloxane film was deposited using an ABCD four step process with an overall precursor dosing scheme shown in Figure 6.3.

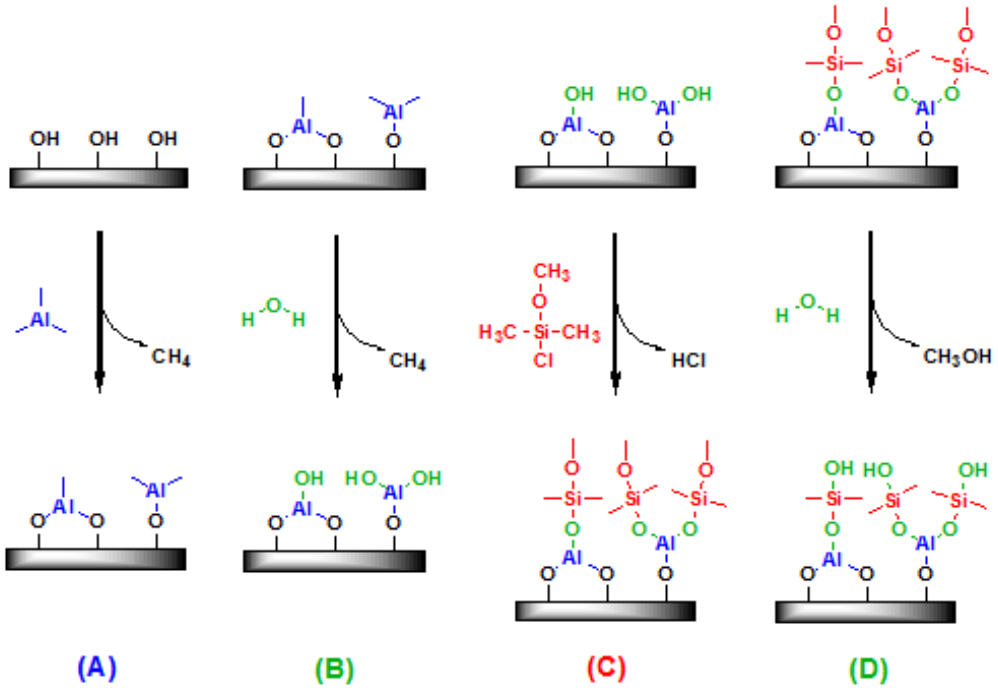

Figure 6.3 Schematic representation of alumina/siloxane MLD using the DMMCS four step deposition process.

This reaction sequence introduces the -Si$(CH_3)_2$-O- linkage into the growing alumina film. The addition of TMA adds -Al-O- subunits into the growing chain and prevents desorption of cyclic siloxanes. The TMA could be introduced during every reaction cycle. The TMA could also be introduced less frequently to grow longer [-Si$(CH_3)_2$-O-]$_n$ chains before inserting the -Al-O- subunit.

Figure 6.4a presents the QCM response during multi-dose deposition of a hybrid film using DMMCS at 200°C. This figure shows that growth of the MLD hybrid film is linear and reproducible. Figure 6.4b shows a closer view of the QCM signal during the steady state growth regime. The pulse/purge timing for one MLD cycle consisted of two 1.5×10^5 L (1 Langmuir (L) = 10^{-6} Torr ·s) consecutive TMA

pulses followed by two 1×10^5 L pulses of water, two 0.8×10^5 L of DMMCS doses, and then two 0.5×10^5 L of water pulses.

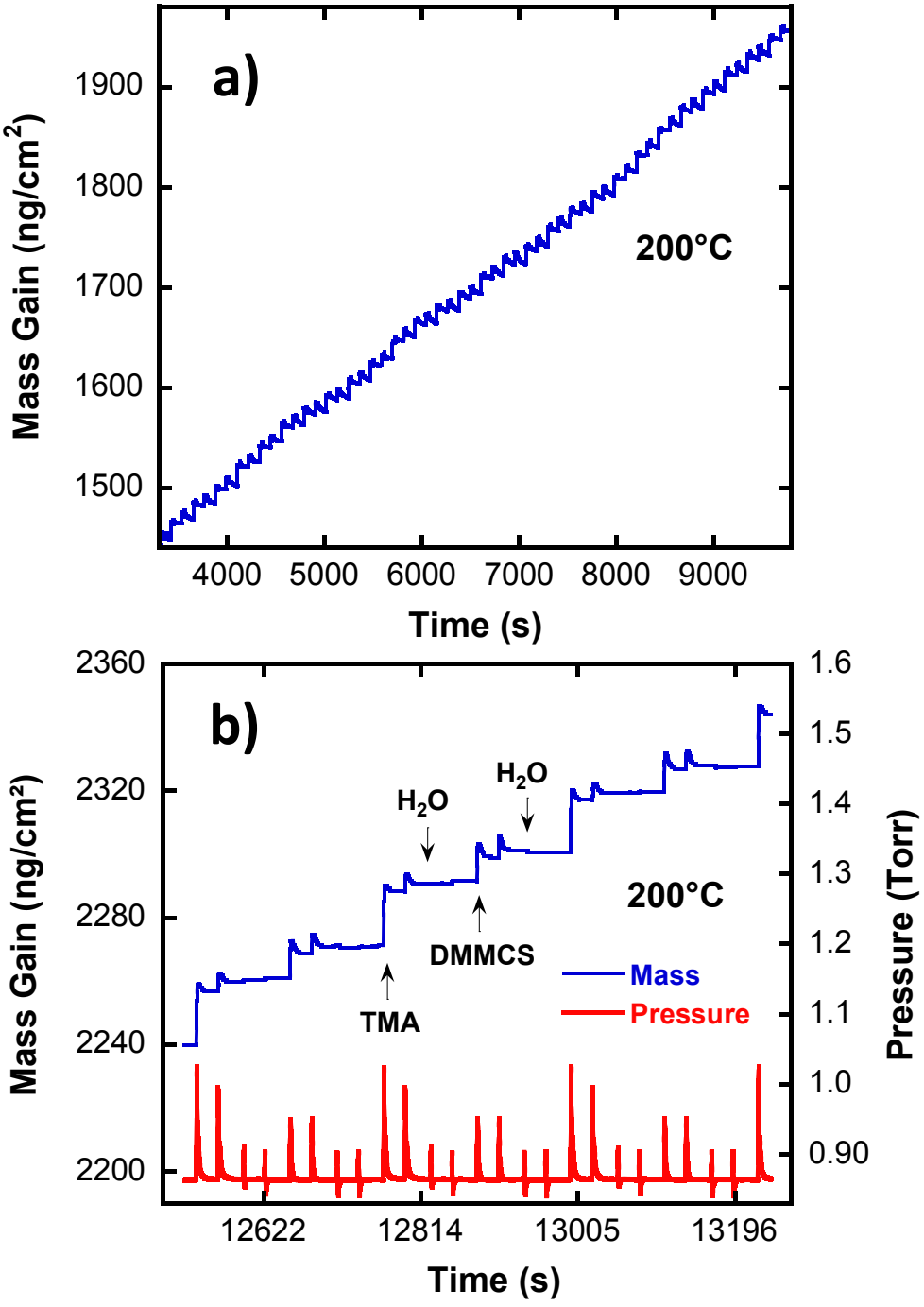

Figure 6.4 QCM results for the four step alumina/siloxane MLD using DMMCS. (a)

Growth over 30 reaction cycles, (b) expanded view of growth during three reaction cycles.

Each dose was separated by a 25 s purge time. The dose quantities were determined from the partial pressures of individual pulses. In the multi-dose growth regime, the precursor surface saturation was determined with the QCM by monitoring the mass gain following multiple pulses until negligible or no mass change was observed. Figure 4b shows that most of the precursor reacted during the first dose and the second dose results in only a small additional mass increase. Here, two 1 s doses of TMA result in a mass gain of ~15 ng/cm^2, and two one second doses of DMMCS result in ~6 ng/cm^2 with a total mass gain of ~21 ng/cm^2. A typical mass gain of ~35 ng/cm^2 at 177°C is observed during TMA/H_2O dose for aluminum oxide ALD [12]. We observe a lower aluminum oxide ALD growth than expected. This is attributed to a loss of density of reactive surface states due to DMMCS surface modification. The H_2O exposures were necessary but did not produce noticeable mass changes. All of the alumina/siloxane MLD films deposited using DMMCS were grown using a multi-dose precursor dosing arrangement with 25 s purge times as described above unless stated otherwise.

Film thicknesses versus number of MLD cycles were studied for films grown at 120 and 200°C (not shown). These films were deposited on silicon wafers and film thicknesses were determined from XRR. The thickness measurements revealed that at 120°C, the growth rate gradually increased with increasing numbers of cycles before reaching ~1.2 Å/cycle for a 300-cycle run. In contrast, at

200°C the growth rate was independent of the number of cycles and remained constant at the value of 0.9 Å/cycle. However, a thickness gradient of about 12 % between front and back samples in the direction of flow in the reactor was observed for the films deposited at 120 °C during a 300 cycle run, indicative of a non-ideal condensation-type reaction. At 200°C, this thickness difference is only 5%. The RMS roughness measured for the films deposited at 120°C was 7 Å, versus 4.5 Å for the films deposited at 200°C. The density of the deposited films at 200°C was around 2.3 g/cm^3. This value is 23% lower than the density of ALD Al_2O_3 of 3.0 g/cm^3 deposited at 180°C [21].

Film thickness measurements were also used to monitor stability of the MLD films in air. Stability tests were performed for a 145 Å thick film deposited at 200°C on a seed layer of alumina. The changes in the Bragg peaks of the sample after ninety days of exposure to air indicated a 10 % increase in total film thickness.

The XPS compositional analysis of the 145 Å films deposited at 200°C showed that these films have an average atomic concentration of 44.6 % oxygen, 18.7 % carbon, 4.5 % silicon, and 32.3% aluminum. The uncertainty in these values is < 2 at. %. These atomic percentages are based on peak areas of each component extracted from an XPS survey scan. The ratio of silicon to carbon is 1 to 4, which is higher than expected from the DMMCS structure. This could be explained by the presence of adventitious carbon on the surface. The Al:O ratio is close to 2:3, which suggests formation of some Al_2O_3 during MLD. The atomic concentration of Si is consistent with the relative mass gain of DMMCS observed during QCM

measurements. Also, XPS showed that deposition temperatures below 180°C result in films with ~2 % chlorine impurities, whereas for films deposited at higher temperatures the chlorine level is below the detection limit (< 0.1 %).

The presence of chlorine impurities in the film suggests poor reactivity of the Si-Cl in DMMCS with hydroxylated surfaces for the lower deposition temperatures. This is also indirectly supported by the high roughness of the films deposited at 120°C, as mentioned earlier. High film roughness and the film gradient along the reactor are indicative of a CVD type reaction. Therefore, the Si-Cl reaction with the hydroxylated surface is one of the limiting factors during low temperature deposition. Consequently, the optimal temperature to grow MLD films using DMMCS is believed to be 180°C or higher.

The growth of MLD films was also studied using in situ FTIR at 180°C. FTIR spectra were recorded after various numbers of MLD cycles and after each reactant exposure. The change in surface species during each reactant dose was monitored by the FTIR difference spectra. The surface species that are added appear as positive absorbance features and the surface species that are removed appear as negative absorbance features. Figure 6.5 displays the FTIR spectra following the TMA, water, DMMCS, and a second water exposure during first MLD cycles. Each presented spectrum is referenced to the previous spectra. The FTIR difference spectrum of the first TMA exposure is referenced against the base Al_2O_3.

Deposition of the MLD hybrid material starts with exposure of TMA. Figure 8a shows the effects of TMA exposure on a hydroxylated Al_2O_3 surface. The features

at 2927, 2852, and 2820 cm^{-1} wavenumbers are assigned to the antisymmetric -CH_3, symmetric -CH_3, and Fermi resonance of methyl groups [14].

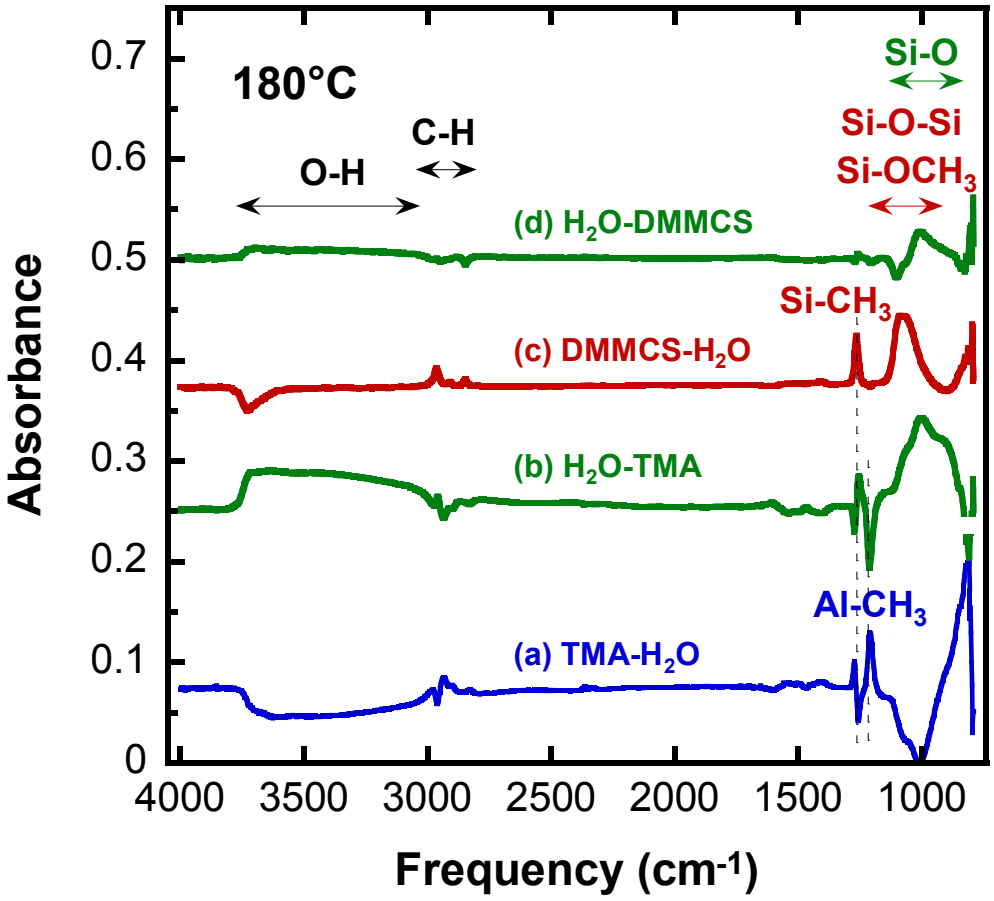

Figure 6.5 In situ FTIR difference spectra after TMA, H_2O, and DMMCS exposures during hybrid MLD film growth at 180°C. a) TMA-H_2O after TMA exposure on a film previously reacted with H_2O, b) H_2O-TMA after H_2O exposure on a film previously reacted with TMA, c) DMMCS-H_2O after DMMCS exposure on a film previously reacted with H_2O, and d) H_2O-DMMCS after H_2O exposure on a film previously reacted with DMMCS.

A strong peak at 1212 cm^{-1} is the symmetric methyl deformation of aluminum-methyl groups. A broad negative band at 3770-3500 cm^{-1} is consistent with the loss

of hydroxyl species on Al_2O_3. This FTIR measurement matches other studies of TMA adsorption on oxide surfaces. The TMA dose functionalizes the surface providing reactive sites for the subsequent water pulses.

The second step is formation of a hydroxyl-terminated surface by water exposure to provide reactive sites for DMMCS. Figure 6.5b is a mirror image of Figure 6.5a, showing loss of methyl groups at 2800 and 1212 cm^{-1} and the rise of a broad feature showing the O-H stretch of hydroxyl groups around 3770-3500 cm^{-1} after dosing water.

A difference spectrum taken after a saturating DMMCS exposure is presented in Figure 6.5c. Positive features appear in the 3000–2800 cm^{-1} range. These peaks are linked to the presence of $-CH_3$ on the surface. Other features support the presence of methyl groups on the surface as well. There is an important peak at 1260 cm^{-1}, showing Si-methyl deformation [22-24]. Finally, a broad positive peak appears at 1190 cm^{-1}. This is assigned to the O-C stretching modes of the methoxy group and the Si-O stretching modes [22-24]. The presence of Si-Cl species at 625 to 425 cm^{-1} cannot be confirmed since this frequency is outside of the detection range of the FTIR instrument [22-24]. Chlorinated surfaces can be formed if methoxy groups preferentially react with the hydroxylated surface. Preferential reaction of the Si-Cl end of the DMMCS molecule versus $Si-OCH_3$ may result from the difference in reported bond energies of 95 and 123 kcal/mol respectively [25].

The final step in this MLD cycle is the hydroxylation of the methoxy group on the DMMCS terminated surface by a second water exposure step. As a result of

water dosing, methoxy groups should be substituted by hydroxyl groups for the next TMA reaction in a new cycle. Figure 5d shows an increase in the vibrations around the 3500 cm^{-1} region, indicating an increase in -OH features on the surface. The negative feature at 1190 cm^{-1} indicates loss of methoxy groups.

Hybrid MLD films contain many vibrational modes that can be used to monitor the self-limiting nature of the DMMCS, TMA, and water reactions. Saturation behavior of the FTIR Si-CH_3 and O-H plotted as integrated absorbance versus of number of DMMCS and H_2O microdoses, indicated self-limiting reactions.

6.3.3 Growth of Hybrid siloxane/alumina MLD using DIPS

Figure 6.6 depicts the three step deposition process of alumina/siloxane MLD using diisopropoylisopropoxysilanol (DIPS) as a siloxane precursor.

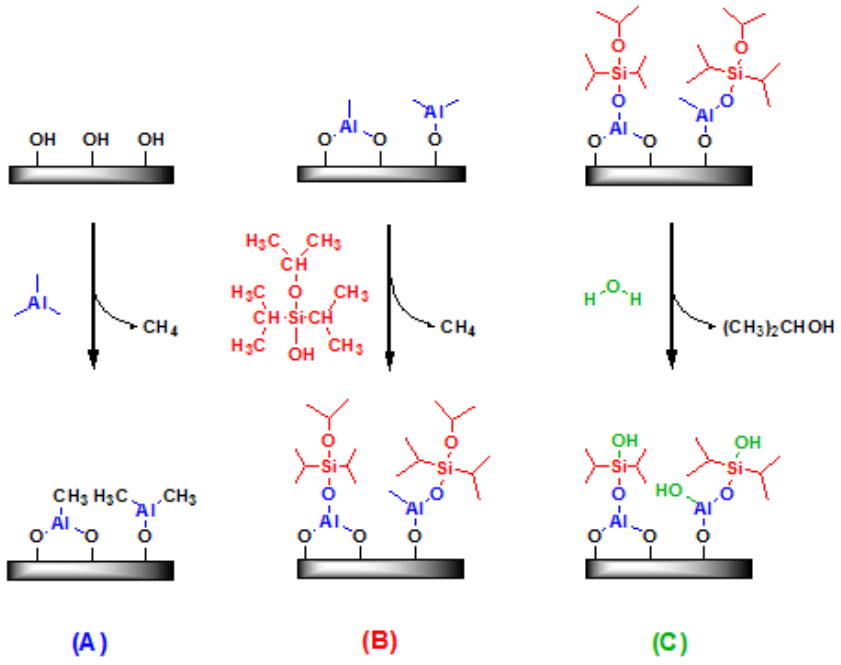

Figure 6.6 Schematic representation of precursor dosing arrangement during the three step alumina/siloxane MLD process using DIPS.

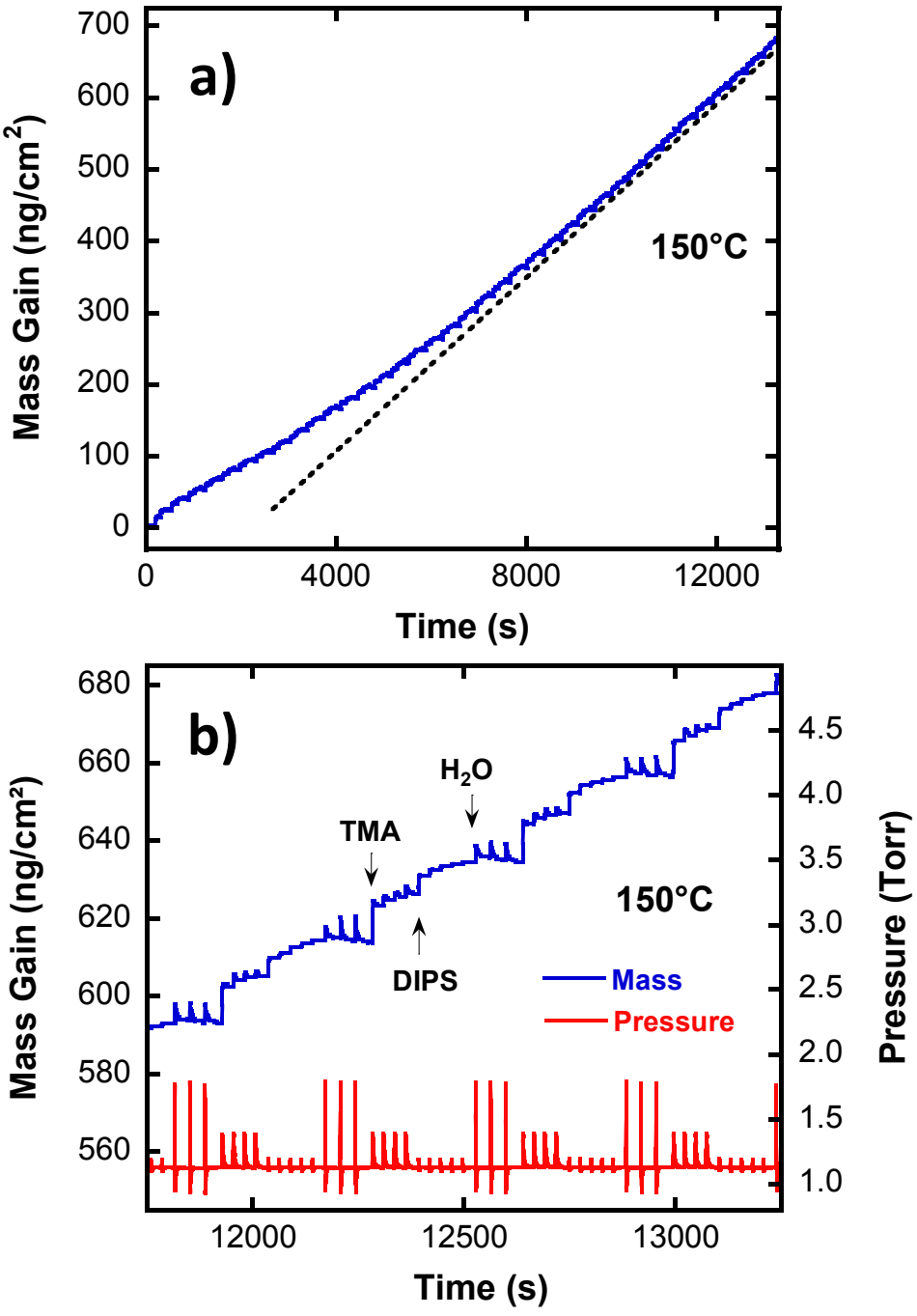

Figure 6.7 QCM results for the three step MLD process using DIPS. (a) Growth over 50 reaction cycles; (b) expanded view of growth during three reaction cycles.

The film growth is reproducible and linear after the initial nucleation period. An expanded QCM profile showing individual mass gains after DIPS, TMA and water pulses at 150°C reaction temperature is presented in Figure 6.7b. The multi-dose pulse/purge timing for one MLD cycle consisted of four 2.5×10^5 L consecutive TMA pulses followed by five 1×10^5 L pulses of DIPS and three 1.5×10^5 L water pulses, where pulses, separated by 25 sec purge times. Figure 6.7b shows that reactions on the surface are self-limiting and precursor multi-dose conditions ensure surface saturation. The total mass gain during a single MLD cycle in the steady state growth regime is 22.3 ng/cm^2. This value is similar to the total mass gain of 21 ng/cm^2 observed in the MLD process using DMMCS at 200°C. In both cases the water dose did not produce a significant change in mass.

QCM showed the mass gain from DIPS to change from 75.5 ng/cm^2 for the first cycle to 22.3 ng/cm^2 for the twentieth cycle. After twenty cycles, the mass increase per cycle during TMA and DIPS deposition remained constant, though a gradual increase in mass gain during the water doses was observed. This is attributed to an increase in water absorption by the bulk of the film that is low density due to the steric effect of large isopropyl ligands on silanol. Both DIPS and DMMCS based MLD systems produce large mass gains during the first cycle on pre-deposited alumina surfaces, consistent with a substrate-enhanced nucleation mechanism [26]. Therefore, during the nucleation stage of deposition, the film is more polymer-like, and becomes closer to Al_2O_3 during steady state growth. Both

DMMCS and DIPS MLD systems exhibit lower growth rates during steady state than ALD aluminum oxide grown using TMA and H_2O.

XRR showed that MLD films deposited on silicon wafers using DIPS at 150°C have a growth rate of 1.2 Å/cycle and a density of 2.0 g/cm^3. These films were grown on predeposited 40 Å thick ALD alumina. This growth rate is consistent with the corresponding QCM growth rate value. This MLD system exhibits a higher growth rate than the 0.9 Å/cycle obtained for the DMMCS system at 200°C. The density of the film deposited using DIPS (2.0 g/cm^3) is lower than the 2.3 g/cm^3 found for DMMCS hybrid films. This can be explained by differences in steric effects of large isopropyl groups is silanol compared to the smaller methyl groups in silane.

The roughness of MLD films deposited using DIPS is ~5 Å (RMS). This is similar to DMMCS hybrid films. This roughness is higher compared to ALD alumina but similar to previously reported MLD films [27]. Ninety days exposure of the MLD films to air resulted in a 0.4 % film thickness increase for the film deposited using DIPS. This is lower than the 10.0 % thickness increase change for the DMMCS system. Therefore, MLD films deposited using DIPS chemistry exhibit higher stability. It is possible that the robustness of the DIPS hybrid films is a result of more favorable chemistry and therefore less trapping of unreacted TMA molecules in the film. The presence of unreacted TMA species is believed to be a contributing factor in the increase in film thickness.

XPS showed the composition of the hybrid film deposited using DIPS to be 36.8 % oxygen, 35.7 % carbon, 5.3 % silicon, and 22.2 % aluminum. The ratio of Si to C is about 1:7, which is expected because of the structure of the DIPS precursor. Also, the Al to O ratio is close to 2:3, suggesting the presence of Al_2O_3. The concentration of silicon in the film is consistent with the QCM mass gains observed for the siloxane doses.

The alumina/siloxane hybrid MLD using DIPS was also studied using in situ FTIR at 150°C. The FTIR spectra were recorded after various numbers of MLD cycles, showing the progressive growth of the hybrid film. Figure 6.8 displays the FTIR spectra following the DIPS exposures after 2, 4, 6, 8, 10, 12 and 15 MLD cycles at 150°C. All spectra are referenced to the Al_2O_3 base layer deposited at 150°C. The deposited film causes the infrared absorbance to progressively increase with the number of MLD cycles. With each cycle, features from 3000-2800 cm^{-1} increase, indicating the addition of C-H stretches to the surface. Five prominent peaks are observed in Fig. 9 at 2971, 2950, 2929, 2901, and 2872 cm^{-1}. These peaks are attributed to C-H stretching vibrations from both $-CH_3$ and -CH surface features [28, 29]. As the C-H features grow, a concurrent increase is observed at 1436, 1388, 1366, and 1252 cm^{-1}. These features are assigned to the symmetric $-CH_3$ deformation, two isopropyl deformations, and a silicon-isopropyl deformation [28, 30].

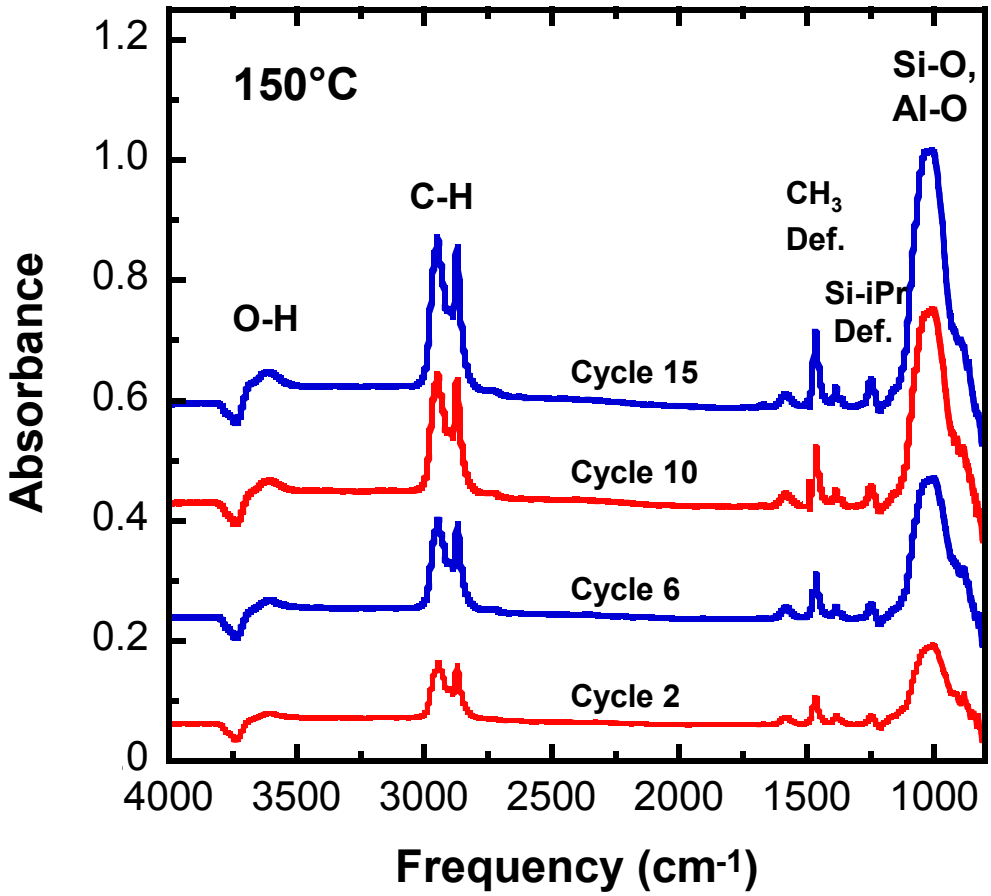

Figure 6.8 FTIR spectra showing growth of hybrid MLD films grown using DIPS after 2, 6, 10, and 15 MLD cycles at 150°C.

The peak at 1252 cm^{-1} is the Si-isopropyl deformation. This peak is unique to silicon-carbon bonds and is not found in the isopropoxy groups. All of these features indicate that the growing MLD film is incorporating more silicon-isopropyl linkages as it deposits. Finally, a strong band below 1100 cm^{-1} also increases in intensity with cycle number. This band has contributions from the Al-O phonon, and transverse optical (TO) Si-O mode, indicating that inorganic components of the film are growing along with the organic features [31, 32]. Finally, the absorbances from 3800-3500 cm^{-1} progressively redshift as the number of MLD cycles increases. This

indicates a transition in the hydroxyl species from the original Al_2O_3 surface to the new siloxane MLD film [33].

The change in surface species during each reaction can be monitored by the FTIR difference spectra shown in Fig. 6.9. This figure shows FTIR difference spectra for the three reaction steps during the 12th MLD cycle at 150°C. The sequential reactions are shown in Figures 6.9a-c. The surface species that are added appear as positive absorbance features and the surface species that are removed appear as negative absorbance features. The FTIR difference spectra for the first TMA exposure referenced against the base Al_2O_3 (TMA-Base), the DIPS exposure referenced against the TMA exposure (DIPS-TMA) and the water exposure referenced against the DIPS exposure (Water-DIPS) are shown in Figures 6.9a-c, respectively. The TMA functionalizes the surface to provide reactive sites for DIPS. Figure 10a shows the effects of TMA on the starting hydroxylated Al_2O_3 surface. Positive features appear at 2927, 2852, and 2820 cm^{-1}. These features are assigned to the antisymmetric CH_3, symmetric CH_3, and Fermi resonance of methyl groups [14]. A strong peak appears at 1212 cm^{-1}, which is the symmetric methyl deformation of aluminum-methyl groups. A broad negative band is observed in Figure 6.9a at 3770-3500 cm^{-1}. This feature is consistent with the loss of hydroxyl species on Al_2O_3. These results match other infrared studies of TMA adsorption on oxide surfaces, indicating that TMA interacts with a hydroxylated surface to produce a methyl-terminated surface. The DIPS is able to react with the methyl-terminated surface, creating an isopropyl and isopropoxy-terminated surface.

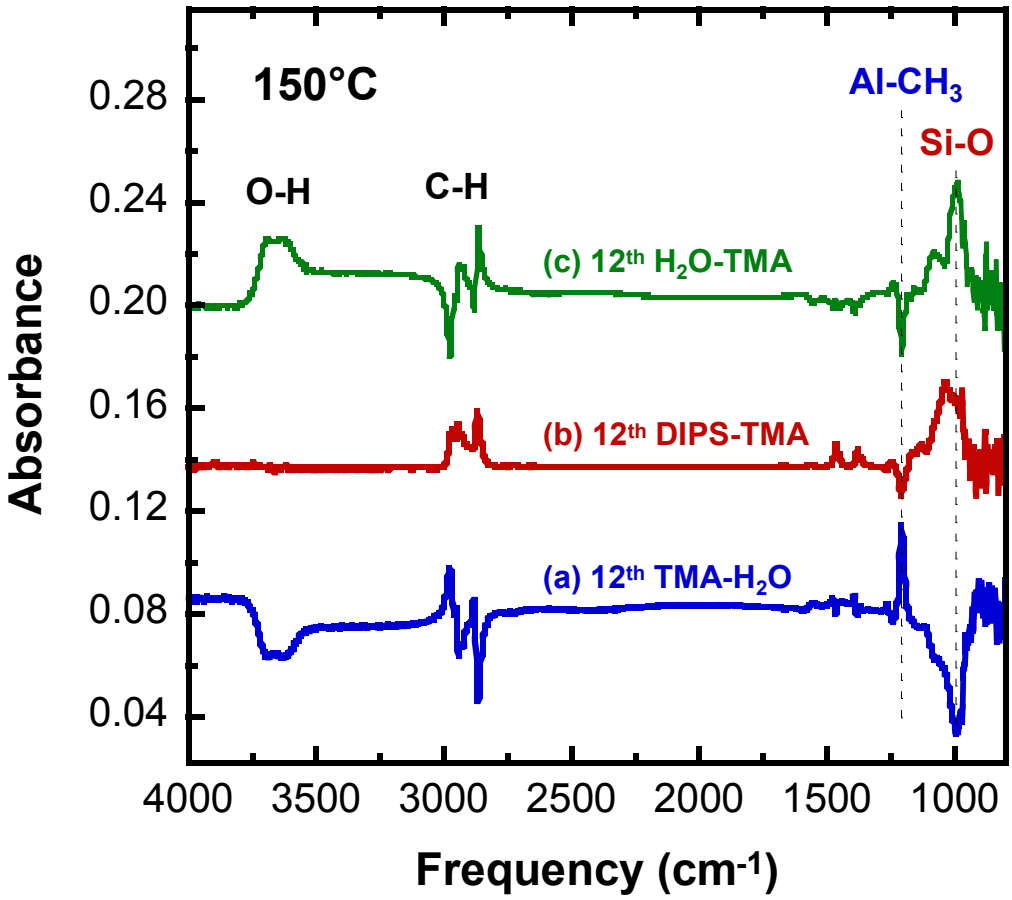

Figure 6.9 FTIR difference spectra after TMA, H_2O, and DIPS exposures during MLD film growth at 150°C. a) TMA-H_2O after TMA exposure on a film previously reacted with H_2O, b) DIPS-TMA after DIPS exposure on a film previously reacted with TMA, and d) H_2O-DIPS after H_2O exposure on a film previously reacted with DIPS.

A difference spectrum taken after a saturating DIPS exposure is presented in Figure 6.9b. Positive absorbances appear in the 3000–2800 cm^{-1} range. These peaks are linked to the presence of CH_3 and CH groups on the surface. Many smaller features support the presence of isopropyl groups on the surface. These are the peaks at 1466, 1383, and 1369 cm^{-1}. The most important peak, however, is the

Si-isopropyl deformation at 1252 cm^{-1}. This peak is unique to silicon-carbon bonds and is not found in the isopropoxy groups. Finally, broad positive peaks appear from 1171–1036 cm^{-1}. These are assigned to the C-O stretching modes of the isopropoxy group and the Si-O stretching modes.

Figure 6.9b confirms that the silanol end of the DIPS molecule is reactive to the methyl-terminated surface. The absence of any features from 3700-3300 shows that no hydroxyl groups are added after DIPS exposure. Hydroxyl groups could be formed if the isopropoxy group of DIPS was reactive with the methyl groups on the surface. They could also be formed if DIPS underwent condensation reactions either in vacuum or upon adsorption. Condensation reactions would replace the isopropoxy group with silanol functionality. A strong negative peak is observed at 1212 cm^{-1} in Figure 6.9b. This peak has been assigned to the Al-CH_3 groups, showing that they are removed after DIPS exposure. It would be difficult to isolate the Al-CH_3 features based on the C-H stretching region alone since DIPS has significant C-H stretching features. Figure 6.9b also shows that 65% of the original concentration of Al-CH_3 has been removed by DIPS. This incomplete reaction may be explained by the steric size of the isopropyl groups blocking available aluminum-methyl features on the surface. This effect would be more pronounced when DIPS reacts with dimethylaluminum species than with monomethylaluminum species.

The final step of siloxane MLD is the formation of a hydroxyl-terminated surface by water exposures. Figure 6.9c looks like a near-mirror image of Figure 6.9b. There is some loss of the vibrations in the 3000–2800cm^{-1} region, indicating

the displacement of C-H features from the surface. Two features in the Figure 6.9b link the loss of these C-H features with the loss of isopropoxy groups on the surface and not removal of isopropyl groups. Isopropoxy groups bound to silicon have two unique peaks at 1170 and 1130 cm^{-1} while isopropyl groups bound to silicon have a prominent peak at 1250 cm^{-1}[28, 34]. Figure 6.9c shows a loss of the 1170 and 1130 cm^{-1} peak and no change in the 1250 cm^{-1} peak, showing that the isopropoxy groups have been lost [29]. The other major negative peaks in Figure 6.9c are deformation modes that are present in both isopropyl and isopropoxy surface groups. The major vibrational features in Figure 6.9 are collated with their assignments in Table 6.1.

Water also interacts with the remaining aluminum-methyl features to create a mixed hydroxylated surface. Figure 6.9c shows a loss of the Al-CH_3 deformation mode at 1212 cm^{-1}. This loss added to the loss in Figure 6.9b, equals the amount of Al-CH_3 gained in the TMA step. Water reacts with the blocked methyl groups on the surface to form Al-OH species. Also, a broad positive peak appears from 3650-3500 cm^{-1}. This feature is attributed to hydroxyl groups bound to silicon and aluminum. This shows that a condensation reaction occurs between the silicon-isopropoxy groups and water, forming silanol surface species. Finally, two broad peaks at 1050 and 1000 cm^{-1} indicate the formation of R_2Si-O and Al-O linkages [29]. There are no broad peaks at 1240 cm^{-1}, which would be the LO phonon mode of silicon dioxide. This shows that the DIPS precursor does not cross-link once it has adsorbed on the surface [29]. Figure 6.9 shows that the siloxane

MLD sequence has created a layer of hydroxyl-terminated film that contains Al-O groups and Si-O linkages with attached organic functionalities.

Experimental (cm^{-1})	Literature (cm^{-1})	Assignment
2971	2968	ν as CH_3 (OP) [34, 35]
2950	2938	ν as CH_3 (IP) [34, 35]
2929	2935	ν CH[35]
2872	2866	ν s CH_3 (OP) [34, 35]
2901	2911	ν s CH_3 (IP) [34, 35]
1580	1612	Weak impurity[27]
1466	1463	δ as CH_3[34, 35]
1383	1376	δ s CH_3 Iso[28, 34]
1369	1362	δ s CH_3 Iso[28, 34]
1252	1250	δ Si-CH [27, 28]
1171	1161	ρ s CH_3 + νSi-O[27, 34]
1130	1125	ν C-O[27, 28, 35]
1036	1024	ν C-O[27, 28, 34, 35]
1000	1000	ρ Si-CH [27, 28]
>1000	1000-900	ν Si-O-Al [27, 28]
2945	-	ν as Al-CH_3
2902	-	ν s Al-CH_3
2829	-	ν CH_3 + δ s CH_3
1433	-	δ as Al-CH_3
1210	-	δ s Al-CH_3

Table 6.1 Vibrational frequencies observed in the FTIR difference spectra in Fig. 6.9 after the DIPS, TMA and H_2O exposures and their assignments.

These infrared studies confirm the mechanism for siloxane MLD shown in Fig. 6.6. FTIR analysis shows that the DIPS precursor adds to the surface through its silanol group, leaving two isopropyl groups and an isopropoxy group on the surface. Some Al-CH_3 groups were left unreacted due to the steric bulk of the isopropyl group. The water reaction converted both the isopropoxy groups and Al-CH_3 groups to hydroxyl species that were reactive to TMA. As the film grew, the Al-O, Si-O, C-H, and Si-C vibrations increased.

The self-limiting nature of the DIPS, TMA, and water reactions were monitored using FTIR vibrational modes. Figure 6.10a presents the integrated absorbance of the O-H and C-H stretch and Al-CH_3 deformation versus TMA exposure. This figure shows that TMA reaction self-limits at an exposure of 0.84 Torr sec. The water and TMA exposures in siloxane growth are roughly the same as that for saturating alumina growth on nanoparticles [35]. A DIPS reacts with the methyl-terminated surface, creating an isopropyl and isopropoxy-terminated surface. The integrated absorbance for the CH stretching, Al-CH_3 and Si-isopropyl deformations versus DIPS exposure is shown in Figure 6.10b. This figure shows that the DIPS reaction is self-limiting and reaches completion after 0.24 Torr·sec exposure of DIPS. It would be difficult to isolate the Al-CH_3 features based on the C-H stretching region alone since DIPS has significant C-H stretching features. Figure 6.10b indicates that 65% of the original concentration of Al-CH_3 has been removed by DIPS. This incomplete reaction may be explained by the steric size of the isopropyl groups blocking available aluminum-methyl features on the surface.

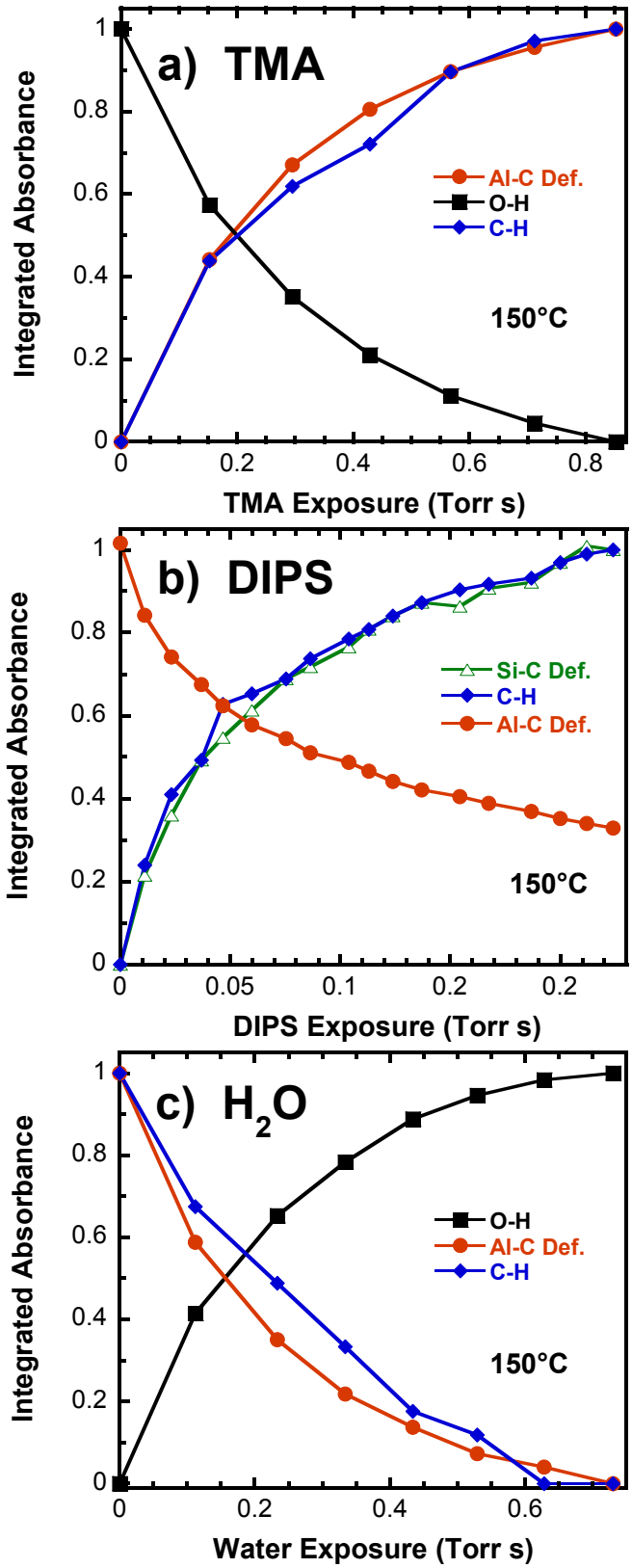

Figure 6.10 Integrated absorbance for a) Al-C deformations versus number of TMA

microdoses, b) Si-C deformations versus number of DIPS microdoses, and c) O-H stretching vibrations versus number of H_2O microdoses at 150°C.

This effect would be more pronounced when DIPS reacts with dimethylaluminum species than with monomethylaluminum species. The final step of siloxane MLD is the formation of a hydroxyl-terminated surface by water exposures. Figure 10c shows the integrated absorbance of the O-H and C-H stretch and Al-CH_3 deformation versus water exposure. This figure indicates that the water reaction is self-limiting and reaches completion after a 0.7 Torr·sec exposure of water.

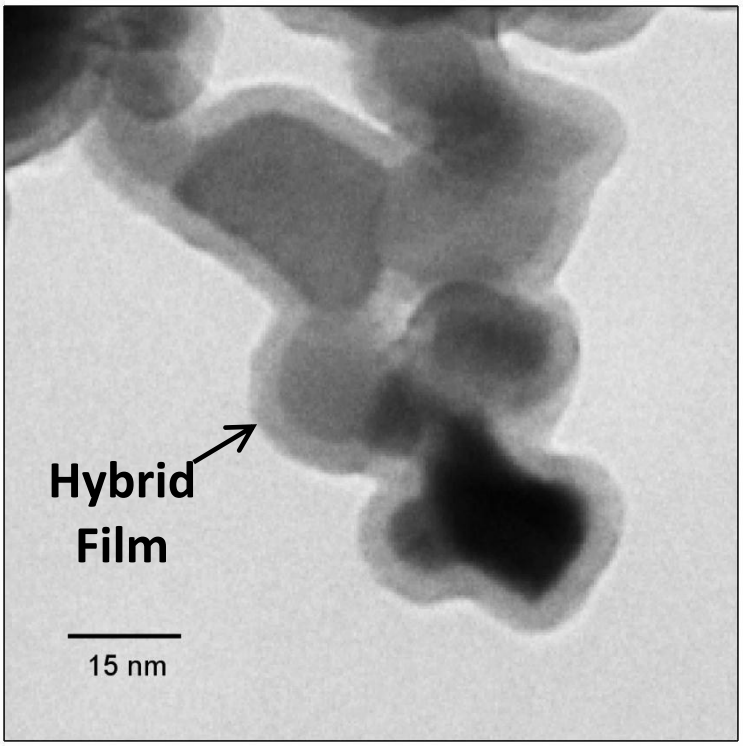

Figure 6.11 TEM image of hybrid MLD film deposited using the DIPS three-step process at 150°C on a ~12 Å seed layer of ALD alumina.

TEM images confirmed that alumina/siloxane MLD can be grown on the nanoparticles. The TEM image of the hybrid film after thirty MLD cycles deposited using DIPS at 150°C is shown in Figure 6.11. This TEM image reveals that the MLD film is very conformal on the ZrO_2 particles. In Figure 6.12, the ZrO_2 nanoparticles are resolved as dark areas surrounded by the lighter MLD and Al_2O_3 film. Subtracting out the 12 Å contribution from the seed layer of Al_2O_3 leaves 31 Å of hybrid MLD. This equates to a growth rate of 1.08 Å/cycle which is close to the film growth rate of 1.2 Å/cycle obtained from XRR.

6.4 Conclusions

This study shows fabrication of hybrid organic-inorganic siloxane/alumina films using MLD methods. QCM and FTIR monitoring techniques indicate that both MLD systems exhibit self-limiting growth. However, TMA/DIPS/H_2O deposition is favorable compared to the TMA/H_2O/DMMCS/H_2O system, mainly due to the use of silanol versus silane. The use of DIPS afforded lower growth temperatures, elimination of an additional step in the deposition process, and avoided a hydrochloric acid byproduct. In addition, hybrid films deposited using DIPS were more stable in air and had a higher growth rate than those grown using DMMCS.

This MLD process could be expanded into a new subset of thin film materials by modifications of the chemistry described within this paper. The amount of cross-linking within the film may be modified by using organometallic reagents with different coordination numbers. Alternatively, replacing the organic

groups on the silanol precursor could affect the hydrophobicity or density of the films. Mechanical properties of the films can also be potentially manipulated by changing the size of the siloxane group.

6.5 Acknowledgments

I would like to acknowledge Dr. David Roberts, former Air Products and Chemicals, Inc. (Allentown, PA, U.S.A.) now Nantero, Inc. (Woburn, MA, U.S.A) for his support during work on this project.

6.6 References

1. Mark, J.E., Allcock, H.R., West, R., , Inorganic Polymers. Oxford University Press, Inc., New York., 2005.

2. Lotters, J.C., et al., The mechanical properties of the rubber elastic polymer polydimethylsiloxane for sensor applications. Journal of Micromechanics and Microengineering, 1997. **7**(3): p. 145-147.

3. Camino, G., S.M. Lomakin, and M. Lazzari, Polydimethylsiloxane thermal degradation - Part 1. Kinetic aspects. Polymer, 2001. **42**(6): p. 2395-2402.

4. Archer, R.D., Inorganic and organometallic polymers. John Wiley & Sons, Inc., New York., 2001.

5. Lewis, H.G.P., T.B. Casserly, and K.K. Gleason, Hot-filament chemical vapor deposition of organosilicon thin films from hexamethylcyclotrisiloxane and octamethylcyclotetrasiloxane. Journal of the Electrochemical Society, 2001. **148**(12): p. F212-F220.

6. Lewis, H.G.P., D.J. Edell, and K.K. Gleason, Pulsed-PECVD films from hexamethylcyclotrisiloxane for use as insulating biomaterials. Chemistry of Materials, 2000. **12**(11): p. 3488-3494.

7. Rouessac, V., S. Roualdes, and J. Durand, In situ Mass Spectrometry analyses of the fragmentation of linear and cyclic siloxanes in a glow discharge compared with ex situ FTIR analyses of the deposits. Chemical Vapor Deposition, 2002. **8**(4): p. 155-161.

8. Fukui, H., et al., Surface Modification of Pigments by the Chemical Vapor-Deposition of Cyclic Dimethylsiloxane. Jocca-Surface Coatings International, 1992. **75**(10): p. 411-&.

9. Foussaier, O., et al., Polydimethylsiloxane-based ORMOSIL microstructure: correlation with compressive behavior. Materials Letters, 2000. **42**(5): p. 305-310.

10. Mackenzie, J.D., Y.J. Chung, and Y. Hu, Rubbery Ormosils and Their Applications. Journal of Non-Crystalline Solids, 1992. **147**: p. 271-279.

11. Sanchez, C., et al., Applications of hybrid organic-inorganic nanocomposites. Journal of Materials Chemistry, 2005. **15**(35-36): p. 3559-3592.

12. Elam, J.W., M.D. Groner, and S.M. George, Viscous flow reactor with quartz crystal microbalance for thin film growth by atomic layer deposition. Review of Scientific Instruments, 2002. **73**(8): p. 2981-2987.

13. Adarnczyk, N.M., A.A. Dameron, and S.M. George, Molecular layer deposition of poly(p-phenylene terephthalamide) films using terephthaloyl chloride and p-phenylenediamine. Langmuir, 2008. **24**(5): p. 2081-2089.

14. Goldstein, D.N., J.A. McCormick, and S.M. George, Al2O3 Atomic Layer Deposition with Trimethylaluminum and Ozone Studied by in Situ Transmission FTIR Spectroscopy and Quadrupole Mass Spectrometry. Journal of Physical Chemistry C, 2008. **112**(49): p. 19530-19539.

15. Rocklein, M.N. and S.M. George, Temperature-induced apparent mass changes observed during quartz crystal microbalance measurements of atomic layer deposition. Analytical Chemistry, 2003. **75**(19): p. 4975-4982.

16. Kantor, S.W., W.T. Grubb, and R.C. Osthoff, The Mechanism of the Acid-Catalyzed and Base-Catalyzed Equilibration of Siloxanes. Journal of the American Chemical Society, 1954. **76**(20): p. 5190-5197.

17. Lubguban, J., et al., Low-k organosilicate films prepared by tetravinyltetramethylcyclotetrasiloxane. Journal of Applied Physics, 2002. **92**(2): p. 1033-1038.

18. Favennec, L., et al., Porous extreme low kappa (EL kappa) dielectrics using a PECVD porogen approach. Materials Science in Semiconductor Processing, 2004. **7**(4-6): p. 277-282.

19. Dvornic, P.R., Lenz, R.W., , High Temperature Siloxane Elastomers. Huthing and Wepf, Basel, 1990.

20. Ivin, K.J., Thermodynamics of addition polymerization. Journal of Polymer Science Part a-Polymer Chemistry, 2000. **38**(12): p. 2137-2146.

21. Groner, M.D., et al., Low-temperature Al2O3 atomic layer deposition. Chemistry of Materials, 2004. **16**(4): p. 639-645.

22. Anderson, D.R., Analysis of Silicones. Editor Smith A.L., Wiley-Interscience, New-York, 1974. Chapter 10.

23. Bellamy, L.J., The Infra-red Spectra of Complex Molecules 3rd ed., Chapman and Hall, London, 1975. Chapter 20.

24. Smith, A.L., Spectrochim. Acta, 1960. **16**: p. 87.

25. Walsh, R., Bond-Dissociation Energy Values in Silicon-Containing Compounds and Some of Their Implications. Accounts of Chemical Research, 1981. **14**(8): p. 246-252.

26. Puurunen, R.L. and W. Vandervorst, Island growth as a growth mode in atomic layer deposition: A phenomenological model. Journal of Applied Physics, 2004. **96**(12): p. 7686-7695.

27. Dameron, A.A., et al., Molecular layer deposition of alucone polymer films using trimethylaluminum and ethylene glycol. Chemistry of Materials, 2008. **20**(10): p. 3315-3326.

28. Smith, A.L., Infrared Spectra-Structure Correlations for Organosilicon Compounds. Spectrochimica Acta, 1960. **16**(1-2): p. 87-105.

29. Smith, A.L., Analysis of silicones. Chemical analysis1974, New York,: Wiley. viii, 407 p.

30. Cunico, R.F. and L. Bedell, The Triisopropylsilyl Group as a Hydroxyl-Protecting Function. Journal of Organic Chemistry, 1980. **45**(23): p. 4797-4798.

31. Ferguson, J.D., A.W. Weimer, and S.M. George, Atomic layer deposition of Al2O3 films on polyethylene particles. Chemistry of Materials, 2004. **16**(26): p. 5602-5609.

32. Tian, R.H., et al., Infrared Characterization of Interfacial Si-O Bond Formation on Silanized Flat SiO2/Si Surfaces. Langmuir, 2010. **26**(7): p. 4563-4566.

33. Tolstoy, V.P., et al., Handbook of infrared spectroscopy of ultrathin films. Wiley-Interscience, New-York, 2003.

34. Rai, V.R. and S. Agarwal, Surface reaction mechanisms during ozone-based atomic layer deposition of titanium dioxide. Journal of Physical Chemistry C, 2008. **112**(26): p. 9552-9554.

35. Ferguson, J.D., A.W. Weimer, and S.M. George, Atomic layer deposition of Al2O3 and SiO2 on BN particles using sequential surface reactions. Applied Surface Science, 2000. **162**: p. 280-292.

CHAPTER VII

ATOMIC LAYER DEPOSITION OF TiV_xO_y AND AlV_xO_y ALLOYS AND EFFECT OF ANNEALING ON FILM MORPHOLOGY

7.1 Introduction

Vanadium impregnated titanium and aluminum oxides are industrially vital catalysts used in the manufacture of important chemicals as well as for reduction of environmental pollutants [1, 2]. Vanadium doping of titanium oxide allows a red shift in the absorption band of TiO_2 for better solar radiation utilization during photo-oxidation catalysis [3, 4]. Titanium-vanadium oxide alloy is also known for its useful thermo- and electrochromic properties [5, 6]. A particle mixture of V_2O_5 and Al_2O_3 and aluminum orthovanadate ($AlVO_4$) has been shown good sensitivity and selectivity toward the detection of nitrogen oxide (NO_x) pollutants [7-9]. Films of vanadium and mixed vanadium-titanium (or aluminum) oxides have been recognized as promising intercalation materials for lithium ion batteries [10-12]. Studies have shown that the crystalline titanium-vanadium oxide system has a higher cyclic stability and intercalation capacity than V_2O_5 [13-15].

In the past, titanium or aluminum-vanadium bulk and film oxide alloys were synthesized by wet chemical [5, 16-18], combustion [19], gas phase [20, 21] and solid-state reactions between oxides [22, 23]. The TiO_2-V_2O_5 and Al_2O_3-V_2O_5 nanolaminate thin films were deposited by atomic layer deposition method [24, 25].

This paper details the nucleation and growth of ALD V_2O_5 with emphasis on TiV_xO_y and AlV_xO_y oxide alloys examined from 90 to 200°C reaction

temperatures where TMA/H_2O and $TiCl_4/H_2O$ and $VOCl_3/H_2O$ deposition chemistries were used for aluminum, titanium, vanadium oxides respectively. The thermal ALD chemistries for Al_2O_3 and TiO_2 are well established, and ALD V_2O_5 on the other hand attracted attention only relatively recently [26, 27]. Vanadium pentoxide is typically deposited using and vanadyl triisopropoxide ($VO(OPr^i)_3$) as vanadium precursor with H_2O, O_3, H_2O_2, or O_2 for thermal and H_2O, or O_2 plasma enhanced ALD [28-31] and recently deposition of V_2O_5 was reported using $VO(thd)_2$ (thd = 2,2,6,6-tetramethylhepta-3,5-dione) and ozone [32]. Vanadium oxychloride hasn't been studied in detail for ALD V_2O_5 although it's less expensive, highly volatile, and stable at elevated temperatures. Other alternative vanadium halide precursors such as vanadium tetrachloride (VCl_4) are known to be less reactive with H_2O [33]. Therefore, we examined in detail the growth of vanadium oxide and its alloys at 115°C using in situ QCM to understand the initial nucleation and steady state growth mechanism. Utilizing a number of ex situ X-ray and optical techniques, films deposited on silicon wafers were characterized for composition, growth rate, and conformality.

Second part of the paper devoted to examine the effect of post-deposition annealing on the crystallinity, morphology, and microstructure of ALD TiV_xO_y and AlV_xO_y thin films. Annealing and the concomitant phase separation phenomenon were explored as a way to synthesize hierarchical nanostructures with different sizes, shapes and porosity. Such complex architectures, especially those based on one-dimensional nanostructures, are expected to display novel functions important

to the development of advanced devices and systems [34, 35]. In the past, growth of single-crystal V_2O_5 nanorods on rutile TiO_2 nanofibers was demonstrated by electrospinning V_2O_5-TiO_2-poly(vinylpyrrolidone) liquid solution at elevated temperatures in air [34]. An ability to reproduce this hierarchical structure via annealing of amorphous ALD TiV_xO_y or AlV_xO_y alloy films will extend the range of substrates available and therefore extend its areas of application. Furthermore, this approach can be potentially extended to fabricate other more complex architectures. Annealing of ALD AlV_xO_y films can provide insight on the effects of high surface energy and crystallization temperature on phase and morphology transformation during the annealing process. In addition, previous publications indicated difficulties with synthesis of crystalline $AlVO_4$ thin films by CVD or sputtering and to the best of our knowledge there no reports on ALD of aluminum orthovanadate [36]. Therefore, in this work, fabrication of crystalline $AlVO_4$ thin film was examined by annealing in air of ALD AlV_xO_y alloy films. Benefits of the use of ALD for thin film synthesis of crystalline $AlVO_4$ include the possibility of utilization of high surface area substrates as well as atomic level mixing of reacting species which can lead to reduction of synthesis temperature and time.

As deposited and annealed ALD films were analyzed using spectroscopic ellipsometry, X-ray photoelectron spectroscopy (XPS), X-ray reflectivity (XRR), scanning electron microscopy (SEM), high-resolution transmission electron microscopy (HRTEM) and Raman spectroscopy.

7.2 Experimental

ALD of vanadium oxide and its titanium and aluminum oxide alloys was carried out in a viscous-flow, hot-wall type reactor described in detail elsewhere [37]. Films were deposited using 99% pure vanadium oxychloride ($VOCl_3$) (Sigma-Aldrich. U.S.A.), 98% pure $TiCl_4$ (Strem Chemicals Inc., U.S.A.), 97% pure trimethylaluminium (TMA) (Sigma-Aldrich. U.S.A.), and chromatography grade water. Vanadium oxychloride is a liquid at the room temperature and has a vapor pressure of 13.8 Torr (20°C), as reported by the vendor. Vanadium and titanium precursors are liquids in ambient conditions and were handled in a glove bag because of its air and moisture sensitivity. Ultra high purity (UHP, 99.999%) grade nitrogen (Airgas, CO, U.S.A.) was used as the purge and carrier gas. The reactor base pressure was ~1 Torr at a N_2 gas flow rate of 195 sccm.

In situ QCM measurements were performed using AT- cut, 6 MHz resonant frequency, polished, gold-plated, quartz crystal sensors (Colorado Crystal Corporation, CO, U.S.A.). The QCM crystal was mounted in a Maxtek BSH-150 bakeable sensor housing (Inficon, NY, U.S.A.) and sealed using high temperature conductive epoxy (Epoxy Technology, H21D Kit, MA, U.S.A.). The QCM was purged with N_2 to prevent deposition on the backside of the crystal [37].

The reactant pulse and purge timing is designated as (t_1, t_2, t_3, t_4) where t_1 is the metal precursor exposure time, t_2 is the purge after the metal precursor exposure, t_3 is the H_2O dose times, and t_4 is the purge time after the H_2O exposures. For a given cycle recipe, the film deposited using 1 cycle of TiO_2 followed by 1 cycle

of V_2O_5 is referred to as 1:1 TiVxOy and 1 cycle TiO_2 and 8 cycles of V_2O_5 denoted as 1:8 TiV_xO_y. Similar rules applied for designation of the AlV_xO_y alloys.

Silicon wafers Si with <100> crystal orientation and dimensions of 2.5 cm × 2.5 cm were used as the substrates for the ex situ analysis of films grown at different conditions. These wafers had a native SiO_2 oxide with a thickness of ~25 Å. The substrates were cleaned with acetone and isopropanol and dried with N_2 gas prior use.

A spectroscopic ellipsometer (M-2000, J.A. Woollam Co., NE, U.S.A.) was used to determine the thickness and refractive index of deposited ALD films. The optical properties were measured for wavelengths ranging from 240 to 800 nm at an incident angle of 75°. The optical constants, n and k, were determined by analysis of measured ellipsometric parameters, Ψ and Δ. Measured data were analyzed using the Tauc-Lorentz oscillator model [38]. The thickness of the ALD films used in the model was determined using X-ray reflectivity (XRR). All refractive indices are reported at the sodium D-line reference wavelength of 590 nm. Refractive indices and band gap data for ALD TiO_2 and Al_2O_3 reported in this work are in excellent agreement with previously reported values [39].

X-ray reflectivity analysis was performed using a high resolution Bede D1 Diffractometer from Bede Scientific. This X-ray diffractometer was equipped with a Cu X-ray tube and monochromator for CuKα radiation at λ=1.54 Å. The XRR analysis was performed with CuKα1 radiation at λ=1.540 Å after removing the CuKα2 radiation at λ=1.544 Å using a channel cut crystal. A filament current of 40

mA and a voltage of 40 kV were used for the measurements. For each sample, the data were fit using the REFS fitting software from Bede Scientific to determine the film thickness, density, and roughness.

XPS survey and depth profile data were acquired using Physical Electronics PHI Model 5600 (Waltham, MA, U.S.A.) photo electron spectrometer system with monochromatic AlKα X-ray source with energy of 1486.6 eV with Ar^+ sputtering ability. The scans were performed with electron pass energy of 187 eV and a resolution of 0.8 eV. The photoelectrons were collected using a hemispherical analyzer.

Surface morphology of metal oxide samples before and after heat treatment were determined using SEM. SEM images were obtained with a beam voltage and current of 5.0 keV and 10 μA, respectively.

High-resolution transmission electron microscopy (HRTEM), with electron exhilaration voltage of 200 kV in combination with selected area electron diffraction (SAED) were used to determine the crystalline nature of synthesized surface features. Nanoparticls, nanorods, and nanowires were placed on copper grids for HRTEM analysis by sonication of annealed samples in isopropanol for 15 minutes and pipetting the solution with suspended nanoparticles onto the grid.

Raman spectra were recorded on a Horiba Jobin Yvon Micro-Raman spectrometer with 532 nm (green) Ar+ laser spot size of ~1.7 mm. The incident laser power used during measurement was limited to 50 mW.

Alloy films were annealed in air for two hours at the set temperature and maintained with a precision of ± 0.1°C in a furnace (Thermolyne-1400, U.S.A.). No programmed temperature ramping was applied. The same ALD coated samples were never annealed twice.

7.3 Results and Discussion

7.3.1 Nucleation and Growth of ALD V_2O_5 on Al_2O_3 and TiO_2

ALD V_2O_5 using $VOCl_3/H_2O$ chemistry was studied at various temperatures on pre deposited ALD Al_2O_3 and TiO_2 surfaces. Figure 7.1a shows a QCM signal at 115°C during the last cycle of TMA and H_2O for ALD Al_2O_3 followed by the first five cycles of vanadium oxide ALD. The QCM profile during vanadium oxide growth shows mass gain with $VOCl_3$ and mass loss with H_2O, which is consistent with a surface reaction mechanism where chlorine ligands on vanadium center are displaced by hydroxyl groups. In the first cycle the first dose of $VOCl_3$ on a hydroxylated alumina surface result in a mass gain of 36.72 ng/cm^2 (Δm_A) and a mass loss of 7.67 ng/cm^2 (Δm_B) after the water dose, with $\Delta m_B/\Delta m_A$ ratios of 0.2. As vanadium oxide deposition preceded further total mass gain gradually decreased from 28.5 ng/cm^2 on the first cycle to ~13.0 ng/cm^2 on the fifth cycle. The $\Delta m_B/\Delta m_A$ ratio is also gradually increased, reaching a value of 0.45 on the fourteenth cycle, suggesting a change in the growth mechanism.

Figure 7.1b shows the plot of the QCM derived mass gain per cycle versus cycle number during vanadium oxide ALD at 90, 115, 135, and 200°C on ALD alumina.

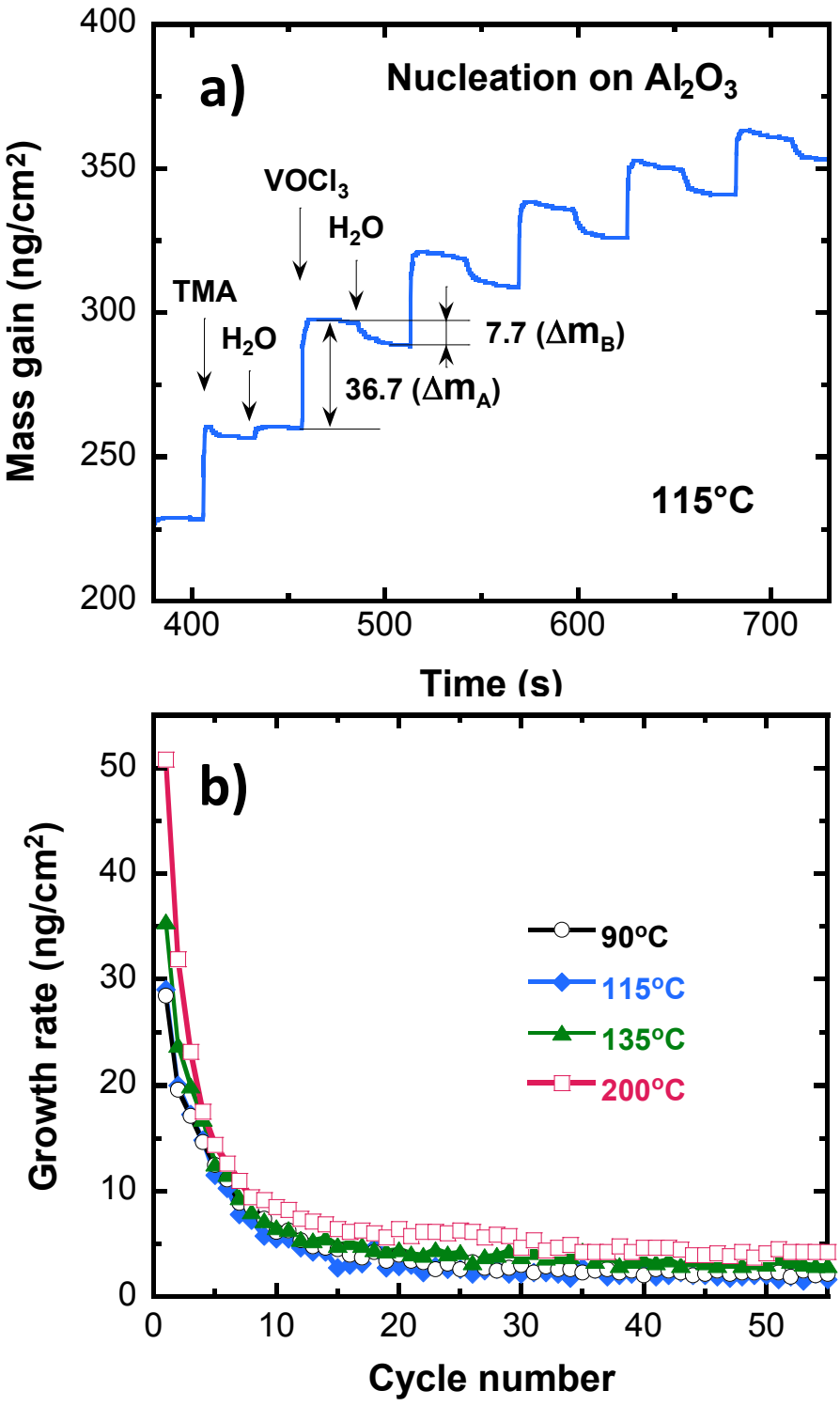

Figure 7.1 QCM measurements of mass gain versus time for V_2O_5 ALD growth on Al_2O_3 ALD surfaces using $VOCl_3$ and H_2O. (a) Nucleation over 5 cycles using a

timing sequence of (3, 25, 3, 25) at 115°C. (b) Change in growth rate per cycle over 55 cycles at 90, 115, 135, and 200°C deposition temperatures.

Gradual decrease in growth rate with cycle number was observed at all examined temperatures. This figure shows that mass gain on the first cycle is temperature dependent with maximum mass gain of 50.8 ng/cm^2 measured at 200°C, which decreases to about 28.5 ng/cm^2 at 90 and 115°C. However, during steady state growth, the growth rate is nearly independent of deposition temperature and equals about 3.0 ng/cm^2/cycle. Here, vanadium oxide film growth was performed using (3, 25, 3, 25) deposition timing. A three second dose of vanadium oxychloride and water was composed of 30 mTorr·s and 150 mTorr·s precursor's exposures, respectively. Study of precursor's saturation behavior did not lead to improvement of the growth rate so that extension of $VOCl_3$ exposure to 12 seconds (240 mTorr·s) and water dose to 12 seconds (840 mTorr·s) at 115°C resulted in an increase in the growth rate only on the ~1.0 ng/cm^2/cycle.

Intrinsic activity and selectivity of supported vanadium catalysts was a strong function of the oxide support and vanadium oxide loading [40]. ALD allows atomic level control of the concentration of the active vanadium oxide component on a support. At 115 or 200°C, total vanadium oxide mass gain from QCM, after twenty $VOCl_3/H_2O$ cycles, virtually leveled off at total mass of ~ 243 ng/cm^2, which is approximately 7.7 × 10^{14} V_2O_5 molecules per cm^2 estimated, using previously reported formula [41]. This suggests that only ~1.5 monolayers of V_2O_5 had been formed, considering that crystalline V_2O_5 contains 4.98 × 10^{14} molecules/cm^2 [2].

However, the value of 7.7×10^{14} molecules/cm^2 is also about 80% of a surface density of 10×10^{14} molecules/cm^2 previously estimated for a two-dimensional polyvanadate oxide layer, which can be formed without crystal V_2O_5 formation [2, 42].

Figure 7.2a shows QCM signal at 115°C during last cycle of $TiCl_4$ and H_2O of ALD TiO_2, followed by the first five cycles of vanadium oxide ALD. In the first cycle, the first dose of $VOCl_3$ on hidroxylated alumina surface resulted in mass gain of 43.3 ng/cm^2 (Δm_A) and mass loss of 17.8 ng/cm^2 (Δm_B) after water dose. This resulted in total mass gain of 25.5 ng/cm^2 on the first cycle on TiO_2, which is slightly less compared to total mass gain of 29.05 ng/cm^2 measured on the first cycle on alumina surface. However, $\Delta m_B/\Delta m_A$ ratio of 0.41 on TiO_2 is two times higher than on Al_2O_3 surface, indicating two distinctly different nucleation mechanisms. Figure 2b depicted growth rate versus cycle number during nucleation of ALD V_2O_5 in the course of 55 cycles. This figure shows that, in similarity to nucleation on Al_2O_3, most of the vanadium oxide mass gain happens during the first 20 cycles with low growth rate of ~0.2 ng/cm^2/cycle during steady state growth regime.

In order to improve ALD V_2O_5 steady state growth rate, the deposition was attempted using 30 % wt. hydrogen peroxide (H_2O_2) – H_2O solution as alternative oxygen source which, did not produce any improvements. In the past, thermal ALD V_2O_5 was deposited using vanadil triisopropoxide (VTIP) and water [28, 31] or H_2O_2 (50 % wt.) as oxygen sources [42]. These publications reported ALD V_2O_5 growth rate of less than 0.5 Å/cycle at deposition temperatures below 190°C.

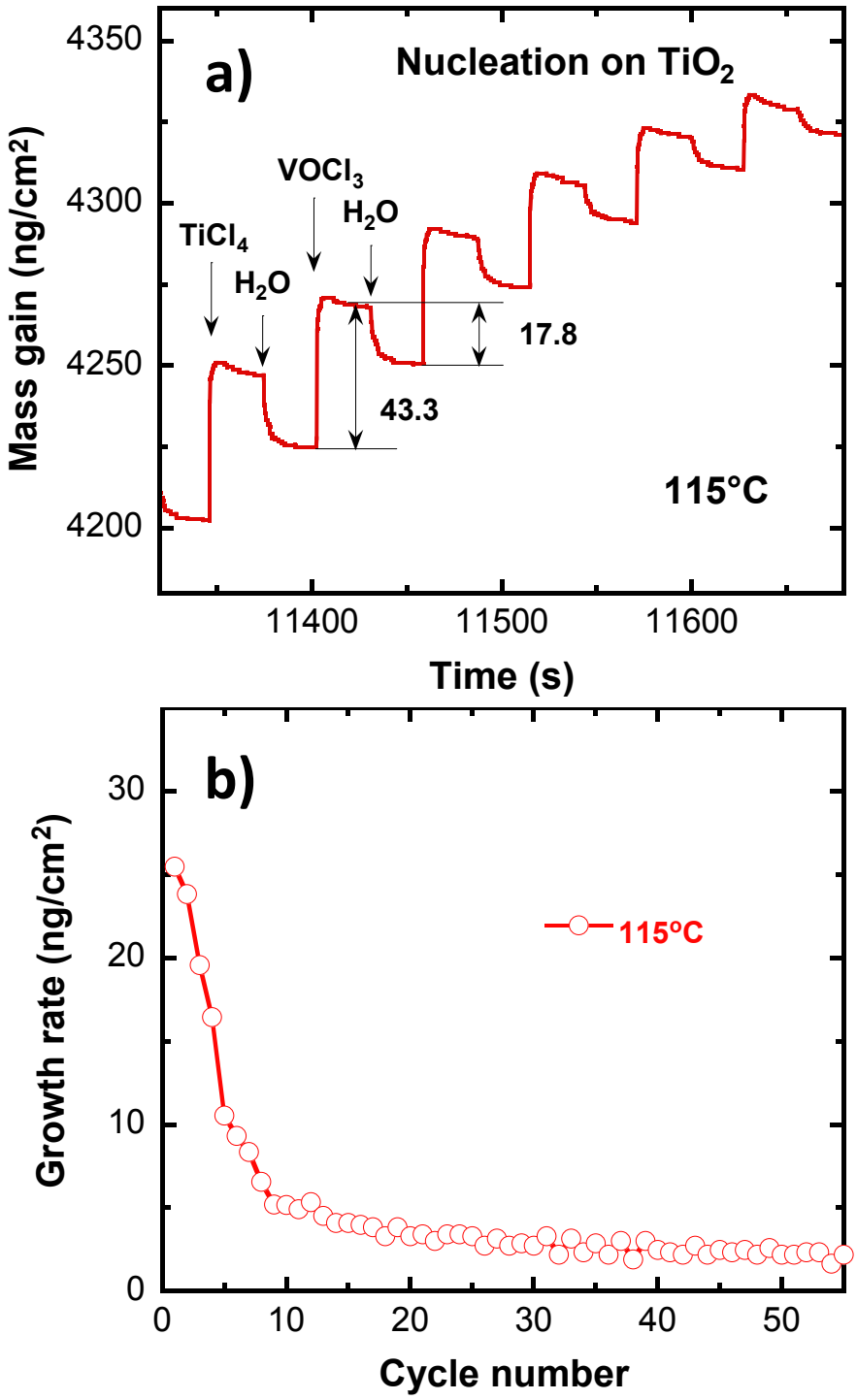

Figure 7.2 QCM measurements of mass gain versus time for V_2O_5 ALD growth on TiO_2 ALD surfaces using $VOCl_3$ and H_2O at 115°C. (a) Nucleation over 5 reaction

cycles using a timing sequence of (3, 25, 3, 25). (b) Change in growth rate over 55 cycles.

At temperatures above 190°C, VTIP exhibits limited thermal stability [28, 31]. Maximum deposition rate of vanadium oxide of ~3.5 ng/cm^2/cycle observed at 200°C in this work is less compared to growth rate of ~16.0 ng/cm^2 per cycle at 150°C for thermal VTIP/H_2O ALD [28]. However, higher growth rate could be partially explained by decomposition of VTIP, which resulted in 6.5 at. % of carbon impurities in deposited films [31]. Overall, limited growth rate the thermal ALD V_2O_5 process is possibly related to either vanadium precursor reaction, resulting in elimination of all three legends with formation of isolated monovanadate VO_4, or polyvanadate type species presence, which was previously observed spectroscopically [30, 43]. These would lead to termination of a surface with V=O**:** species with limited number hydroxyl groups for continues growth. In this instance, one may try use of H_2 gas to react with V=O**:** bond in order to regeneration of surface hydroxyl groups.

7.3.2 ALD of TiV_xO_y and AlV_xO_y alloys

7.3.2.1 QCM Study

Figure 7.3a shows QCM signal versus time during steady state 1:1 AlV_xO_y alloy growth performed at 115°C by depositing one cycle of TMA/H_2O with (1, 30, 3, 30) dose timing, followed by one cycle of $VOCl_3$/H_2O with (2, 30, 3, 30) timing. This figure shows mass gain of 35.6 ng/cm^2 during TMA/H_2O cycle and 40.0 ng/cm^2 for $VOCl_3$/H_2O,with total mass gain in 1:1 cycle of 75.6 ng/cm^2.

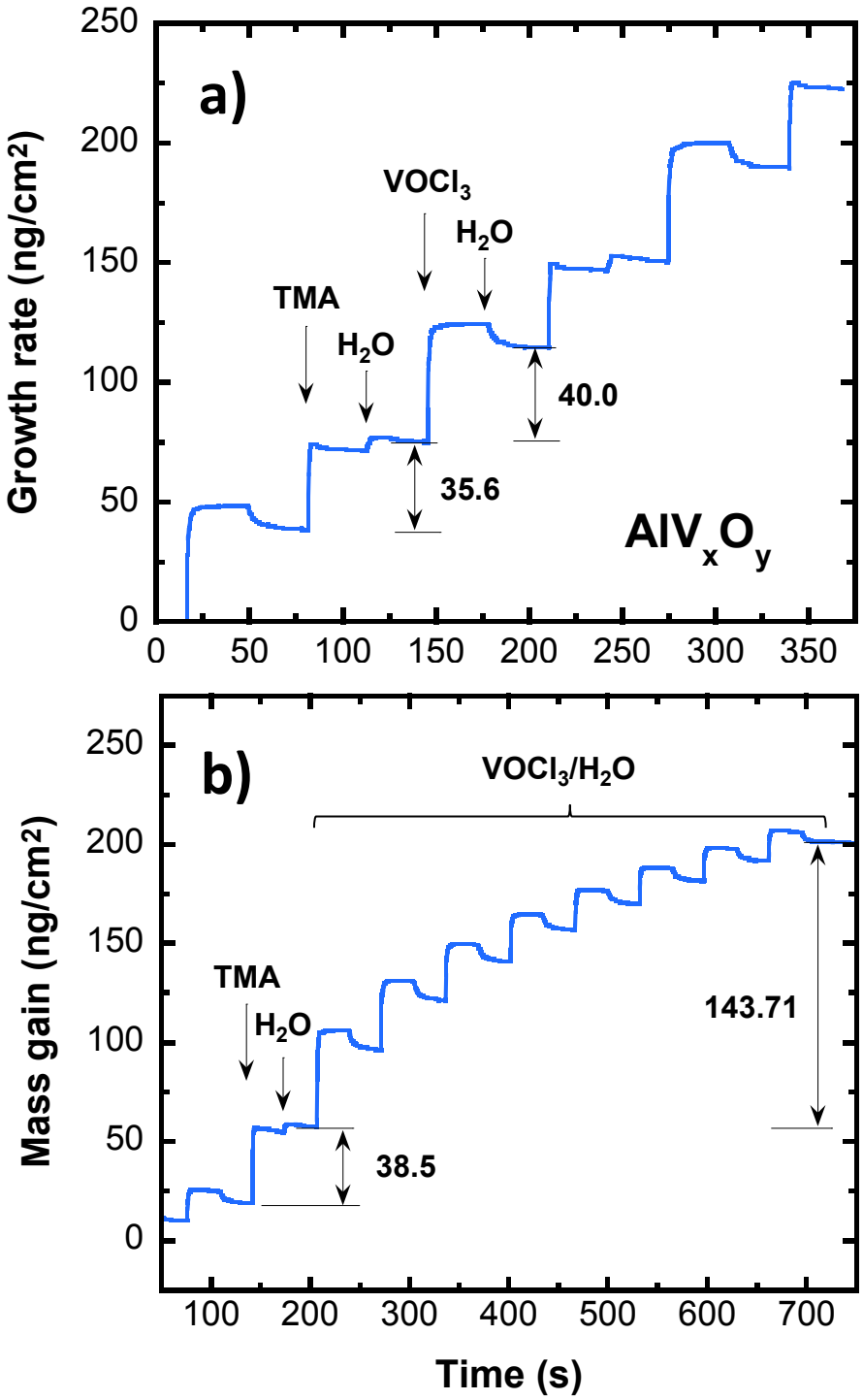

Figure 7.3 QCM measurements of mass gain versus time for AlV_xO_y ALD using TMA, $VOCl_3$, and H_2O during steady state growth at 115°C. (a) Expanded view of growth during two reaction cycles of (1:1) AlV_xO_y ALD using timing sequence of (1,

30, 3, 30) for TMA/H_2O and (2, 30, 3, 30) for $VOCl_3$/H_2O cycles. (b) Expanded view of growth during one reaction cycles of (1:8) AlV_xO_y ALD using the same cycle timing.

In order to maximize concentration of vanadium oxide in AlV_xO_y alloy, deposition was also performed with 1:8 arrangements where one cycle of TMA/H_2O was followed by eight $VOCl_3$/H_2O cycles, as depicted in Figure 7.3b. Here, growth rate of 1:8 AlV_xO_y alloy is 182.21 ng/cm^2/cycle measured during steady state growth regime. It was noticed that mass gain of ALD Al_2O_3 cycle is slightly increased from total mass gain of 35.6 ng/cm^2 measured during 1:1 AlV_xO_y deposition to value of 38.5 ng/cm^2 when 1:8 alloy was deposited. Both of these values are higher compared to growth rate of 31.2 ng/cm^2/cycle observed after TMA/H_2O dose during ALD Al_2O_3 performed at the same deposition conditions. The QCM profile during TMA/H_2O cycles shown in Fig. 7.3 is consistent with what would typically be observed for ALD Al_2O_3 using TMA and H_2O [37]. All precursors' dose times were experimentally determined to be the optimal for complete surface saturation. The results presented in Fig. 7.3a,b suggest that despite difficulty of growing ALD V_2O_5 by itself, the aluminum-vanadium oxide alloys can be deposited reproducibly with good growth rate.

QCM during steady state growth of 1:1 and 1:8 TiV_xO_y alloys is depicted in Fig. 7.4a and 7.4b respectively. These alloys are grown by alternating cycles of $TiCl_4$/H_2O with (3, 30, 4, 30) dose timing and $VOCl_3$/H_2O with (3, 30, 4, 30) timing at 115°C. Used precursor dose timings were experimentally determined to be optimal to insure surface saturation condition.

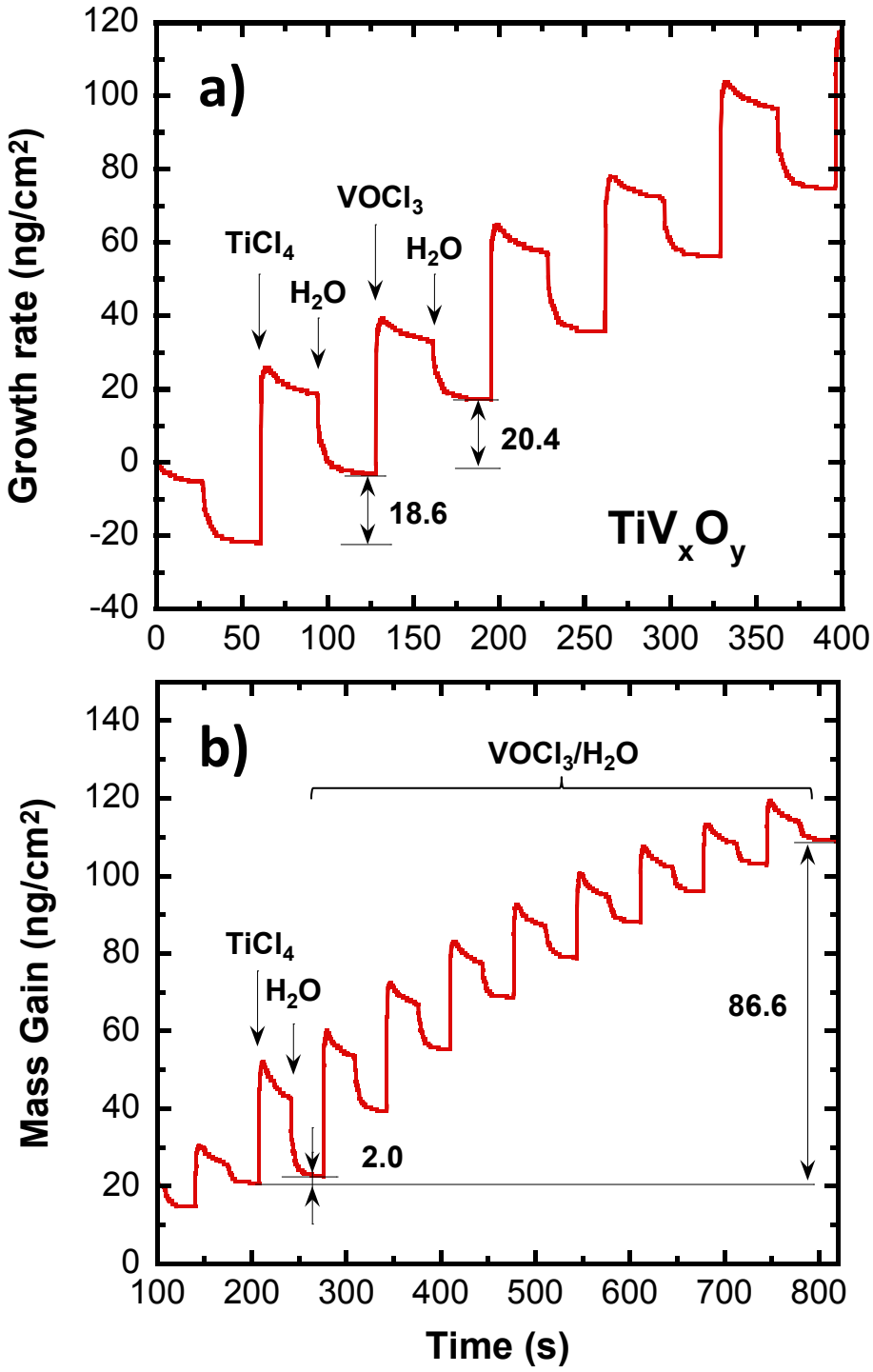

Figure 7.4 QCM measurements of mass gain versus time for TiV_xO_y ALD using $TiCl_4$, $VOCl_3$, and H_2O during steady state growth at 115°C. (a) Expanded view of growth during two reaction cycles of (1:1) TiV_xO_y ALD using timing sequence of (3,

30, 4, 30) and (3, 30, 4, 30) for $TiCl_4/H_2O$ and $VOCl_3/H_2O$ cycles. (b) Expanded view of growth during one reaction cycles of (1:8) TiV_xO_y ALD using the same cycle timing.

During steady state 1:1 TiV_xO_y film growth, the mass gain of 18.6 ng/cm^2 was measured for $TiCl_4/H_2O$ cycle and 20.4 ng/cm^2 for $VOCl_3/H_2O$ cycle with total growth rate of 39.0 ng/cm^2 per cycle (Fig. 7.4a). The total mass gain measured for 1:8 TiV_xO_y cycle was 88.6 ng/cm^2, which is significantly lower than 182.21 ng/cm^2/cycle observed for 1:8 AlV_xO_y alloy. When eight $VOCl_3/H_2O$ cycles used to grow 1:8 TiV_xO_y films, the mass gain during $TiCl_4/H_2O$ dose reduced down to ~2.0 ng/cm^2. This mass gain was significantly less compared to the 23.0 ng/cm^2/cycle growth rate that was observed during steady state ALD TiO_2, performed using $TiCl_4/H_2O$ at the same deposition conditions. This effect of reduction of the growth rate is the opposite of what was observed for AlV_xO_y alloys, where mass gain after TMA/H_2O increased for 1:1 and 1:8 type alloys. Similar growth behavior was observed during ALD Al_2O_3-V_2O_5 and TiO_2-V_2O_5 nanolaminates where V_2O_5 was deposited using VTIP/(H_2O_2 (50% Wt.) + H_2O) chemistry [24]. Noticeably, $\Delta m_B/\Delta m_A$ ratio of 0.9 calculated for $TiCl_4/H_2O$ cycle for 1:8 TiV_xO_y is much higher than 0.5 observed for ALD TiO_2. This indicates higher mass losses after H_2O dose during 1:8 TiV_xO_y depositions per mass, gained after $TiCl_4$ dose compared to ALD TiO_2.

The QCM data presented in Fig. 7.3 and 7.4 show that for ALD AlV_xO_y and TiV_xO_y films, one cycle of TMA/H_2O or $TiCl_4/H_2O$ is affectively regenerate reactive surface sites for following $VOCl_3/H_2O$ cycles. This is well depicted in Fig. 7.5, where

both AlV_xO_y and TiV_xO_y types of alloys demonstrate highly reproducible and linear growth during deposition at 115°C.

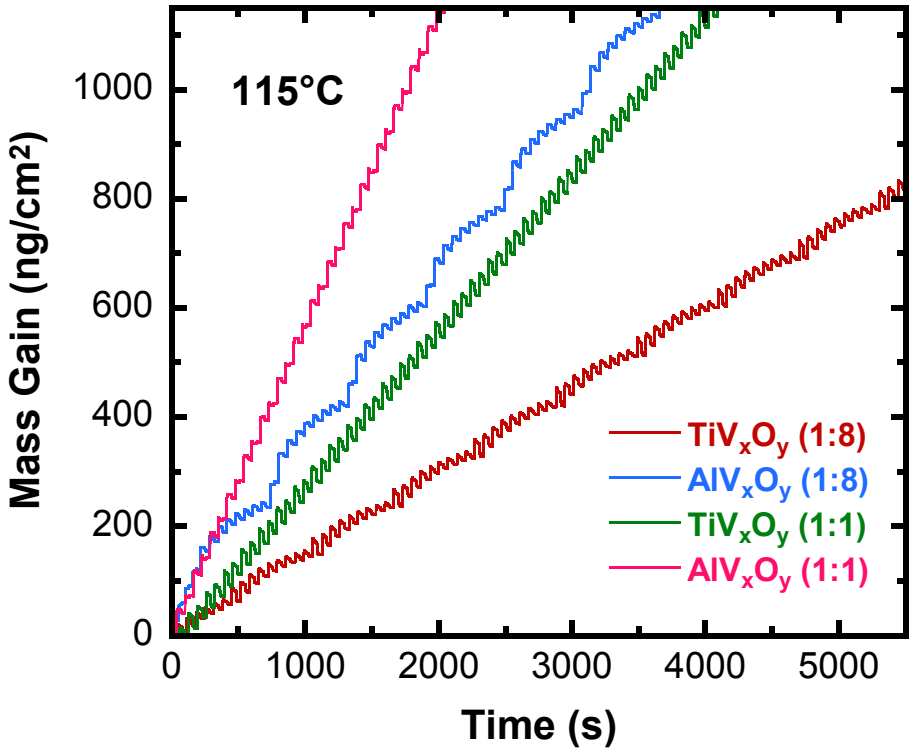

Figure 7.5 QCM measurements of mass gain versus time for (1:1) and (1:8) of AlV_xO_y, TiV_xO_y ALD during steady state deposition using timing sequence of (1, 30, 3, 30) for TMA/H_2O, and (3, 30, 4, 30) for $TiCl_4$/H_2O and $VOCl_3$/H_2O cycles at 115°C.

All the alloy films used for ex situ characterization and annealing studies were deposited at 115°C, unless noted otherwise.

7.3.2.2 XRR and XPS Analysis

Ex situ XRR of 1:1 AlV_xO_y and TiV_xO_y films deposited on Si<100> wafer at 115°C showed growth rate of 2.5 Å/cycle and 1.2 Å/cycle, respectively. Density deduced from fitting software were 3.23 g/cm^3 and 3.5 g/cm^3 for aluminum and

titanium alloys, respectively. XRR of 1:8 AlV_xO_y and TiV_xO_y films deposited showed growth rate of 5.5 Å/cycle and 2.7 Å/cycle respectively, with densities of deposited films of 3.24 g/cm^3 and 3.3 g/cm^3 for aluminum and titanium alloys, respectively. Higher growth rate for aluminum-vanadium oxide alloy is consistent with QCM measurements. For comparison, density of ALD Al_2O_3 is 3.0 g/cm^3 and ALD TiO_2 3.7 g/cm^3 deposited at the same temperature where crystalline V_2O_5 has reported density of 3.35 g/cm^3 [44]. Therefore, density for aluminum-vanadium oxide is increased compared to ALD Al_2O_3, and for titanium-vanadium oxide it decreased compared to ALD TiO_2 consistent with alloy formation. The root mean square (RMS) roughness of these alloy films with thickness ~300 Å was approximately about 4.5 Å.

The film densities obtained and the growth per cycle obtained by ex situ XRR analysis can be used to calculate the expected mass gain per cycle [41]. The mass deposition rates observed by the QCM measurements at 115°C for all AlV_xO_y and TiV_xO_y films are in agreement with the XRR results.

XPS survey scan of 1:8 titanium-vanadium oxide film showed that it had composition of Ti (9.95 at. %),V (7.66 at. %), O(50.21 at. %), and C(32.18 at. %) and 1:8 aluminum-vanadium oxide alloy had Al (10.53 at. %),V (8.41 at. %), O(44.33 at. %), C(33.86 at. %), and Cl(1.88 at. %). The chlorine impurities for titanium-vanadium alloys below detection limit of the instrument (0.01%) was indicative of efficient ALD chemistry even at low 115°C deposition temperature. Carbon impurities in aluminum-vanadium oxide were below detection limit after argon

sputtering. Presence of chlorine impurities in 1:8 AlV_xO_y film can be attributed to formation of high melting temperature aluminum chloride type salts [45]. From XPS data, 1:8 titanium-vanadium and aluminum-vanadium alloy films designation as $TiVO_5$ and $AlVO_4Cl_{0.2}$ for further were used through the paper. XPS analysis of survey spectra for 1:1 films revealed $TiV_{0.1}O_3$ and $AlV_{0.2}O_2Cl_{0.1}$ film composition. It was noticed that argon sputtering led to alteration of Ti/V and Al/V atomic ratios due to preferential etching. Therefore, stoichiometries of the films were derived from the survey scans by neglecting residual carbon.

Our calculations show that the atomic percent of vanadium in both types of alloys is lower than expected from QCM data. In the literature, similar reduced concentration of vanadium atoms has been attributed to substitution reaction during $TiCl_4$ dose [25]. Thermochemical calculations illustrate this possibility by the ΔG value [46]: $2V_2O_5 + 3TiCl_4 = 4VOCl_3 + 3TiO_2$ ($\Delta G_{115°C} = -76.5$ kcal/mol). Negative value of Gibbs free energy suggests favorability of formation of the volatile vanadium oxychloride as a result of $TiCl_4$ exposure on vanadium oxide terminated surface during $TiCl_4/H_2O$ cycle step at 115°C deposition. Therefore, this ALD process operates near the equilibrium between deposition and etching.

7.3.2.3 Optical Properties

Figure 7.6a shows a plot of the refractive index, n, versus wavelength measured by ellipsometry for 360 Å thick $TiVO_6$ and 770 Å thick $AlVO_4Cl_{0.2}$ films in comparison to ALD TiO_2 and Al_2O_3 deposited at 115°C.

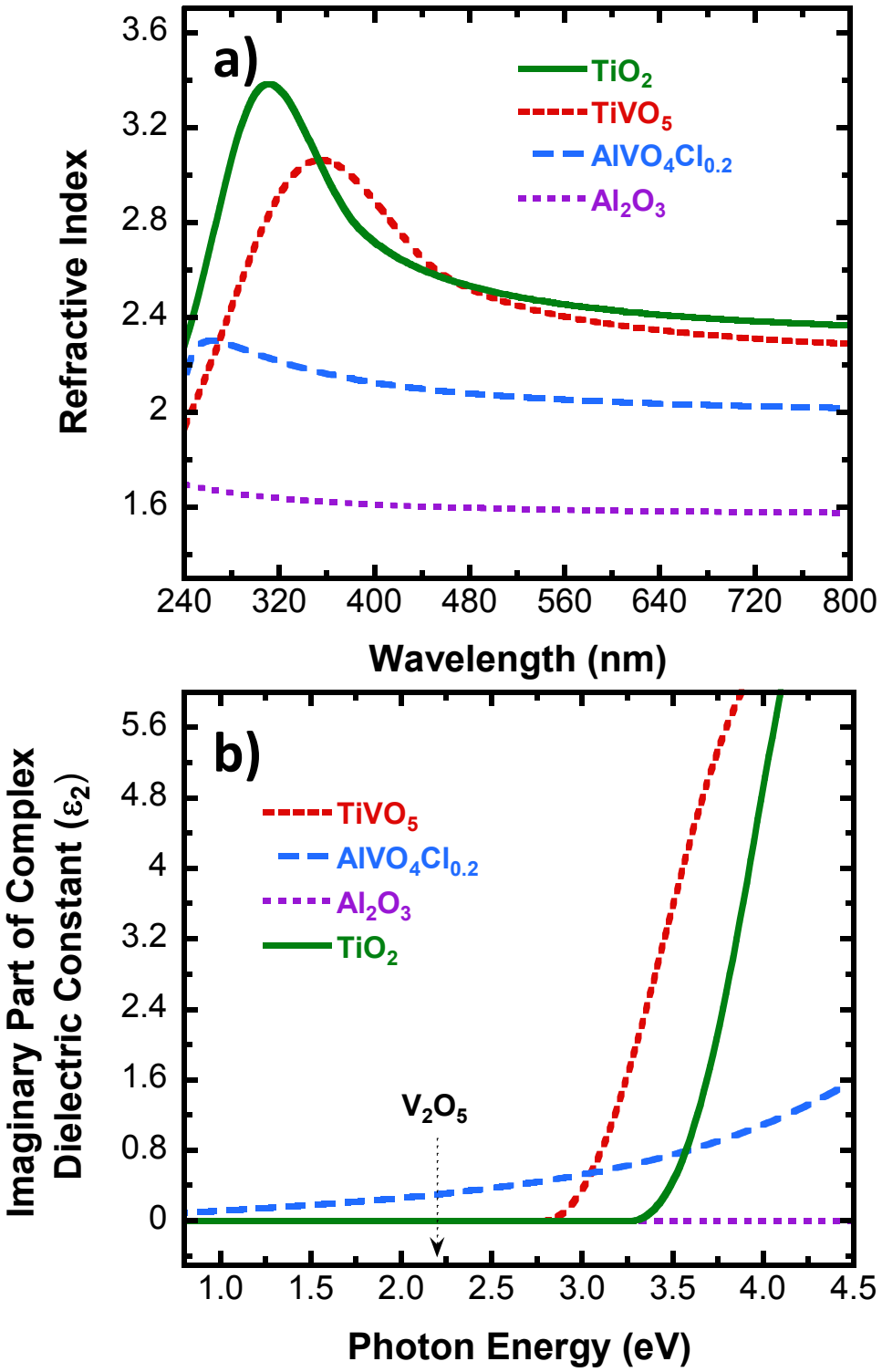

Figure 7.6 Optical constants of $AlVO_4Cl_{0.2}$, $TiVO_6$, Al_2O_3, and TiO_2 ALD films. The $AlVO_4Cl_{0.2}$ and $TiVO_6$ alloys were deposited with (1:8) arrangement and timing of

(1, 30, 3, 30) for TMA/H_2O, and (3, 30, 4, 30) for $TiCl_4/H_2O$ and $VOCl_3/H_2O$ cycles at 115°C. (a) Refractive index versus wavelength and (b) Imaginary part of complex dielectric constant versus photon energy.

At 590 nm wavelength $TiVO_5$ and $AlVO_4Cl_{0.2}$ have index of refraction of 2.38 and 2.04, respectively. Refractive indices of amorphous ALD TiO_2, Al_2O_3 measured in this work and previously reported amorphous ALD V_2O_5 are 2.4, 1.6, and ~2.2, respectively [32]. This figure indicates that alloying vanadium oxide with titanium oxide results in a slight decrease in refractive index where refractive index of aluminum-vanadium oxide is increased. Therefore, refractive index values for $TiVO_5$ and $AlVO_4Cl_{0.2}$ are considered between V_2O_5 and TiO_2 or Al_2O_3.

Band gaps for the alloys TiO_2, Al_2O_3 were derived from the dependence of the imaginary part of the complex dielectric constant, ε_2, on photon energy [38]. Figure 7.6b shows the plot of the imaginary part of complex dielectric constant (ε_2) versus wavelength measured. The band gap is determined at the point where ε_2 becomes non-zero [38]. This figure shows that band gap value shifted from 3.3 eV for ALD TiO_2 to 2.7 eV for $TiVO_5$ films. For comparison, literature band gap value for sputtered V_2O_5 is ~2.15 eV [47]. This shift in band gap is consistent with previous observations for co-sputtered TiO_2-VO_2 alloy, which had been found to follows follow additive low in optical properties [21].

In contrast to TiO_2 and V_2O_5, the Al_2O_3 has a large band gap of about 8.8eV, and therefore in non-absorptive over the measured optical range [48]. Interestingly, $AlVO_4Cl_{0.2}$ oxide deposited in this work showed absorption throughout entire

measured wavelength range, therefore not obeying additive low, as in the case of $TiVO_6$. Figure 6b shows that optical properties of aluminum-vanadium oxide alloy differ from parent Al_2O_3 and V_2O_5 oxides. This phenomenon might be related to chlorine impurity point defects that produce electronic states within the band gap and can trap or detrap electrons or holes. Optical properties are affected because the energy of for detrapping can be supplied by photon absorption. In the past, similar optical behavior was observed for phosphorus-vanadium oxide thin films [25].

Color of the 360 Å thick as deposited $TiVO_6$ was yellow, which is the characteristic color of crystalline V_2O_5, whereas 770 Å film of $AlVO_4Cl_{0.2}$ had a deep blue color [33].

7.3.3 Annealing Experiments

7.3.3.1 ALD $TiVO_5$ oxide

Titanium-vanadium oxide alloy films with thickness of 360 Å used in annealing experiments were deposited with 1:8 cycle ratio arrangement and were smooth with RMS roughness of ~4.0 Å determined from XRR. The annealing was performed at 350, 450, 500, and 550°C in air for two hours at every temperature. Surface scanning electron microscopy (SEM) imaging was used to monitor change in the thin film morphology. SEM imaging of the $TiVO_5$ films after 350°C annealing showed slight film roughening with no detectable surface features. SEM images of the films annealed at 450, 500, and 550°C are shown in Figure 7.7. Figure 7.7a exhibits surface of the $TiVO_5$ film annealed at 450°C.

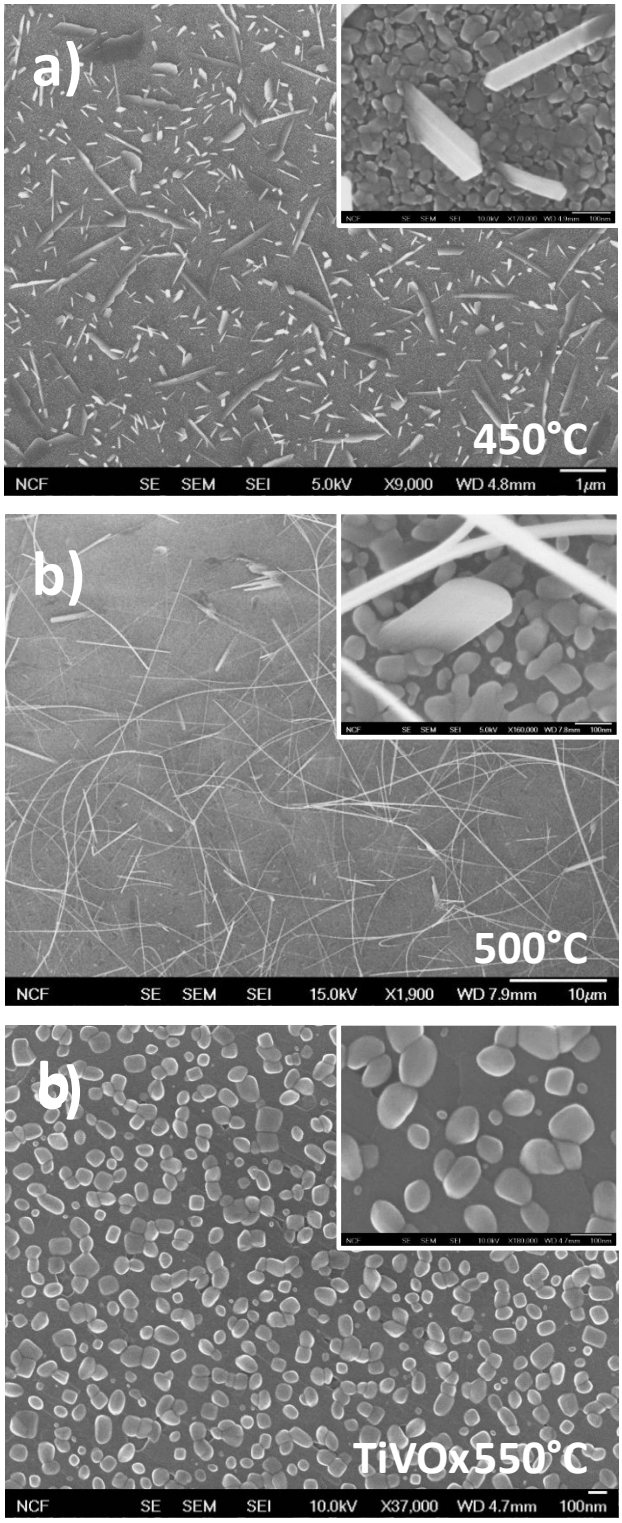

Figure 7.7 SEM images of the surface of 360 Å thick $TiVO_6$ ALD films annealed in air for 2 hours at (a) 450°C, (b) 500°C, (c) 550°C.

The annealing resulted in significant surface reconstruction with formation of the surface uniformly covered with nanosized features. The image shows two types of structures grown from the substrate: one is small and narrow, with nanorod crystals formed under angle with respect to the substrate, and the second is larger elongated terraces or "knife edged" type features. The length of small nanorods varied from 100 to 150 nm, and elongated futures are an average 2μm in length. A close-up view of the surface presented in the inset of Fig. 7.7a reveals substrate that cowered with nanoparticles varying in size from 10 to 80 nm in diameter. Annealing at 450°C of the $TiV_{0.1}O_3$ films deposited using 1:1 arrangement was not observable using SEM features.

Figure 7.7b depicted the surface of the $TiVO_5$ film annealed at 500°C. This sample contains long nanowires of various diameters ranging from about 10 to 500 nm freely residing on the substrate. Nanowires as long as ~60 μm in length were found. Some nanowires came into contact and were at the various stages of merging or growing form the substrate, as shown in the inset image of the figure. This image indicates that the tip of the nanowires is rounded in contrast to sharp ended nanorods obtained at 450°C. This image also revealed that a nanoparticle density per unit area for 500°C annealed samples is lower compared to the one observed for 450°C annealed samples (inset in Fig. 7.7a). This may suggest that some particles were "consumed" to promote the growth of short nanorods observed at 450°C to long nanowires at 500°C.

Figure 7.7c shows the result of annealing the alloy film at 550°C. The image shows that sample surface is uniformly covered with nanoparticles that have an average size of 80 nm. Nanorods and nanowires on the surface were absent and only nanoparticles were observed. The shapes of the nanoparticles are mostly rectangular, but with rounded corners.

The microstructure of the nano features formed as a result of annealing was studied by HRTEM. Figure 8a shows the bright-field image of a nanorod obtained during 450°C annealing. Its selected area electron diffraction pattern (SAED) is shown as an inset. Lattice fringes of a nanorod shown in Fig. 8b with regular spacing of 0.57 nm and 0.32 nm are consistent with interplanar distance of (200) and (101) planes of crystalline V_2O_5, respectively. This suggests V_2O_5 growth direction of (010). The well-resolved fringes along with SAED diffractogram pattern confirm single crystalline nature of the V_2O_5 nanorods.

Pure vanadium oxide formation is in good agreement with TiO_2-V_2O_5 phase diagram which predicts that neither complex oxide nor solid solutions form at 450°C and that the oxides should be present in segregated form [49]. This suggests that background particles could be either pure or mixed TiO_2 and V_2O_5 nanoparticles in case of partial phase separation.

Formation of a single crystal V_2O_5 at 475°C was previously reported for electrospun fibers derived from titanium-vanadium binary oxide sol-gel solution [34]. V_2O_5 single crystal nanorods have been also reported to form at 450°C from magnetron sputtered amorphous V_2O_5 film [50].

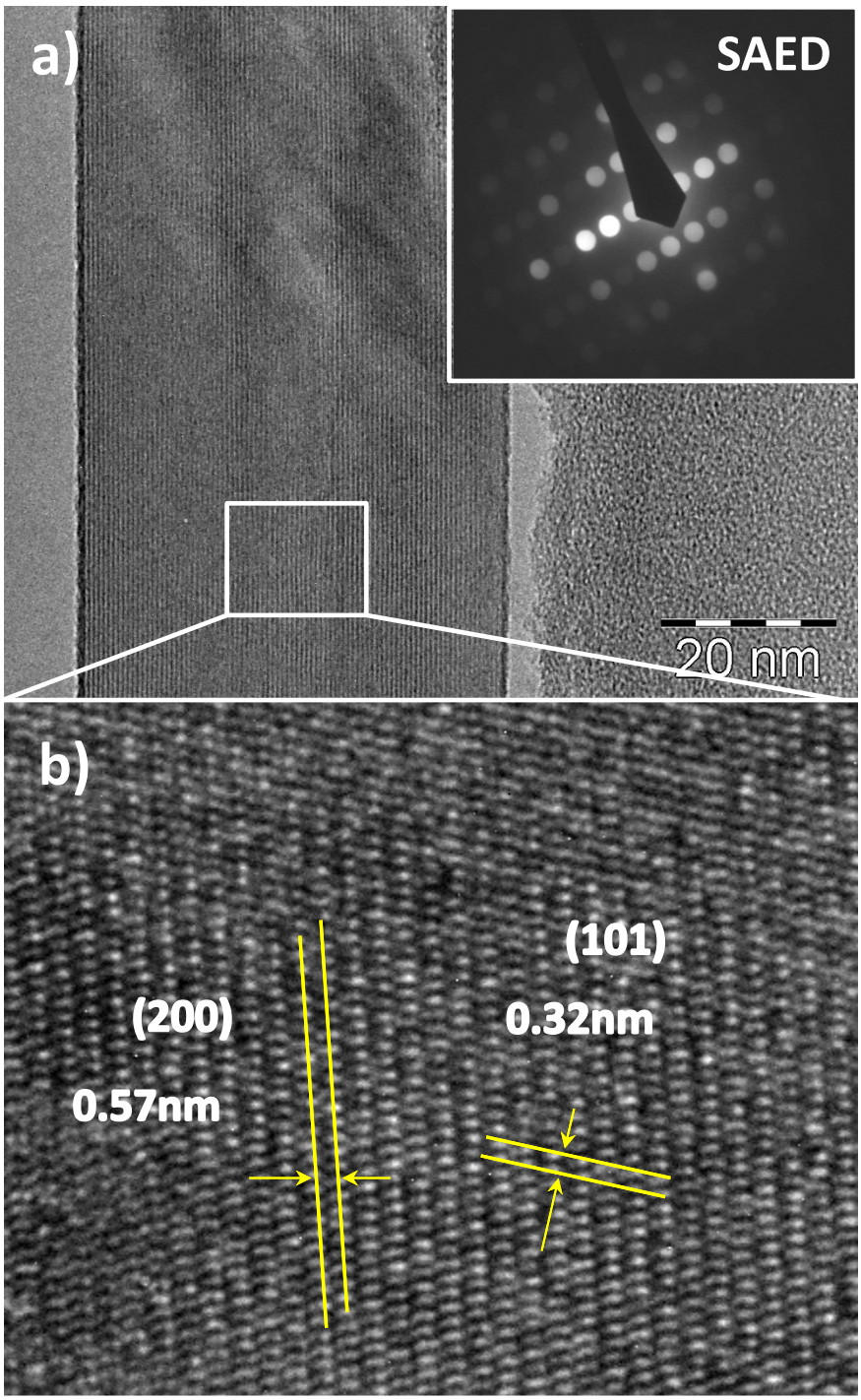

Figure 7.8 HRTEM images and electron diffraction patterns of the nanocrystals grown on the surface of the 360 Å thick $TiVO_6$ ALD film annealed in air for 2 hours at 450°C.

A crystallization temperature of ALD V_2O_5 deposited using $VO(OPr^i)_3/H_2O$ has been reported to be 400 to 450°C during annealing in oxygen [31]. Surface migration (diffusion) is believed to play an important role in V_2O_5 nanocrystal growth [51]. High mobility of V_2O_5 is attributed to its relatively low Tamman temperature of ~370°C, the temperature at which atoms from the bulk exhibit mobility [2, 52]. Appearance of the first crystallites at 450°C for ALD $TiVO_6$ observed in this work is close to the Tamman temperature of V_2O_5. However, ALD V_2O_5 deposited using $VO(OPr^i)_3/H_2O_2$ chemistry has a reported appearance of V_2O_5 crystals after annealing in air for one hour at temperatures as low as 150°C [24]. This temperature is near the Huttig temperature, which is approximately one-third of the bulk melting temperature of vanadium oxide of ~230°C, enough to make the species already located on the surface adequately mobile to undergo agglomeration [52]. This suggests that V_2O_5 crystallization temperature may depend on choice of V_2O_5 deposition chemistry, and concentration of the secondary phase present either as another oxide, as shown in this work, or as an impurity, as was pointed out in a previous publication [31]. Detailed knowledge of crystallization behavior of V_2O_5 is important for application in lithium ion battery and catalysis [2, 31].

Morphological changes of TiO_2 from film to nanoparticle form after annealing in air have been previously reported for SiO_2-TiO_2 nanolaminates [53]. This particle formation is in line with nanoparticle formation on the surface of the annealed $TiVO_6$ films. It is possible that surface particulates shown in the inset of Fig. 7.7a for 450°C annealed samples have a TiO_2-V_2O_5 closed shell structure, where

titanium oxide particles uniformly cowered with vanadium oxide film. The driving force for formation of such structures would be different in their surface energy of V_2O_5 (~10 × 10^{-6} Jcm^{-2}) and TiO_2 (~33 × 10^{-6} Jcm^{-2}) [52]. Lowering of the surface free energy by forming a layer of surface vanadium oxide on the high surface energy titanium oxide support is a commonly observed phenomenon [2, 43]. Although crystalline V_2O_5 by itself is known to be poor catalyst, TiO_2 supported V_2O_5 is known for its high catalytic activity [2]. The surface energy argument implies that V_2O_5 can also preferentially wet underlying native oxide SiO_2 on the substrate since it has slightly higher surface energy (~40 × 10^{-6} Jcm^{-2}) compared to TiO_2 [52], despite the fact that some researchers report difficulties of V_2O_5 wetting SiO_2 [43]. Therefore, hierarchical nanostructured formed after annealing ALD $TiVO_6$ can be useful for catalytic application.

High resolution TEM imaging of the nanowires was obtained at 500°C and nanoparticles at 550°C, as shown in Figure 7.9. Figure 7.9a shows a high resolution TEM image of a nanowire with lattice fringes of 0.4 nm, which is consistent with interplanar distance of (101) planes of orthorombic V_2O_5 [34]. Synthesis of long single-crystal V_2O_5 nanowires form ALD films that have not previously been reported. The rounded tip of the nanowires after annealing at 500°C as shown in the inset of Fig. 7b can be explained by formation of additional (010) facet in a crystal, which in combination with (310) and (310) plains can result in the circular-like tip previously reported for powder synthesized orthorhombic V_2O_5 nanorods [51].

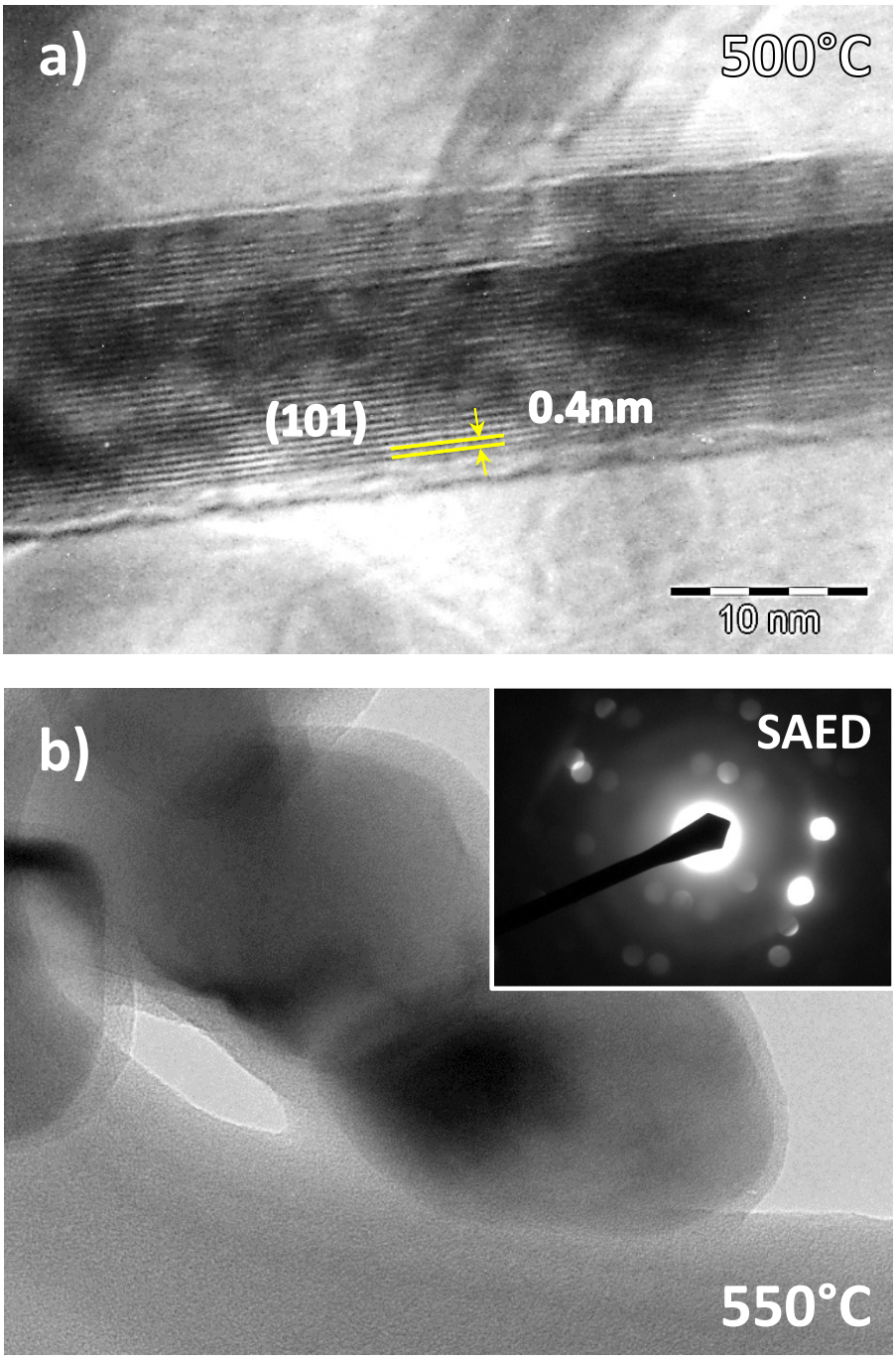

Figure 7.9 HRTEM images and electron diffraction patterns of (a) nanowires grown at on the surface of the 360 Å thick $TiVO_6$ ALD film after annealing in air for 2 hours at 500°C. (b) nanoparticles grown at on the surface of the 360 Å thick $TiVO_6$ ALD film after annealing in air for 2 hours at 550°C.

Phase segregation observed after 500°C annealing is in agreement with TiO_2-V_2O_5 phase diagram [49].

Curiously, annealing in air for 2 hours at 500°C of ALD V_2O_5 film deposited using $VO(OPr^i)_3/H_2O$ chemistry showed only formation of crystalline V_2O_5 grains with mean size of 450 nm [54]. At the same time, sputtered V_2O_5 films can be fully transformed to nanorods after annealing in air at ~450°C [50].

HRTEM of particles obtained after $TiVO_6$ annealing at 550°C is shown in Fig. 7.9b. This image shows a single crystalline particle with lattice fringes and SAED pattern consistent with single crystal V_2O_5. Also, the appearance of a circular pattern in SAED image is indicative of the presence of an additional polycrystalline phase. At this temperature phase, the diagram predicts formation of rutile TiO_2-V_2O_5 solid solution with additional crystalline V_2O_5 [49]. This may indicate that some of the particles shown in Fig. 7.7c are not fully reacted single-crystal V_2O_5. Loss of nanowires structure at 550°C annealing found in this work is similar to observations made for nanorods synthesized by annealing of a glass sputtered V_2O_5 [50]. This reference suggests that at 550°C vanadium oxide forms a thin film from nanorods on a surface of the glass substrate. Something similar can be applicable in our case with vanadium oxide film formation between nanoparticles and native SiO_2 of a silicon substrate. Background surface texturing at 550 °C anneal can be noticed on inset image of Fig.7.7c.

Raman spectroscopy of bulk transition metal oxides encompasses a vest well-established area of knowledge [55]. In this work, we used Raman spectroscopy

technique as a complementary to SEM and HRTEM. Figure 10 shows Raman scattering spectrum of pristine Si<100> substrate and the ALD $TiVO_6$ coated alloy samples annealed at 450, 500, and 550°C. Raman spectrum of the sample annealed at 450 and 500°C showed bands at 144, 192, 282, 402, and 695 cm^{-1}, corresponding to the crystalline V_2O_5 orthorhombic phase [33, 56].

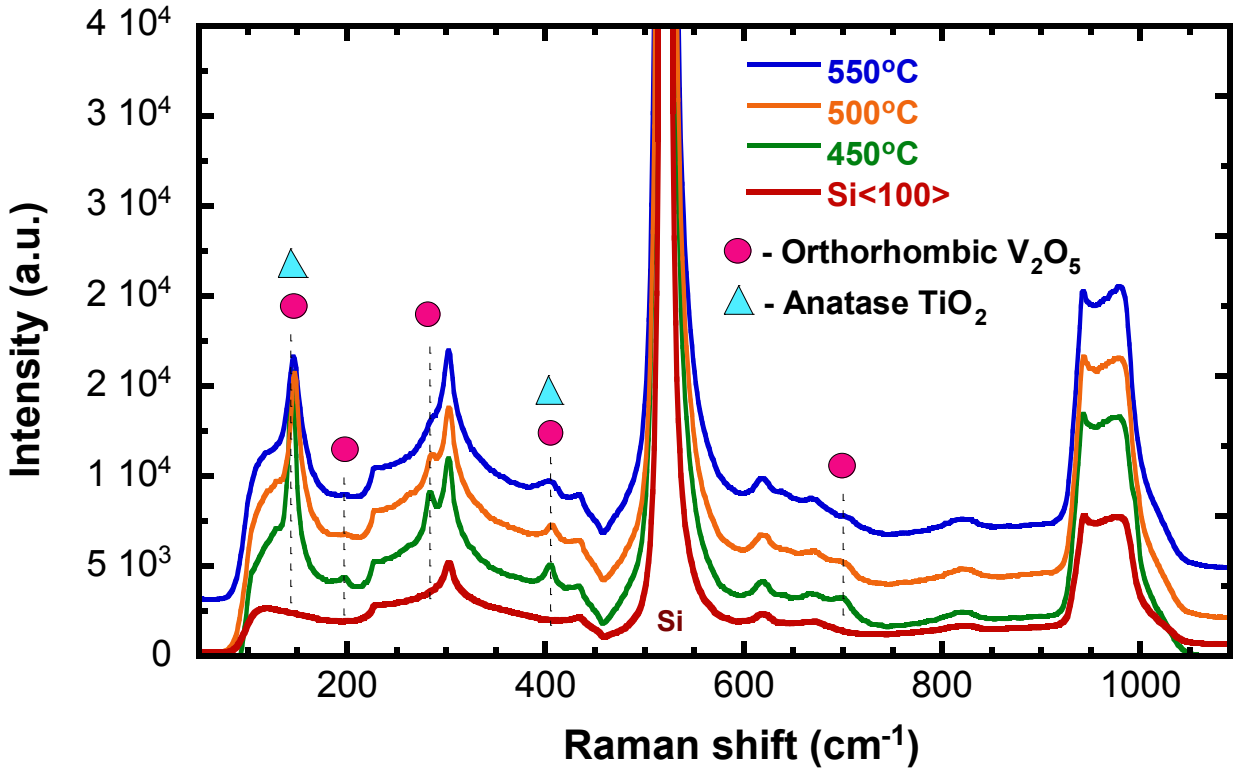

Figure 7.10 Raman spectra of bare Si<100> wafer and 360 Å thick $TiVO_6$ ALD film annealed in air for 2 hours at 450, 500, and 550°C.

However, bands at 144 and 402 cm^{-1} can be also attributed to anatase TiO_2 phase [57]. The presence of anatase phase of titanium oxide is in accordance with the TiO_2-V_2O_5 phase diagram [49]. This observation differs compared to electrospun TiO_2-V_2O_5 nanofibers synthesized at 475°C, where TiO_2 is reported to be in rutile

phase [34]. Anatase TiO_2 supported V_2O_5 is known to be more catalytically active than rutile TiO_2 supported vanadium oxide [58].

The Raman spectra acquired for 550°C annealed sample shows intensity reduction in all TiO_2-V_2O_5 peaks. This loss in peak intensities is similar to what was observed for crystalline V_2O_5 films sputtered on silicon wafer or glass substrate and annealed at 550°C [50, 56]. The phase diagram predicts that at this temperature there is a solid state reaction between rutile TiO_2 and V_2O_5, with the formation of mixed solid state solution [49].

According to existing SiO_2-TiO_2 phase diagram, high temperature annealing should not result in alloying between native SiO_2 and segregated TiO_2 [53].

7.3.3.2 ALD $AlVO_4Cl_{0.2}$ oxide

Aluminum-vanadium oxide films with thickness of 770 Å used in annealing experiments were deposited with 1:8 cycle ratio and were smooth with RMS roughness of ~5.0 Å determined from XRR. The annealing for these films was performed at 450, 500, 550, and 630°C.

The annealing of $AlVO_4Cl_{0.2}$ at 450°C resulted in surface roughening and pore formation with no prominent surface features. Figure 7.11 depicted surface transformations during the $AlVO_4Cl_{0.2}$ films anneal at 500, 550, and 630°C, as obtained by SEM imaging. As shown in Fig. 7.11a, annealing at 500°C results in formation of ~50µm size mounds from which branched vanadium oxide features resembling "bird footprint" are grown.

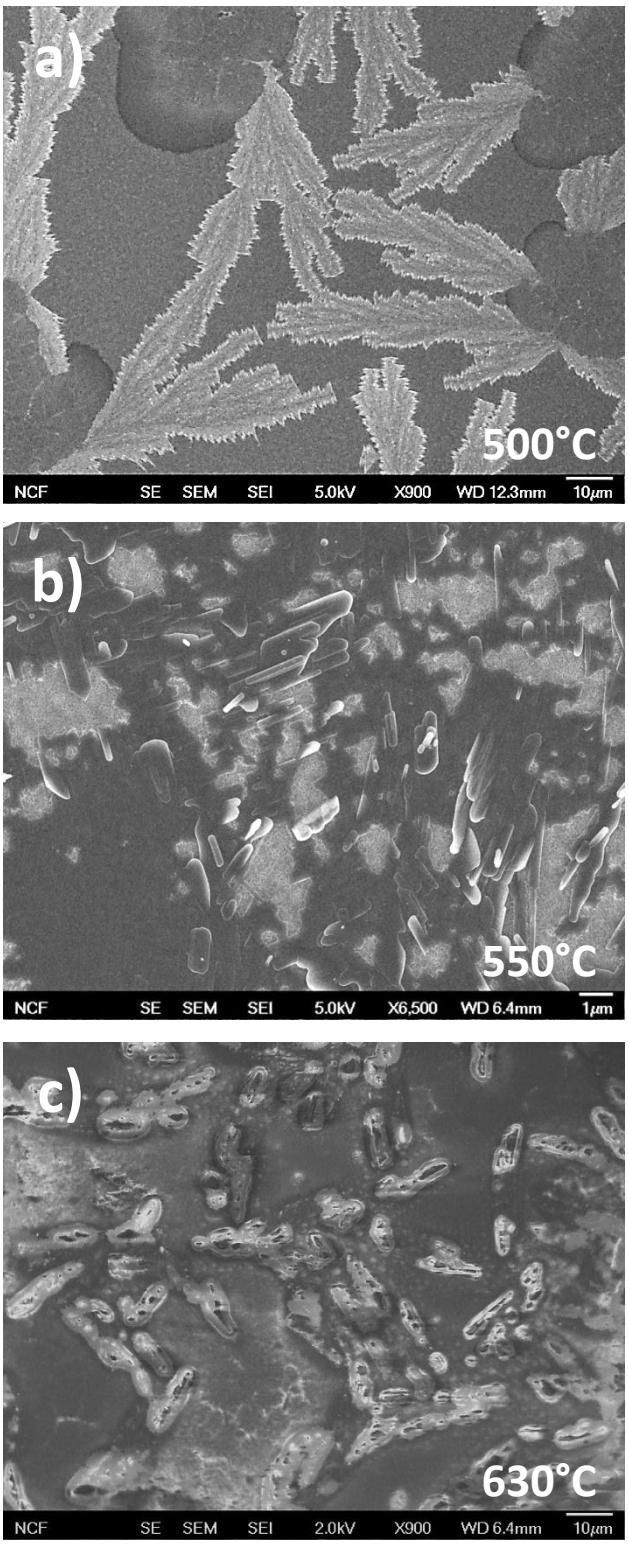

Figure 7.11 SEM images of the surface of 770 Å thick $AlVO_4Cl_{0.2}$ ALD films

annealed in air for 2 hours at (a) 500°C, (b) 550°C, (c) 630°C.

This type of feature has not been observed for ALD $TiVO_6$ annealed films. The surface of a sample annealed at 550°C is illustrated in Figure 7.10b. In this case, the surface turned into fine size porous film with a segregated thin film on the top. In contrast to 450°C annealed ALD $TiVO_6$ films, in the case of $AlVO_4Cl_{0.2}$, the rods are grown under a very low angle from segregated film rather than from the bulk. The vanadium oxide crystals have mostly rounded tips.

Annealing temperature of 630°C was chosen in an attempt to achieve synthesis of crystalline aluminum orthovanadate ($AlVO_4$) via solid state reaction in the ALD $AlVO_4Cl_{0.2}$ film. Previous publication reported full or partial $AlVO_4$ formation at anneal temperatures around 650°C [36, 59]. Figure 7.11c shows SEM image of ALD $AlVO_4Cl_{0.2}$ film surface after annealing at 630°C. The annealing resulted in crystalline island formations grown in direction normal to the substrate.

Figure 7.12 shows Raman scattering spectrum of Si<100> before deposition in comparison to ALD $AlVO_4Cl_{0.2}$ coated samples annealed at 500, 550, and 630°C. Raman spectra taken for 450°C annealed sample did not showed show any peaks. Raman pattern obtained for 500 and 550°C samples confirmed orthorhombic nature of the V_2O_5 futures as shown in Fig. 7.10a,b [56]. These Raman spectra do not exhibit a crystalline pattern of Al_2O_3 since its crystallization temperature is about 900°C [60]. Delayed appearance of vanadium oxide crystals in $AlVO_4Cl_{0.2}$ compared to $TiVO_6$ films can be related to several factors. It can be hypothesized here that vanadium atom diffusion through amorphous aluminum oxide network is more

difficult than diffusion through the surface of TiO_2 particles. A higher surface energy of Al_2O_3 (~90 × 10^{-6} Jcm^{-2}) compared to TiO_2 (~40 × 10^{-6} Jcm^{-2}) also may contribute to slow vanadium atom diffusion since it needs to overcome stronger cohesive forces of vanadium atoms with aluminum oxide than with TiO_2 [52].

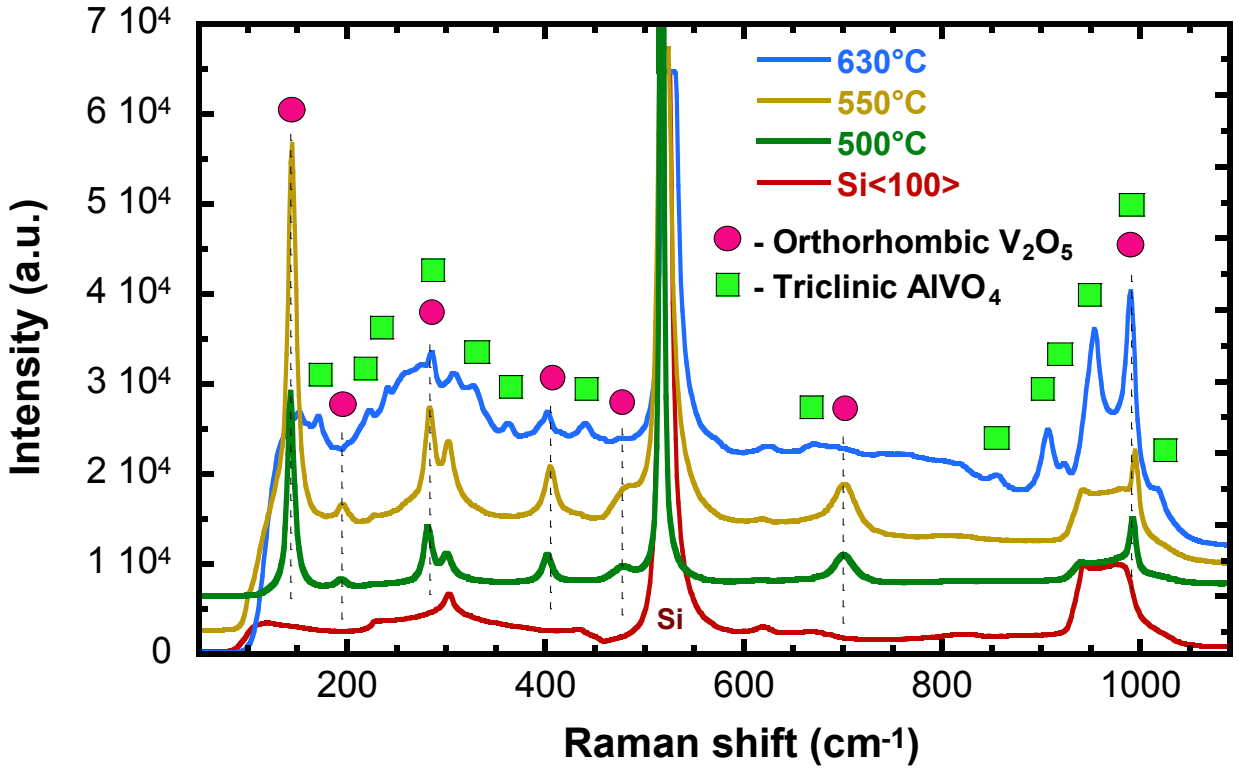

Figure 7.12 Raman spectra of bare Si<100> wafer and 770 Å thick $AlVO_4Cl_{0.2}$ ALD film annealed in air for 2 hours at 500, 550, and 630°C.

Strong cohesion of V_2O_5 to the surface of the Al_2O_3 may play a role in the formation of the specific morphology observed in Fig. 7.11a, where V_2O_5 is mostly in a form of film rather than in nanorod crystals. Perhaps vanadium oxide nanorods start forming when sufficient thickness of V_2O_5 is achieved and the substrate effect is diminished.

The phase diagram for Al_2O_3-V_2O_5 system predicts formation of $AlVO_4$ at temperatures above 500°C [61]. However, we did not observe Raman signatures of crystalline $AlVO_4$ for 550°C annealed samples. Perhaps a period of longer than 2 hours of heat treatment is needed to achieve solid state reaction to synthesize crystalline $AlVO_4$.

Raman spectrum obtained for 630°C annealed sample is consistent with previous experimental results and theoretical predictions for crystalline $AlVO_4$ [62]. To obtain this pattern, Raman laser spot had to be pointed at the crystals. No detectable pattern was observed when the laser was pointed off the crystal. This result confirms the occurrence of the solid state reaction in amorphous $AlVO_4Cl_{0.2}$ film with synthesis of a seeds of crystalline $AlVO_4$. Island morphology suggests that transformation is not full. Longer heat treatment may result in expansion of the islands, eventually forming an $AlVO_4$ film. Therefore, more detailed investigation is needed to optimize conditions for $AlVO_4$ film formation.

At examined annealing temperatures, segregated Al_2O_3 does not form alloys with substrate's native SiO_2,as indicated by Al_2O_3-SiO_2 phase diagram [63].

7.4 Conclusions

Heat treatment in air of the ALD TiVxOy and $AlVxOyCl_z$ oxides leads to formation of unique film morphology. Phase separation in ALD TiVxOy results in formation of a surface with uniformly distributed nanoparticles with singe-crystal V_2O_5 short nanorads or microns long nanowires, depending on the annealing temperature. At 450°C, annealing self-assembled TiO_2 is the form of polycrystalline

anatase form. In contrast to titanium-vanadium oxide, annealing of aluminum-vanadium oxide films led to distinctly different morphology due to difference in wetting of V_2O_5 by TiO_2 and Al_2O_3. High crystallization temperature of Al_2O_3 compared to TiO_2 stimulated the formation of finely textured amorphous Al_2O_3 film rather than the crystalline particles observed in the case of TiO_2. Solid state reaction of intimately mixed aluminum, vanadium, and oxygen atoms achieved during ALD allowed synthesis of islands of crystalline $AlVO_4$.

Demonstrated results suggest that properties of individual oxide such as crystallization, melting temperatures, and surface energy play a vital role in surface transformation during heat treatment in air. In principal, an ability to control these parameters opens a path for synthesis of a surface with desired morphology and properties.

7.5 Acknowledgements

Authors of this article would like to acknowledge Dr. Roy Gaiss (NCF, CU Boulder) and Wei Wang (Mechanical Engineering department, CU Boulder) for their generous assistance in obtaining HRTEM and SEM images.

7.6 References

1. Blangenois, N., et al., Influence of the co-precipitation pH on the physico-chemical and catalytic properties of vanadium aluminum oxide catalyst. Applied Catalysis a-General, 2004. **263**(2): p. 163-170.

2. Weckhuysen, B.M. and D.E. Keller, Chemistry, spectroscopy and the role of supported vanadium oxides in heterogeneous catalysis. Catalysis Today, 2003. **78**(1-4): p. 25-46.

3. Masih, D., H. Yoshitake, and Y. Izumi, Photo-oxidation of ethanol on mesoporous vanadium-titanium oxide catalysts and the relation to vanadium(IV) and (V) sites. Applied Catalysis a-General, 2007. **325**(2): p. 276-282.

4. Anpo, M., Preparation, characterization, and reactivities of highly functional titanium oxide-based photocatalysts able to operate under UV-visible light irradiation: Approaches in realizing high efficiency in the use of visible light. Bulletin of the Chemical Society of Japan, 2004. **77**(8): p. 1427-1442.

5. Tsuyumoto, I. and K. Nawa, Thermochromism of titanium-vanadium oxide thin films prepared from peroxotitanate and peroxovanadate solutions. Solid State Ionics, 2008. **179**(21-26): p. 1227-1229.

6. Yang, Y., D. Kim, and P. Schmuki, Electrochromic properties of anodically grown mixed V2O5-TiO2 nanotubes. Electrochemistry Communications, 2011. **13**(10): p. 1021-1025.

7. Ishihara, T., et al., The Mixed-Oxide Al2O3-V2O5 as a Semiconductor Gas Sensor for No and No2. Sensors and Actuators, 1989. **19**(3): p. 259-265.

8. Zakrzewska, K., Mixed oxides as gas sensors. Thin Solid Films, 2001. **391**(2): p. 229-238.

9. Wang, Z.C., et al., Catalytic Redox Reactions in the CO/N2O System Mediated by the Bimetallic Oxide-Cluster Couple AlVO3+/AlVO4+. Angewandte Chemie-International Edition, 2011. **50**(51): p. 12351-12354.

10. BaddourHadjean, R., et al., A kinetic study of lithium transport in a new Li intercalation material Al0.11V2O5.15 synthesized via a sol-gel process. Journal of the Electrochemical Society, 1996. **143**(7): p. 2083-2088.

11. Lim, J.W., et al., High electrochromic performance of co-sputtered vanadium-titanium oxide as a counter electrode. Solar Energy Materials and Solar Cells, 2009. **93**(12): p. 2069-2074.

12. Wang, Y., et al., Nanostructured vanadium oxide electrodes for enhanced lithium-ion intercalation. Advanced Functional Materials, 2006. **16**(9): p. 1133-1144.

13. Lee, K. and G.Z. Cao, Enhancement of intercalation properties of V2O5 film by TiO2 addition. Journal of Physical Chemistry B, 2005. **109**(24): p. 11880-11885.

14. Ozer, N., S. Sabuncu, and J. Cronin, Electrochromic properties of sol-gel deposited Ti-doped vanadium oxide film. Thin Solid Films, 1999. **338**(1-2): p. 201-206.

15. Takahashi, K., et al., Fabrication and Li+-intercalation properties of V2O5-TiO2 composite nanorod arrays. Applied Physics a-Materials Science & Processing, 2006. **82**(1): p. 27-31.

16. Shyue, J.J. and M.R. De Guire, Single-step preparation of mesoporous, anatase-based titanium-vanadium oxide and its application. Journal of the American Chemical Society, 2005. **127**(36): p. 12736-12742.

17. Nielsen, U.G., et al., Aluminum orthovanadate (AlVO4): Synthesis and characterization by Al-27 and V-51 MAS and MQMAS NMR Spectroscopy. Inorganic Chemistry, 2002. **41**(24): p. 6432-6439.

18. Yamaguchi, O., et al., Formation of Alvo4 Solid-Solution from Alkoxides. Journal of the American Ceramic Society, 1987. **70**(8): p. C198-C200.

19. Ekambaram, S. and K.C. Patil, Rapid Synthesis and Properties of FeVO4, AlVO4, YVO4, and Eu3+-Doped YVO4. Journal of Alloys and Compounds, 1995. **217**(1): p. 104-107.

20. Qureshi, U., T.D. Manning, and I.P. Parkin, Atmospheric pressure chemical vapour deposition of VO(2) and VO2/TiO2 films from the reaction of VOCl3, TiCl4 and water. Journal of Materials Chemistry, 2004. **14**(7): p. 1190-1194.

21. Kakiuchida, H., et al., Optical characterization of titanium-vanadium oxide films. Japanese Journal of Applied Physics Part 1-Regular Papers Brief Communications & Review Papers, 2007. **46**(2): p. 621-626.

22. Habel, D., et al., Phase development in the catalytic system V2O5/TiO2 under oxidising conditions. Journal of the European Ceramic Society, 2006. **26**(15): p. 3287-3294.

23. Abdalla, F.H.A., G.A. ElShobaky, and N.A. Hassan, Effect of sodium oxide doping on solid-solid interactions between V2O5 and Al2O3. Journal of Thermal Analysis, 1996. **47**(6): p. 1777-1785.

24. Elam, J.W.e.a., Nucleation, Growth and Crystallization of ALD Catalytic Oxide Layers. Posters from the ALD 2005 Conference. **http://www.es.anl.gov/energy_systems/docs/atomic_layer_deposition/V2O5%20%20Poster%20-%20Klamut.pdf**.

25. Malygin, A.A., Synthesis of multicomponent oxide low-dimensional systems on the surface of porous silicon dioxide using the molecular layering method. Russian Journal of General Chemistry, 2002. **72**(4): p. 575-589.

26. Puurunen, R.L., Surface chemistry of atomic layer deposition: A case study for the trimethylaluminum/water process. Journal of Applied Physics, 2005. **97**(12).

27. Koltsov, S.I., Structural Changes of Silica Gel during Formation on Its Surface of Titanium Dioxide Layers. Zhurnal Prikladnoi Khimii, 1970. **43**(9): p. 1956-&.

28. Badot, J.C., et al., Atomic layer epitaxy of vanadium oxide thin films and electrochemical behavior in presence of lithium ions. Electrochemical and Solid State Letters, 2000. **3**(10): p. 485-488.

29. Chen, X.Y., et al., Ozone-Based Atomic Layer Deposition of Crystalline V2O5 Films for High Performance Electrochemical Energy Storage. Chemistry of Materials, 2012. **24**(7): p. 1255-1261.

30. Feng, H., et al., Oxidative dehydrogenation of cyclohexane over alumina-supported vanadium oxide nanoliths. Journal of Catalysis, 2010. **269**(2): p. 421-431.

31. Musschoot, J., et al., Comparison of Thermal and Plasma-Enhanced ALD/CVD of Vanadium Pentoxide. Journal of the Electrochemical Society, 2009. **156**(7): p. P122-P126.

32. Østreng, E., Nilsen, O., Fjellvåg, H.,, Optical properties of vanadium pentoxide deposited by ALD. J. Phys. Chem. C, 2012. **116**(36): p. 19444–19450.

33. Field, M.N. and I.P. Parkin, Atmospheric pressure chemical vapour deposition of vanadium(v) oxide films on glass substrates from reactions of VOCl3 and VCl4 with water. Journal of Materials Chemistry, 2000. **10**(8): p. 1863-1866.

34. Ostermann, R., et al., V2O5 nanorods on TiO2 nanofibers: A new class of hierarchical nanostructures enabled by electrospinning and calcination. Nano Letters, 2006. **6**(6): p. 1297-1302.

35. Wang, Z.L., Nanobelts, nanowires, and nanodiskettes of semiconducting oxides - From materials to nanodevices. Advanced Materials, 2003. **15**(5): p. 432-436.

36. Leyer, B., et al., Preparation of AlVO4-films for sensor application via a sol-gel/spin-coating technique. Thin Solid Films, 1997. **310**(1-2): p. 228-233.

37. Elam, J.W., M.D. Groner, and S.M. George, Viscous flow reactor with quartz crystal microbalance for thin film growth by atomic layer deposition. Review of Scientific Instruments, 2002. **73**(8): p. 2981-2987.

38. Fujiwara, H., Spectroscopic Ellipsometry: Principles and Applications. John Wiley & Sons, Ltd.: West Sussex, England, 2007.

39. Langereis, E., et al., In situ spectroscopic ellipsometry as a versatile tool for studying atomic layer deposition. Journal of Physics D-Applied Physics, 2009. **42**(7).

40. Khodakov, A., et al., Structure and catalytic properties of supported vanadium oxides: Support effects on oxidative dehydrogenation reactions. Journal of Catalysis, 1999. **181**(2): p. 205-216.

41. Burton, B.B., D.N. Goldstein, and S.M. George, Atomic Layer Deposition of MgO Using Bis(ethylcyclopentadienyl)magnesium and H2O. Journal of Physical Chemistry C, 2009. **113**(5): p. 1939-1946.

42. Feng, H., et al., Catalytic nanoliths. Chemical Engineering Science, 2009. **64**(3): p. 560-567.

43. Haber, J., Fifty years of my romance with vanadium oxide catalysts. Catalysis Today, 2009. **142**(3-4): p. 100-113.

44. CRC Handbook of Chemistry & Physics, 92nd Edition, 2011-2012.

45. Juppo, M., et al., Trimethylaluminum as a reducing agent in the atomic layer deposition of Ti(Al)N thin films. Chemical Vapor Deposition, 2001. **7**(5): p. 211-217.

46. HSC Chemistry, E., Outokumpu Research Oy: Pori, Finland, 2002.

47. Watanabe, H., K. Itoh, and O. Matsumoto, Properties of V2O5 thin films deposited by means of plasma MOCVD. Thin Solid Films, 2001. **386**(2): p. 281-285.

48. Demkov, A.A., et al., Complex band structure and the band alignment problem at the Si-high-k dielectric interface. Physical Review B, 2005. **71**(19).

49. Habel, D., et al., Phase Relations in the System TiO2-V2Ox under Oxidizing and Reducing Conditions. Journal of Phase Equilibria and Diffusion, 2008. **29**(6): p. 482-487.

50. Zou, C.W., et al., Temperature sensitive crystallization of V2O5: from amorphous film to beta-V2O5 nanorods. Crystengcomm, 2010. **12**(3): p. 691-693.

51. Glushenkov, A.M., et al., A novel approach for real mass transformation from V2O5 particles to nanorods. Crystal Growth & Design, 2008. **8**(10): p. 3661-3665.

52. Spivey J.J., A.S.K., Knozinger H., Taglauer E., , Toward supported oxide catalysts via solid-solid wetting. Catalysis, 1993. **10**: p. 1-40.

53. Sankur, H. and W. Gunning, Crystallization and Diffusion in Composite Tio2-Sio2 Thin-Films. Journal of Applied Physics, 1989. **66**(10): p. 4747-4751.

54. Badot, J.C., et al., Electrical properties of V2O5 thin films obtained by atomic layer deposition (ALD). Journal of Materials Chemistry, 2004. **14**(23): p. 3411-3415.

55. Spivey J.J., A.S.K., Wachs I.E., Hardcastle F.D.,, Applications of raman spectroscopy to heterogeneous catalysis. Catalysis, 1993. **10**: p. 102-153.

56. Su, Q., et al., Raman spectroscopic characterization of the microstructure of V2O5 films. Journal of Solid State Electrochemistry, 2008. **12**(7-8): p. 919-923.

57. Chang, H. and P.J. Huang, Thermo-Raman studies on anatase and rutile. Journal of Raman Spectroscopy, 1998. **29**(2): p. 97-102.

58. Saleh, R.Y., et al., The Interaction of V2o5 with Tio2(Anatase) - Catalyst Evolution with Calcination Temperature and O-Xylene Oxidation. Journal of Catalysis, 1986. **98**(1): p. 102-114.

59. Arisi, E., et al., Preparation and characterization of AlVO4 compound. Journal of Materials Science, 2004. **39**(6): p. 2107-2111.

60. Jakschik, S., et al., Crystallization behavior of thin ALD-Al2O3 filMS. Thin Solid Films, 2003. **425**(1-2): p. 216-220.

61. Dabrowska, G., P. Tabero, and M. Kurzawa, Phase Relations in the Al2O3-V2O5-MoO3 System in the Solid State. The Crystal Structure of AlVO4. Journal of Phase Equilibria and Diffusion, 2009. **30**(3): p. 220-229.

62. Brazdova, V., M.V. Ganduglia-Pirovano, and J. Sauer, Crystal structure and vibrational spectra of AlVO4. A DFT study. Journal of Physical Chemistry B, 2005. **109**(1): p. 394-400.

63. Aramaki, S. and R. Roy, Revised Phase Diagram for the System Al2O3-SiO2. Journal of the American Ceramic Society, 1962. **45**(5): p. 229-242.

CHAPTER VIII

MOLECULAR LAYER DEPOSITION TITANICONE FILMS USING $TiCl_4$ AND ETHYLENE GLYCOL OR GLYCEROL: GROWTH AND PROPERTIES

8.1 Introduction

Molecular layer deposition (MLD) can be performed using the sequential self-limiting exposures of either organic precursors or organic and metal precursors [1, 2]. MLD is distinguished from atomic layer deposition (ALD) because a molecular fragment can be added during one of the sequential exposures. MLD was originally defined for the growth of all-organic polyimide [3, 4] and polyamide [5, 6] polymers. Polythiourea [7] and thiol-ene [8] polymers can also be grown using MLD techniques. In addition, organic and metal precursors can be combined to deposit hybrid organic-inorganic materials [9-11]. The reaction of metal precursors with organic diols or triols forms metal alkoxide polymer films that are known as "metalcones" [12].

The first metalcone MLD films were the "alucones" grown using trimethylaluminum (TMA) and ethylene glycol (EG) as the reactants [9]. A second class of metalcone MLD films were the "zincones" grown using diethylzinc (DEZ) and EG as the reactants [10, 11]. One of the difficulties with homobifunctional reactants, such as EG, is that "double reactions" can occur when both hydroxyl groups on the EG reactant react with the surface [2, 11]. To avoid the problem of double reactions that can inhibit film growth, other types of alucone MLD films have also been demonstrated using TMA, ethanolamine (EA) and maleic anhydride (MA) as the reactants [13, 14]. Double reactions were avoided because EA is a

heterobifunctional monomer and MA is a ring-opening reactant. Alucone MLD has also been demonstrated using TMA and glycidol as a heterobifunctional reactant [15, 16]. Other types of hybrid organic-inorganic MLD films can also be grown based on metal precursors and carboxylic acid reactants, [17, 18] self-assembled monolayers combined with metal oxide ALD, [19, 20] or DEZ and hexadiyne followed by UV polymerization [21].

Titanium-containing hybrid organic-inorganic films can also be deposited using $TiCl_4$ and diols and triols. These films can be designated as "titanicones". In this study, the growth of titanicone MLD films is reported using $TiCl_4$ and either EG or GL. Because GL is a triol, titanicone films grown using GL should lead to more bridging between the titanium alkoxide polymer chains and should display a higher mechanical toughness than titanicone films grown using EG. These studies focused on $TiCl_4$ as the titanium metal precursor because of the high vapor pressure and thermal stability of $TiCl_4$. A schematic of titanicone MLD using $TiCl_4$ and EG is shown in Figure 8.1. A schematic of titanicone MLD using $TiCl_4$ and GL is displayed in Figure 8.2.

The growth of titanicone films using $TiCl_4$ and EG or GL was examined in situ using quartz crystal microbalance (QCM) experiments. These QCM measurements measured film growth rates and confirmed self-limiting surface chemistry for the reaction of $TiCl_4$ with both EG and GL. Ex situ X-ray reflectivity experiments also measured linear growth rates and obtained the density of the titanicone films. The properties of the titanicone films grown using EG and GL

were compared using nanoindentation studies to measure the elastic modulus and hardness. Additional studies explored the effect of annealing and UV exposure on the titanicone films.

The titanicone films are potentially useful for a wide variety of applications. The titanicone films grown using $TiCl_4$ and GL are expected to have higher toughness than the titanicone films grown using $TiCl_4$ and EG.

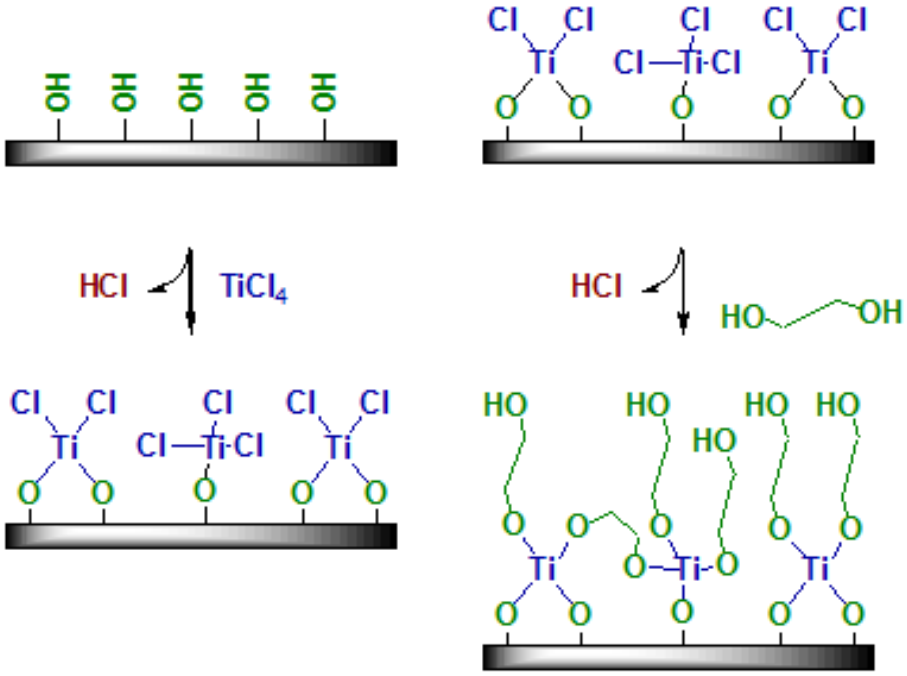

Figure 8.1 Schematic of titanicone MLD using $TiCl_4$ and ethylene glycol (EG).

These titanicone films grown using GL could be useful to fabricate flexible multilayer gas diffusion barriers for organic electronics and thin film solar applications [22, 23]. TiO_2 is also known for its biocompatibility and resistance to H_2O corrosion [24-26]. Because of its similarity with TiO_2, titanicone films may be utilized as flexible protective coatings for biological implants. TiO_2 also has catalytic and photocatalytic properties [27]. Porous TiO_2 frameworks formed by the

annealing of titanicone films may serve as catalytic supports. Titanicone films can also be modified or patterned using ultraviolet light. The resulting porous TiO_2 films could serve as TiO_2 scaffolds for dye-sensitized solar cells or photocatalytic membranes [28, 29].

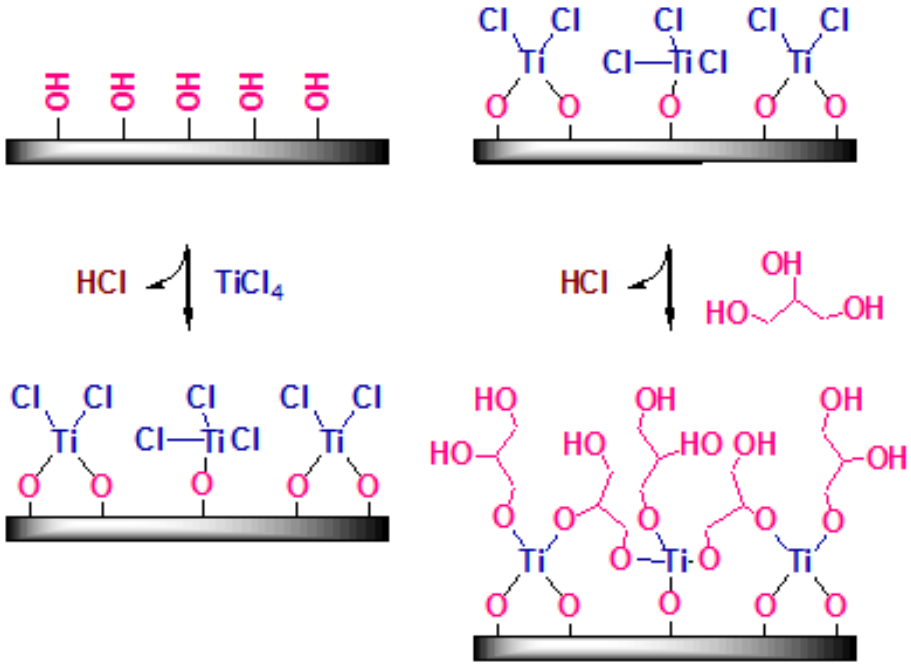

Figure 8.2 Schematic of titanicone MLD using $TiCl_4$ and glycerol (GL).

The sequential, self-limiting reactions used to grow ALD or MLD films typically deposit ~1 Å every reaction cycle. The resulting film growth rates are slow if the reaction cycle times are long. However, the reaction cycle times depend upon the reactor design. Optimized reactor designs can reduce the reaction cycle times for Al_2O_3 ALD to ~1s. Similar reaction cycle times should be possible for MLD processes. New "spatial ALD" reactors may also be able to reduce the MLD cycle times [30]. Consequently, the growth rate of the titanicone films should be sufficient for the various applications.

8.2 Experimental

Titanicone MLD was performed in a viscous-flow, hot-wall type reactor described in detail elsewhere [31]. Films were deposited using $TiCl_4$ (98% pure, Strem Chemicals Inc., U.S.A.), ethylene glycol (99.8% pure, Sigma-Aldrich. U.S.A.), and glycerol (99.5% pure, Sigma-Aldrich. U.S.A.). All precursors were handled in a glove bag due to their air and moisture sensitivity. Before use, the EG was degassed using several freeze/pump/thaw cycles with liquid nitrogen. The EG vessel was heated to 65°C and EG was dosed directly into the reactor. Prior to use, GL was degassed by pumping on the EG through the reactor without performing freeze-pump-thaw cycles. The glycerol vessel was heated to 120°C. A N_2 gas stream entrained the GL by flowing over the head space in the GL vessel. Ultra high purity grade nitrogen (99.999% pure, Airgas, CO, U.S.A.) was used as the purge and carrier gas in the reactor. The reactor base pressure was ~1 Torr at a N_2 gas flow rate of 195 sccm.

In situ QCM measurements were performed using AT- cut, 6 MHz resonant frequency, polished, gold-plated, quartz crystal sensors (Colorado Crystal Corporation, CO, U.S.A.). The QCM crystal was mounted in a Maxtek BSH-150 bakeable sensor housing (Inficon, NY, U.S.A.) and sealed using high temperature conductive epoxy (Epoxy Technology, H21D Kit, MA, U.S.A.). The QCM was purged with N_2 to prevent deposition on the backside of the crystal [31].

The reactant pulse and purge timing is designated as (t_1, t_2, t_3, t_4) where t_1 is the $TiCl_4$ exposure time, t_2 is the purge after the $TiCl_4$ exposure, t_3 is the EG or

GL dose times, and t_4 is the purge time after the EG or GL exposures. For the TiO_2 ALD and Al_2O_3 ALD, the timing sequences were (2.5, 35, 1.5, 35) and (1, 35, 1, 35), respectively, at 115°C. Silicon wafers with dimensions of 2.5 cm x 2.5 cm were used as the substrates for the ex situ analysis of films grown at different conditions. These wafers had a native SiO_2 oxide with a thickness of ~25 Å. The error bars obtained for titanicone growth using $TiCl_4$ and EG on silicon wafers represent the variation from three samples during the same experiment at different reactor positions. The error bars obtained for titanicone growth using $TiCl_4$ and GL on silicon wafers represent the variation from three different samples after 100, 150, and 200 reaction cycles.

A spectroscopic ellipsometer (M-2000, J. A. Woollam Co., NE, U.S.A.) was used to determine the thickness and refractive index of deposited MLD and ALD films. The optical properties were measured for wavelengths ranging from 239 nm to 1686 nm at an incident angle of 75°. The optical constants, n and k, were determined by analysis of measured ellipsometric parameters, Ψ and Measured data were analyzed using the Tauc-Lorentz oscillator model [32]. The thickness of the MLD films was determined using X-ray reflectivity (XRR). All refractive indices are reported at the sodium D-line reference wavelength of 590 nm unless stated otherwise.

X-ray reflectivity analysis was performed using a high resolution Bede D1 Diffractometer from Bede Scientific. This X-ray diffractometer was equipped with a Cu X-ray tube and monochromator for CuKα radiation at λ=1.54 Å. The XRR

analysis was performed with CuKα1 radiation at λ=1.540 Å after removing the CuKα2 radiation at λ=1.544 Å using a channel cut crystal. A filament current of 40 mA and a voltage of 40 kV were used for the measurements. An XRR scan was performed using a 10 arcsec step size and a 5 s acquisition time. For each sample, the data were fit using the REFS fitting software from Bede Scientific to determine the film thickness, density, and roughness.

X-ray photoelectron spectroscopy (XPS) survey scans were performed using a Physical Electronics PHI Model 5600 spectrometer with a monochromatic AlKα X-ray source with energy of 1486.6 eV. The scans were performed with an electron pass energy of 187 eV and a resolution of 0.8 eV. The photoelectrons were collected using a hemispherical analyzer. XPS enabled the determination of the Ti to O ratio in deposited MLD films.

Elastic modulus and hardness of the MLD films were characterized using a nanoindenter (Nano Dynamic Contact Module (DCM), Agilent Technologies, Inc.) equipped with a diamond Berkovich tip. The data were evaluated according to the Oliver-Pharr method [33]. The Oliver-Pharr method used in conjunction with the continuous stiffness method (CSM) can characterize specimens over a range of thicknesses. The titanicone films had thicknesses of ~500 nm deposited onto Si<100>.

Prior to indentation, the nanoindenter was calibrated using fused silica to obtain the area coefficients for the tip. Indentations were performed to a depth of 100 nm for the titanicone films grown using EG and 50 nm for the titanicone films

grown using GL at a constant loading rate of 0.05 s^{-1}. The maximum load was held for 10 s for stabilization and then rapidly unloaded at the rate of 250 μNs^{-1}. The load was also held at 1% of the maximum load for 30 s to obtain a thermal drift correction. For all indentation experiments, test locations were separated by 100 µm to ensure isolation between the 10 test sites.

Titanicone films were annealed in air for two hours at the set temperature and maintained with a precision of ± 0.1°C in a furnace (Thermolyne-1400, U.S.A.). Some titanicone samples were also subjected to programmed temperature ramping and cooling in the furnace. UV exposure experiments were performed using a 500 Watt Hg vapor light source (Newport Corp., CA, U.S.A.). The spectral emission was restricted to the wavelength region of 350-450 nm. A radiant power of 45 mW/cm^2 was measured at the sample surface.

8.3 Results & Discussion

8.3.1 Titanicone MLD using $TiCl_4$ and Ethylene Glycol

8.3.1.1 Quartz Crystal Microbalance Studies

The QCM measurements for titanicone films grown using $TiCl_4$ and EG were performed at various temperatures from 90 to 170°C. Figure 8.3a displays QCM signals during titanicone growth at 115°C on Al_2O_3 ALD surfaces.

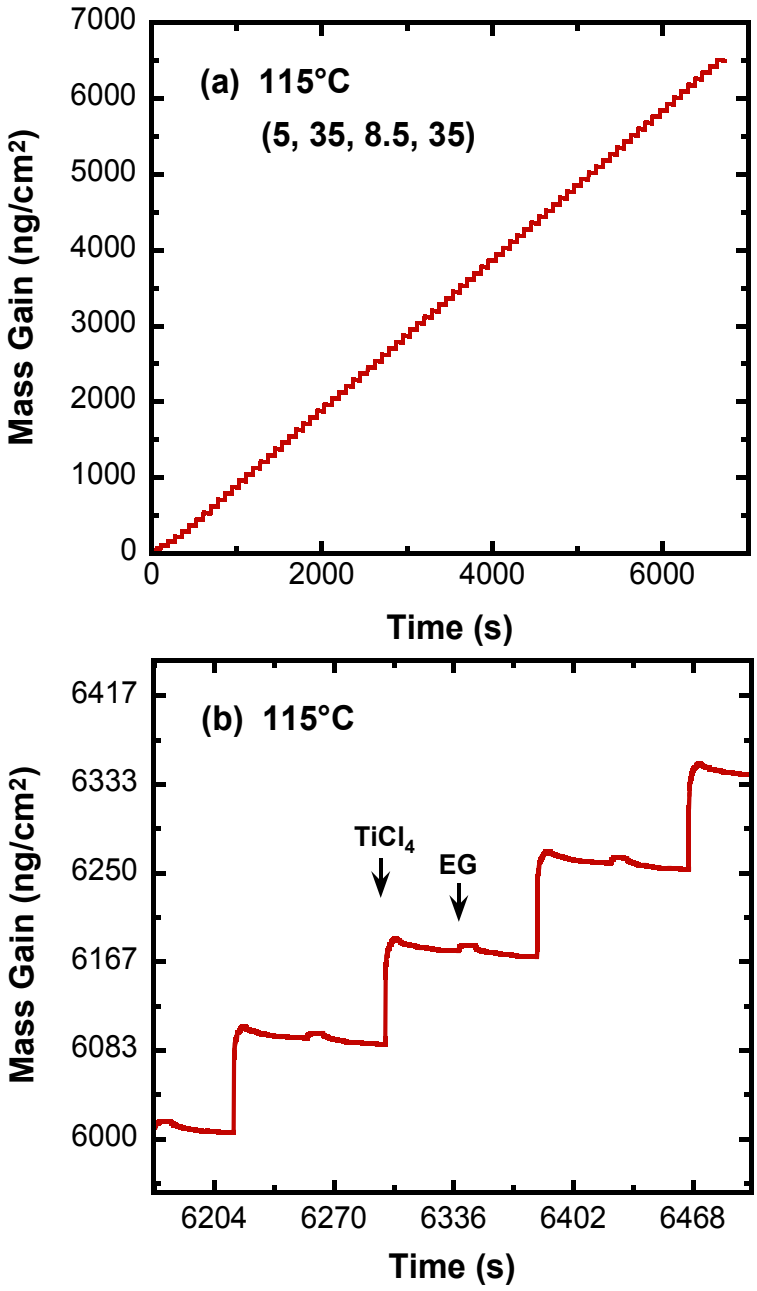

Figure 8.3 QCM measurements of mass gain versus time for titanicone growth on Al_2O_3 ALD surfaces using $TiCl_4$ and EG at 115°C. (a) Growth over 80 reaction cycles using a timing sequence of (5, 35, 8.5, 35). (b) Expanded view of growth during four reaction cycles.

The titanicone growth is reproducible and linear after the initial nucleation period. An expanded view of the QCM signal in the linear growth regime is presented in Figure 8.3b. The $TiCl_4$ dose leads to a large mass gain and the EG dose produces a negligible mass change. A total mass gain of 83 ng/cm^2/cycle was observed at steady state at 115°C for the QCM measurements in Figure 8.3 using a (5, 35, 8.5, 35) timing sequence. The QCM profiles had similar shapes at all deposition temperatures.

The ratio of the mass changes after the $TiCl_4$ and EG exposures in Figure 8.3b can be compared with the predicted ratio of the mass changes from the proposed schematic for the reaction in Figure 8.1. The schematic predicts a small mass gain for the EG reaction that is ~22% of the mass gain for the $TiCl_4$ reaction. In contrast, Figure 8.3b shows a very small mass change for the EG reaction. The mass change for the EG reaction exists on a slowly decreasing mass change that begins after the previous $TiCl_4$ exposure. This slowly decreasing mass change may result from unreacted $TiCl_4$ slowly desorbing from the film after the $TiCl_4$ exposure.

The smaller than expected mass change for the EG reaction may also result from an EG precursor reacting with two TiCl surface species to produce -Ti-$O(CH_2)_2O$-Ti- surface species. These "double reactions" are predicted to display a mass loss that is ~9% of the mass gain from the $TiCl_4$ reaction with two TiOH surface species. The predicted mass gain from the EG reaction is progressively lower for higher proportions of double reactions. In the limit that all the EG reactions occur as double reactions, the film would be composed of $Ti(-O(CH_2)_2O-)_2$

species and the mass change would be negative for the EG reaction. Similar titanium glycolate derivatives have been identified in previous studies [34-36]. The self-limiting behavior of the surface reactions was studied at 90, 100 and 115°C. The QCM results showing mass gain versus $TiCl_4$ and EG exposures are shown in Figure 8.4a and 8.4b, respectively.

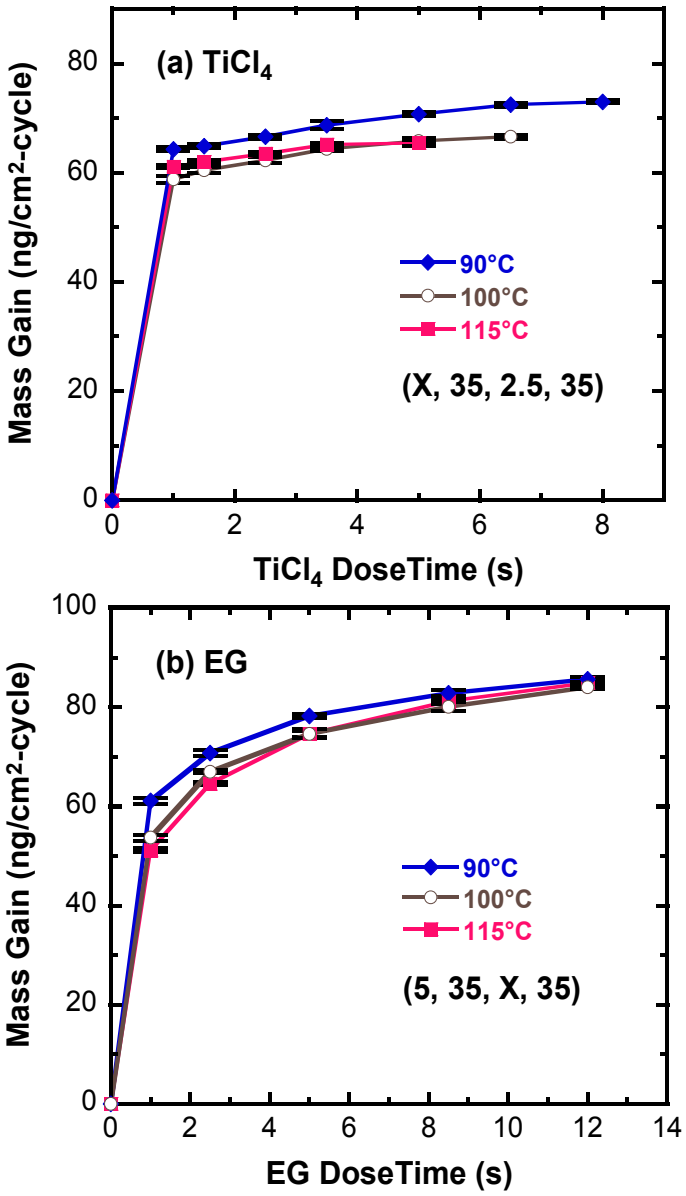

Figure 8.4 QCM measurements of mass gain versus reactant dose time for titanicone growth in the steady state regime at 90, 100 and 115°C. (a) Mass gain versus $TiCl_4$ dose time using a timing sequence of (X, 35, 2.5, 35). (b) Mass gain versus EG dose time using a timing sequence of (5, 35, X, 35).

The timing sequence used for the $TiCl_4$ exposure in Figure 8.4a was (X, 35, 2.5, 35). A 5 s dose of $TiCl_4$ that yields a 25 mTorr·s exposure produces saturation behavior. The timing sequence in Figure 8.4b was (5, 35, X, 35). An 8.5 s dose of EG that yields a 260 mTorr·s exposure produces saturation behavior. A timing sequence of (5, 35, 8.5, 35) was used for all further experiments to ensure that the $TiCl_4$ and EG reactions both reached completion.

QCM measurements were used to examine the effect of purge time after the $TiCl_4$ and EG doses at temperatures from 90 to 135°C. The purge times after the EG doses did not affect the mass gain at all examined temperatures. However, Figure 5 shows that the purge time after the $TiCl_4$ dose results in a slight reduction in mass gain for growth at 90, 100 and 115°C. In contrast, purge times had a much more noticeable affect at 135°C. The mass gains are lower at 135°C and they decrease significantly versus purge time.

The reduction of mass gain versus purge time after the $TiCl_4$ dose may result from unreacted $TiCl_4$ desorption from the titanicone film. $TiCl_4$ desorption was suggested from the QCM results in Figure 3b. $TiCl_4$ desorption would be larger at the higher growth temperature of 135°C. There also may be "double reactions" of EG with $TiCl_4$ that produce $Ti(\text{-}O(CH_2)_2O\text{-})_2$ species in the titanicone film. These

$Ti(-O(CH_2)_2O-)_2$ species may desorb more rapidly at higher growth temperatures and limit the mass gain after the $TiCl_4$ dose.

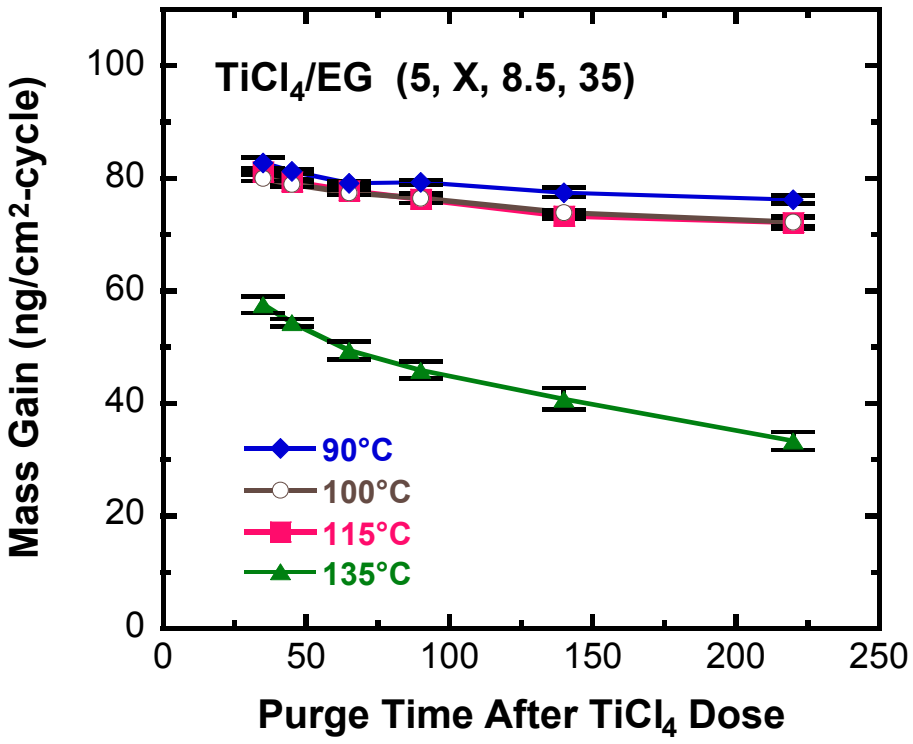

Figure 8.5 QCM measurements of mass gain versus purge time after $TiCl_4$ dose at 90, 100, 115 and 135°C with a timing sequence of (5, X, 8.5, 35).

8.3.1.2 XRR and XPS Analysis

XRR analysis was used to characterize titanicone films grown using $TiCl_4$ and EG at temperatures from 90°C to 135°C. Figure 8.6 shows the film thickness versus number of reaction cycles derived from XRR analysis using a timing sequence of (5, 35, 8.5, 35). A growth rate of ~4.5 Å/cycle is obtained from the slope of the fitted line in Figure 8.6. The titanicone films with a thickness of ~450 Å after 100 MLD cycles were visually very smooth and uniform. The titanicone films with a

thickness of ~100 Å after 25 cycles had a root mean squared (RMS) roughness of ~4 Å. The titanicone films with a thickness of ~450 Å after 100 cycles had an RMS roughness of ~6.3 Å.

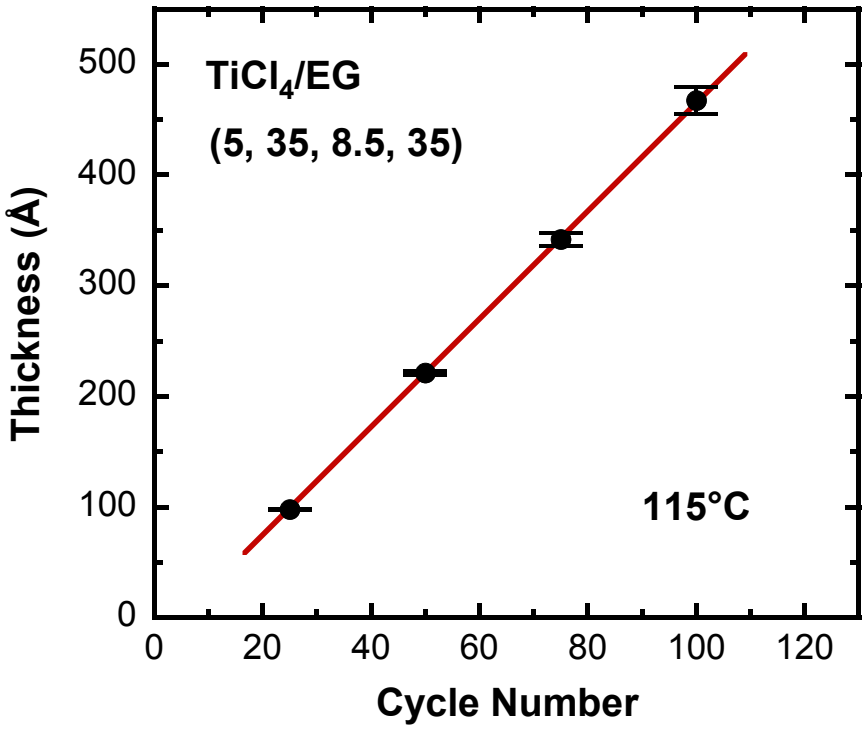

Figure 8.6 XRR measurements of film thickness versus cycle number for titanicone growth on Si<100> wafers using $TiCl_4$ and EG at 115°C with a timing sequence of (5, 35, 8.5, 35).

The titanicone growth rate and density versus deposition temperature were measured by depositing 50 MLD cycles directly on Si<100> wafers. The growth rates and densities are displayed in Figure 8.7. The film growth rate is 4.6 Å/cycle at 90°C and slightly decreases to 4.4 Å/cycle at temperatures between 100°C and 115°C. An additional reduction to 4.1 Å/cycle is observed at 125°C before a large

decrease to 1.5 Å/cycle at 135°C. The large error bars for the growth rate at 135°C occur because of film thickness gradients within the reactor.

Figure 8.7 shows that density of deposited films remains fairly constant at ~1.8 g/cm^3 over the full range of temperatures.

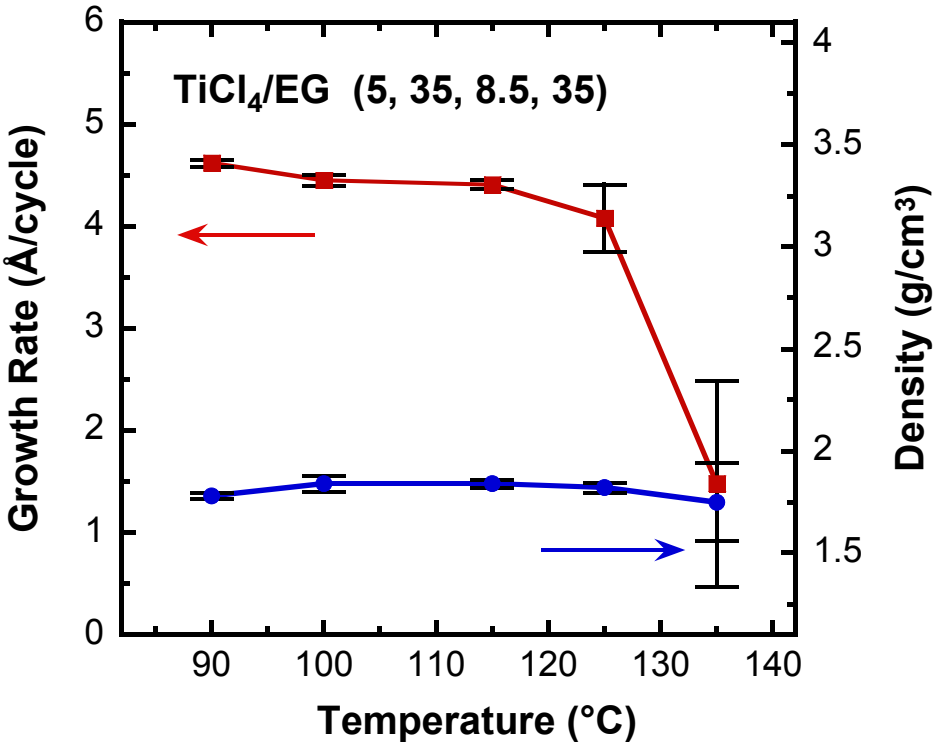

Figure 8.7 XRR measurements of growth rate and density versus temperature for titanicone growth on Si<100> wafers using $TiCl_4$ and EG with a timing sequence of (5, 35, 8.5, 35). The film thicknesses and density were measured after 50 reaction cycles.

The growth rate of 4.6 Å/cycle at 100 and 115°C on the silicon wafers is in good agreement with the growth rate of 83 ng/cm^2/cycle from the QCM studies and the density of ~1.8 g/cm^3 from XRR analysis. XRR analysis also revealed that the RMS roughness for the films in Figure 7 grown using 50 MLD cycles was constant at ~5.2

Å. These results suggest that the optimal temperature range for titanicone film growth using EG is between 90-115°C. 115°C is the preferred temperature because of the larger temperature difference between the EG source and the reaction chamber.

Figure 8.7 also shows that the titanicone growth rate drops dramatically at 135°C. This drop may be related to the decreasing mass gain versus purge time after the $TiCl_4$ dose at 135°C that was observed in Figure 5. Therefore, the reduction of growth rate at 135°C in Figure 7 may be attributed to the desorption of unreacted $TiCl_4$ species. In addition, depending on the fraction of "double reactions" between EG and $TiCl_4$, the reduction in growth rate may be caused by the desorption of $Ti(-O(CH_2)_2O-)_2$ species.

The stability of titanicone films was determined by monitoring the change in thickness of films over an extended period of time in atmosphere following deposition. XRR analysis indicated a 20% thickness reduction over 25 days for films with an initial thickness of 220 Å. The film thickness decreased by about 15% in the first 5 days of air exposure. The thickness reduction for the titanicone film grown using $TiCl_4$ and EG is similar to the thickness reduction observed for observed for alucone films grown using TMA and EG [9].

XPS survey scans of several titanicone films deposited at 115°C using a timing sequence of (5, 35, 8.5, 35) showed the presence of chlorine impurities ranging from 3.0 to 3.6 at. %. Titanium and oxygen content was 8.2 and 32.8 at. %, respectively, indicating a Ti:O ratio of ~1:4. Efforts to reduce the chlorine content

by using a water dose after the EG dose did not result in the reduction of chlorine content. In addition, grazing incidence X-ray diffraction scans of titanicone films deposited at 115°C showed no diffraction peaks. This observation is consistent with an amorphous titanicone film.

The presence of chlorine in the titanicone films and the probability of "double reactions" suggests an alternative schematic for the growth of titanicone films using EG. The new schematic is shown in Figure 8.8.

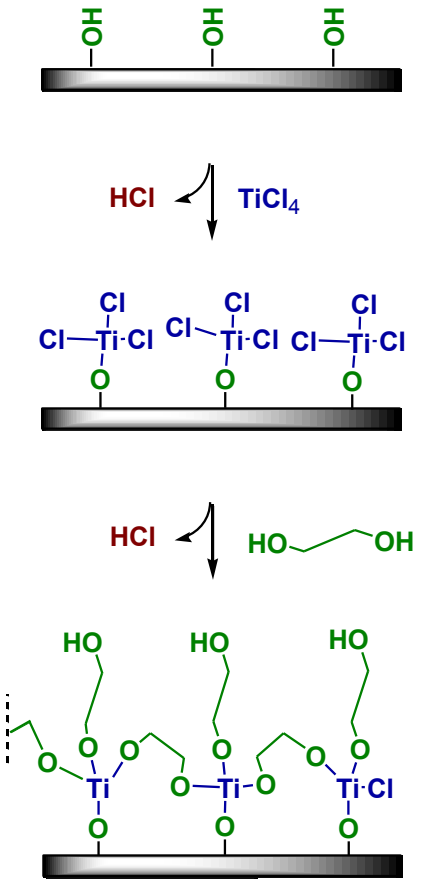

Figure 8.8 Alternative schematic of titanicone MLD using $TiCl_4$ and ethylene glycol. This schematic shows chlorine incorporated in the titanicone film and a larger fraction of "double reactions" than the schematic in Figure 8.1. The Cl:Ti ratio in the schematic is similar to the Cl:Ti ratio observed by XPS analysis. The greater

number of double reactions compared with the schematic in Figure 8.1 will also produce a smaller predicted mass gain for the EG exposure.

8.3.2 Titanicone MLD using $TiCl_4$ and Glycerol

8.3.2.1 Quartz Crystal Microbalance Studies

Figure 8.9a shows the mass gain versus time during titanicone MLD using $TiCl_4$ and GL with a (1, 30, 1, 30) timing sequence at 130°C. This titanicone film was deposited on a TiO_2 ALD substrate grown using $TiCl_4$ and H_2O. There is only a short nucleation period of ~3 cycles on TiO_2 ALD substrates. The titanicone growth is then extremely linear.

Figure 8.9b displays an expanded view of the mass gains versus time in the steady state growth regime. The total mass gain is 50.3 ng/cm^2/cycle. The $TiCl_4$ dose accounts for a 48.6 ng/cm^2 mass gain. The GL dose accounts for a 1.7 ng/cm^2 mass gain. QCM measurements were also conducted at 150, 170, 190 and 210°C. The QCM signal shape during reactant exposures was very similar at all temperatures.

The conditions for self-limiting reactions were also determined for temperatures ranging from 130 to 210°C. The $TiCl_4$ and GL reactions both reached completion with ~1 second exposures. $TiCl_4$ doses of 1 s yielded $TiCl_4$ exposures of 10 mTorr·s. GL doses of 1 s yielded GL exposures of 15 mTorr·s. Temperature-dependent QCM measurements revealed a gradual decrease in titanicone growth rate at higher temperatures. The growth rate was ~49 ng/cm^2/cycle at 130°C and decreased to ~34 ng/cm^2/cycle at 210°C with a (1, 30, 1, 30) timing sequence.

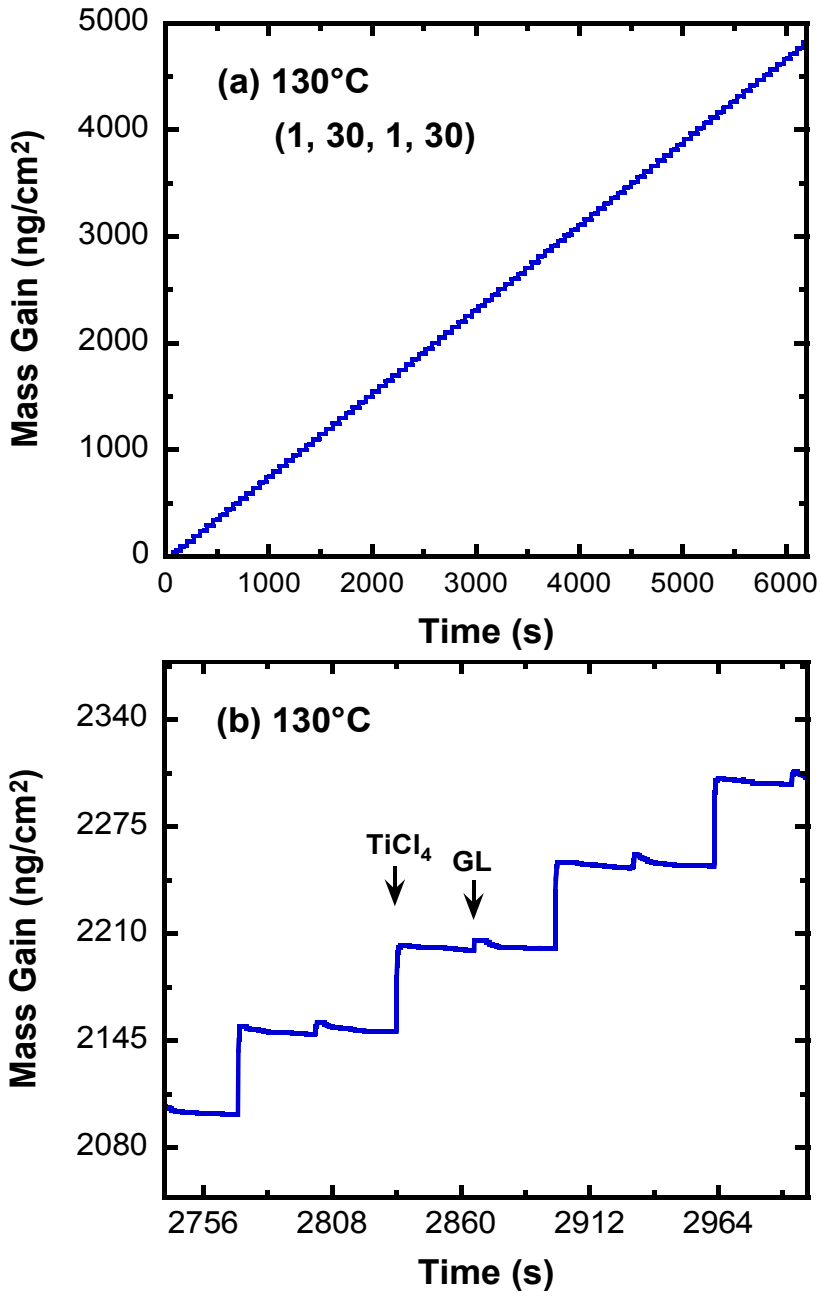

Figure 8.9 QCM measurements of mass gain versus time for titanicone growth on TiO_2 ALD surfaces using $TiCl_4$ and GL at 130°C. (a) Growth over 90 reaction cycles using a timing sequence of (1, 30, 1, 30). (b) Expanded view of growth during four reaction cycles.

8.3.2.2 XRR and XPS Analysis

The growth rate and density ware measured for titanicone films grown using $TiCl_4$ and GL. Figure 8.10 presents the results from XRR analysis for temperatures from 130 to 210°C. Deposition below 130°C was not possible because the GL reactant vessel is heated to 120°C to increase the vapor pressure. These films were deposited using 100, 150, and 200 MLD cycles with a (1, 30, 1, 30) timing sequence on Si<100> wafers. Figure 10 indicates that the titanicone growth rate at 130°C is 2.8 Å/cycle.

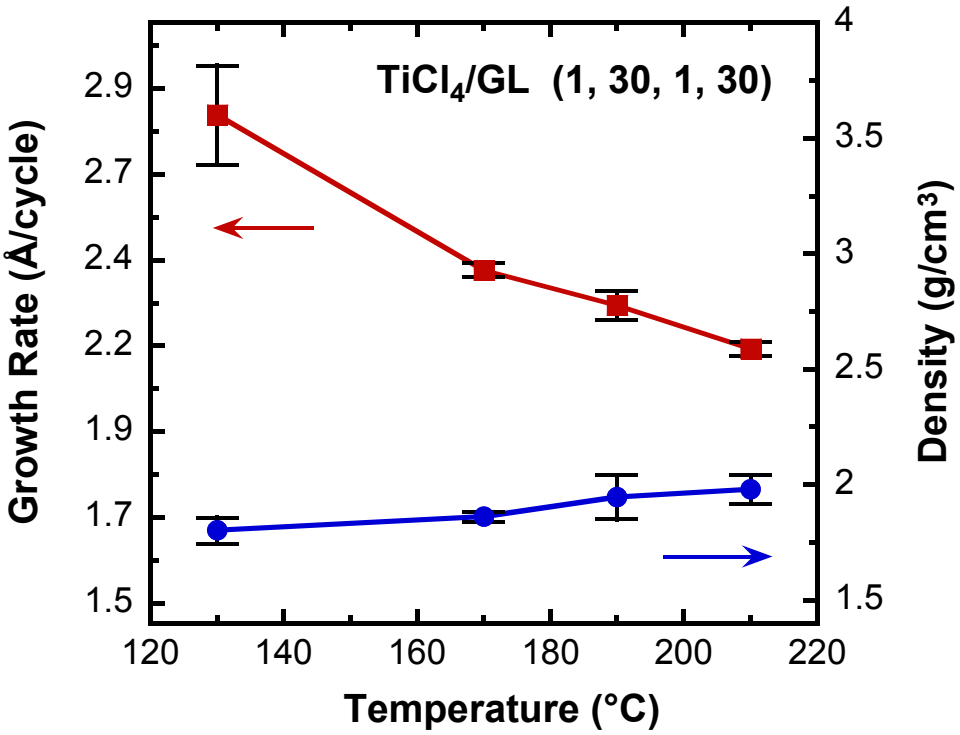

Figure 8.10 XRR measurements of growth rate and density versus temperature for titanicone growth on Si<100> wafers using $TiCl_4$ and GL with a timing sequence of (1, 30, 1, 30). The film thicknesses and density were measured after 50 reaction cycles.

The growth rate gradually decreases to 2.1 Å/cycle at 210°C. This observation of a growth rate that decreases at higher temperatures is consistent with the QCM results. This temperature dependence is also similar to earlier results for the temperature dependence of alucone and zincone MLD [9, 11]. The density of the titanicone films grown using GL increases slightly from 1.8 g/cm^3 at 130°C to 1.98 g/cm^3 at 210°C. The density of 1.8 g/cm^3 is similar to the density of the titanicone films grown using EG. These titanicone density values are much lower than the density of 3.7 g/cm^3 for TiO_2 ALD films grown at 115°C using $TiCl_4$ and H_2O.

The average RMS roughness of titanicone films grown using GL at various temperatures was ~5 Å for 100 Å thick films. XPS survey scans were performed for the titanicone films deposited at 150°C using GL with a (1, 30, 1, 30) timing sequence. These films had chlorine impurities at the level of 1.6 at. %. The titanium and oxygen content was 5.7 and 30.2 at. %, respectively. These results are consistent with a Ti:O ratio of ~1:5. This Ti:O ratio indicates that there is more oxygen in the titanicone films grown using GL. More oxygen is consistent with additional bridging between the titanium centers and higher oxygen coordination numbers in the titanicone films grown using GL.

XRR analysis also revealed that the titanicone films grown using GL did not display a thickness reduction upon exposure to air. Instead of a reduction, a small increase in the thickness was observed after ambient exposure. These results are also consistent with more bridging between the polymer chains improving the stability of the titanicone films.

8.3.3 Titanicone Film Properties

8.3.3.1 Mechanical Properties

Elastic modulus and hardness of titanicone films were determined using nanoindentation techniques. Figure 8.11 shows nanoindentation results for titanicone films with a thickness of ~500 nm grown using EG and GL at 115°C and 150°C, respectively.

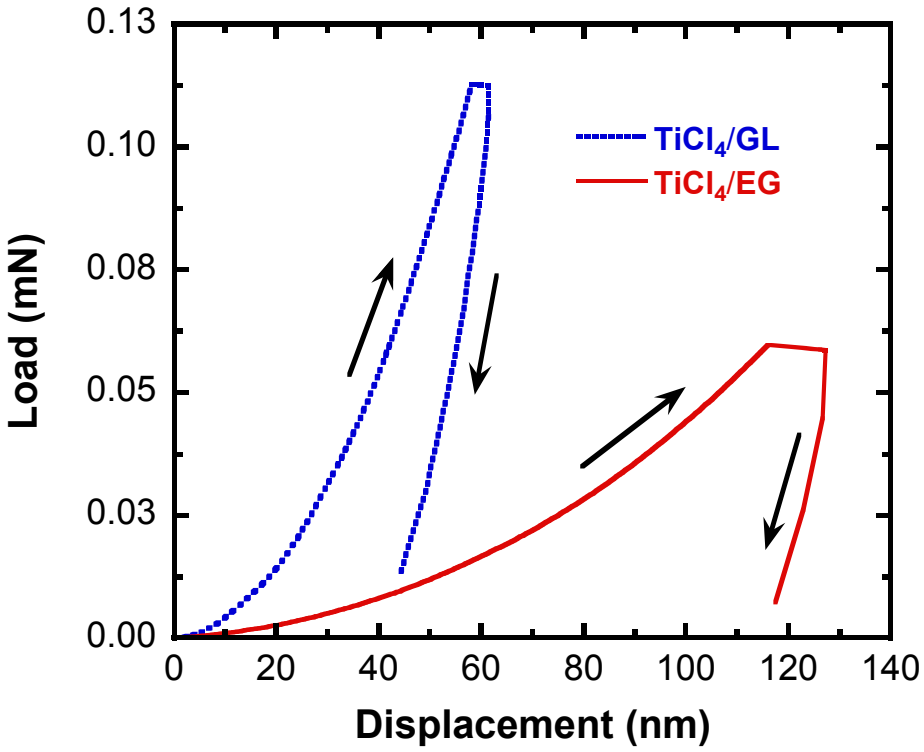

Figure 8.11 Nanoindentation measurements of load versus displacement for titanicone films with a thickness of ~500 nm. The titanicone films were grown using EG and GL at 115°C and 150°C with timing sequences of (4.5, 60, 4.5, 60) and (1, 30, 1, 30), respectively.

Arrows in the graph show the direction of loading and unloading. Analysis of the data indicates that titanicone films grown using EG have an elastic modulus of 8.04

± 0.40 GPa and a hardness of 0.25 ± 0.01 GPa. In comparison, the titanicone films grown using GL have an elastic modulus of 30.6 ± 0.1 GPa and a hardness of 2.62 ± 0.09 GPa.

The elastic modulus and hardness values for titanicone films grown using EG are the lowest of those reported for metalcone films. The lowest earlier values are an elastic modulus of 13.2 ± 5.0 GPa and hardness of 0.27 ± 0.10 GPa for the ABC alucone MLD films deposited at 90°C [37]. The elastic modulus of titanicone films grown using GL is similar to previously reported values of 36.8 ± 5.6 GPa for alucone films deposited using TMA and EG at 150°C [37]. However, the hardness of the alucone films is significantly lower at 0.47 ± 0.07 GPa [37]. The hardness of the titanicone films grown using either EG or GL is also much lower than the hardness of 125 ± 10.0 GPa for TiO_2 ALD [38].

8.3.3.2 Effect of Thermal Annealing

Annealing of metalcone films can potentially result in low density mesoporous thin metal oxide films [39, 40]. Figure 8.12 shows film thicknesses derived from XRR analysis versus annealing temperature for titanicone films grown using EG and GL. The initial film thicknesses were ~450 Å for the titanicone film deposited using EG at 115°C and ~600 Å for the titanicone film deposited using GL at 150°C. The titanicone film deposited using GL has a better thermal stability up to 400°C than the titanicone film deposited using EG.

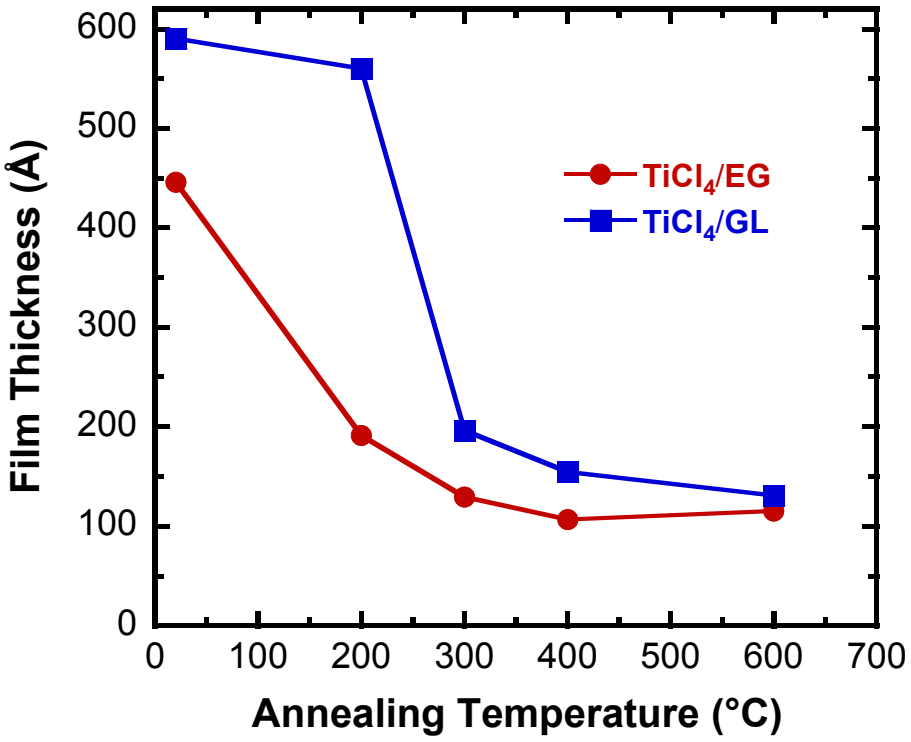

Figure 8.12 XRR measurements of film thickness versus annealing temperature in air for titanicone films grown using EG and GL at 115°C and 150°C, with timing sequences of (5, 35, 8.5, 35) and (1, 30, 1, 30), respectively.

The higher stability could result from the higher network connectivity in the titanicone film grown using GL. Similar behavior has been observed in thermogravimetric analysis of solution-derived titanium glycolate and titanium glycerolate materials. The glycol-based film has a decomposition temperature at ~320°C [36, 41]. In comparison, the glycerol-based film has a higher decomposition temperature of ~350°C [42].

The electron density of the annealed titanicone films versus temperature for the same samples in Figure 8.12 is presented in Figure 8.13. The electron density is

reported rather than the mass density because the exact composition of the titanicone films versus annealing is not known [43, 44].

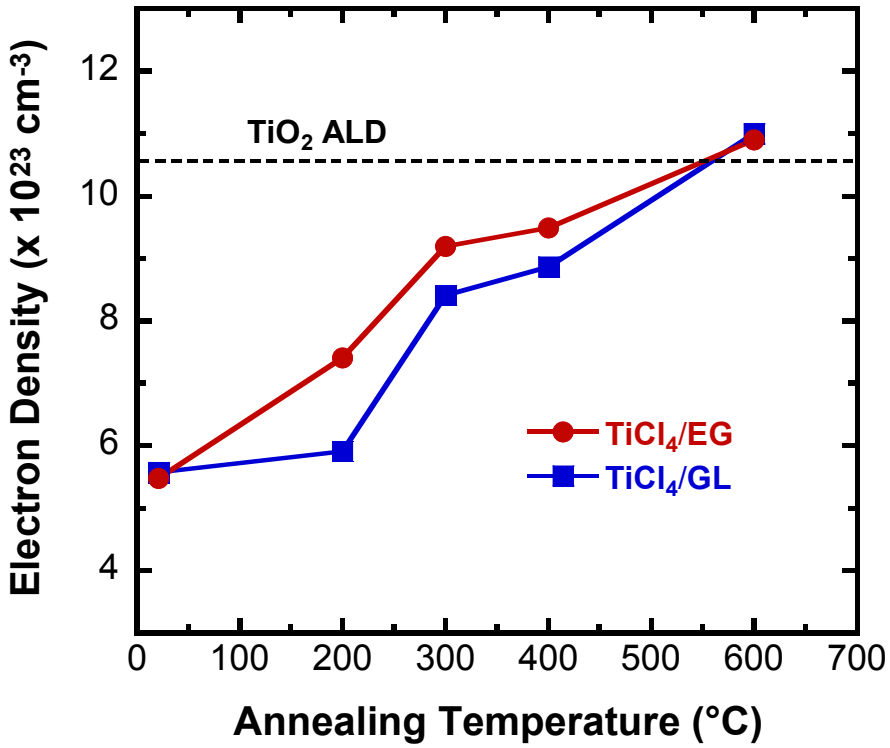

Figure 8.13 XRR measurements of electron density versus annealing temperature in air for titanicone films grown using EG and GL at 115°C and 150°C, with timing sequences of (5, 35, 8.5, 35) and (1, 30, 1, 30), respectively.

The electron density of the TiO_2 ALD films grown using $TiCl_4$ and H_2O at 115°C is shown for comparison. There is a nearly linear increase in electron density with annealing temperature that is consistent with an increase in film density. Films annealed at temperatures above 400°C displayed an electron density slightly higher than the electron density of TiO_2 ALD films grown at 115°C. No significant difference in final electron density was observed for titanicone samples grown using $TiCl_4$ and EG that were incrementally heated at 1°C/min to the target temperature

compared with samples that were placed in the furnace at the target temperature. Titanicone films grown using $TiCl_4$ and EG exhibited X-ray diffraction peaks consistent with anatase TiO_2 after annealing to 400°C.

XPS depth profiles of titanicone films grown using both EG and GL and then annealed at 400°C indicated no carbon content above the detection limit of the instrument at 0.1 at. %. These films annealed at 400°C have been converted to TiO_2. In addition, no significant increase in film roughness was observed for the annealed samples compared with the original, titanicone films. Titanicone films grown using EG and GL and then annealed at 400°C had RMS roughnesses of 7 Å and 5 Å, respectively.

8.3.3.3 Optical Properties

Figure 8.14a shows the refractive index, n, versus wavelength for titanicone films grown using EG at 115°C with a thickness of 250 Å. The refractive index is also shown for titanicone films grown using GL at 150°C with a thickness of 600 Å. The titanicone films grown using EG and GL exhibited refractive indices at 590 nm of 1.7 and 1.8, respectively. The refractive index of TiO_2 ALD films deposited at 115°C is also displayed for comparison. The refractive indices for the TiO_2 ALD films are much higher than the titanicone films. The TiO_2 ALD film has a refractive index of 2.4 at 590 nm. A lowering of the refractive index for the metalcones compared with the parent metal oxides has also been observed for other metalcones [9]. In addition, solution-derived titanium glycolate nanoparticles have a lower refractive index of 1.88 [45].

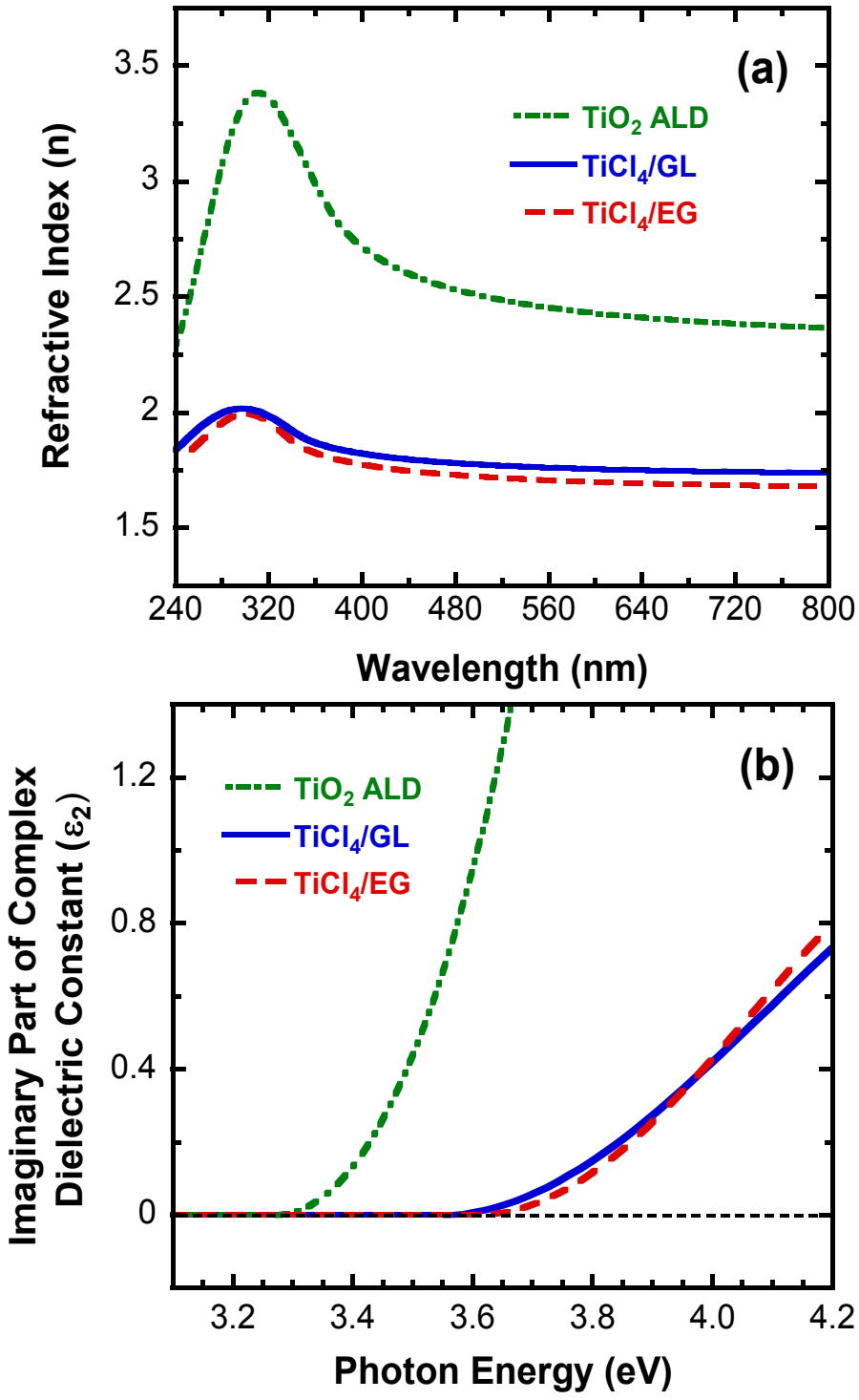

Figure 8.14 Optical constants of titanicone MLD and TiO_2 ALD films. The titanicone films were grown using EG and GL at 115°C and 150°C with timing sequences of (5, 35, 8.5, 35) and (1, 30, 1, 30), respectively. The TiO_2 ALD film was

grown at 115°C. (a) Refractive index versus wavelength and (b) Imaginary part of complex dielectric constant versus photon energy.

Refractive index values of ~2.3 at 590 nm were also measured for titanicone films annealed at 400°C. The refractive index of ~2.3 is very similar to the refractive index of TiO_2 ALD films grown at 115°C. The comparable refractive indices and electron densities for the annealed titanicone films and the TiO_2 ALD films argue that the thermally annealed titanicone films have been converted to non-porous TiO_2 films.

Band gaps for the titanicone films grown using EG and GL at 115°C and 150°C, respectively, were derived from the dependence of the imaginary part of the complex dielectric constant, ε_2, on photon energy [32]. A plot of □$_2$ versus photon energy is shown in Figure 14b. The bandgap is determined at the point where ε_2 becomes non-zero [32]. The band gaps of the titanicone films grown using EG and GL are nearly identical and equal to ~3.6 eV. In comparison, the bandgap for the TiO_2 ALD film is ~3.3 eV. This bandgap for TiO_2 ALD is in good agreement with previously reported values [27]. The blue shift in the bandgap for the titanicone films relative to the TiO_2 ALD film is consistent with smaller "TiO_2 units" in the titanicone films that display quantum confinement effects. A bandgap of 3.34 eV was also observed for rod-like titanium glycolate [46].

8.3.3.4 Effect of UV Exposure

The titanicone films were also exposed to ultraviolet light to evaluate their potential for photolithography. The titanicone film with an initial thickness of ~500

Å was grown using EG at 115°C. Figure 8.15 shows titanicone film thickness versus UV exposure time.

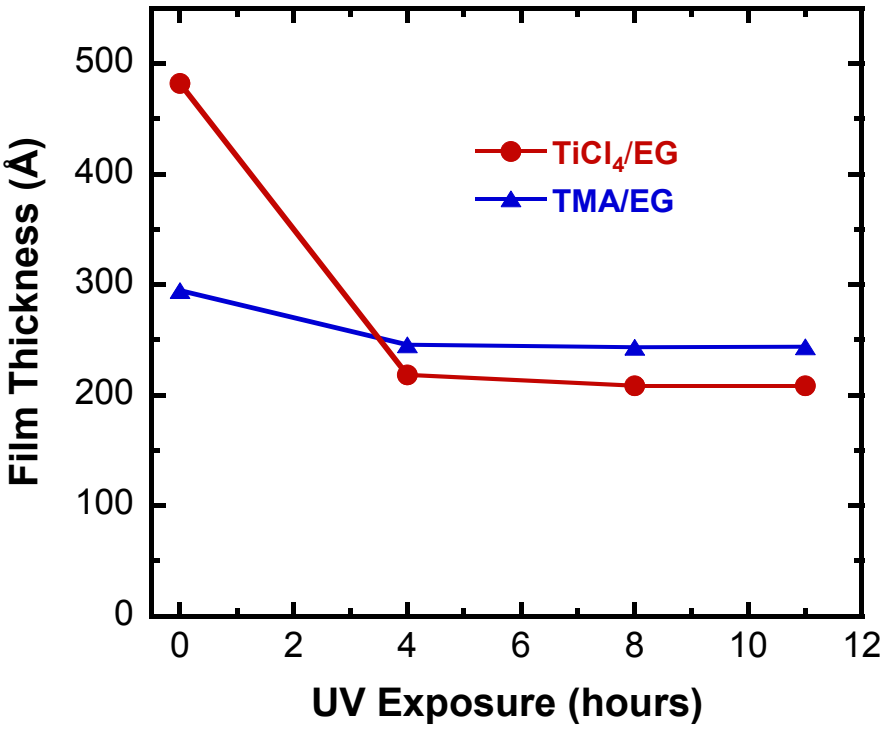

Figure 8.15 XRR measurements of film thickness versus UV exposure for titanicone films grown at 115°C using $TiCl_4$ and EG with a timing sequence of (5, 35, 8.5, 35) and alucone films grown at 115°C using TMA and EG with a timing sequence of (1, 35, 4.5, 35).

After the first 4 hours of UV exposure, the film thickness was reduced to about half of its original thickness. Only a slight reduction in thickness was observed when the exposure time was extended to 8 hours. No change in thickness was detected after 8 hours.

An XPS depth profile analysis was performed for the titanicone film after 11 hours of UV exposure. This XPS analysis showed no carbon in the film within

the XPS detection limit of 0.1 at. %. The titanicone film has been converted to TiO_2 after 11 hours of UV exposure. Most of this conversion has probably been achieved after 4 hours of UV exposure. XRR measurements of the UV-exposed sample revealed a density for the TiO_2 film of 2.7 g/cm^3. This density value is about 27% less than the TiO_2 ALD film grown at 115°C and the TiO_2 films derived from thermal annealing. This TiO_2 film is believed to be porous. BET surface area measurements are needed to confirm the film porosity.

The UV lamp may be heating the film and causing the changes from thermal rather than photocatalytic processes. To check for thermal annealing effects, an alucone MLD film with a thickness of ~300 Å was used as a control sample. Alucone films with a thickness of ~300 Å were deposited at 115°C using TMA and EG [9]. Because alucone or Al_2O_3 are not known to be photocatalytically active, minor UV absorption and minimal thickness changes are expected after UV exposure.

Figure 8.15 shows the result of UV exposure on this alucone film. Four hours of UV exposure resulted in only a 17% reduction in the alucone film thickness. No change in thickness was observed for longer UV exposures. These results argue that the effects of heat generated from the UV lamp are minimal. The thickness of alucone films grown using TMA and EG is known to reduce by ~22% in ambient after 5-6 days [9]. In addition, the possible effects of ozone generated by the UV exposure are also small. The comparison between the titanicone and

alucone samples suggest that photolithography of titanicones to yield a patterned TiO_2 film is viable.

8.4 Conclusions

A new class of metalcone films known as "titanicones" was grown using $TiCl_4$ and either EG or GL. Titanicone films were grown using $TiCl_4$ and EG at temperatures between 90-135°C and $TiCl_4$ and GL at higher temperatures between 130-210°C. QCM measurements showed that the surface chemistry for titanicone MLD was self-limiting for $TiCl_4$ and either EG or GL exposures. XRR analysis revealed that the growth rate of titanicone films grown using EG was ~4.5 Å/cycle from 90 to 115°C. The growth rate of titanicone films grown using GL decreased with temperature from 2.8 Å/cycle at 130°C to 2.1 Å/cycle at 210°C. QCM measurements were in agreement with the XRR analysis given a titanicone film density of 1.7-1.8 g/cm^3.

The differences between the EG and GL reactants change the network bonding in the titanicone films. Because of the extra hydroxyl group for chemical bonding, GL should increase the bridging between the polymer chains in the titanicone film. This additional bridging between the titanium centers should change the titanicone film properties and improve the film stability. Nanoindentation experiments revealed that the elastic modulus and hardness of the titanicone films grown using GL were much higher than titanicone films grown using EG. Annealing experiments also observed a higher thermal stability for the titanicone films grown using GL.

The titanicone films can also be processed using either thermal annealing or UV light exposure to yield TiO_2 films. Thermal annealing the titanicone films in air was observed to remove the carbon constituents and yield TiO_2 films with a density of ~3.3 g/cm^3 that is slightly higher than the density of TiO_2 ALD films. The titanicone films absorbed light in the ultraviolet and displayed an absorption threshold that was consistent with an optical bandgap of ~3.6 eV. Prolonged ultraviolet exposures on the titanicone films produced porous TiO_2 films with a low density of 2.7 g/cm^3. UV-exposed titanicone MLD films could be used to produce porous TiO_2 films for a variety of applications.

8.5 Acknowledgements

This work was funded by the National Science Foundation. Equipment used in this research was obtained from the Air Force Office of Scientific Research. Additional personnel support was received from the DARPA Center on Nanoscale Science and Technology for Integrated Micro/Nano-Electromechanical Transducers (iMINT) funded by DARPA/MEMS S&T Fundamentals Program (HR0011-06-1-0048). The authors would like to thank Noemi Leick from Eindhoven University of Technology in the Netherlands for her assistance with the spectroscopic ellipsometry analysis. In addition, the authors thank Kalvis Terauds in the Department of Mechanical Engineering at the University of Colorado for his support with the UV experiments.

8.6 References

1. George, S.M., Atomic Layer Deposition: An Overview. Chemical Reviews, 2010. **110**: p. 111-131.

2. George, S.M., B. Yoon, and A.A. Dameron, Surface Chemistry for Molecular Layer Deposition of Organic and Hybrid Organic-Inorganic Polymers. Accounts of Chemical Research, 2009. **42**(4): p. 498-508.

3. Yoshimura, T., S. Tatsuura, and W. Sotoyama, Polymer films formed with monolayer growth steps by molecular layer deposition. Applied Physics Letters, 1991. **59**(4): p. 482.

4. Yoshimura, T., et al., Quantum wire and dot formation by chemical vapor deposition and molecular layer deposition of one-dimensional conjugated polymer. Applied Physics Letters, 1992. **60**(3): p. 268.

5. Adamczyk, N.M., A.A. Dameron, and S.M. George, Molecular Layer Deposition of Poly(p-phenylene terephthalamide) Films Using Terephthaloyl Chloride and p-Phenylenediamine. Langmuir, 2008. **24**: p. 2081-2089.

6. Du, Y. and S.M. George, Molecular Layer Deposition of Nylon 66 Films Examined Using in Situ FTIR Spectroscopy. Journal of Physical Chemistry C, 2007. **111**: p. 8509-8617.

7. Loscutoff, P.W., H.-B.-R. Lee, and S.F. Bent, Deposition of Ultrathin Polythiourea Films by Molecular Layer Deposition. Chemistry of Materials, 2010. **22**: p. 5563-5569.

8. Li, Y., D. Wang, and J.M. Buriak, Molecular Layer Deposition of Thiol-Ene Multilayers on Semiconductor Surfaces. Langmuir, 2010. **26**(2): p. 1232-1238.

9. Dameron, A.A., et al., Molecular Layer Deposition of Alucone Polymer Films Using Trimethylaluminum and Ethylene Glycol. Chemistry of Materials, 2008. **20**: p. 3315-3326.

10. Peng, Q., et al., "Zincone" Zinc Oxide-Organic Hybrid Polymer Thin Films Formed by Molecular Layer Deposition. Chemistry of Materials, 2009. **21**(5): p. 820-830.

11. Yoon, B., et al., Molecular Layer Deposition of Hybrid Organic-Inorganic Polymer Films using Diethylzinc and Ethylene Glycol. Chemical Vapor Deposition, 2009. **15**: p. 112-121.

12. George, S.M., et al., Metalcones: Hybrid Organic-Inorganic Films Fabricated Using Atomic and Molecular Layer Deposition Techniques. Journal for Nanoscience and Nanotechnology, 2011. **11**(9): p. 7948-7955.

13. Seghete, D., et al., Importance of Trimethylaluminum Diffusion in Three-Step ABC Molecular Layer Deposition Using Trimethylaluminum, Ethanolamine, and Maleic Anhydride. Langmuir, 2010. **26**(24): p. 19045-19051.

14. Yoon, B., et al., Molecular Layer Deposition of Hybrid Organic-Inorganic Alucone Polymer Films Using a Three-Step ABC Reaction Sequence. Chemistry of Materials, 2009. **21**(22): p. 5365-5374.

15. Gong, B., Q. Peng, and G.N. Parsons, Conformal Organic - Inorganic Hybrid Network Polymer Thin Films by Molecular Layer Deposition using Trimethylaluminum and Glycidol. Journal of Physical Chemistry B, 2011. **115**(19): p. 5930-5938.

16. Lee, Y., et al., Molecular Layer Deposition of Aluminum Alkoxide Polymer Films Using Trimethylaluminum and Glycidol. Langmuir, 2011. **27**(24): p. 15155-15164.

17. Klepper, K.B., O. Nilsen, and H. Fjellvag, Deposition of thin films of organic-inorganic hybrid materials based on aromatic carboxylic acids by atomic layer deposition. Dalton Transactions, 2010. **39**(48): p. 11628-11635.

18. Klepper, K.B., et al., Atomic layer deposition of organic-inorganic hybrid materials based on saturated linear carboxylic acids. Dalton Transactions, 2011. **40**(17): p. 4636-4646.

19. Lee, B.H., et al., Vapor-Phase Molecular Layer Deposition of Self-Assembled Multilayers for Organic Thin-Film Transistor. Journal for Nanoscience and Nanotechnology, 2009. **9**(12): p. 6962-6967.

20. Lee, B.H., et al., Rapid Vapor-Phase Fabrication of Organic-Inorganic Hybrid Superlattices with Monolayer Precision. Journal of the American Chemical Society, 2007. **129**: p. 16034-16041.

21. Cho, S., et al., High-Performance Two-Dimensional Polydiacetylene with a Hybrid Inorganic-Organic Structure. Angewandte Chemie International Edition, 2011. **50**(12): p. 2742-2746.

22. Cordero, N., J. Yoon, and Z.G. Suo, Channel cracks in a hermetic coating consisting of organic and inorganic layers. Applied Physics Letters, 2007. **90**(11).

23. Graff, G.L., R.E. Williford, and P.E. Burrows, Mechanisms of vapor permeation through multilayer barrier films: Lag time versus equilibrium permeation. Journal of Applied Physics, 2004. **96**(4): p. 1840-1849.

24. Abdulagatov, A.I., et al., Al2O3 and TiO2 ALD on Copper for Water Corrosion Resistance. ACS Applied Materials & Interfaces, 2011. **3**: p. 4593-4601.

25. Liu, J.X., et al., Sol-gel deposited TiO2 film on NiTi surgical alloy for biocompatibility improvement. Thin Solid Films, 2003. **429**(1-2): p. 225-230.

26. Shabalovskaya, S.A., On the nature of the biocompatibility and on medical applications of NiTi shape memory and superelastic alloys. Biomedical Engineering, 1996. **6**(4): p. 267-289.

27. Linsebigler, A.L., G.Q. Lu, and J.T. Yates, Photocatalysis on TiO2 Surfaces: Principles, Mechanisms, and Selected Results. Chemical Reviews, 1995. **95**(3): p. 735-758.

28. Bach, U., et al., Solid-state dye-sensitized mesoporous TiO2 solar cells with high photon-to-electron conversion efficiencies. Nature, 1998. **395**(6702): p. 583-585.

29. Gratzel, M., Photoelectrochemical cells. Nature, 2001. **414**(6861): p. 338-344.

30. Poodt, P., et al., Spatial atomic layer deposition: A route towards further industrialization of atomic layer deposition. Journal of Vacuum Science & Technology A, 2012. **30**(1).

31. Elam, J.W., M.D. Groner, and S.M. George, Viscous flow reactor with quartz crystal microbalance for thin film growth by atomic layer deposition. Review of Scientific Instruments, 2002. **73**(8): p. 2981-2987.

32. Fujiwara, H., Spectroscopic Ellipsometry: Principles and Applications2007, West Sussex, England: John Wiley & Sons, Ltd.

33. Oliver, W.C. and G.M. Pharr, Measurement of hardness and elastic modulus by instrumented indentation: advances in understanding and refinements to methodology. Journal of Materials Research, 2004. **19**: p. 3-20.

34. Bradley, D.C., et al., Alkoxo and Aryloxo Derivatives of Metals, 2001, San Diego: Academic Press.

35. Reeves, R.E. and L.W. Mazzeno, The Composition of Some Tetra-t-butyl Titanate-Glycol Reaction Products. Journal of the American Chemical Society, 1954. **76**(9): p. 2533-2536.

36. Wang, D., et al., Hydrothermal synthesis and characterization of a novel one-dimensional titanium glycolate complex single crystal: Ti(OCH2CH2O)2. Chemistry of Materials, 1999. **11**(8): p. 2008-2012.

37. Miller, D.C., et al., Thermomechanical properties of aluminum alkoxide (alucone) films created using molecular layer deposition. Acta Materialia, 2009. **57**: p. 5083-5092.

38. Latella, B.A., et al., Enhanced adhesion of atomic layer deposited titania on polycarbonate substrates. Thin Solid Films, 2007. **515**(5): p. 3138-3145.

39. Liang, X., et al., Nanocoating Hybrid Polymer Films on Large Quantities of Cohesive Nanoparticles by Molecular Layer Deposition. AIChE Journal, 2009. **55**(4): p. 1030-1039.

40. Liang, X.H., et al., Ultra-thin microporous-mesoporous metal oxide films prepared by molecular layer deposition (MLD). Chemical Communications, 2009(46): p. 7140-7142.

41. Jiang, X.C., et al., Ethylene glycol-mediated synthesis of metal oxide nanowires. Journal of Materials Chemistry, 2004. **14**(4): p. 695-703.

42. Das, J., et al., A facile nonaqueous route for fabricating titania nanorods and their viability in quasi-solid-state dye-sensitized solar cells. Journal of Materials Chemistry, 2010. **20**(21): p. 4425-4431.

43. Holy, V., U. Pietsch, and T. Baumbach, High Resolution X-ray Scattering from Thin Films and Multilayers1999, Berlin: Springer-Verlag.

44. Phung, T.M., et al., Determination of the composition of ultra-thin Ni-Si films on Si. X-ray Spectrometry, 2008. **37**: p. 608.

45. Jiang, X.C., T. Herricks, and Y.N. Xia, Monodispersed spherical colloids of titania: Synthesis, characterization, and crystallization. Advanced Materials, 2003. **15**(14): p. 1205.

46. Han, J.J., et al., Fabrication of TiO2 microrod with desired shapes from rod-like titanium glycolate. Chemistry Letters, 2007. **36**(11): p. 1352-1353.

CHAPTER IX

SYNTHESIS OF METAL OXIDE-CARBON COMPOSIT THIN FILMS BY PYROLYSIS OF MLD FILMS

9.1 Introduction

The TiO_2 thin films has a number of important technological applications, among which are energy storage [1, 2], photo-catalysis [3], biotechnology [4], or dyesensitized solar cells [5]. While the semiconducting nature of TiO_2 is crucial for many of these applications, the limited conductivity prevents an even broader and efficient use in applications that require a fast electron transport, such as functional electrodes or as electrocatalyst supports. In this work, we demonstrate how to overcome this limitation by synthesis of TiO_2:C composite thin films by post processing of titanium alkoxide thin films. The heat treatment of these films in inert atmosphere (pyrolysis) resulted in removal of hydrogen from organic constituency and the self-organization of titanium-oxygen domains with formation of atomically mixed carbon doped TiO_2 composite which showed significant improvement in conductivity. This composite can be used, for example, as an inert electrode with substantial overpotential for O_2 evolution, or as a highly efficient support for electrocatalytic reactions, such as in methanol-based fuel cells [6], second generation phtocatalysis [7, 8], Li ion batteries [1, 9] or serve as a precursor for synthesis of refractory titanium carbide thin films via carbothermal reduction of TiO_2 [10].

The titanium alcoxide thin films used for pyrolysis are deposited by molecular layer deposition (MLD) techniques using alternative, self-limiting surface reaction between $TiCl_4$ and glycerol (GL), as shown in Fig.9.1.

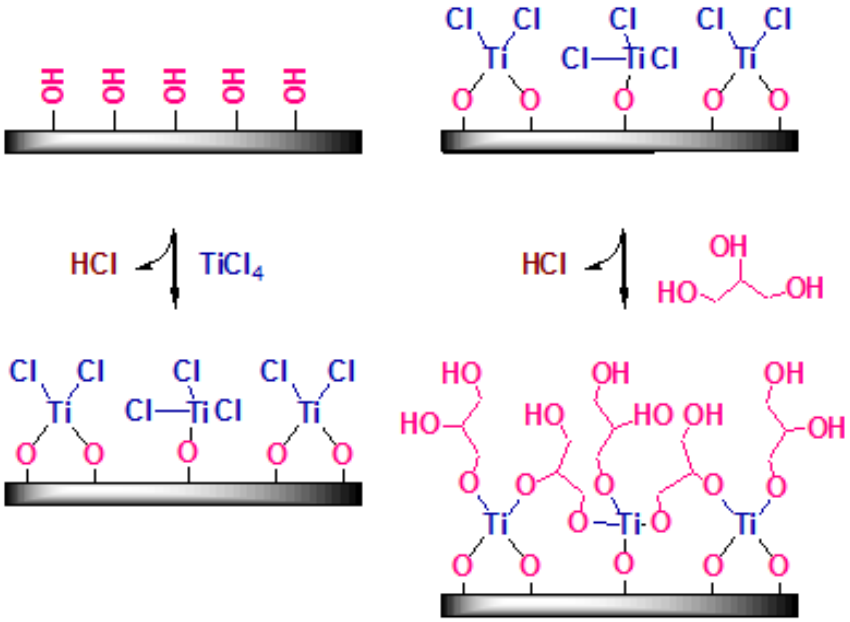

Figure 9.1 Schematic of TiGL MLD using $TiCl_4$ and glycerol (GL).

This titanium alcoxide thin film is called titanicones [11]. MLD titanicone film can be also deposited using $TiCl_4$ and ethylene glycol (EG) chemistry [11]. In the past, taitanim oxide-carbon composite thin film and bulk materials were synthesized by metal organic chemical vapor deposition (MOCVD) [12, 13], sol-gel [14], hydrothermal [14, 15], impregnation [16], oxidative annealing of TiC [17], and a number of other solution and gas phase methods [18]. In comparison to traditional thin film deposition methods, MLD offers atomic level mixing, thickness, and composition control with ability of conformal coating of a high surface area nanoparticles and nanostructures [19].

MLD titanicone is part of a special set of hybrid organic-inorganic films called metalcones. Metalcones were deposited using various metal precursors and organic alcohols that yield metal alkoxide films. So far metacone films have been successfully deposited using Al, Ti, Zn, Zr, Hf, Mn metal precursors, where ethylene glycol ($C_2H_6O_2$), glycerol ($C_3H_8O_3$), hydroquinone ($C_6H_6O_2$), or tetrafluorohydroquinone ($C_6F_4O_2$) were used as organic precursors [20]. A result of pyrolysis of these metalcones at 900°C is also presented. These metal oxide-carbon composite materials can be used in radiation dosimetry (Al_2O_3:C) [21], electronics and thermal catalysis (ZrO_2:C, HfO_2:C) [22-24], pseudocapacitance supercapacitors electrode material (MnO_x:C) [25], and room-temperature ferromagnetic thin film (ZnO:C) [26]. A variety of available organic precursors for MLD in synergy with wide range inorganic materials that can be deposited by ALD offers unprecedented level of composition control of depositing film prior to heat treatment. The significance of the proposed route for synthesis of metal oxide-carbon composite thin films is not only in its versatility, but also in the basic limitation of ALD to deposit thin film of carbon. A number of ex situ characterization techniques were employed to analyze post pyrolyzed MLD films. Nanostructure and morphology of the films were examined with Raman spectroscopy, while scanning electron microscopy (SEM), grazing incidence X-ray diffraction (GIXRD), and Xray photoelectron spectroscopy (XPS) were used to examine bulk morphology and composition of the films. Electrical properties were measured using a four-point probe technique.

9.2 Experimental

Metalcone MLD was performed in a viscous-flow, hot-wall type reactor described in detail elsewhere [27]. The films were deposited using metal precursors: titanium tetrachloride ($TiCl_4$, 98% pure, Strem Chemicals Inc., U.S.A.), trimethylaluminum ($Al(CH_3)_3$, 97%, Sigma-Aldrich. U.S.A.), diethylzinc (52.0 wt. %, Sigma-Aldrich. U.S.A.), bis(ethylcyclopentadienyl)manganese(II) ($Mn(C_5H_4C_2H_5)_2$, ≥98 %, Strem Chemicals Inc., U.S.A.), zirconium tetra-tert-butoxide ($Zr(OC(CH_3)_3)_4$, 99.999%, Sigma-Aldrich. U.S.A.), and tetrakis(diethylamino)halfnium, ($Hf(N(CH_3)_2)_4$, 99.99%, Sigma-Aldrich. U.S.A.) with organic diols ethylene glycol ($C_2H_6O_2$, 99.8%, Sigma-Aldrich. U.S.A.), hydroquinone ($C_6H_6O_2$, ≥99%, Sigma-Aldrich. U.S.A.), and triol glycerol ($C_3H_8O_3$, 99.5%, Sigma-Aldrich. U.S.A.). All precursors were handled in a glove bag due to their air and moisture sensitivity. Ultra high purity grade nitrogen (99.999%, Airgas, CO, U.S.A.) was used as the purge and carrier gas in the reactor. The reactor base pressure was ~1 Torr at a N_2 gas flow rate of 195 sccm.

Titanicone films grown using $TiCl_4$ and glycerol, denoted as TiGL, and $TiCl_4$ and ethylene glycol as TiEG, were deposited at 150°C and 115°C respectively, with deposition timing sequences (1, 35, 1, 35) and (5, 35, 8, 35) respectively [11]. AlEG, AlGL, AlHQ, AlFHQ, ZnEG, ZnHQ, ZrEG, HfEG thin films were deposited at 150°C using conditions reported previously [20, 28-30]. Thicknesses of pyrolysed tanicone films were 115 or 500 nm, where thickness of other pyrolyzed metalcone films varied from 100 nm to 500 nm. Silicon wafers with dimensions of 2.5 cm × 2.5 cm

were used as the substrates for MLD films grow. These wafers had a native SiO_2 oxide with a thickness of ~25 Å, unless specified otherwise.

Electrical measurements on pyrolized MLD films deposited on Si wafer with 400 nm thermal SiO_2 insulator were conducted using four-point probe technique. The sheet resistance data obtained by four-point probe were used to estimate film resistivity.

Pyrolysis of MLD films was performed in the Centorr M-60 (Centorr Vacuum Industries, NH, U.S.A.) high temperature furnace. Prior to pyrolysis the furnace was pumped down with a diffusion pump and then back filled with ultra-high purity argon (Airgas, CO, U.S.A.) with concentration of O_2, H_2O, CO, CO_2 impurities below 3ppm according to certificate. Heating and cooling rates of the samples was 5°C per minute, with bake time at target temperature of 1 hour.

Raman spectra were recorded on a Horiba Jobin Yvon Micro-Raman spectrometer at room temperature in ambient atmosphere. For excitation at 532 nm (green), an Ar+ laser was used with laser spot size of ~1.7 mm. The samples were measured with incident laser power of 1 or 50 mW.

Film crystallinity was determined by grazing incidence X-ray diffraction (GIXRD) scans performed using a Bede D1 X-ray diffractometer (Bede Scientific Inc. CO, U.S.A.). This X-ray diffractometer was equipped with a Cu X-ray tube and monochromator for CuKα radiation at λ=1.54 Å. The filament current was 40 mA and the voltage was 40 kV. For the GIXRD, the incident angle was ω=0.5° and the detector (2θ) was scanned from 20 to 80°.

X-ray photoelectron spectroscopy (XPS) survey scans were performed using a Physical Electronics PHI Model 5600 spectrometer with a monochromatic AlKα X-ray source with an energy of 1486.6 eV. Film analysis was conducted in a high-vacuum XPS system 1×10^{-9} Torr equipped with in situ Ar+ sputtering capability for depth profiling. The scans were performed with electron pass energy of 187 eV and a resolution of 0.8 eV. The photoelectrons were collected using a hemispherical analyzer. XPS depth profile enabled us to determine change in the relative concentration of titanium, oxygen and carbon atoms through films.

All the SEM images shown in this work were obtained with a beam voltage and current of 3.0–5.0 keV and 1–10 A, respectively.

9.3 Results and Discussion

9.3.1 Spectroscopic Characterization Pyrolyzed TiGL MLD Films

9.3.1.1 Raman Spectroscopy

Raman spectroscopy was applied to determine the structure of carbon and metal oxide phase as well as changes with pyrolysis temperature. Raman spectra of pristine 500 nm thick TiGL films and pyrolyzed at 600, 700, 800, and 900°C temperatures presented in Figure 9.2. The spectra were recorded over a region between 1050 to 3000 cm^{-1} and baseline corrected at 2000 cm^{-1} wavenumbers. The Raman spectra show one pair of bands around 1600 cm^{-1} and 1330 cm^{-1} wavenumbers that increased in intensity with increase in temperature. These peaks are usually designated G (graphitic) and D (disordered) Raman bands, which are commonly observed in the spectra of amorphous carbon materials containing

nanocrystalline graphitic domains. The G and D peaks are due to sp^2-carbon sites only and the G peak is due to the band stretching of all pairs of sp^2 in both rings and chains [31].

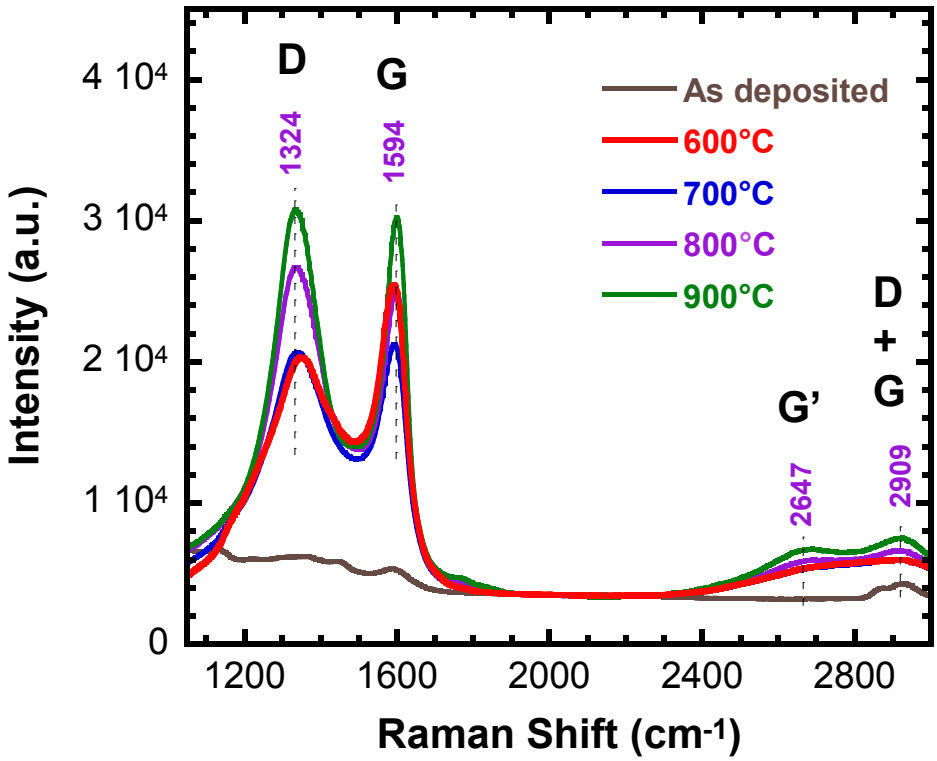

Figure 9.2 Raman spectra of as deposited 500 nm TiGL film and pyrolyzed from 600 to 900°C.

The D peak is due to the breading modes of sp^2 carbon atoms in rings within disordered carbonaceous structure due to double resonant Raman scattering [32, 33]. Raman spectra of various graphitizable and non graphitizable carbonaceous materials such as pyrolytic graphite, activated charcoal, or glassy carbon also exhibit peaks at around 1594 and 1324 cm^{-1} wavenumbers [34]. A second pair of peaks located at 2647and 2906 cm^{-1} wavenumbers, called G'-band overtone of the D-band and a D+G combination mode, respectively. The G' appears in the second-

order Raman spectra of disordered graphite [35]. Its intensity increase with temperature is indication of enhancement in the graphitic order in the free carbon phase of the samples. This suggests that these disordered carbons are related to a class of soft, graphitizable at temperatures exceeding 2000°C carbon [36].

As shown in Fig. 9.2, the intensity of G peak is highest compared to D peak at 600°C, and starting from 700°C, their peak intensities are almost equal. In the past, a similar trend in Raman spectra were observed with increase in pyrolysis temperature for organic thin films such as photoresist, polyparaphenylene (PPP), phenylcarbyne polymers, or hydrogenated CVD carbon [37-40]. The ratio of intensity of D peak to that of G peak I(D)/I(G) is believed to vary as the square of graphite cluster size (L_a) [31]. An increase in the ratio with pyrolysis temperature suggests that the graphitic crystal size is growing with rising temperature. The transition where I(D)/I(G) becomes ~1 at temperatures in between 600 and 700°C for pyrolysed TiGL is similar to the above mentioned polymers. This temperature region coincides with temperature of intense dehydrogenation of organics and hydrogenated carbon during the pyrolysis process [41-43]. At lower pyrolysis temperatures, polymeric networks contain a large concentration of dangling bonds that are reduced as graphitization intensifies and as the temperature of pyrolysis is raised [44]. Therefore, heat treatment below 700°C results in the formation of a carbonized polymer composite with large polymeric chains, and above 700°C, a more TiO_2:C composite-like film is formed. Narrowing and upwards frequency shift of the G peak is associated with growth in size and/or a number of graphite crystallites

[45]. An increase in pyrolysis temperature resulted in the G band position slightly shifting from 1583 cm^{-1} at 600°C to a higher frequency of 1598 cm^{-1} at 900°C, and the D band shifted from 1332 cm^{-1} toward lower frequencies of 1324 cm^{-1}. The G peak position shift and decrease in the full width at half maximum of the G peak (FWHMG) are similar to what has been observed with hydrogenated amorphous carbon pyrolyzed from 400 to 1000°C [32]. The FWHMG decrease indicates increased ordering of the sp^2 regions that accompanies the effusion of hydrogen species [32, 46].

Because the integral intensity of the G band is equal to the D band in pyrolyzed films, which indicates that the overall disorder of graphene layers in the carbon phases is believed to be comparatively low.

9.3.1.2 X-ray Diffraction

In contrast to Raman spectroscopy, the GIXRD samples long range order in materials. Figure 9.3 shows GIXRD diffractograms of the TiGL films, with original thickness of 500 nm, without heat treatment and pyrolyzed at various temperatures. As deposited TiGL film had amorphous structure. Weak crystalline phase peaks begin to appear at 2θ of 24.6 and 55.4 degrees at 600°C, corresponding to (101) and (211) diffraction planes of anatase form of TiO_2 (Joint Committee for Powder Diffraction Standard JCPDS 86-1156). This crystallization temperature is higher than what has been reported in the literature for the first appearance of the anatase TiO_2 peaks for annealed TiO_2 gel and thin films of 300-400°C in air [47-50].

Similarly, in this work, inhibition of crystallization temperature was observed during pyrolysis of titanium alkoxide gels [51].

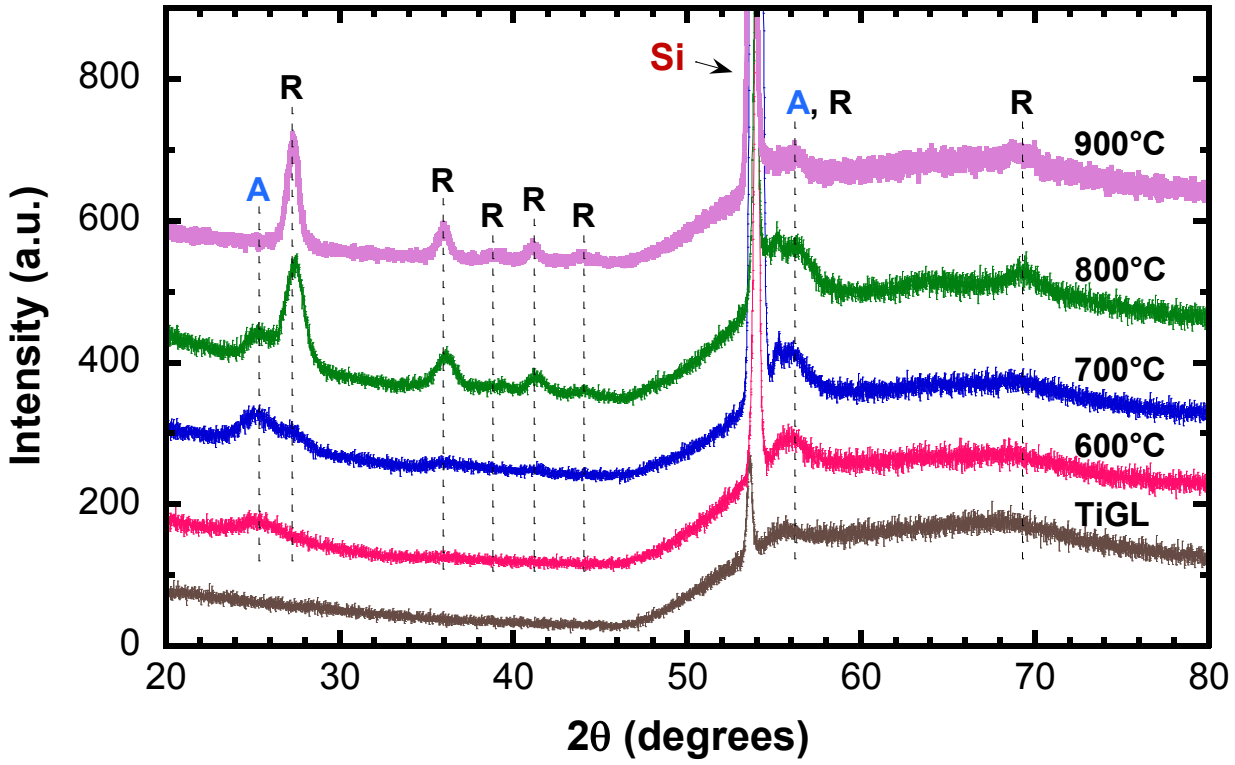

Figure 9.3 GIXRD diffractograms of TiGL films pyrolzed from 600 to 900°C.

This effect was explained by hindrance of crystallization by organic functional groups and constrain of amorphous TiO_2 in a carbon matrix. Further increase of the pyrolysis temperature to 700°C gives rise to small peaks of rutile TiO_2. By 900°C, anatase phase disappears and the sample showed only well-defined peaks at 27.28, 35.9, 38.7, 41.09, 43.7, and 68.5 degrees, corresponding to (110), (101), (200), (111), (210), and (301) rutile TiO_2 (JCPDS 86-0148). At 900°C, the most pronounced rutile TiO_2 peak at 2θ of 27.28 degrees became narrower. For samples treated at 600, 700, and 800°C, diffraction lines are very broad, indicating titanium oxide crystallites of nanometer size. Sharpening of the peaks with temperature indicates increases in

TiO_2 crystallite size. The XRD analysis has a detection limit of 1-2 vol.%; therefore, the identification of the first nanocrystals starting to grow in the amorphous bulk material by XRD is not possible [52].

The TiGL samples heat treated at 1200°C showed sharp peaks corresponding to cubic ß-SiC. This resulted from penetration of free carbon in the pyrolyzed films through native SiO_2 film as well as reaction with underling silicon wafer. As calculations show, this reaction is thermodynamically favorable: Si(s) + 3C(s) → SiC(s) ($\Delta G_{1200°C}$ = -14.3 kcal/mol). Negative value of Gibbs free energy indicates favorability of spontaneous reaction of silicon and carbon. This reaction is thermodynamically favorable even at lower temperatures; however, diffraction peaks of crystalline SiC were observed only at 1200°C. When 450 nm thick thermal SiO_2 was used as a barrier, silicon carbide formation was prevented. GIXRD diffractogram of 1200°C treated sample had very broad peaks at 22 degrees corresponding to (002) peak of crystalline graphite [39]. Intensity of this peak increased heat treatment temperature raised to 1300°C, indicating graphitizing behavior.

GIXRD analysis of TiGL films with original thickness of about 115 nm pyrolysis at the same temperatures and conditions as 500 nm films showed diffraction peaks starting at 700°C and presence of only a rutile TiO_2 phase. This suggests that at lower thicknesses the composite film has low volume fraction of crystalline TiO_2 and that crystallite size is below detection limited of the instrument.

9.3.1.3 Optical and SEM Imaging

Surface of the TiGL films pyrolyzed up to 900°C were smooth, uniform, and free of cracks. A slight change in color compared to that of deposited films was noticed, which is attributed to change in film thickness and density. Optical image showing surface of 500nm TiGL film after pyrolysis at 800°C is presented in Figure 9.4a.

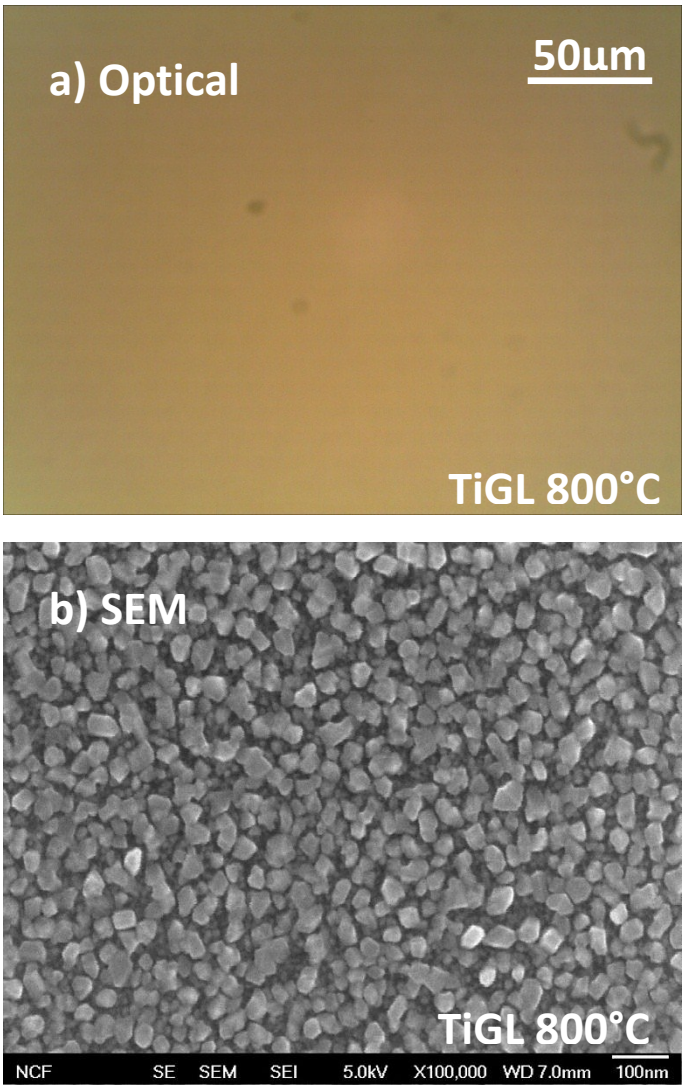

Figure 9.4 Optical image of a surface of TiGL film pyrolyzed at 800°C (a); SEM of the surface of the 800°C pyrolyzed TiGL film (b).

This image shows that pyrolyzed film has no cracks or defects. Formation of crack systems is a common problem for liquid phase coated polymer derived ceramics [53]. When heat treated at 1200°C, the surface of the TiGL film became black in color. Black color samples were also observed for titanium glycolates nanorods synthesized from solution chemistry after having been heated in argon at 1300°C [54]. In this work, we noticed that the black coating formed after pyrolysis at 1200°C was soft and easily removable. This is understood as manifestation of the graphitic nature of the carbon in the composite film.

Surface morphology of 800°C pyrolyzed TiGL film was examined in detail, using SEM as presented at Fig 9.4b. This high resolution image shows that film is uniformly covered with nanoparticles having average diameters of about 50 nm. These titanium oxide nanoparticles may form because of either the presence of a trace amount of oxygen in the heat treatment chamber or physisorbed or diffused water or oxygen in or near the surface layer of the film after exposure to the air prior to pyrolysis.

9.3.1.4 X-ray Photoelectron Spectroscopy

XPS survey scan of untreated 500 nm thick TiGL film showed composition of $Ti_5O_{25}C_{68}Cl_2$ where chlorine is present as an impurity from the deposition process [11]. High carbon concentration is due to the presence of residual carbon after exposure to air prior to XPS. If chlorine is present as unreacted Ti-Cl bonds, as opposed to trapped HCl byproducts of the surface reaction, it can participate in

pyrolysis of hydrocarbons through thermodynamically favorable formation of volatile HCl at low pyrolysis temperatures [55].

Result of the XPS depth profile for 800°C pyrolyzed TiGL film is presented at Fig. 9.5a.

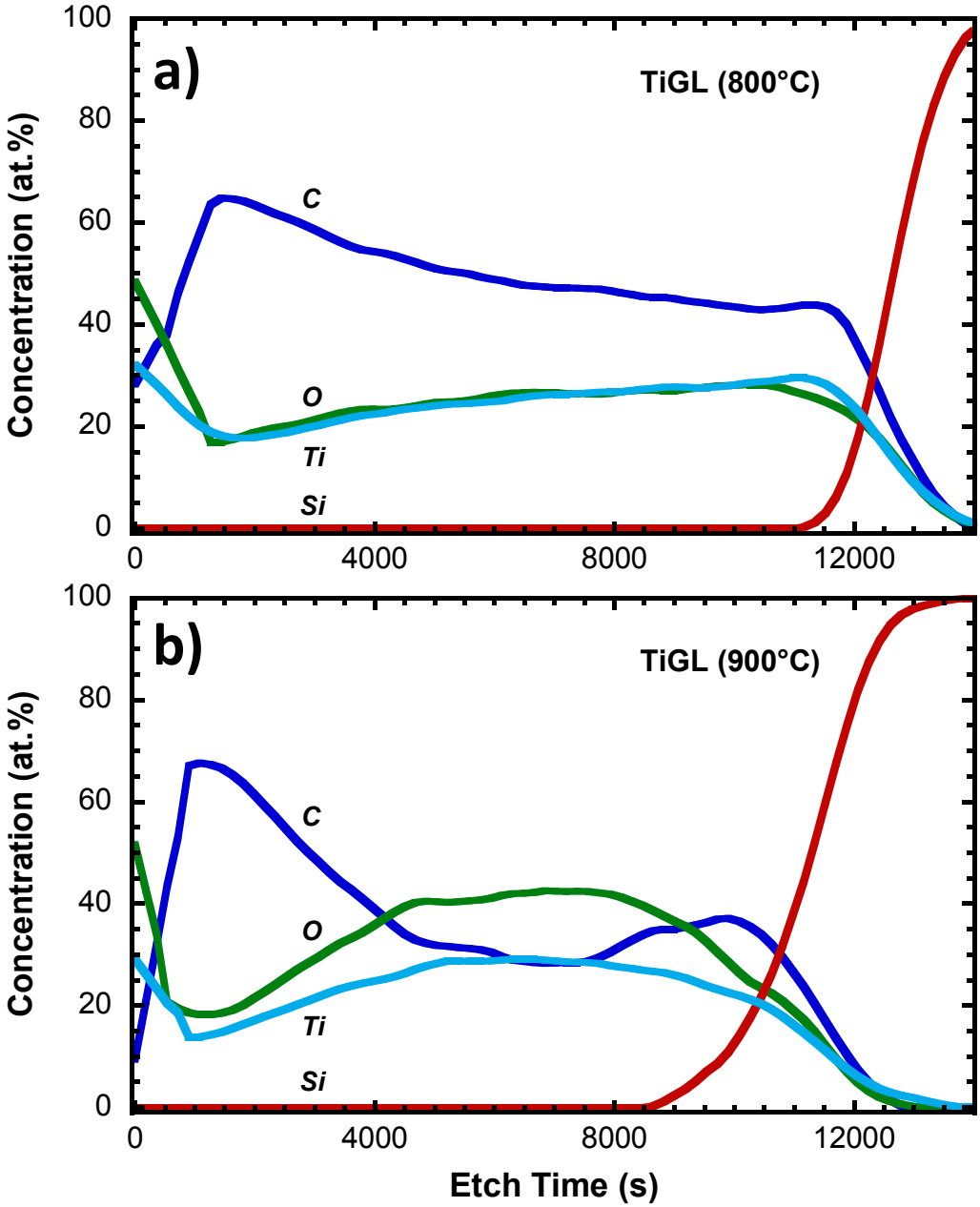

Figure 9.5 XPS depth profile of TiGL films pyrolyzed at 800°C (a); and 900°C (b).

Initially, there is slightly increased atomic concentration of Ti and O, which is consistent with observed particles at the surface of the film shown by SEM (Fig. 9.4a). Carbon distributed through the bulk of the film with some increase in concentration at the surface. In the bulk of the film, the ratio of Ti to O is 1/1. This could be an artifact of preferential sputtering of oxygen [56, 57] or it could be formation of non-stoichiometric anatase and rutile phase of TiO_2, as indicated by XRD. This titanium oxide non-stoichiometry can be also attributed to carbothermal reduction of TiO_2. However, this possibility can be dismissed since according to thermochemical calculations,the reaction $TiO_2(s) + 3C(s) \rightarrow TiC(s) + 2CO(g)$ is feasible only at a minimum temperature of 1282°C where Gibbs free energy $\Delta G = 0$ [58, 59].

The result of of XPS depth profile of a 500nm TiGL pyrolyzed at 900°C is shown in Fig. 9.5b. This figure shows that carbon was not distributed through the titanium oxide matrix uniformly, with concentration variations from 30 to 70% in the bulk of the film. Elevated concentration of carbon was found near the surface of the film, suggesting greater phase separation between TiO_2 and C compared to the 800°C sample. Compared to the 800°C sample, the 900°C heat treated film shows reduction in film thickness as is evident from shorter sputter time. This is expected, considering that polymer dehydrogenation processes typically continues until 1000-1100°C [60]. This may suggest that preferential removal of oxygen for the 800°C sample is related to increased concentration of hydrogen. In this case, preferential removal of oxygen would occur via formation of water. The ratio of Ti/O for 900°C in

the bulk of the film is 3/4 and concentration of the carbon at the lowest point in the bulk of the film is about 30 at. %. Overall, XPS shows that film at 900°C has a highly hierarchical structure as a consequence of temperature activated self-organization and phase separation processes in the composite film.

Depth profile of TiGL film deposited on silicon with native oxide and pyrolized at 1200°C, in agreement with XRD data, confirmed the presence of SiC in addition to titanium oxide and carbon. This observation suggests that reactivity of a substrate can be potentially manipulated in order to use free carbon as reactive species to synthesize complex film architectures.

9.3.2 Electrical Properties of Pyrolyzed TiGL films

Electrical properties of the produced titanium oxide-carbon composite thin films were assessed using a four point probe measurement technique. Figure 9.6 depicts change in sheet resistance (Ohm/□) versus pyrolysis temperature of TiGL, which had original thickness of about 115 nm deposited on silicon wafers with 450 nm thick SiO_2. Thick, insulating SiO_2 layer was used to eliminate substrate effect on the measurements. The films were pyrolyzed with increment[s] of 50°C from 500 to 900°C. The as deposited TiGL sample was too resistive and could not be measured by the four-point probe setup.

The results showed show that from 500 to 700°C that the sheet resistance of composite films decreases dramatically. This effect is attributed to significant change in the film composition, in particular to the H/C ratio, as dehydrogenation of the film intensifies [37, 41, 61]. When π - bond associated with groups of carbon

atoms in the sp^2 state are present, electrons are delocalized and become available as charge carriers [44].

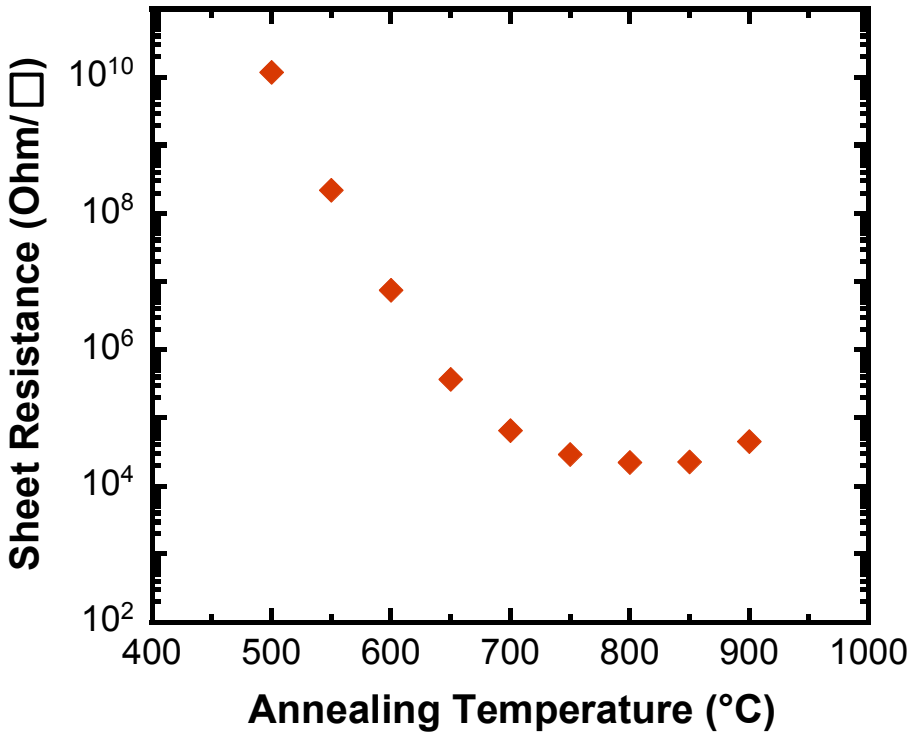

Figure 9.6 Dependence of electrical sheet resistance of TiGL films on heart treatment temperature.

This pyrolysis temperature region is also characterized by initial growth in the free radical concentration, a number of which are reduced at higher temperatures [44]. At temperatures above 700°C, the resistance changed not as dramatically, which suggests that most of the dehydrogenation process occurred prior to that temperature. Previously, a similar evolution in electrical conductivity was noticed by others during pyrolysis of silica based hybrids as well as during heat treatment of pure organic polymers [38, 52].

The resistivity of the 800°C treated sample was calculated by dividing the sheet resistance value on thickness of the film of 88 nm obtained from cross sectional SEM, which was found to be $\rho = 2 \times 10^{-1}$ Ohm*cm. Fully oxidized TiO_2 is an insulator with a resistivity on the order of 1×10^{13} Ohm*cm [62]. Hence, resistivity of TiO_2:C composite produced by pyrolysis of TiGL film has more than thirteen orders of magnitudes lower resistivity than rutile TiO_2. On the other hand, CVD carbon deposited by thermal decomposition of acetylene (C_2H_2) at 950°C shows lower resistivity of 4.5×10^{-3} Ohm*cm [63]. Highly oriented pyrolytic graphite (HOPG) has two-dimensional resistivity of $(1\text{-}3) \times 10^{-1}$ Ohm*cm in the c direction and $(4\text{-}5) \times 10^{-4}$ Ohm*cm in the a-b (in plane) direction [64]. This makes fabricated TiO_2:C film comparable in resistivity to that of nano-crystalline (CVD) and even HOPG carbon materials. Therefore, electrical conductivity of TiGL MLD thin films can be effectively altered from highly insulating (as deposited) to semiconducting with a one-step pyrolysis process.

The TiO_2:C obtained from this work may have two potential mechanisms of electrical conductivity previously identified for SiO_2:C polymer derived ceramics: tunneling (phonon assisted hopping between localized states) or percolation [65]. More research into the microstructure of synthesized TiO_2:C is necessary in order to identify which of the two mechanisms is operative.

Overall, conductivity of polymer derived ceramic film can be manipulated in a wide range, depending on the polymeric precursor, composition (dopant), pyrolysis temperature, and atmosphere [52].

9.3.3 Pyrolysis of Various Metalcone MLD Films

This section presents the survey of MLD metal alkoxide films of titanium (TiEG), aluminum (AlGL, AlEG, AlHQ, AlFHQ), zinc (ZnGL, ZnHQ), zirconium (ZrEG), hafnium (HfEG), and manganese (MnEG) pyrolyzed at 900°C. For better visualization of organic alcohol molecules used in deposition process of the MLD films, they are presented in Fig. 9.7.

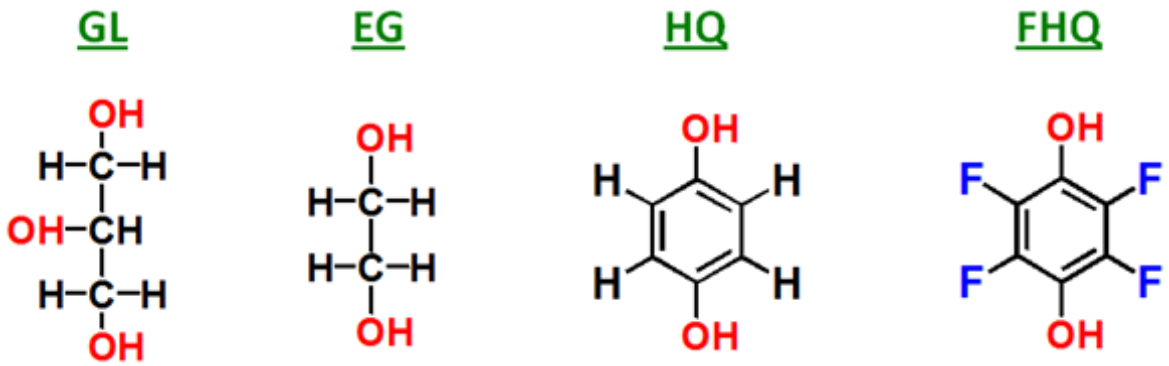

Figure 9.7 Various organic alcohol molecules used during metalcone MLD.

There are two aliphatic molecules, ethylene glycol (EG) and glycerol (GL), and two aromatic compounds, hydroquinone (HQ) and tetrafluorohydroquinone (FHQ). All films were deposited at 150°C, except that TiEG was deposited at 115°C, using conditions reported previously [11, 20, 28, 29]. No cracks were observed in the films after examination with optical microscope, except for TiEG film deposited at 115°C. It should be emphasized here that TiEG films were the only samples where cracks were observed. This can be caused by difference in the coefficient of thermal expansion (CTE) between substrate and the film, shrinkage, and rupture during intense removal of volatile by-products of pyrolysis. This can be avoided by reducing

the thickness of the original film, by alloying the film with other materials, or by reducing temperature ramp cool rate during pyrolysis [53].

Pyrolysis results for TiEG are of particular interest since it is closely related to TiGL, and the effect of substitution of GL to EG on morphology of pyrolyzed films can be discussed. MLD TiEG growth process using $TiCl_4$ and ethylene glycol schematically presented in Fig. 9.8 [11].

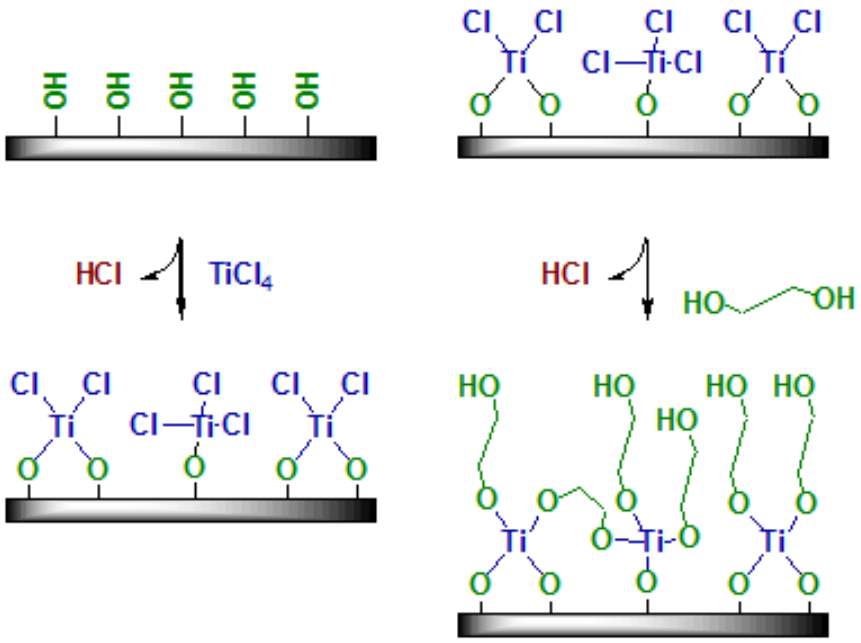

Figure 9.8 Schematic of TiEG MLD using $TiCl_4$ and ethylene glycol (EG).

XPS survey scan of the 500nm TiGL prior to 900°C pyrolysis showed composition of $Ti_8O_{33}C_{55}Cl_4$ with combined Ti and O atomic concentration on ~30% higher than in TiGL film ($Ti_5O_{25}C_{68}Cl_2$). This comparison assumes that films have the same amount of residual carbon on the surface as a consequence of exposure to air prior to XPS. At the same time, a higher concentration of Ti-O domains is consistent with

a higher degree of packing in TiEG compared to TiGL, due to lower steric effect imposed by EG molecule compared to GL.

SEM imaging of surfaces of 500 nm thick TiEG and TiGL films pyrolyzed at 900°C is presented in Fig. 9.9.

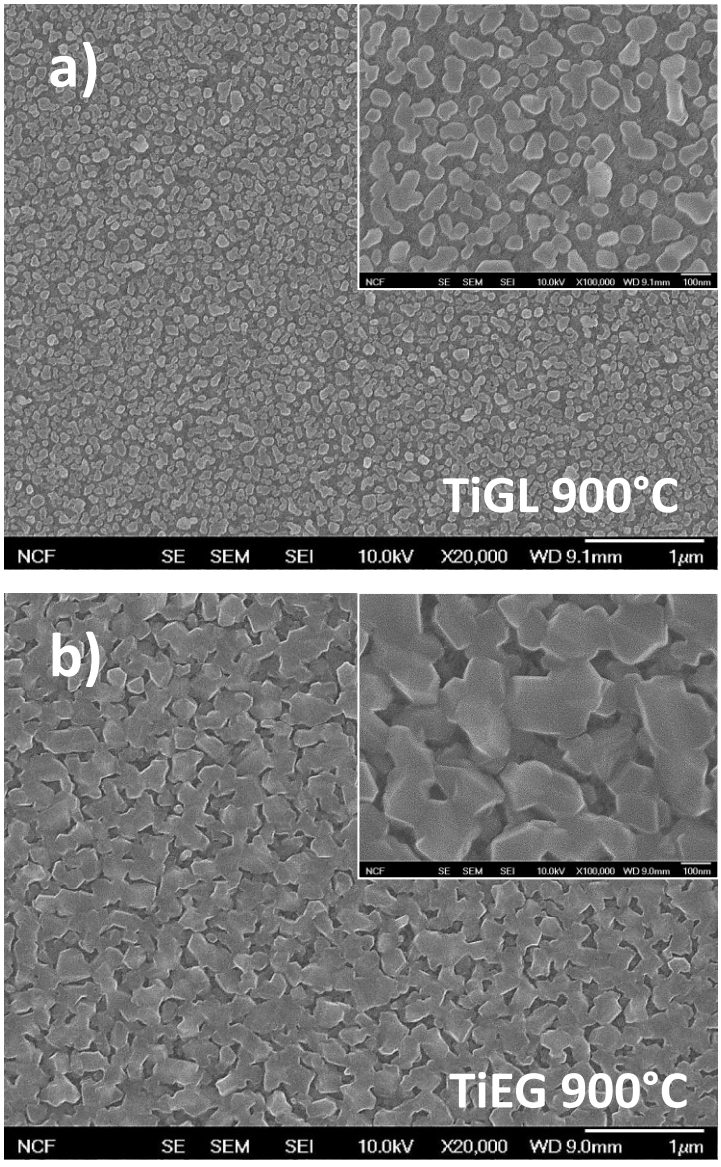

Figure 9.9 Surface morphology from SEM for TiGL (a), and TiEG films (b), both pyrolyzed at 900°C.

Inset images represent zoomed in views of the larger images. These pictures show that both surfaces are covered with large crystallites with average size of 200 nm for TiEG film and smaller average size of 80 nm for TiGL. This observation is in good agreement with previous reports where increase in concentration of TiO_2 in an alloy results in formation greater size TiO_2 nanocrystals upon heating [66].

Raman spectra of the TiGL and TiEG pyrolyzed at 900°C are presented in Figure 9.10.

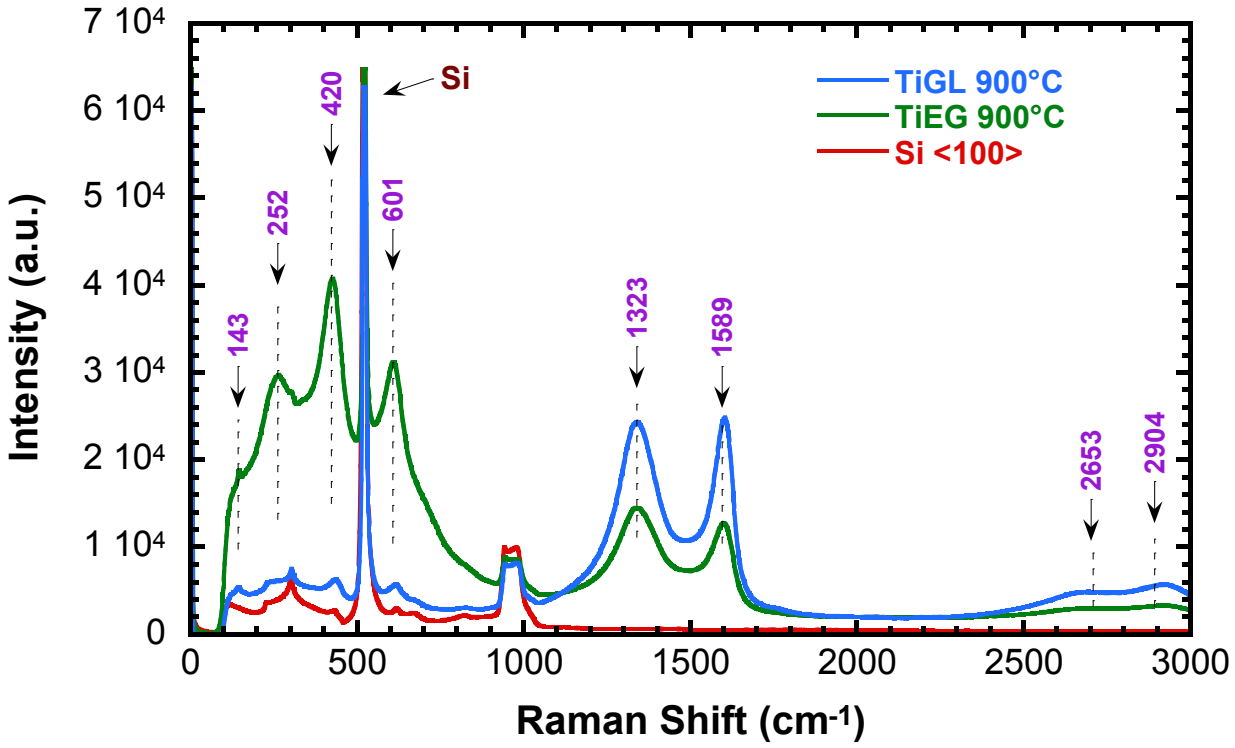

Figure 9.10 Raman spectra for TiGL and TiEG films and pyrolyzed at 900°C.

The spectra were recorded over a wide region, between 0 to 3000 cm^{-1}, and normalized with respect to each other. Both of these samples exhibit D and G peaks of graphitic carbon. The TiEG sample displayed lower intensity D and G signals and a stronger D peak compared to the G peak. In contrast, TiGL samples exhibit

higher intensity narrow D and G peaks, with stronger G peak compared to D peak. Greater intensity of D and G peaks for TiGL compared to TiEG suggests that it has higher sp^2 carbon content. Observed greater D peak intensity compared to G peak for TiEG is indicative of increased disorder in the carbon phase compare to TiGL [31]. Presence of larger TiO_2 crystallites in TiEG is manifested in appearance of strong broad peaks around 142, 252, 420, and 601 cm^{-1} wavenumbers, attributed to rutile TiO_2 [67]. The rutile TiO_2 peaks have also appeared for the TiGL sample, but they are lower in intensity. This is direct evidence of correlation between TiO_2 grain size and its Ti-O domain concentration in untreated titanicone films.

Raman spectra of alucone AlGL, AlEG, AlHQ, and AlFHQ films pyrolyzed at 900°C are presented in Figure 9.11.

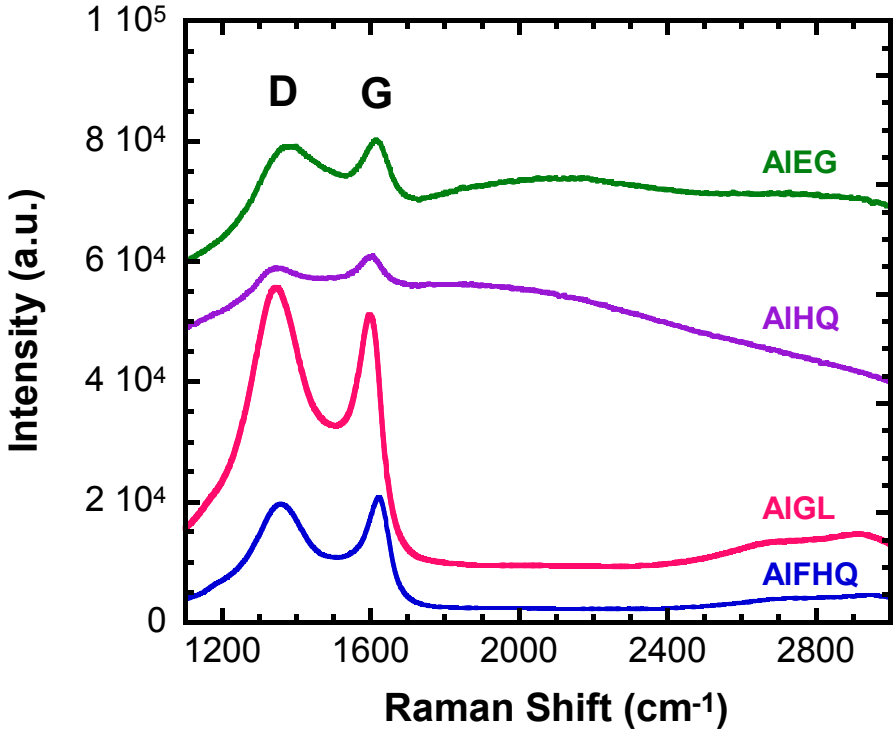

Figure 9.11 Raman spectra of different alucone MLD films pyrolyzed at 900°C.

This figure shows noticeably high background photoluminescence for AlHQ and AlEG pyrolyzed samples, with reduced photoluminescence for AlGL and AlFHQ. Similarly, photolyminescent properties have been observed for amorphous SiO_2:C composite thin films [52]. In the case of SiO_2:C, photoluminescence was attributed to formation of sp^2 C clusters in amorphous SiO_2 matrix after pyrolysis [52, 68]. We speculate here that origins of photoluminescence observed in this work for Al_2O_3:C is similar to that of SiO_2:C films. Both Al_2O_3 and SiO_2 are high crystallization temperatures oxides that can limit carbon diffusion in amorphous oxide matrix and can stimulate the carbon cluster formation. This may also cause trapping of byproducts of pyrolysis such as hydrogen which can result in formation of various forms of hydrogenated carbon known to result in photoluminescent background in Raman spectra of carbon [69, 70]. This suggests that pyrolyzed MLD alucones can have promising photoluminescence properties. More research is necessary to identify reasons for high photoluminescence in AlHQ and AlEG compared to that in AlGL and AlFHQ thin films.

The surface SEM image of AlEG pyrolyzed at 900°C is shown in Fig. 9.12. This picture shows that the film has flat topography with pores that most likely formed by the expulsion of gases generated during pyrolysis of organics. In contrast to pyrolyzed TiEG, this film doesn't show nanocrystalline grained surface morphology. Aluminum oxide has relatively high crystallization temperature of 900°C when annealed in inert atmosphere [71, 72]; therefore, low mobility of

aluminum ions or atoms in the bulk of the film is likely, and as a consequence, distinctly different morphology of the Al_2O_3:C can be expected.

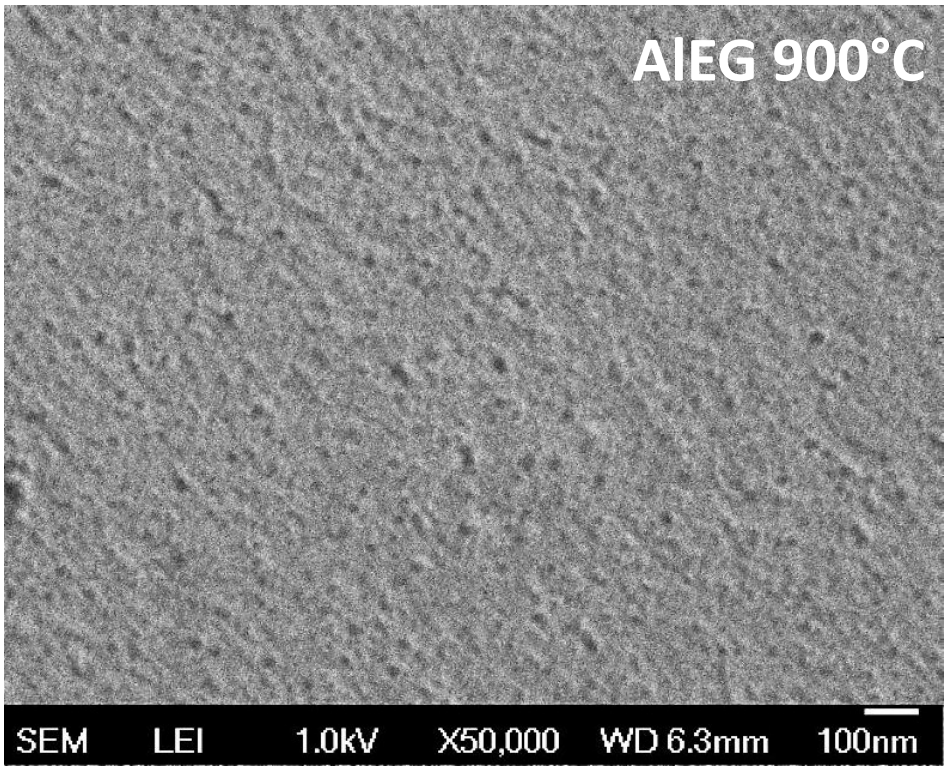

Figure 9.12 SEM image of a surface of the AlEG film pyrolyzed at 900°C.

Raman spectra of 900°C pyrolyzed ZnGL, ZnHQ, ZrEG, HfEG, and MnEG films are presented in Fig. 9.13. The D and G peaks appeared in the spectra of ZnGL, ZnHQ, ZrEG, and HfEG samples. Peak intensity may differ due to difference in thickness of as deposited metalcone film. The presence of sp^2 carbon suggests formation of aluminum, zinc, zirconium, and hafnium oxide-carbon composites. The slight frequency shift for D and G bands for different metalcones may be related to strained-induced Raman shift. GIXRD analysis showed ZrEG and HfEG films contain crystalline oxides. Additional research is needed to evaluate the effect of pyrolysis on electrical conductivity of these composite films. In this instance,

semiconducting electrical properties can be expected for pyrolyzed metalcones deposited using aromatic compounds hydroquinone and tetrafluorohydroquinone. Previously reported research results suggest that polycyclic form of carbon formed after pyrolysis of aromatic polymers can display semiconducting properties [61].

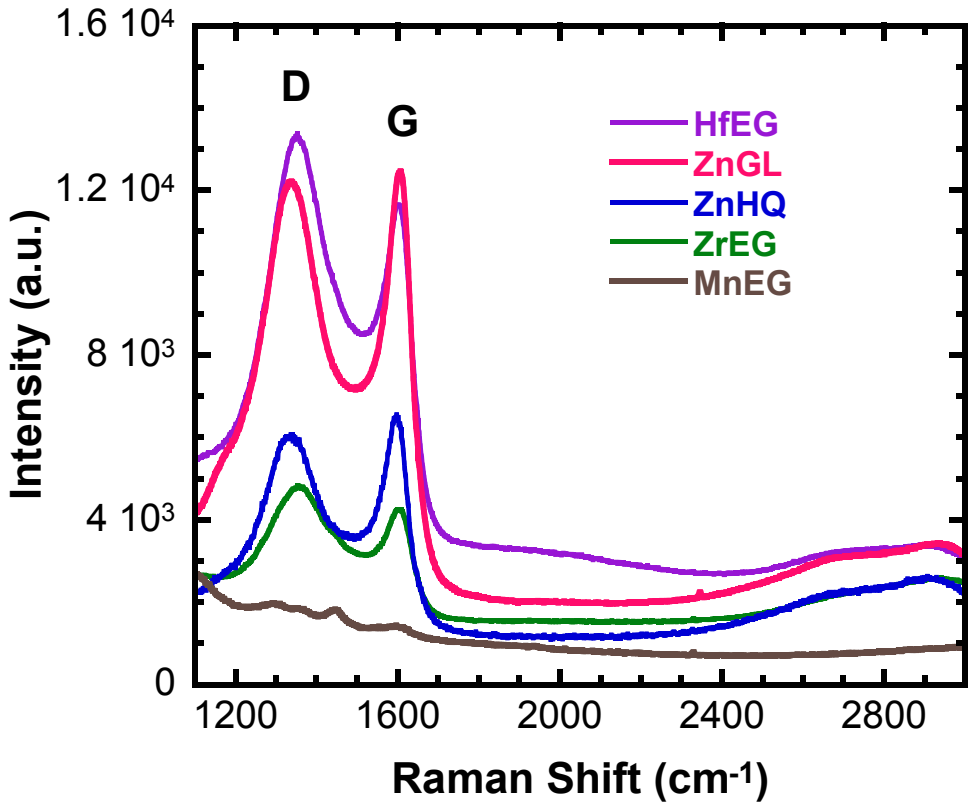

Figure 9.13 Raman spectra of ZnGL, ZnHQ, ZrEG, HfEG, and MnEG MLD films pyrolyzed at 900°C.

On the other hand, MnEG film did not show any D and G peaks. Absence of these peaks in Raman spectra was observed in several MnEG samples of different thicknesses. XPS depth profile of pyrolyzed MnEG film showed carbon concentration below detection limit of the instrument (0.01%), Mn and O atoms in ratio of 2/3, and silicon impurity through the film. Manganese oxide alloying with

silicon substrate, as a result of heat treatment, had been observed previously [73]. Absence of carbon in the film can be the outcome of specific pyrolysis mechanism which has been found to be temperature dependent, so D and G peaks were observed for MnEG samples pyrolyzed at 600°C.

9.4 Conclusions

Pyrolysis of metalcone films enabled us to synthesize a new class of nanostructured metal oxide - carbon composite thin films. Analysis of pyrolyzed films permitted identification of several key processes. At lower heat treatment temperatures (<1000°C), pyrolysis leads to dehydrogenation of organic constituency with formation of free sp^3 and sp^2 hybridized carbon where the sp^2 carbon is present in form of nanographitic crystallites, as indicated by appearance of characteristic D and G peaks in Raman spectrum. Graphitization process was intensified with increase in pyrolysis temperature. Presence of graphitized carbon in the TiO_2:C composite is believed to be responsible for the significant increase in electrical conductivity after heat treatment. The dehydrogenation processes of organics in TiGL are accompanied by self-organization of Ti-O domains to crystalline anatase and then to rutile TiO_2. Size of the TiO_2 crystallite grains was higher for TiEG film deposited using ethylene glycol pyrolyzed at the same temperature. XPS analysis revealed signs of phase separation between carbon and TiO_2 as they form. At higher temperatures (>1000°C), carbon formed larger graphitic crystallites, as evidenced from the change in color and from X-ray diffraction data. Raman spectroscopy analysis of 900°C pyrolyzed ZnGL, ZnHQ, ZrEG and HfEG films showed

appearance of D and G signature peaks of graphic carbon in similarity to TiGL and TiEG. In MnEG, D and G peaks appeared only at lower 600°C pyrolysis temperature. Pyrolysis of alucone AlHQ and AlEG led to synthesis of photoluminescent composite films. This property of Al_2O_3:C films can be attributed to specific morphology of synthesize films.

9.5 Acknowledgements

The authors would like to thank Viginia Anderson from George's group in University of Colorado in Boulder for her assistance with the X-ray reflectivity and diffraction analysis.

9.6 References

1. Ji, L.W., et al., Recent developments in nanostructured anode materials for rechargeable lithium-ion batteries. Energy & Environmental Science, 2011. **4**(8): p. 2682-2699.

2. Wu, H.B., et al., Nanostructured metal oxide-based materials as advanced anodes for lithium-ion batteries. Nanoscale, 2012. **4**(8): p. 2526-2542.

3. Fujishima, A. and K. Honda, Electrochemical Photolysis of Water at a Semiconductor Electrode. Nature, 1972. **238**(5358): p. 37-+.

4. Raulio, M., et al., Destruction of Deinococcus geothermalis biofilm by photocatalytic ALD and sol-gel TiO2 surfaces. Journal of Industrial Microbiology & Biotechnology, 2006. **33**(4): p. 261-268.

5. Park, K., et al., Effect of an Ultrathin TiO2 Layer Coated on Submicrometer-Sized ZnO Nanocrystallite Aggregates by Atomic Layer Deposition on the Performance of Dye-Sensitized Solar Cells. Advanced Materials, 2010. **22**(21): p. 2329-2332.

6. Hahn, R., et al., Semimetallic TiO2 Nanotubes. Angewandte Chemie-International Edition, 2009. **48**(39): p. 7236-7239.

7. Khan, S.U.M., M. Al-Shahry, and W.B. Ingler, Efficient photochemical water splitting by a chemically modified n-TiO2 2. Science, 2002. **297**(5590): p. 2243-2245.

8. Wang, H. and J.P. Lewis, Second-generation photocatalytic materials: anion-doped TiO2. Journal of Physics-Condensed Matter, 2006. **18**(2): p. 421-434.

9. Etacheri, V., et al., Challenges in the development of advanced Li-ion batteries: a review. Energy & Environmental Science, 2011. **4**(9): p. 3243-3262.

10. Edited by Weimer A. W., Carbide nitride and boride materials synthesis and processing. London: Chapman & Hall, 1997.

11. Abdulagatov, A.I., et al., Molecular Layer Deposition of Titanicone Films using TiCl4 and Ethylene Glycol or Glycerol: Growth and Properties. Chemistry of Materials, 2012. **24**(15): p. 2854-2863.

12. Kuo, C.S., et al., Carbon-containing nano-titania prepared by chemical vapor deposition and its visible-light-responsive photocatalytic activity. Journal of Molecular Catalysis a-Chemical, 2007. **270**(1-2): p. 93-100.

13. Wu, G., et al., Synthesis and characterization of carbon-doped TiO2 nanostructures with enhanced visible light response. Chemistry of Materials, 2007. **19**(18): p. 4530-4537.

14. Sakthivel, S. and H. Kisch, Daylight photocatalysis by carbon-modified titanium dioxide. Angewandte Chemie-International Edition, 2003. **42**(40): p. 4908-4911.

15. Ren, W.J., et al., Low temperature preparation and visible light photocatalytic activity of mesoporous carbon-doped crystalline TiO2. Applied Catalysis B-Environmental, 2007. **69**(3-4): p. 138-144.

16. Huang, C.H., et al., Photocatalytic Activity and Characterization of Carbon-Modified Titania for Visible-Light-Active Photodegradation of Nitrogen Oxides. International Journal of Photoenergy, 2012.

17. Irie, H., Y. Watanabe, and K. Hashimoto, Carbon-doped anatase TiO2 powders as a visible-light sensitive photocatalyst. Chemistry Letters, 2003. **32**(8): p. 772-773.

18. Leary, R. and A. Westwood, Carbonaceous nanomaterials for the enhancement of TiO2 photocatalysis. Carbon, 2011. **49**(3): p. 741-772.

19. George, S.M., Atomic Layer Deposition: An Overview. Chemical Reviews, 2010. **110**(1): p. 111-131.

20. Lee, B.H., et al., Growth and Properties of Hybrid Organic-Inorganic Metalcone Films Using Molecular Layer Deposition Techniques. Advanced Functional Materials, 2012.

21. Akselrod, M.S., et al., Highly Sensitive Thermoluminescent Anion-Defect Alpha-Al2o3-C Single-Crystal Detectors. Radiation Protection Dosimetry, 1990. **33**(1-4): p. 119-122.

22. Dutta, G., et al., Effects of O vacancies and C doping on dielectric properties of ZrO2: A first-principles study. Applied Physics Letters, 2006. **89**(20).

23. Trunschke, A., et al., Transition metal oxide/carbon composite catalysts for n-alkane aromatization: structure and catalytic properties. Applied Catalysis a-General, 2001. **208**(1-2): p. 381-392.

24. Hoang, D.L., et al., Zirconia carbon composites as monofunctional catalysts in C6+ alkane aromatization. Applied Catalysis a-General, 1999. **182**(2): p. 385-397.

25. Lin, Y.H., et al., Manganese Oxide/Carbon Aerogel Composite: an Outstanding Supercapacitor Electrode Material. Advanced Energy Materials, 2011. **1**(5): p. 901-907.

26. Pan, H., et al., Room-temperature ferromagnetism in carbon-doped ZnO. Physical Review Letters, 2007. **99**(12).

27. Elam, J.W., M.D. Groner, and S.M. George, Viscous flow reactor with quartz crystal microbalance for thin film growth by atomic layer deposition. Review of Scientific Instruments, 2002. **73**(8): p. 2981-2987.

28. Lee, B.H., Anderson, V. R., George, S. M., Metalcone and Metalcone/Metal Oxide Alloys Grown Using Atomic and Molecular Layer Deposition. ECS Trans., 2011. **41**(2): p. 131-138.

29. George, S.M., et al., Metalcones: Hybrid Organic-Inorganic Films Fabricated Using Atomic and Molecular Layer Deposition Techniques. Journal of Nanoscience and Nanotechnology, 2011. **11**(9): p. 7948-7955.

30. Lee, B.H., George, S. M., , unpublished.

31. Ferrari, A.C. and J. Robertson, Interpretation of Raman spectra of disordered and amorphous carbon. Physical Review B, 2000. **61**(20): p. 14095-14107.

32. Ferrari, A.C. and J. Robertson, Resonant Raman spectroscopy of disordered, amorphous, and diamondlike carbon. Physical Review B, 2001. **64**(7).

33. Maultzsch, J., S. Reich, and C. Thomsen, Double-resonant Raman scattering in graphite: Interference effects, selection rules, and phonon dispersion. Physical Review B, 2004. **70**(15).

34. Chu, P.K. and L.H. Li, Characterization of amorphous and nanocrystalline carbon films. Materials Chemistry and Physics, 2006. **96**(2-3): p. 253-277.

35. Nemanich, R.J. and S.A. Solin, 1st-Order and 2nd-Order Raman-Scattering from Finite-Size Crystals of Graphite. Physical Review B, 1979. **20**(2): p. 392-401.

36. Kaspar, J., et al., Electrochemical study of lithium insertion into carbon-rich polymer-derived silicon carbonitride ceramics. Electrochimica Acta, 2010. **56**(1): p. 174-182.

37. Kostecki, R., et al., Surface studies of carbon films from pyrolyzed photoresist. Thin Solid Films, 2001. **396**(1-2): p. 36-43.

38. Sun, Z., et al., Structure and properties of hard carbon films depending on heat treatment temperatures via polymer precursor. Diamond and Related Materials, 1999. **8**(6): p. 1107-1113.

39. Matthews, M.J., et al., Raman spectra of polyparaphenylene-based carbon prepared at low heat-treatment temperatures. Applied Physics Letters, 1996. **68**(8): p. 1078-1080.

40. Kumar, S., Unhydrogenated Diamond-Like Carbon-Films Prepared by Dc Plasma Chemical Vapor-Deposition at Room-Temperature. Applied Physics Letters, 1991. **58**(17): p. 1836-1838.

41. Zheng, T., Q. Zhong, and J.R. Dahn, High-Capacity Carbons Prepared from Phenolic Resin for Anodes of Lithium-Ion Batteries. Journal of the Electrochemical Society, 1995. **142**(11): p. L211-L214.

42. Conway, N.M.J., et al., Defect and disorder reduction by annealing in hydrogenated tetrahedral amorphous carbon. Diamond and Related Materials, 2000. **9**(3-6): p. 765-770.

43. Xiang, H.Q., S.B. Fang, and Y.Y. Jiang, Carbonaceous anodes for lithium-ion batteries prepared from phenolic resins with different cross-linking densities. Journal of the Electrochemical Society, 1997. **144**(7): p. L187-L190.

44. Hunt, D.R., Jenkins G. M., Takezawa T., , The effect of tensile stress upon the resistivity of a polymeric carbon. Carbon, 1976. **14**: p. 105-109.

45. Dillon, R.O., J.A. Woollam, and V. Katkanant, Use of Raman-Scattering to Investigate Disorder and Crystallite Formation in as-Deposited and Annealed Carbon-Films. Physical Review B, 1984. **29**(6): p. 3482-3489.

46. Knight, D.S. and W.B. White, Characterization of Diamond Films by Raman-Spectroscopy. Journal of Materials Research, 1989. **4**(2): p. 385-393.

47. Gnanasekar, K.I., et al., Direct conversion of TiO2 sol to nanocrystalline anatase at 85 degrees C. Journal of Materials Research, 2002. **17**(6): p. 1507-1512.

48. Li, G.H., et al., Structural and optical properties of TiO2 thin film and TiO2+2 wt.% ZnFe2O4 composite film prepared by r.f. sputtering. Thin Solid Films, 2000. **368**(1): p. 163-167.

49. Hou, Y.Q., et al., Influence of annealing temperature on the properties of titanium oxide thin film. Applied Surface Science, 2003. **218**(1-4): p. 97-105.

50. Wang, X.D., J. Shen, and Q. Pan, Raman spectroscopy of sol-gel derived titanium oxide thin films. Journal of Raman Spectroscopy, 2011. **42**(7): p. 1578-1582.

51. Preiss, H., L.M. Berger, and D. Schultze, Studies on the carbothermal preparation of titanium carbide from different gel precursors. Journal of the European Ceramic Society, 1999. **19**(2): p. 195-206.

52. Colombo, P., et al., Polymer-Derived Ceramics: 40 Years of Research and Innovation in Advanced Ceramics. Journal of the American Ceramic Society, 2010. **93**(7): p. 1805-1837.

53. Riedel, R., et al., Silicon-based polymer-derived ceramics: Synthesis properties and applications - A review. Journal of the Ceramic Society of Japan, 2006. **114**(1330): p. 425-444.

54. Krasil'nikov, V.N., et al., Synthesis and properties of titanium glycolate Ti(OCH(2)CH(2)O)(2). Russian Journal of Inorganic Chemistry, 2008. **53**(7): p. 1065-1069.

55. Edited by Walker, P.L., Chemistry and Physics of Carbon Mercel Dekker, New York, , 1971. **7**: p. 243.

56. Babelon, P., et al., SEM and XPS studies of titanium dioxide thin films grown by MOCVD. Thin Solid Films, 1998. **322**(1-2): p. 63-67.

57. Kubart, T., T. Nyberg, and S. Berg, Modelling of low energy ion sputtering from oxide surfaces. Journal of Physics D-Applied Physics, 2010. **43**(20).

58. Koc, R., Kinetics and phase evolution during carbothermal synthesis of titanium carbide from ultrafine titania/carbon mixture. Journal of Materials Science, 1998. **33**(4): p. 1049-1055.

59. Gruner, W., S. Stolle, and K. Wetzig, Formation of COx species during the carbothermal reduction of oxides of Zr, Si, Ti, Cr, W, and Mo. International Journal of Refractory Metals & Hard Materials, 2000. **18**(2-3): p. 137-145.

60. Wu, R.L.C., et al., Physical and Tribological Properties of Rapid Thermal Annealed Diamond-Like Carbon-Films. Surface & Coatings Technology, 1992. **55**(1-3): p. 576-580.

61. Jenkins, G.M., Kawamura K., , Polymeric Carbons. Carbon Fibre, Glass and Char. Cambridge University Press, 1976: p. p. 94.

62. McCormick, J.R., et al., A four-point probe correlation of oxygen sensitivity to changes in surface resistivity of TiO2(001) and Pd-modified TiO2(001). Surface Science, 2003. **545**(1-2): p. L741-L746.

63. Graham, A.P., et al., An investigation of the electrical properties of pyrolytic carbon in reduced dimensions: Vias and wires. Journal of Applied Physics, 2010. **107**(11).

64. Pierson, H.O., Handbook of carbon, graphite, diamond, and fullerenes: properties, processing, and applications. William Andrew, 1993: p. p. 157.

65. Cordelair, J. and P. Greil, Electrical conductivity measurements as a microprobe for structure transitions in polysiloxane derived Si-O-C ceramics. Journal of the European Ceramic Society, 2000. **20**(12): p. 1947-1957.

66. Sankur, H. and W. Gunning, Crystallization and Diffusion in Composite Tio2-Sio2 Thin-Films. Journal of Applied Physics, 1989. **66**(10): p. 4747-4751.

67. Chang, H. and P.J. Huang, Thermo-Raman studies on anatase and rutile. Journal of Raman Spectroscopy, 1998. **29**(2): p. 97-102.

68. Karakuscu, A., et al., White Luminescence from Sol-Gel-Derived SiOC Thin Films. Journal of the American Ceramic Society, 2009. **92**(12): p. 2969-2974.

69. Robertson, J., Recombination and photoluminescence mechanism in hydrogenated amorphous carbon. Physical Review B, 1996. **53**(24): p. 16302-16305.

70. Casiraghi, C., et al., Bonding in hydrogenated diamond-like carbon by Raman spectroscopy. Diamond and Related Materials, 2005. **14**(3-7): p. 1098-1102.

71. Jakschik, S., et al., Crystallization behavior of thin ALD-Al2O3 filMS. Thin Solid Films, 2003. **425**(1-2): p. 216-220.

72. Katamreddy, R., et al., Post deposition annealing of aluminum oxide deposited by atomic layer deposition using tris(diethylamino)aluminum and water vapor on Si(100). Thin Solid Films, 2007. **515**(17): p. 6931-6937.

73. Qin, X.D., H.X. Sun, and F. Zaera, Thermal chemistry of Mn-2(CO)(10) during deposition of thin manganese films on silicon oxide and on copper surfaces. Journal of Vacuum Science & Technology A, 2012. **30**(1).

BIBLIOGRAPHY

1. Ishihara, K., et al., Characterization of Cvd-Tin Films Prepared with Metalorganic Source. Japanese Journal of Applied Physics Part 1-Regular Papers Short Notes & Review Papers, 1990. **29**(10): p. 2103-2105.

2. Lange, S., et al., Pulse magnetron sputtering in a reactive gas mixture of variable composition to manufacture multilayer and gradient optical coatings. Thin Solid Films, 2006. **502**(1-2): p. 29-33.

3. Klem, J.F., et al., Characterization of Thin Algaas/Ingaas/Gaas Quantum-Well Structures Bonded Directly to Sio2/Si and Glass Substrates. Journal of Applied Physics, 1989. **66**(1): p. 459-462.

4. Rossnagel, S.M., Sherman, A. and Turner, F., Plasma-enhanced atomic layer deposition of Ta and Ti for interconnect diffusion barriers. Journal of Vacuum Science & Technology B, 2000. **18**(4): p. 2016-2020.

5. George, S.M., Atomic Layer Deposition: An Overview. Chemical Reviews, 2010. **110**(1): p. 111-131.

6. Elam, J.W., Dasgupta, N.P., and Prinz, F.B., ALD for clean energy conversion, utilization, and storage. Mrs Bulletin, 2011. **36**(11): p. 899-906.

7. Elam, J.W., et al., Conformal coating on ultrahigh-aspect-ratio nanopores of anodic alumina by atomic layer deposition. Chemistry of Materials, 2003. **15**(18): p. 3507-3517.

8. Parsons, G.N., George, S.M. and Knez, M., Progress and future directions for atomic layer deposition and ALD-based chemistry. Mrs Bulletin, 2011. **36**(11): p. 865-871.

9. Malygin, A.A., The Molecular Layering Method as a Basis of Chemical Nanotechnology Natural Microporous Materials in Environmental Technology NATO ASI Series, 1999. **362**: p. 487-495.

10. Parsons, G.N., George, S.M., Knez, M.,, Progress and future directions for atomic layer deposition and ALD-based chemistry. MRS Bull. , 2011. **36**: p. 865.

11. Puurunen, R.L., Surface chemistry of atomic layer deposition: A case study for the trimethylaluminum/water process. Journal of Applied Physics, 2005. **97**(12).

12. Malygin, A.A., Molecular layering technology and some of its applications. Russian Journal of Applied Chemistry, 1996. **69**(10): p. 1419-1426.

13. Riley, L.A., et al., Improved Mechanical Integrity of ALD-Coated Composite Electrodes for Li-Ion Batteries. Electrochemical and Solid State Letters, 2011. **14**(3): p. A29-A31.

14. Malygin, A.A., Trifonov, S.A., and Tsvetkova, M.N., Perspectives of application of the molecular layer deposition technique for controlling operational properties of materials for shipbuilding. Russian Journal of General Chemistry, 2010. **80**(10): p. 2181-2191.

15. Abdulagatov, A.I., et al., Al2O3 and TiO2 Atomic Layer Deposition on Copper for Water Corrosion Resistance. Acs Applied Materials & Interfaces, 2011. **3**(12): p. 4593-4601.

16. Malygin, A.A., Synthesis of multicomponent oxide low-dimensional systems on the surface of porous silicon dioxide using the molecular layering method. Russian Journal of General Chemistry, 2002. **72**(4): p. 575-589.

17. Aleskovskii, V.B., Chemistry and Technology of Solids. Journal of Applied Chemistry of the Ussr, 1974. **47**(10): p. 2207-2217.

18. Malygin, A.A., The molecular layering nanotechnology: Basis and application. Journal of Industrial and Engineering Chemistry, 2006. **12**(1): p. 1-11.

19. Sanchez, C., et al., Applications of hybrid organic-inorganic nanocomposites. Journal of Materials Chemistry, 2005. **15**(35-36): p. 3559-3592.

20. Mammeri, F., et al., Mechanical properties of hybrid organic-inorganic materials. Journal of Materials Chemistry, 2005. **15**(35-36): p. 3787-3811.

21. Sanchez, C., et al., Optical properties of functional hybrid organic-inorganic nanocomposites. Advanced Materials, 2003. **15**(23): p. 1969-1994.

22. Dameron, A.A., et al., Molecular layer deposition of alucone polymer films using trimethylaluminum and ethylene glycol. Chemistry of Materials, 2008. **20**(10): p. 3315-3326.

23. Lee, Y., et al., Molecular Layer Deposition of Aluminum Alkoxide Polymer Films Using Trimethylaluminum and Glycidol. Langmuir, 2011. **27**(24): p. 15155-15164.

24. Seghete, D., et al., Importance of Trimethylaluminum Diffusion in Three-Step ABC Molecular Layer Deposition Using Trimethylaluminum, Ethanolamine, and Maleic Anhydride. Langmuir, 2010. **26**(24): p. 19045-19051.

25. George, S.M., Yoon, B. and Dameron, A.A., Surface Chemistry for Molecular Layer Deposition of Organic and Hybrid Organic-Inorganic Polymers. Accounts of Chemical Research, 2009. **42**(4): p. 498-508.

26. George, S.M., et al., Metalcones: Hybrid Organic-Inorganic Films Fabricated Using Atomic and Molecular Layer Deposition Techniques. Journal of Nanoscience and Nanotechnology, 2011. **11**(9): p. 7948-7955.

27. Seghete, D., et al., Sacrificial layers for air gaps in NEMS using alucone molecular layer deposition. Sensors and Actuators a-Physical, 2009. **155**(1): p. 8-15.

28. Miller, D.C., et al., The mechanical robustness of atomic-layer- and molecular-layer-deposited coatings on polymer substrates. Journal of Applied Physics, 2009. **105**(9).

29. Yu, M.A., et al., H-2 Separation Using Defect-Free, Inorganic Composite Membranes. Journal of the American Chemical Society, 2011. **133**(6): p. 1748-1750.

30. Smith, D.L., Thin-film deposition: principles and practice. McGraw-Hill Inc., 1995.

31. Elam, J.W., M.D. Groner, and S.M. George, Viscous flow reactor with quartz crystal microbalance for thin film growth by atomic layer deposition. Review of Scientific Instruments, 2002. **73**(8): p. 2981-2987.

32. Oura, K., Lifshits, V. G., Saranin, A. A., Zotov, A. V., Katayama, M., Surface science. Springer-Verlag Berlin 2003: p. 66.

33. http://tap.iop.org/atoms/xray/530/page_47297.html.

34. Segmuller, A., Characterization of Epitaxial Thin-Films by X-ray-Diffraction. Journal of Vacuum Science & Technology a-Vacuum Surfaces and Films, 1991. **9**(4): p. 2477-2482.

35. Clemens, B.M. and J.A. Bain, Stress Determination in Textured Thin-Films Using X-ray-Diffraction. Mrs Bulletin, 1992. **17**(7): p. 46-51.

36. http://www.texample.net/tikz/examples/principle-of-X-ray-photoelectron-spectroscopy-xps/.

37. Hand Book of Chemistry and Physics, 89th Edition 2008-2009.

38. Harris, D.C., Durable 3-5 mu m transmitting infrared window materials. Infrared Physics & Technology, 1998. **39**(4): p. 185-201.

39. Swamy, V., N.A. Dubrovinskaya, and L.S. Dubrovinsky, High-temperature powder X-ray diffraction of yttria to melting point. Journal of Materials Research, 1999. **14**(2): p. 456-459.

40. Huignard, A., et al., Growth by laser ablation of Y2O3 and Tm : Y2O3 thin films for optical applications. Journal of Materials Chemistry, 2000. **10**(2): p. 549-554.

41. Gaboriaud, R.J., et al., Yttrium sesquioxide, Y2O3, thin films deposited on Si by ion beam sputtering: microstructure and dielectric properties. Thin Solid Films, 2001. **400**(1-2): p. 106-110.

42. Kahn, A., et al., Low threshold monocrystalline Nd:(Gd, Lu)2O3 channel waveguide laser. Optics Express, 2009. **17**(6): p. 4412-4418.

43. Kahn, A., et al., Amplification in epitaxially grown Er:(Gd, LU)2O3 waveguides for active integrated optical devices. Journal of the Optical Society of America B-Optical Physics, 2008. **25**(11): p. 1850-1853.

44. Miu, D., et al., alpha-Axis growth of ferroelectric SrBi2Ta2O9 thin films on silicon. Materials Letters, 2005. **59**(10): p. 1243-1247.

45. Suzuki, K., Tanaka, K., Fu, D. S.,, Electroceramics In Japan VII (Key Engineering Materials). 2004. **269**: p. 49-52.

46. Lu, F.X., et al., Magnetron sputtered oxidation resistant and antireflection protective coatings for freestanding diamond film IR windows. Diamond and Related Materials, 2009. **18**(2-3): p. 244-248.

47. Dukel'skii, K.V. and S.K. Evstrop'ev, Forming protective nanosize Y2O3 coatings on crystal phosphors. Journal of Optical Technology, 2008. **75**(11): p. 737-740.

48. Shi, G.D., et al., Influence of Metal-Layer Thickness on Annealing behaviors of a NiCoCrAl/YSZ Multiscalar Microlaminate produced by EB-PVD. Journal of Alloys and Compounds, 2009. **476**(1-2): p. 830-835.

49. Wang, Y.Q., et al., High temperature cyclic oxidation behavior of Y2O3-ZrO2 thermal barrier coatings irradiated by high-intensity pulsed ion beam. Journal of Central South University of Technology, 2009. **16**(1): p. 13-17.

50. Xu, Z.H., et al., Double-ceramic-layer thermal barrier coatings of La2Zr2O7/YSZ deposited by electron beam-physical vapor deposition. Journal of Alloys and Compounds, 2009. **473**(1-2): p. 509-515.

51. Montero, X., et al., Spinel and Perovskite Protection Layers Between Crofer22APU and La0.8Sr0.2FeO3 Cathode Materials for SOFC Interconnects. Journal of the Electrochemical Society, 2009. **156**(1): p. B188-B196.

52. Tanaka, M., et al., Delamination toughness of electron beam physical vapor deposition (EB-PVD)Y2O3-ZrO2 thermal barrier coatings by the pushout method: Effect of thermal cycling temperature. Journal of Materials Research, 2008. **23**(9): p. 2382-2392.

53. Dubourdieu, C., et al., Addition of yttrium into HfO2 films: Microstructure and electrical properties. Journal of Vacuum Science & Technology A, 2009. **27**(3): p. 503-514.

54. Shimada, S., et al., Thermal plasma CVD of PSZ and double layered TiN/PSZ coatings by injection of alkoxides solutions with H2O. Surface & Coatings Technology, 2008. **202**(19): p. 4644-4652.

55. Alarcon-Flores, G., et al., Optical and structural characteristics of Y2O3 thin films synthesized from yttrium acetylacetonate. Journal of Materials Science, 2008. **43**(10): p. 3582-3588.

56. Pan, T.M. and K.M. Liao, Structural properties and sensing characteristics of Y2O3 sensing membrane for pH-ISFET. Sensors and Actuators B-Chemical, 2007. **127**(2): p. 480-485.

57. Mölsä, H., Niinistö, L., Utriainen, M., , Growth of yttrium oxide thin films from ß-diketonate precursor. Advanced Materials for Optics and Electronics, 1994. **4**(6): p. 389–400.

58. Putkonen, M., et al., Low-temperature ALE deposition of Y2O3 thin films from beta-diketonate precursors. Chemical Vapor Deposition, 2001. **7**(1): p. 44-50.

59. Gusev, E.P., et al., Ultrathin high-K metal oxides on silicon: processing, characterization and integration issues. Microelectronic Engineering, 2001. **59**(1-4): p. 341-349.

60. Van, T.T. and J.P. Chang, Radical-enhanced atomic layer deposition of Y2O3 via a beta-diketonate precursor and O radicals. Surface Science, 2005. **596**(1-3): p. 1-11.

61. Niinisto, J., M. Putkonen, and L. Niinisto, Processing of Y2O3 thin films by atomic layer deposition from cyclopentadienyl-type compounds and water as precursors. Chemistry of Materials, 2004. **16**(15): p. 2953-2958.

62. Majumder, P., et al., Atomic layer deposition of Y2O3 films on silicon using tris(ethylcyclopentadienyl) yttrium precursor and water vapor. Journal of the Electrochemical Society, 2008. **155**(8): p. G152-G158.

63. de Rouffignac, P., J.S. Park, and R.G. Gordon, Atomic layer deposition of Y2O3 thin films from yttrium tris(N,N'-diisopropylacetamidinate) and water. Chemistry of Materials, 2005. **17**(19): p. 4808-4814.

64. Elliott, S.D., Improving ALD growth rate via ligand basicity: Quantum chemical calculations on lanthanum precursors. Surface & Coatings Technology, 2007. **201**(22-23): p. 9076-9081.

65. Ren, J., et al., Surface reaction mechanism of Y2O3 atomic layer deposition on the hydroxylated Si<100>-2 x 1: A density functional theory study. Applied Surface Science, 2009. **255**(16): p. 7136-7141.

66. Niu, D., R.W. Ashcraft, and G.N. Parsons, Water absorption and interface reactivity of yttrium oxide gate dielectrics on silicon. Applied Physics Letters, 2002. **80**(19): p. 3575-3577.

67. Kuroda, Y., et al., Specific adsorption behavior of water on a Y2O3 surface. Langmuir, 2000. **16**(17): p. 6937-6947.

68. Smith, D.W., An Acidity Scale for Binary Oxides. Journal of Chemical Education, 1987. **64**(6): p. 480-482.

69. Elam, J.W., et al., Atomic layer deposition of In2O3 using cyclopentadienyl indium: A new synthetic route to transparent conducting oxide films. Chemistry of Materials, 2006. **18**(15): p. 3571-3578.

70. Elam, J.W., Z.A. Sechrist, and S.M. George, ZnO/Al2O3 nanolaminates fabricated by atomic layer deposition: growth and surface roughness measurements. Thin Solid Films, 2002. **414**(1): p. 43-55.

71. Ritala, M., et al., Growth of Titanium-Dioxide Thin-Films by Atomic Layer Epitaxy. Thin Solid Films, 1993. **225**(1-2): p. 288-295.

72. Elam, J.W., ALD workshop at 8th International Conference on Atomic Layer Deposition - ALD 2008.

73. Elliott, S.D., 8th International Conference on Atomic Layer Deposition - ALD 2008.

74. Scherrer, P., Goett. Nachr., 1918. **2**: p. 98.

75. Crist, B.V., Handbook of Monochromatic XPS Spectra, 2000.

76. Chambers, J.J., et al., Effects of surface pretreatments on interface structure during formation of ultra-thin yttrium silicate dielectric films on silicon. Applied Surface Science, 2001. **181**(1-2): p. 78-93.

77. Ulrich, M.D., et al., Bonding and structure of ultrathin yttrium oxide films for Si field effect transistor gate dielectric applications. Journal of Vacuum Science & Technology B, 2003. **21**(4): p. 1792-1797.

78. Durand, C., et al., Structural and electrical characterizations of yttrium oxide films after postannealing treatments. Journal of the Electrochemical Society, 2005. **152**(12): p. F217-F225.

79. Durand, C., et al., Microstructure and electrical characterizations of yttrium oxide and yttrium silicate thin films deposited by pulsed liquid-injection plasma-enhanced metal-organic chemical vapor deposition. Journal of Applied Physics, 2004. **96**(3): p. 1719-1729.

80. Barr T.L. Electron Spectroscopy for Chemical Analysis Examination of Rare Earth and Near Rare Earth Species, Quantitative Surface Analysis of Materials. ASTM STP 643; McIntyre N.S. Ed.; American Society for Testing and Materials: Philadelphia, 178; pp 83-104.

81. Niu, D., et al., Chemical, physical, and electrical characterizations of oxygen plasma assisted chemical vapor deposited yttrium oxide on silicon. Journal of the Electrochemical Society, 2003. **150**(5): p. F102-F109.

82. Nigara, Y., Measurement of the Optical Constants of Yttrium Oxide. Jpn. J. Appl. Phys., 1968. **7**: p. 404-408.

83. Heitmann, W., Reactively Evaporated Films of Scandia and Yttria. Applied Optics, 1973. **12**(2): p. 394-397.

84. Masetti, E., Piegari, A.M., Tirabassi, A.,, Optical characterization of low-absorbing thin films in the visible and infrared spectrum (SPIE Proceedings Paper). Optical Thin Films and Applications, 1990. **1270**: p. 125-437.

85. Atanassov, G., R. Thielsch, and D. Popov, Optical-Properties of TiO2, Y2O3 and Ceo2 Thin-Films Deposited by Electron-Beam Evaporation. Thin Solid Films, 1993. **223**(2): p. 288-292.

86. Edited By Palik, E.D., Handbook of Optical Constants of Solids, Academic Press, 1998.

87. Bezuidenhout, D.F. and R. Pretorius, The Optical-Properties of Evaporated Y2O3 Films. Thin Solid Films, 1986. **139**(2): p. 121-132.

88. Arnon, O. and J. Chou, Wide Band Measurement of the Refractive-Index of Optical Thin-Films during Their Deposition. Thin Solid Films, 1982. **89**(3): p. 268-268.

89. George, S.M., A.W. Ott, and J.W. Klaus, Surface chemistry for atomic layer growth. Journal of Physical Chemistry, 1996. **100**(31): p. 13121-13131.

90. Groner, M.D., et al., Low-temperature Al2O3 atomic layer deposition. Chemistry of Materials, 2004. **16**(4): p. 639-645.

91. Niinisto, L., et al., Advanced electronic and optoelectronic materials by Atomic Layer Deposition: An overview with special emphasis on recent progress in processing of high-k dielectrics and other oxide materials. Physica Status Solidi a-Applied Research, 2004. **201**(7): p. 1443-1452.

92. Technology Roadmap for Semiconductors. http://www.itrs.net/.International, 2007.

93. Kim, H., Atomic layer deposition of metal and nitride thin films: Current research efforts and applications for semiconductor device processing. Journal of Vacuum Science & Technology B, 2003. **21**(6): p. 2231-2261.

94. Zaera, F., The surface chemistry of thin film atomic layer deposition (ALD) processes for electronic device manufacturing. Journal of Materials Chemistry, 2008. **18**(30): p. 3521-3526.

95. Ahn, C.H., et al., Characteristics of TiN thin films grown by ALD using TiCl(4)and NH3. Metals and Materials International, 2001. **7**(6): p. 621-625.

96. Satta, A., et al., Growth mechanism and continuity of atomic layer deposited TiN films on thermal SiO2. Journal of Applied Physics, 2002. **92**(12): p. 7641-7646.

97. Juppo, M., A. Rahtu, and M. Ritala, In situ mass spectrometry study on surface reactions in atomic layer deposition of TiN and Ti(Al)N thin films. Chemistry of Materials, 2002. **14**(1): p. 281-287.

98. Kim, J., et al., Physical properties of highly Conformal TiN thin films grown by atomic layer deposition. Japanese Journal of Applied Physics Part 1-Regular Papers Short Notes & Review Papers, 2003. **42**(3): p. 1375-1379.

99. Kim, J., et al., Properties including step coverage of TiN thin films prepared by atomic layer deposition. Applied Surface Science, 2003. **210**(3-4): p. 231-239.

100. Tiznado, H. and F. Zaera, Surface chemistry in the atomic layer deposition of TiN films from TiCl4 and ammonia. Journal of Physical Chemistry B, 2006. **110**(27): p. 13491-13498.

101. Elers, K.E., et al., TiCl4 as a precursor in the TiN deposition by ALD and PEALD. Journal of the Electrochemical Society, 2005. **152**(8): p. G589-G593.

102. Hiltunen, L., et al., Nitrides of Titanium, Niobium, Tantalum and Molybdenum Grown as Thin-Films by the Atomic Layer Epitaxy Method. Thin Solid Films, 1988. **166**(1-2): p. 149-154.

103. Ritala, M., et al., Atomic layer epitaxy growth of TiN thin films from TiI4 and NH3. Journal of the Electrochemical Society, 1998. **145**(8): p. 2914-2920.

104. Ritala, M., et al., Atomic Layer Epitaxy Growth of Tin Thin-Films. Journal of the Electrochemical Society, 1995. **142**(8): p. 2731-2737.

105. Ritala, M., et al., Effects of intermediate zinc pulses on properties of TiN and NbN films deposited by atomic layer epitaxy. Applied Surface Science, 1997. **120**(3-4): p. 199-212.

106. Juppo, M., et al., Trimethylaluminum as a reducing agent in the atomic layer deposition of Ti(Al)N thin films. Chemical Vapor Deposition, 2001. **7**(5): p. 211-217.

107. Heil, S.B.S., et al., Low-temperature deposition of TiN by plasma-assisted atomic layer deposition. Journal of the Electrochemical Society, 2006. **153**(11): p. G956-G965.

108. Min, J.S., et al., Atomic layer deposition of TiN films by alternate supply of tetrakis(ethylmethylamino)-titanium and ammonia. Japanese Journal of Applied Physics Part 1-Regular Papers Short Notes & Review Papers, 1998. **37**(9A): p. 4999-5004.

109. Kim, H.K., et al., Metalorganic atomic layer deposition of TiN thin films using TDMAT and NH3. Journal of the Korean Physical Society, 2002. **41**(5): p. 739-744.

110. Elam, J.W., et al., Surface chemistry and film growth during TiN atomic layer deposition using TDMAT and NH3. Thin Solid Films, 2003. **436**(2): p. 145-156.

111. Kim, J.Y., et al., Remote plasma enhanced atomic layer deposition of TiN thin films using metalorganic precursor. Journal of Vacuum Science & Technology A, 2004. **22**(1): p. 8-12.

112. Kim, J.Y., et al., Remote plasma-enhanced atomic-layer deposition of TiN by using TDMAT with a NH3 plasma. Journal of the Korean Physical Society, 2004. **45**(6): p. 1639-1643.

113. Juppo, M., M. Ritala, and M. Leskela, Use of 1,1-dimethylhydrazine in the atomic layer deposition of transition metal nitride thin films. Journal of the Electrochemical Society, 2000. **147**(9): p. 3377-3381.

114. Bejarano, G., J. Caicedo, and J.M. Saldana, Mechanical and tribological properties enhancement of heat treated AISI 4340 steel by using a TiN/TiAlN multilayer coating system. Revista Facultad De Ingenieria-Universidad De Antioquia, 2008(44): p. 36-42.

115. Barshilia, H.C., et al., Optical properties and thermal stability of TiAlN/AlON tandem absorber prepared by re active DC/RF magnetron sputtering. Solar Energy Materials and Solar Cells, 2008. **92**(11): p. 1425-1433.

116. Koo, J., et al., Study on the characteristics of TiAlN thin film deposited by atomic layer deposition method. Journal of Vacuum Science & Technology a-Vacuum Surfaces and Films, 2001. **19**(6): p. 2831-2834.

117. Kim, J.Y., et al., Compositional variations of TiAlN films deposited by metalorganic atomic layer deposition method. Japanese Journal of Applied Physics Part 1-Regular Papers Short Notes & Review Papers, 2002. **41**(2A): p. 562-565.

118. Fujieda, S., M. Mizuta, and Y. Matsumoto, Low-temperature metalorganic chemical vapour deposition of AIN for surface passivation of GaAs. Advanced Materials for Optics and Electronics, 1996. **6**(3): p. 127-134.

119. Fujieda, S., M. Mizuta, and Y. Matsumoto, Growth-Characterization of Low-Temperature MOCVD Gan - Comparison between N2h4 and Nh3. Japanese Journal of Applied Physics Part 1-Regular Papers Short Notes & Review Papers, 1987. **26**(12): p. 2067-2071.

120. Morishita, S., S. Sugahara, and M. Matsumura, Atomic-layer chemical-vapor-deposition of silicon-nitride. Applied Surface Science, 1997. **112**: p. 198-204.

121. Burton, B.B., A.R. Lavoie, and S.M. George, Tantalum nitride atomic layer deposition using (tert-butylimido) tris(diethylamido) tantalum and hydrazine. Journal of the Electrochemical Society, 2008. **155**(7): p. D508-D516.

122. Vogt, K.W., L.A. Naugher, and P.A. Kohl, Low-Temperature Nitridation of Transition-Metals with Hydrazine. Thin Solid Films, 1995. **256**(1-2): p. 106-115.

123. Schmidt, E.W., Hydrazine and its Derivatives: Preparation, Properties, Applications; . 2nd ed., 2001.

124. Goldstein, D.N., J.A. McCormick, and S.M. George, Al2O3 Atomic Layer Deposition with Trimethylaluminum and Ozone Studied by in Situ Transmission FTIR Spectroscopy and Quadrupole Mass Spectrometry. Journal of Physical Chemistry C, 2008. **112**(49): p. 19530-19539.

125. Puurunen, R.L. and W. Vandervorst, Island growth as a growth mode in atomic layer deposition: A phenomenological model. Journal of Applied Physics, 2004. **96**(12): p. 7686-7695.

126. Rocklein, M.N. and S.M. George, Temperature-induced apparent mass changes observed during quartz crystal microbalance measurements of atomic layer deposition. Analytical Chemistry, 2003. **75**(19): p. 4975-4982.

127. Jeon, H., et al., Study on the characteristics of TiN thin film deposited by the atomic layer chemical vapor deposition method. Journal of Vacuum Science & Technology a-Vacuum Surfaces and Films, 2000. **18**(4): p. 1595-1598.

128. Juppo, M., et al., Atomic layer deposition of titanium nitride thin films using tert-butylamine and allylamine as reductive nitrogen sources. Electrochemical and Solid State Letters, 2002. **5**(1): p. C4-C6.

129. Kim, J.Y., et al., Comparison of TiN films deposited using tetrakisdimethylaminotitanium and tetrakisdiethylaminotitanium by the atomic layer deposition method. Japanese Journal of Applied Physics Part 1-Regular Papers Short Notes & Review Papers, 2003. **42**(7A): p. 4245-4248.

130. Kim, J.Y., et al., Comparison of TiN and TiAlN as a diffusion barrier deposited by atomic layer deposition. Journal of the Korean Physical Society, 2002. **40**(1): p. 176-179.

131. Logothetidis, S., et al., Room temperature oxidation behavior of TiN thin films. Thin Solid Films, 1999. **338**(1-2): p. 304-313.

132. Musschoot, J., et al., Atomic layer deposition of titanium nitride from TDMAT precursor. Microelectronic Engineering, 2009. **86**(1): p. 72-77.

133. Scott, D.W., et al., Hydrazine - Heat Capacity, Heats of Fusion and Vaporization, Vapor Pressure, Entropy and Thermodynamic Functions. Journal of the American Chemical Society, 1949. **71**(7): p. 2293-2297.

134. Tillner-Roth, R., Harms-Watzenberg, F., Baehr, H.D., Eine neue Fundamentalgleichung für Ammoniak. DKV-Tagungsbericht 1993(20): p. 167-181.

135. Snyder, M.Q., et al., An infrared study of the surface chemistry of titanium nitride atomic layer deposition on silica from TiCl4 and NH3. Thin Solid Films, 2006. **514**(1-2): p. 97-102.

136. Giguere, P.A. and I.D. Liu, On the Infrared Spectrum of Hydrazine. Journal of Chemical Physics, 1952. **20**(1): p. 136-140.

137. Amores, J.M.G., et al., An FT-IR study of ammonia adsorption and oxidation over anatase-supported metal oxides. Applied Catalysis B-Environmental, 1997. **13**(1): p. 45-58.

138. Devillepin, J. and A. Novak, Infrared and Raman-Spectra of Crystals of Hydrazinium Chloride and Bromide at Low-Temperature .1. Intramolecular Vibrations. Molecular Crystals and Liquid Crystals, 1974. **27**(3-4): p. 391-415.

139. Snyder, R.G. and J.C. Decius, The Infrared Spectra of N2h6cl2 and N2h6f2. Spectrochimica Acta, 1959. **13**(4): p. 280-290.

140. Moore, G.E. and R.M. Badger, The Infrared Spectra and Structure of the Chloramines and Nitrogen Trichloride. Journal of the American Chemical Society, 1952. **74**(23): p. 6076-6080.

141. Chuang, C.C., J.S. Shiu, and J.L. Lin, Interaction of hydrazine and ammonia with TiO2. Physical Chemistry Chemical Physics, 2000. **2**(11): p. 2629-2633.

142. Troyan, J.E., Properties, Production, and Uses of Hydrazine. Industrial and Engineering Chemistry, 1953. **45**(12): p. 2608-2612.

143. Dillon, A.C., et al., Ammonia Decomposition on Silicon Surfaces Studied Using Transmission Fourier-Transform Infrared-Spectroscopy. Journal of Vacuum Science & Technology a-Vacuum Surfaces and Films, 1991. **9**(4): p. 2222-2230.

144. Heubusch, H.P., Pugmire T. K, The Compatibility of Stainless Steels with Nitrogen Tetroxide and Hydrazine AIAA Paper 90-2063, 1990. **A90-43356**: p. 36.

145. Leidheiser Jr., H., The Corrosion of Copper, Tin, and Their Alloys. 1971, New York: John Wiley and Sons, Inc.

146. Feng, Y., et al., The corrosion behaviour of copper in neutral tap water .2. Determination of corrosion rates. Corrosion Science, 1996. **38**(3): p. 387-395.

147. Feng, Y., et al., The corrosion behaviour of copper in neutral tap water .1. Corrosion mechanisms. Corrosion Science, 1996. **38**(3): p. 369-385.

148. Jeon, B., et al., Atomistic insights into aqueous corrosion of copper. Journal of Chemical Physics, 2011. **134**(23).

149. Pehkonen, S.O., A. Palit, and X. Zhang, Effect of specific water quality parameters on copper corrosion. Corrosion, 2002. **58**(2): p. 156-165.

150. Sobue, K., et al., Effect of free carbon dioxide on corrosion behavior of copper in simulated water. Surface and Coatings Technology, 2003. **169**: p. 662-665.

151. Feng, Y., et al., Corrosion mechanisms and products of copper in aqueous solutions at various pH values. Corrosion, 1997. **53**(5): p. 389-398.

152. Boulay, N. and M. Edwards, Role of temperature, chlorine, and organic matter in copper corrosion by-product release in soft water. Water Research, 2001. **35**(3): p. 683-690.

153. Lau, K.H., A. Sanjurjo, and B.J. Wood, Aluminum and alumina coatings on copper by chemical vapor deposition in fluidized bed reactors. Surface and Coatings Technology, 1992. **54**(1-3): p. 234-240.

154. Sanjurjo, A., et al., Titanium-based coatings on copper by chemical vapor deposition in fluidized bed reactors. Surface and Coatings Technology, 1991. **49**(1-3): p. 110-115.

155. Itoh, M., H. Nishihara, and K. Aramaki, A Chemical Modification of Alkanethiol Self-Assembled Monolayers with Alkyltrichlorosilanes for the Protection of Copper Against Corrosion. Journal of The Electrochemical Society, 1994. **141**(8): p. 2018-2023.

156. Itoh, M., H. Nishihara, and K. Aramaki, Preparation and Evaluation of Two-Dimensional Polymer Films by Chemical Modification of an Alkanethiol Self-Assembled Monolayer for Protection of Copper Against Corrosion. Journal of The Electrochemical Society, 1995. **142**(11): p. 3696-3704.

157. Yamamoto, Y., H. Nishihara, and K. Aramaki, Self-Assembled Layers of Alkanethiols on Copper for Protection Against Corrosion. Journal of The Electrochemical Society, 1993. **140**(2): p. 436-443.

158. Brusic, V., et al., Copper Corrosion With and Without Inhibitors. Journal of The Electrochemical Society, 1991. **138**(8): p. 2253-2259.

159. Wu, Y.C., et al., Effect of KI on Improving Copper Corrosion Inhibition Efficiency of Benzotriazole in Sulfuric Acid Electrolytes. Journal of The Electrochemical Society, 1993. **140**(10): p. 2791-2800.

160. Youda, R., H. Nishihara, and K. Aramaki, A SERS study on inhibition mechanisms of benzotriazole and its derivatives for copper corrosion in sulphate solutions. Corrosion Science, 1988. **28**(1): p. 87-96.

161. Brusic, V., M. Angelopoulos, and T. Graham, Use of polyaniline and its derivatives in corrosion protection of copper and silver. Journal of The Electrochemical Society, 1997. **144**(2): p. 436-442.

162. Cicileo, G.P., et al., Comparative study of organic inhibitors of copper corrosion. Corrosion Science, 1999. **41**(7): p. 1359-1375.

163. Tallman, D.E., et al., Electroactive conducting polymers for corrosion control Part 1. General introduction and a review of non-ferrous metals. Journal of The Electrochemical Society, 2002. **6**(2): p. 73-84.

164. Lin, Y. and H. Yasuda, Effect of plasma polymer deposition methods on copper corrosion protection. Journal of Applied Polymer Science, 1996. **60**(4): p. 543-555.

165. Patil, S., S.R. Sainkar, and P.P. Patil, Poly(o-anisidine) coatings on copper: synthesis, characterization and evaluation of corrosion protection performance. Applied Surface Science, 2004. **225**(1-4): p. 204-216.

166. Dillon, A.C., et al., Surface chemistry of Al2O3 deposition using Al(CH3)3 and H2O in a binary reaction sequence. Surface Science, 1995. **322**(1-3): p. 230-242.

167. Ott, A.W., et al., Al3O3 thin film growth on Si<100> using binary reaction sequence chemistry. Thin Solid Films, 1997. **292**(1-2): p. 135-144.

168. Marin, E., et al., Corrosion protection of AISI 316 stainless steel by ALD alumina/titania nanometric coatings. Journal of Coatings Technology and Research, 2011. **8**(5): p. 655-659.

169. Matero, R., et al., Atomic layer deposited thin films for corrosion protection. Journal de Physique IV, 1999. **9**(P8): p. 493-499.

170. Shan, C.X., X.H. Hou, and K.L. Choy, Corrosion resistance of TiO2 films grown on stainless steel by atomic layer deposition. Surface and Coatings Technology, 2008. **202**(11): p. 2399-2402.

171. Shan, C.X., et al., Improvement in corrosion resistance of CrN coated stainless steel by conformal TiO2 deposition. Surface and Coatings Technology, 2008. **202**(10): p. 2147-2151.

172. Groner, M.D., et al., Electrical characterization of thin Al2O3 films grown by atomic layer deposition on silicon and various metal substrates. Thin Solid Films, 2002. **413**(1-2): p. 186-197.

173. Carcia, P.F., et al., Gas diffusion ultrabarriers on polymer substrates using Al2O3 atomic layer deposition and SiN plasma-enhanced chemical vapor deposition. Journal of Applied Physics, 2009. **106**(2): p. 023533.

174. Carcia, P.F., et al., Ca test of Al2O3 gas diffusion barriers grown by atomic layer deposition on polymers. Applied Physics Letters, 2006. **89**(3): p. 031915.

175. Groner, M.D., et al., Gas diffusion barriers on polymers using Al2O3 atomic layer deposition. Applied Physics Letters, 2006. **88**(5): p. 051907.

176. Cooper, R., et al., Protection of polymer from atomic-oxygen erosion using Al2O3 atomic layer deposition coatings. Thin Solid Films, 2008. **516**(12): p. 4036-4039.

177. Minton, T.K., et al., Protecting Polymers in Space with Atomic Layer Deposition Coatings. ACS Applied Materials & Interfaces, 2010. **2**(9): p. 2515-2520.

178. Dameron, A.A., et al., Gas diffusion barriers on polymers using multilayers fabricated by Al2O3 and rapid SiO2 atomic layer deposition. The Journal of Physical Chemistry C, 2008. **112**(12): p. 4573-4580.

180. Sun, Q.F., et al., Improvement of water resistance and dimensional stability of wood through titanium dioxide coating. Holzforschung, 2010. **64**(6): p. 757-761.

181. Taruta, S., et al., Effect of titania addition on crystallization process and some properties of calcium mica-apatite glass-ceramics. Journal of Non-Crystalline Solids, 2003. **321**(1-2): p. 96-102.

182. Liu, C., Recent developments in polymer MEMS. Advanced Materials, 2007. **19**(22): p. 3783-3790.

183. Ritala, M., et al., Titanium Isopropoxide as a Precursor in Atomic Layer Epitaxy of Titanium-Dioxide Thin-Films. Chemistry of Materials, 1993. **5**(8): p. 1174-1181.

184. Cocke, D.L., et al., The low-temperature thermal oxidation of copper,Cu3O2, and its influence on past and future studies. Vacuum, 2005. **79**(1-2): p. 71-83.

185. Zhang, Y.D., et al., Electroplating to visualize defects in Al2O3 thin films grown using atomic layer deposition. Thin Solid Films, 2009. **517**(11): p. 3269-3272.

186. ImageJ. http://rsbweb.nih.gov/ij/. 2010.

187. Wind, R.A. and S.M. George, QCM Studies of Al2O3 ALD using TMA & H2O at 125C. The Journal of Physical Chemistry A, 2010. **114**: p. 1281-1289.

188. Wilson, C.A., R.K. Grubbs, and S.M. George, Nucleation and growth during Al2O3 atomic layer deposition on polymers. Chemistry of Materials, 2005. **17**(23): p. 5625-5634.

189. Aarik, J., et al., Anomalous effect of temperature on atomic layer deposition of titanium dioxide. Journal of Crystal Growth, 2000. **220**(4): p. 531-537.

190. Triani, G., et al., Low temperature atomic layer deposition of titania thin films. Thin Solid Films, 2010. **518**(12): p. 3182-3189.

191. Ye, Q., et al., Hydrophilic properties of nano-TiO2 thin films deposited by RF magnetron sputtering. Vacuum, 2007. **81**(5): p. 627-631.

192. Roach, P., N.J. Shirtcliffe, and M.I. Newton, Progess in superhydrophobic surface development. Soft Matter, 2008. **4**(2): p. 224-240.

193. Mark, J.E., Allcock, H.R., West, R., , Inorganic Polymers. Oxford University Press, Inc., New York., 2005.

194. Lotters, J.C., et al., The mechanical properties of the rubber elastic polymer polydimethylsiloxane for sensor applications. Journal of Micromechanics and Microengineering, 1997. **7**(3): p. 145-147.

195. Camino, G., S.M. Lomakin, and M. Lazzari, Polydimethylsiloxane thermal degradation - Part 1. Kinetic aspects. Polymer, 2001. **42**(6): p. 2395-2402.

196. Archer, R.D., Inorganic and organometallic polymers. John Wiley & Sons, Inc., New York., 2001.

197. Lewis, H.G.P., T.B. Casserly, and K.K. Gleason, Hot-filament chemical vapor deposition of organosilicon thin films from hexamethylcyclotrisiloxane and octamethylcyclotetrasiloxane. Journal of the Electrochemical Society, 2001. **148**(12): p. F212-F220.

198. Lewis, H.G.P., D.J. Edell, and K.K. Gleason, Pulsed-PECVD films from hexamethylcyclotrisiloxane for use as insulating biomaterials. Chemistry of Materials, 2000. **12**(11): p. 3488-3494.

199. Rouessac, V., S. Roualdes, and J. Durand, In situ Mass Spectrometry analyses of the fragmentation of linear and cyclic siloxanes in a glow discharge compared with ex situ FTIR analyses of the deposits. Chemical Vapor Deposition, 2002. **8**(4): p. 155-161.

200. Fukui, H., et al., Surface Modification of Pigments by the Chemical Vapor-Deposition of Cyclic Dimethylsiloxane. Jocca-Surface Coatings International, 1992. **75**(10): p. 411-&.

201. Foussaier, O., et al., Polydimethylsiloxane-based ORMOSIL microstructure: correlation with compressive behavior. Materials Letters, 2000. **42**(5): p. 305-310.

202. Mackenzie, J.D., Y.J. Chung, and Y. Hu, Rubbery Ormosils and Their Applications. Journal of Non-Crystalline Solids, 1992. **147**: p. 271-279.

203. Adarnczyk, N.M., A.A. Dameron, and S.M. George, Molecular layer deposition of poly(p-phenylene terephthalamide) films using terephthaloyl chloride and p-phenylenediamine. Langmuir, 2008. **24**(5): p. 2081-2089.

204. Kantor, S.W., W.T. Grubb, and R.C. Osthoff, The Mechanism of the Acid-Catalyzed and Base-Catalyzed Equilibration of Siloxanes. Journal of the American Chemical Society, 1954. **76**(20): p. 5190-5197.

205. Lubguban, J., et al., Low-k organosilicate films prepared by tetravinyltetramethylcyclotetrasiloxane. Journal of Applied Physics, 2002. **92**(2): p. 1033-1038.

206. Favennec, L., et al., Porous extreme low kappa (EL kappa) dielectrics using a PECVD porogen approach. Materials Science in Semiconductor Processing, 2004. **7**(4-6): p. 277-282.

207. Dvornic, P.R., Lenz, R.W., High Temperature Siloxane Elastomers. Huthing and Wepf, Basel, 1990.

208. Ivin, K.J., Thermodynamics of addition polymerization. Journal of Polymer Science Part a-Polymer Chemistry, 2000. **38**(12): p. 2137-2146.

209. Anderson, D.R., Analysis of Silicones. Editor Smith A.L., Wiley-Interscience, New-York, 1974. Chapter 10.

210. Bellamy, L.J., The Infra-red Spectra of Complex Molecules 3rd ed., Chapman and Hall, London, 1975. Chapter 20.

211. Smith, A.L., Spectrochim. Acta, 1960. **16**: p. 87.

212. Walsh, R., Bond-Dissociation Energy Values in Silicon-Containing Compounds and Some of Their Implications. Accounts of Chemical Research, 1981. **14**(8): p. 246-252.

213. Smith, A.L., Infrared Spectra-Structure Correlations for Organosilicon Compounds. Spectrochimica Acta, 1960. **16**(1-2): p. 87-105.

214. Smith, A.L., Analysis of silicones. Chemical analysis1974, New York,: Wiley. viii, 407 p.

215. Cunico, R.F. and L. Bedell, The Triisopropylsilyl Group as a Hydroxyl-Protecting Function. Journal of Organic Chemistry, 1980. **45**(23): p. 4797-4798.

216. Ferguson, J.D., A.W. Weimer, and S.M. George, Atomic layer deposition of Al2O3 films on polyethylene particles. Chemistry of Materials, 2004. **16**(26): p. 5602-5609.

217. Tian, R.H., et al., Infrared Characterization of Interfacial Si-O Bond Formation on Silanized Flat SiO2/Si Surfaces. Langmuir, 2010. **26**(7): p. 4563-4566.

218. Tolstoy, V.P., et al., Handbook of infrared spectroscopy of ultrathin films. Wiley-Interscience, New-York, 2003.

219. Rai, V.R. and S. Agarwal, Surface reaction mechanisms during ozone-based atomic layer deposition of titanium dioxide. Journal of Physical Chemistry C, 2008. **112**(26): p. 9552-9554.

220. Ferguson, J.D., A.W. Weimer, and S.M. George, Atomic layer deposition of Al2O3 and SiO2 on BN particles using sequential surface reactions. Applied Surface Science, 2000. **162**: p. 280-292.

221. Blangenois, N., et al., Influence of the co-precipitation pH on the physico-chemical and catalytic properties of vanadium aluminum oxide catalyst. Applied Catalysis a-General, 2004. **263**(2): p. 163-170.

222. Weckhuysen, B.M. and D.E. Keller, Chemistry, spectroscopy and the role of supported vanadium oxides in heterogeneous catalysis. Catalysis Today, 2003. **78**(1-4): p. 25-46.

223. Masih, D., H. Yoshitake, and Y. Izumi, Photo-oxidation of ethanol on mesoporous vanadium-titanium oxide catalysts and the relation to vanadium(IV) and (V) sites. Applied Catalysis a-General, 2007. **325**(2): p. 276-282.

224. Anpo, M., Preparation, characterization, and reactivities of highly functional titanium oxide-based photocatalysts able to operate under UV-visible light irradiation: Approaches in realizing high efficiency in the use of visible light. Bulletin of the Chemical Society of Japan, 2004. **77**(8): p. 1427-1442.

225. Tsuyumoto, I. and K. Nawa, Thermochromism of titanium-vanadium oxide thin films prepared from peroxotitanate and peroxovanadate solutions. Solid State Ionics, 2008. **179**(21-26): p. 1227-1229.

226. Yang, Y., D. Kim, and P. Schmuki, Electrochromic properties of anodically grown mixed V2O5-TiO2 nanotubes. Electrochemistry Communications, 2011. **13**(10): p. 1021-1025.

227. Ishihara, T., et al., The Mixed-Oxide Al2O3-V2O5 as a Semiconductor Gas Sensor for No and No2. Sensors and Actuators, 1989. **19**(3): p. 259-265.

228. Zakrzewska, K., Mixed oxides as gas sensors. Thin Solid Films, 2001. **391**(2): p. 229-238.

229. Wang, Z.C., et al., Catalytic Redox Reactions in the CO/N2O System Mediated by the Bimetallic Oxide-Cluster Couple AlVO3+/AlVO4+. Angewandte Chemie-International Edition, 2011. **50**(51): p. 12351-12354.

230. BaddourHadjean, R., et al., A kinetic study of lithium transport in a new Li intercalation material Al0.11V2O5.15 synthesized via a sol-gel process. Journal of the Electrochemical Society, 1996. **143**(7): p. 2083-2088.

231. Lim, J.W., et al., High electrochromic performance of co-sputtered vanadium-titanium oxide as a counter electrode. Solar Energy Materials and Solar Cells, 2009. **93**(12): p. 2069-2074.

232. Wang, Y., et al., Nanostructured vanadium oxide electrodes for enhanced lithium-ion intercalation. Advanced Functional Materials, 2006. **16**(9): p. 1133-1144.

233. Lee, K. and G.Z. Cao, Enhancement of intercalation properties of V2O5 film by TiO2 addition. Journal of Physical Chemistry B, 2005. **109**(24): p. 11880-11885.

234. Ozer, N., S. Sabuncu, and J. Cronin, Electrochromic properties of sol-gel deposited Ti-doped vanadium oxide film. Thin Solid Films, 1999. **338**(1-2): p. 201-206.

235. Takahashi, K., et al., Fabrication and Li+-intercalation properties of V2O5-TiO2 composite nanorod arrays. Applied Physics a-Materials Science & Processing, 2006. **82**(1): p. 27-31.

236. Shyue, J.J. and M.R. De Guire, Single-step preparation of mesoporous, anatase-based titanium-vanadium oxide and its application. Journal of the American Chemical Society, 2005. **127**(36): p. 12736-12742.

237. Nielsen, U.G., et al., Aluminum orthovanadate (AlVO4): Synthesis and characterization by Al-27 and V-51 MAS and MQMAS NMR Spectroscopy. Inorganic Chemistry, 2002. **41**(24): p. 6432-6439.

238. Yamaguchi, O., et al., Formation of Alvo4 Solid-Solution from Alkoxides. Journal of the American Ceramic Society, 1987. **70**(8): p. C198-C200.

239. Ekambaram, S. and K.C. Patil, Rapid Synthesis and Properties of FeVO4, AlVO4, YVO4, and Eu3+-Doped YVO4. Journal of Alloys and Compounds, 1995. **217**(1): p. 104-107.

240. Qureshi, U., T.D. Manning, and I.P. Parkin, Atmospheric pressure chemical vapour deposition of VO(2) and VO2/TiO2 films from the reaction of VOCl3, TiCl4 and water. Journal of Materials Chemistry, 2004. **14**(7): p. 1190-1194.

241. Kakiuchida, H., et al., Optical characterization of titanium-vanadium oxide films. Japanese Journal of Applied Physics Part 1-Regular Papers Brief Communications & Review Papers, 2007. **46**(2): p. 621-626.

242. Habel, D., et al., Phase development in the catalytic system V2O5/TiO2 under oxidising conditions. Journal of the European Ceramic Society, 2006. **26**(15): p. 3287-3294.

243. Abdalla, F.H.A., G.A. ElShobaky, and N.A. Hassan, Effect of sodium oxide doping on solid-solid interactions between V2O5 and Al2O3. Journal of Thermal Analysis, 1996. **47**(6): p. 1777-1785.

244. Elam, J.W.e.a., Nucleation, Growth and Crystallization of ALD Catalytic Oxide Layers. Posters from the ALD 2005 Conference. **http://www.es.anl.gov/energy_systems/docs/atomic_layer_deposition/V2O5%20%20Poster%20-%20Klamut.pdf**.

245. Koltsov, S.I., Structural Changes of Silica Gel during Formation on Its Surface of Titanium Dioxide Layers. Zhurnal Prikladnoi Khimii, 1970. **43**(9): p. 1956-&.

246. Badot, J.C., et al., Atomic layer epitaxy of vanadium oxide thin films and electrochemical behavior in presence of lithium ions. Electrochemical and Solid State Letters, 2000. **3**(10): p. 485-488.

247. Chen, X.Y., et al., Ozone-Based Atomic Layer Deposition of Crystalline V2O5 Films for High Performance Electrochemical Energy Storage. Chemistry of Materials, 2012. **24**(7): p. 1255-1261.

248. Feng, H., et al., Oxidative dehydrogenation of cyclohexane over alumina-supported vanadium oxide nanoliths. Journal of Catalysis, 2010. **269**(2): p. 421-431.

249. Musschoot, J., et al., Comparison of Thermal and Plasma-Enhanced ALD/CVD of Vanadium Pentoxide. Journal of the Electrochemical Society, 2009. **156**(7): p. P122-P126.

250. Østreng, E., Nilsen, O., Fjellvåg, H.,, Optical properties of vanadium pentoxide deposited by ALD. J. Phys. Chem. C, 2012. **116**(36): p. 19444–19450.

251. Field, M.N. and I.P. Parkin, Atmospheric pressure chemical vapour deposition of vanadium(v) oxide films on glass substrates from reactions of VOCl3 and VCl4 with water. Journal of Materials Chemistry, 2000. **10**(8): p. 1863-1866.

252. Ostermann, R., et al., V2O5 nanorods on TiO2 nanofibers: A new class of hierarchical nanostructures enabled by electrospinning and calcination. Nano Letters, 2006. **6**(6): p. 1297-1302.

253. Wang, Z.L., Nanobelts, nanowires, and nanodiskettes of semiconducting oxides - From materials to nanodevices. Advanced Materials, 2003. **15**(5): p. 432-436.

254. Leyer, B., et al., Preparation of AlVO4-films for sensor application via a sol-gel/spin-coating technique. Thin Solid Films, 1997. **310**(1-2): p. 228-233.

255. Fujiwara, H., Spectroscopic Ellipsometry: Principles and Applications. John Wiley & Sons, Ltd.: West Sussex, England, 2007.

256. Langereis, E., et al., In situ spectroscopic ellipsometry as a versatile tool for studying atomic layer deposition. Journal of Physics D-Applied Physics, 2009. **42**(7).

257. Khodakov, A., et al., Structure and catalytic properties of supported vanadium oxides: Support effects on oxidative dehydrogenation reactions. Journal of Catalysis, 1999. **181**(2): p. 205-216.

258. Burton, B.B., D.N. Goldstein, and S.M. George, Atomic Layer Deposition of MgO Using Bis(ethylcyclopentadienyl)magnesium and H2O. Journal of Physical Chemistry C, 2009. **113**(5): p. 1939-1946.

259. Feng, H., et al., Catalytic nanoliths. Chemical Engineering Science, 2009. **64**(3): p. 560-567.

260. Haber, J., Fifty years of my romance with vanadium oxide catalysts. Catalysis Today, 2009. **142**(3-4): p. 100-113.

261. CRC Handbook of Chemistry & Physics, 92nd Edition, 2011-2012.

262. Juppo, M., et al., Trimethylaluminum as a reducing agent in the atomic layer deposition of Ti(Al)N thin films. Chemical Vapor Deposition, 2001. **7**(5): p. 211-217.

263. HSC Chemistry, E., Outokumpu Research Oy: Pori, Finland, 2002.

264. Watanabe, H., K. Itoh, and O. Matsumoto, Properties of V2O5 thin films deposited by means of plasma MOCVD. Thin Solid Films, 2001. **386**(2): p. 281-285.

265. Demkov, A.A., et al., Complex band structure and the band alignment problem at the Si-high-k dielectric interface. Physical Review B, 2005. **71**(19).

266. Habel, D., et al., Phase Relations in the System TiO2-V2Ox under Oxidizing and Reducing Conditions. Journal of Phase Equilibria and Diffusion, 2008. **29**(6): p. 482-487.

267. Zou, C.W., et al., Temperature sensitive crystallization of V2O5: from amorphous film to beta-V2O5 nanorods. Crystengcomm, 2010. **12**(3): p. 691-693.

268. Glushenkov, A.M., et al., A novel approach for real mass transformation from V2O5 particles to nanorods. Crystal Growth & Design, 2008. **8**(10): p. 3661-3665.

269. Spivey J.J., A.S.K., Knozinger H., Taglauer E., , Toward supported oxide catalysts via solid-solid wetting. Catalysis, 1993. **10**: p. 1-40.

270. Sankur, H. and W. Gunning, Crystallization and Diffusion in Composite Tio2-Sio2 Thin-Films. Journal of Applied Physics, 1989. **66**(10): p. 4747-4751.

271. Badot, J.C., et al., Electrical properties of V2O5 thin films obtained by atomic layer deposition (ALD). Journal of Materials Chemistry, 2004. **14**(23): p. 3411-3415.

272. Spivey J.J., A.S.K., Wachs I.E., Hardcastle F.D.,, Applications of raman spectroscopy to heterogeneous catalysis. Catalysis, 1993. **10**: p. 102-153.

273. Su, Q., et al., Raman spectroscopic characterization of the microstructure of V2O5 films. Journal of Solid State Electrochemistry, 2008. **12**(7-8): p. 919-923.

274. Chang, H. and P.J. Huang, Thermo-Raman studies on anatase and rutile. Journal of Raman Spectroscopy, 1998. **29**(2): p. 97-102.

275. Saleh, R.Y., et al., The Interaction of V2o5 with Tio2(Anatase) - Catalyst Evolution with Calcination Temperature and O-Xylene Oxidation. Journal of Catalysis, 1986. **98**(1): p. 102-114.

276. Arisi, E., et al., Preparation and characterization of AlVO4 compound. Journal of Materials Science, 2004. **39**(6): p. 2107-2111.

277. Jakschik, S., et al., Crystallization behavior of thin ALD-Al2O3 filMS. Thin Solid Films, 2003. **425**(1-2): p. 216-220.

278. Dabrowska, G., P. Tabero, and M. Kurzawa, Phase Relations in the Al2O3-V2O5-MoO3 System in the Solid State. The Crystal Structure of AlVO4. Journal of Phase Equilibria and Diffusion, 2009. **30**(3): p. 220-229.

279. Brazdova, V., M.V. Ganduglia-Pirovano, and J. Sauer, Crystal structure and vibrational spectra of AlVO4. A DFT study. Journal of Physical Chemistry B, 2005. **109**(1): p. 394-400.

280. Aramaki, S. and R. Roy, Revised Phase Diagram for the System Al2O3-SiO2. Journal of the American Ceramic Society, 1962. **45**(5): p. 229-242.

281. George, S.M., B. Yoon, and A.A. Dameron, Surface Chemistry for Molecular Layer Deposition of Organic and Hybrid Organic-Inorganic Polymers. Accounts of Chemical Research, 2009. **42**(4): p. 498-508.

282. Yoshimura, T., S. Tatsuura, and W. Sotoyama, Polymer films formed with monolayer growth steps by molecular layer deposition. Applied Physics Letters, 1991. **59**(4): p. 482.

283. Yoshimura, T., et al., Quantum wire and dot formation by chemical vapor deposition and molecular layer deposition of one-dimensional conjugated polymer. Applied Physics Letters, 1992. **60**(3): p. 268.

284. Adamczyk, N.M., A.A. Dameron, and S.M. George, Molecular Layer Deposition of Poly(p-phenylene terephthalamide) Films Using Terephthaloyl Chloride and p-Phenylenediamine. Langmuir, 2008. **24**: p. 2081-2089.

285. Du, Y. and S.M. George, Molecular Layer Deposition of Nylon 66 Films Examined Using in Situ FTIR Spectroscopy. Journal of Physical Chemistry C, 2007. **111**: p. 8509-8617.

286. Loscutoff, P.W., H.-B.-R. Lee, and S.F. Bent, Deposition of Ultrathin Polythiourea Films by Molecular Layer Deposition. Chemistry of Materials, 2010. **22**: p. 5563-5569.

287. Li, Y., D. Wang, and J.M. Buriak, Molecular Layer Deposition of Thiol-Ene Multilayers on Semiconductor Surfaces. Langmuir, 2010. **26**(2): p. 1232-1238.

288. Peng, Q., et al., "Zincone" Zinc Oxide-Organic Hybrid Polymer Thin Films Formed by Molecular Layer Deposition. Chemistry of Materials, 2009. **21**(5): p. 820-830.

289. Yoon, B., et al., Molecular Layer Deposition of Hybrid Organic-Inorganic Polymer Films using Diethylzinc and Ethylene Glycol. Chemical Vapor Deposition, 2009. **15**: p. 112-121.

290. Yoon, B., et al., Molecular Layer Deposition of Hybrid Organic-Inorganic Alucone Polymer Films Using a Three-Step ABC Reaction Sequence. Chemistry of Materials, 2009. **21**(22): p. 5365-5374.

291. Gong, B., Q. Peng, and G.N. Parsons, Conformal Organic - Inorganic Hybrid Network Polymer Thin Films by Molecular Layer Deposition using Trimethylaluminum and Glycidol. Journal of Physical Chemistry B, 2011. **115**(19): p. 5930-5938.

292. Klepper, K.B., O. Nilsen, and H. Fjellvag, Deposition of thin films of organic-inorganic hybrid materials based on aromatic carboxylic acids by atomic layer deposition. Dalton Transactions, 2010. **39**(48): p. 11628-11635.

293. Klepper, K.B., et al., Atomic layer deposition of organic-inorganic hybrid materials based on saturated linear carboxylic acids. Dalton Transactions, 2011. **40**(17): p. 4636-4646.

294. Lee, B.H., et al., Vapor-Phase Molecular Layer Deposition of Self-Assembled Multilayers for Organic Thin-Film Transistor. Journal for Nanoscience and Nanotechnology, 2009. **9**(12): p. 6962-6967.

295. Lee, B.H., et al., Rapid Vapor-Phase Fabrication of Organic-Inorganic Hybrid Superlattices with Monolayer Precision. Journal of the American Chemical Society, 2007. **129**: p. 16034-16041.

296. Cho, S., et al., High-Performance Two-Dimensional Polydiacetylene with a Hybrid Inorganic-Organic Structure. Angewandte Chemie International Edition, 2011. **50**(12): p. 2742-2746.

297. Cordero, N., J. Yoon, and Z.G. Suo, Channel cracks in a hermetic coating consisting of organic and inorganic layers. Applied Physics Letters, 2007. **90**(11).

298. Graff, G.L., R.E. Williford, and P.E. Burrows, Mechanisms of vapor permeation through multilayer barrier films: Lag time versus equilibrium permeation. Journal of Applied Physics, 2004. **96**(4): p. 1840-1849.

299. Abdulagatov, A.I., et al., Al2O3 and TiO2 ALD on Copper for Water Corrosion Resistance. ACS Applied Materials & Interfaces, 2011. **3**: p. 4593-4601.

300. Liu, J.X., et al., Sol-gel deposited TiO2 film on NiTi surgical alloy for biocompatibility improvement. Thin Solid Films, 2003. **429**(1-2): p. 225-230.

301. Shabalovskaya, S.A., On the nature of the biocompatibility and on medical applications of NiTi shape memory and superelastic alloys. Biomedical Engineering, 1996. **6**(4): p. 267-289.

302. Linsebigler, A.L., G.Q. Lu, and J.T. Yates, Photocatalysis on TiO2 Surfaces: Principles, Mechanisms, and Selected Results. Chemical Reviews, 1995. **95**(3): p. 735-758.

303. Bach, U., et al., Solid-state dye-sensitized mesoporous TiO2 solar cells with high photon-to-electron conversion efficiencies. Nature, 1998. **395**(6702): p. 583-585.

304. Gratzel, M., Photoelectrochemical cells. Nature, 2001. **414**(6861): p. 338-344.

305. Poodt, P., et al., Spatial atomic layer deposition: A route towards further industrialization of atomic layer deposition. Journal of Vacuum Science & Technology A, 2012. **30**(1).

306. Fujiwara, H., Spectroscopic Ellipsometry: Principles and Applications2007, West Sussex, England: John Wiley & Sons, Ltd.

307. Oliver, W.C. and G.M. Pharr, Measurement of hardness and elastic modulus by instrumented indentation: advances in understanding and refinements to methodology. Journal of Materials Research, 2004. **19**: p. 3-20.

308. Bradley, D.C., et al., Alkoxo and Aryloxo Derivatives of Metals, 2001, San Diego: Academic Press.

309. Reeves, R.E. and L.W. Mazzeno, The Composition of Some Tetra-t-butyl Titanate-Glycol Reaction Products. Journal of the American Chemical Society, 1954. **76**(9): p. 2533-2536.

310. Wang, D., et al., Hydrothermal synthesis and characterization of a novel one-dimensional titanium glycolate complex single crystal: Ti(OCH2CH2O)2. Chemistry of Materials, 1999. **11**(8): p. 2008-2012.

311. Miller, D.C., et al., Thermomechanical properties of aluminum alkoxide (alucone) films created using molecular layer deposition. Acta Materialia, 2009. **57**: p. 5083-5092.

312. Latella, B.A., et al., Enhanced adhesion of atomic layer deposited titania on polycarbonate substrates. Thin Solid Films, 2007. **515**(5): p. 3138-3145.

313. Liang, X., et al., Nanocoating Hybrid Polymer Films on Large Quantities of Cohesive Nanoparticles by Molecular Layer Deposition. AIChE Journal, 2009. **55**(4): p. 1030-1039.

314. Liang, X.H., et al., Ultra-thin microporous-mesoporous metal oxide films prepared by molecular layer deposition (MLD). Chemical Communications, 2009(46): p. 7140-7142.

315. Jiang, X.C., et al., Ethylene glycol-mediated synthesis of metal oxide nanowires. Journal of Materials Chemistry, 2004. **14**(4): p. 695-703.

316. Das, J., et al., A facile nonaqueous route for fabricating titania nanorods and their viability in quasi-solid-state dye-sensitized solar cells. Journal of Materials Chemistry, 2010. **20**(21): p. 4425-4431.

317. Holy, V., U. Pietsch, and T. Baumbach, High Resolution X-ray Scattering from Thin Films and Multilayers1999, Berlin: Springer-Verlag.

318. Phung, T.M., et al., Determination of the composition of ultra-thin Ni-Si films on Si. X-ray Spectrometry, 2008. **37**: p. 608.

319. Jiang, X.C., T. Herricks, and Y.N. Xia, Monodispersed spherical colloids of titania: Synthesis, characterization, and crystallization. Advanced Materials, 2003. **15**(14): p. 1205.

320. Han, J.J., et al., Fabrication of TiO2 microrod with desired shapes from rod-like titanium glycolate. Chemistry Letters, 2007. **36**(11): p. 1352-1353.

321. Ji, L.W., et al., Recent developments in nanostructured anode materials for rechargeable lithium-ion batteries. Energy & Environmental Science, 2011. **4**(8): p. 2682-2699.

322. Wu, H.B., et al., Nanostructured metal oxide-based materials as advanced anodes for lithium-ion batteries. Nanoscale, 2012. **4**(8): p. 2526-2542.

323. Fujishima, A. and K. Honda, Electrochemical Photolysis of Water at a Semiconductor Electrode. Nature, 1972. **238**(5358): p. 37-+.

324. Raulio, M., et al., Destruction of Deinococcus geothermalis biofilm by photocatalytic ALD and sol-gel TiO2 surfaces. Journal of Industrial Microbiology & Biotechnology, 2006. **33**(4): p. 261-268.

325. Park, K., et al., Effect of an Ultrathin TiO2 Layer Coated on Submicrometer-Sized ZnO Nanocrystallite Aggregates by Atomic Layer Deposition on the Performance of Dye-Sensitized Solar Cells. Advanced Materials, 2010. **22**(21): p. 2329-2332.

326. Hahn, R., et al., Semimetallic TiO2 Nanotubes. Angewandte Chemie-International Edition, 2009. **48**(39): p. 7236-7239.

327. Khan, S.U.M., M. Al-Shahry, and W.B. Ingler, Efficient photochemical water splitting by a chemically modified n-TiO2 2. Science, 2002. **297**(5590): p. 2243-2245.

328. Wang, H. and J.P. Lewis, Second-generation photocatalytic materials: anion-doped TiO2. Journal of Physics-Condensed Matter, 2006. **18**(2): p. 421-434.

329. Etacheri, V., et al., Challenges in the development of advanced Li-ion batteries: a review. Energy & Environmental Science, 2011. **4**(9): p. 3243-3262.

330. Edited by Weimer A. W., Carbide nitride and boride materials synthesis and processing. London: Chapman & Hall, 1997.

331. Abdulagatov, A.I., et al., Molecular Layer Deposition of Titanicone Films using TiCl4 and Ethylene Glycol or Glycerol: Growth and Properties. Chemistry of Materials, 2012. **24**(15): p. 2854-2863.

332. Kuo, C.S., et al., Carbon-containing nano-titania prepared by chemical vapor deposition and its visible-light-responsive photocatalytic activity. Journal of Molecular Catalysis a-Chemical, 2007. **270**(1-2): p. 93-100.

333. Wu, G., et al., Synthesis and characterization of carbon-doped TiO2 nanostructures with enhanced visible light response. Chemistry of Materials, 2007. **19**(18): p. 4530-4537.

334. Sakthivel, S. and H. Kisch, Daylight photocatalysis by carbon-modified titanium dioxide. Angewandte Chemie-International Edition, 2003. **42**(40): p. 4908-4911.

335. Ren, W.J., et al., Low temperature preparation and visible light photocatalytic activity of mesoporous carbon-doped crystalline TiO2. Applied Catalysis B-Environmental, 2007. **69**(3-4): p. 138-144.

336. Huang, C.H., et al., Photocatalytic Activity and Characterization of Carbon-Modified Titania for Visible-Light-Active Photodegradation of Nitrogen Oxides. International Journal of Photoenergy, 2012.

337. Irie, H., Y. Watanabe, and K. Hashimoto, Carbon-doped anatase TiO2 powders as a visible-light sensitive photocatalyst. Chemistry Letters, 2003. **32**(8): p. 772-773.

338. Leary, R. and A. Westwood, Carbonaceous nanomaterials for the enhancement of TiO2 photocatalysis. Carbon, 2011. **49**(3): p. 741-772.

340. Lee, B.H., et al., Growth and Properties of Hybrid Organic-Inorganic Metalcone Films Using Molecular Layer Deposition Techniques. Advanced Functional Materials, 2012.

341. Akselrod, M.S., et al., Highly Sensitive Thermoluminescent Anion-Defect Alpha-Al2o3-C Single-Crystal Detectors. Radiation Protection Dosimetry, 1990. **33**(1-4): p. 119-122.

342. Dutta, G., et al., Effects of O vacancies and C doping on dielectric properties of ZrO2: A first-principles study. Applied Physics Letters, 2006. **89**(20).

343. Trunschke, A., et al., Transition metal oxide/carbon composite catalysts for n-alkane aromatization: structure and catalytic properties. Applied Catalysis a-General, 2001. **208**(1-2): p. 381-392.

344. Hoang, D.L., et al., Zirconia carbon composites as monofunctional catalysts in C6+ alkane aromatization. Applied Catalysis a-General, 1999. **182**(2): p. 385-397.

345. Lin, Y.H., et al., Manganese Oxide/Carbon Aerogel Composite: an Outstanding Supercapacitor Electrode Material. Advanced Energy Materials, 2011. **1**(5): p. 901-907.

346. Pan, H., et al., Room-temperature ferromagnetism in carbon-doped ZnO. Physical Review Letters, 2007. **99**(12).

348. Lee, B.H., Anderson, V. R., George, S. M., Metalcone and Metalcone/Metal Oxide Alloys Grown Using Atomic and Molecular Layer Deposition. ECS Trans., 2011. **41**(2): p. 131-138.

349. Lee, B.H., George, S. M., , unpublished.

350. Ferrari, A.C. and J. Robertson, Interpretation of Raman spectra of disordered and amorphous carbon. Physical Review B, 2000. **61**(20): p. 14095-14107.

351. Ferrari, A.C. and J. Robertson, Resonant Raman spectroscopy of disordered, amorphous, and diamondlike carbon. Physical Review B, 2001. **64**(7).

352. Maultzsch, J., S. Reich, and C. Thomsen, Double-resonant Raman scattering in graphite: Interference effects, selection rules, and phonon dispersion. Physical Review B, 2004. **70**(15).

353. Chu, P.K. and L.H. Li, Characterization of amorphous and nanocrystalline carbon films. Materials Chemistry and Physics, 2006. **96**(2-3): p. 253-277.

354. Nemanich, R.J. and S.A. Solin, 1st-Order and 2nd-Order Raman-Scattering from Finite-Size Crystals of Graphite. Physical Review B, 1979. **20**(2): p. 392-401.

355. Kaspar, J., et al., Electrochemical study of lithium insertion into carbon-rich polymer-derived silicon carbonitride ceramics. Electrochimica Acta, 2010. **56**(1): p. 174-182.

356. Kostecki, R., et al., Surface studies of carbon films from pyrolyzed photoresist. Thin Solid Films, 2001. **396**(1-2): p. 36-43.

357. Sun, Z., et al., Structure and properties of hard carbon films depending on heat treatment temperatures via polymer precursor. Diamond and Related Materials, 1999. **8**(6): p. 1107-1113.

358. Matthews, M.J., et al., Raman spectra of polyparaphenylene-based carbon prepared at low heat-treatment temperatures. Applied Physics Letters, 1996. **68**(8): p. 1078-1080.

359. Kumar, S., Unhydrogenated Diamond-Like Carbon-Films Prepared by Dc Plasma Chemical Vapor-Deposition at Room-Temperature. Applied Physics Letters, 1991. **58**(17): p. 1836-1838.

360. Zheng, T., Q. Zhong, and J.R. Dahn, High-Capacity Carbons Prepared from Phenolic Resin for Anodes of Lithium-Ion Batteries. Journal of the Electrochemical Society, 1995. **142**(11): p. L211-L214.

361. Conway, N.M.J., et al., Defect and disorder reduction by annealing in hydrogenated tetrahedral amorphous carbon. Diamond and Related Materials, 2000. **9**(3-6): p. 765-770.

362. Xiang, H.Q., S.B. Fang, and Y.Y. Jiang, Carbonaceous anodes for lithium-ion batteries prepared from phenolic resins with different cross-linking densities. Journal of the Electrochemical Society, 1997. **144**(7): p. L187-L190.

363. Hunt, D.R., Jenkins G. M., Takezawa T., , The effect of tensile stress upon the resistivity of a polymeric carbon. Carbon, 1976. **14**: p. 105-109.

364. Dillon, R.O., J.A. Woollam, and V. Katkanant, Use of Raman-Scattering to Investigate Disorder and Crystallite Formation in as-Deposited and Annealed Carbon-Films. Physical Review B, 1984. **29**(6): p. 3482-3489.

365. Knight, D.S. and W.B. White, Characterization of Diamond Films by Raman-Spectroscopy. Journal of Materials Research, 1989. **4**(2): p. 385-393.

366. Gnanasekar, K.I., et al., Direct conversion of TiO2 sol to nanocrystalline anatase at 85 degrees C. Journal of Materials Research, 2002. **17**(6): p. 1507-1512.

367. Li, G.H., et al., Structural and optical properties of TiO2 thin film and TiO2+2 wt.% ZnFe2O4 composite film prepared by r.f. sputtering. Thin Solid Films, 2000. **368**(1): p. 163-167.

368. Hou, Y.Q., et al., Influence of annealing temperature on the properties of titanium oxide thin film. Applied Surface Science, 2003. **218**(1-4): p. 97-105.

369. Wang, X.D., J. Shen, and Q. Pan, Raman spectroscopy of sol-gel derived titanium oxide thin films. Journal of Raman Spectroscopy, 2011. **42**(7): p. 1578-1582.

370. Preiss, H., L.M. Berger, and D. Schultze, Studies on the carbothermal preparation of titanium carbide from different gel precursors. Journal of the European Ceramic Society, 1999. **19**(2): p. 195-206.

371. Colombo, P., et al., Polymer-Derived Ceramics: 40 Years of Research and Innovation in Advanced Ceramics. Journal of the American Ceramic Society, 2010. **93**(7): p. 1805-1837.

372. Riedel, R., et al., Silicon-based polymer-derived ceramics: Synthesis properties and applications - A review. Journal of the Ceramic Society of Japan, 2006. **114**(1330): p. 425-444.

373. Krasil'nikov, V.N., et al., Synthesis and properties of titanium glycolate Ti(OCH(2)CH(2)O)(2). Russian Journal of Inorganic Chemistry, 2008. **53**(7): p. 1065-1069.

374. Edited by Walker, P.L., Chemistry and Physics of Carbon Mercel Dekker, New York, , 1971. **7**: p. 243.

375. Babelon, P., et al., SEM and XPS studies of titanium dioxide thin films grown by MOCVD. Thin Solid Films, 1998. **322**(1-2): p. 63-67.

376. Kubart, T., T. Nyberg, and S. Berg, Modelling of low energy ion sputtering from oxide surfaces. Journal of Physics D-Applied Physics, 2010. **43**(20).

377. Koc, R., Kinetics and phase evolution during carbothermal synthesis of titanium carbide from ultrafine titania/carbon mixture. Journal of Materials Science, 1998. **33**(4): p. 1049-1055.

378. Gruner, W., S. Stolle, and K. Wetzig, Formation of COx species during the carbothermal reduction of oxides of Zr, Si, Ti, Cr, W, and Mo. International Journal of Refractory Metals & Hard Materials, 2000. **18**(2-3): p. 137-145.

379. Wu, R.L.C., et al., Physical and Tribological Properties of Rapid Thermal Annealed Diamond-Like Carbon-Films. Surface & Coatings Technology, 1992. **55**(1-3): p. 576-580.

380. Jenkins, G.M., Kawamura K., , Polymeric Carbons. Carbon Fibre, Glass and Char. Cambridge University Press, 1976: p. p. 94.

381. McCormick, J.R., et al., A four-point probe correlation of oxygen sensitivity to changes in surface resistivity of TiO2(001) and Pd-modified TiO2(001). Surface Science, 2003. **545**(1-2): p. L741-L746.

382. Graham, A.P., et al., An investigation of the electrical properties of pyrolytic carbon in reduced dimensions: Vias and wires. Journal of Applied Physics, 2010. **107**(11).

383. Pierson, H.O., Handbook of carbon, graphite, diamond, and fullerenes: properties, processing, and applications. William Andrew, 1993: p. p. 157.

384. Cordelair, J. and P. Greil, Electrical conductivity measurements as a microprobe for structure transitions in polysiloxane derived Si-O-C ceramics. Journal of the European Ceramic Society, 2000. **20**(12): p. 1947-1957.

385. Chang, H. and P.J. Huang, Thermo-Raman studies on anatase and rutile. Journal of Raman Spectroscopy, 1998. **29**(2): p. 97-102.

386. Karakuscu, A., et al., White Luminescence from Sol-Gel-Derived SiOC Thin Films. Journal of the American Ceramic Society, 2009. **92**(12): p. 2969-2974.

387. Robertson, J., Recombination and photoluminescence mechanism in hydrogenated amorphous carbon. Physical Review B, 1996. **53**(24): p. 16302-16305.

388. Casiraghi, C., et al., Bonding in hydrogenated diamond-like carbon by Raman spectroscopy. Diamond and Related Materials, 2005. **14**(3-7): p. 1098-1102.

389. Jakschik, S., et al., Crystallization behavior of thin ALD-Al2O3 filMS. Thin Solid Films, 2003. **425**(1-2): p. 216-220.

390. Katamreddy, R., et al., Post deposition annealing of aluminum oxide deposited by atomic layer deposition using tris(diethylamino)aluminum and water vapor on Si<100>. Thin Solid Films, 2007. **515**(17): p. 6931-6937.

391. Qin, X.D., H.X. Sun, and F. Zaera, Thermal chemistry of Mn-2(CO)(10) during deposition of thin manganese films on silicon oxide and on copper surfaces. Journal of Vacuum Science & Technology A, 2012. **30**(1).